# Active and Passive Aeroelastic control of Long-Span Suspension Bridges

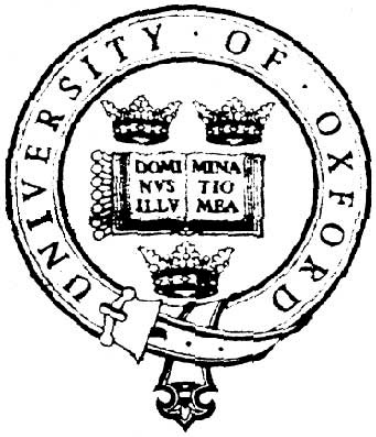


**Konstantinos Nikolaos Bakis**

Department of Engineering

University of oxford

This dissertation is submitted for the degree of

*Doctor of Philosophy (DPhil)*

New College

Hilary term 2016

To slenderness ...

# Declaration

I hereby declare that except where specific reference is made to the work of others, the contents of this dissertation are original and have not been submitted in whole or in part for consideration for any other degree or qualification in this, or any other university. This dissertation is my own work and contains nothing which is the outcome of work done in collaboration with others, except as specified in the text and Acknowledgements.

Konstantinos Nikolaos Bakis

Hilary term 2016

# Acknowledgements

A number of people have contributed greatly to the realization of the work presented in this thesis. Foremost, I would like to gratefully acknowledge my thesis supervisors Prof. Martin Williams and Prof. David Limebeer. They made this project possible, provided an excellent working environment and allowed me to pursue my interests and maintain my own research pace. The outcome of this work would not have been the same without the inspiring support and rich experience in the aerodynamic field of Prof. Michael Graham from Imperial College London. I can think of no person more apt in technical detail than Dr. Matteo Massaro, he provided an invaluable boost and contributed resourcefully to this research endeavour. I would also like to acknowledge Prof. Tom Wyatt for his helpful suggestions.

The financial support provided by the IKY-State Scholarship Foundation by means of the ESPA European fund 2007-2013 is greatly appreciated for its contribution to my research project. I would also like to gratefully thank New College and Dr. Robert Easton for their additional support.

My experience would not have been the same without the motivational support from the people in the Engineering Department of Oxford University as was all those who made my stay in the U.K. to be cherished for many years to come. Giacomo, Neo, Lea and Lida to name a few.

Last but not least I would like to thank my parents, Betty and Evangelos, and my sister, Sandra, for their patience and unconditional support. My thoughts always turned to them in times of doubt and distress.

# ABSTRACT

## Active and passive Aeroelastic Control of Long-Span Suspension Bridges

A Thesis Submitted for the degree of Doctor of Philosophy

Konstantinos Nikolaos Bakis
New College, Oxford, Hilary term 2016

Long-span bridges constitute landmark projects, whose iconic impact blends together aesthetic creativity and structural competence. The simplicity of their form is contrasted by the magnitude of their scale, and the span length, in particular, relates to the structure's technical efficiency as well as to its visual impression. Simple extrapolation of rather conventional concepts, however, does not usually lead to great progress in technological development and this might prove to be the case for the aeroelastic performance of such structures as the trend to increase their slenderness continues.

The aim of this work is to establish a framework for implementing control devices, primarily in the form of aerodynamic appendices, for suppressing aeroelastic instabilities and mitigating wind induced vibrations in long-span bridges. First, a simplified, sectional structural bridge model is created, and its interaction with a constant velocity airstream is analysed using thin-aerofoil theory. Two different passive control strategies are then considered, separately and in combination. The first makes use of trailing and leading-edge flaps adjacent to the bridge deck. The rotating motion of the flaps is triggered by the deck's movement through a combination of connecting springs, dampers and the newly introduced inerter device. The second approach combines the aerodynamic stabilizing effect of the flaps with a driving force provided by a suspended mass, placed inside the box girder. For both strategies, special attention is given to ensuring that the proposed passive control system attains optimum robustness margins, that is, maximum tolerance to the uncertainties which accompany any physical system.

The analysis is then generalized by extending it to a discretized bridge aeroelastic model, which considers full multimodal interaction. The structural component of the modelling makes use of a reduced-size finite element formulation, in which the contribution of both the girder and the main cables is combined into single structural elements, thus reducing computation effort. The introduction of aerodynamic forces follows both thin-aerofoil theory and the flutter derivatives approach and the fluid-structure interaction is cast in a state space form in the Laplace domain. This framework is particularly convenient for control analysis and design. Two control approaches are considered: an active approach, which demands an external power source and digital control system, and a purely passive mechanical network approach, building on the earlier sectional investigation. The passive control configuration proposed has the advantages of: simultaneously increasing flutter and torsional divergence limits, being easily implementable while avoiding the use of external linkages and finally dispensing the need to be anchored to a ground reference point. Implementation of the proposed feedback mechanism to the bridge aeroelastic model proves its effectiveness during the early construction stages of a suspension bridge as well as in its completed stage.

# Contents

# List of Figures

# List of Tables

# Chapter 1

# Introduction

## 1.1 Modern trends in long-span bridges

Cable supported bridges have been present since the dawn of our technological civilization. Their aesthetic appeal originates from the expression of the structure's static function. It is often the case that the structural shape offers a visualization of the flow of internal forces as well as harmonically integrating the bridge within its social and physical environment. Simplicity of form, structural efficiency and economy are the three pillars which determine the structure's social value and to this end development in structural materials and construction technology, over the past decades, has contributed greatly. It is this increase in flexibility and slenderness ratio however, that demands the need for a thorough dynamic aeroelastic analysis during the design stage. The past three decades have seen a rapid

Figure 1.1 Akashi Kaikyo Bridge.

growth in the construction of long-span cable supported bridges, especially in Japan, China

and northern Europe. The world's longest suspension bridge, the Akashi Kaikyo Bridge (central span: 1991 *m*) opened in 1998, Figure 1.1, and the world's longest cable stayed bridge, the Russky bridge (central span: 1104 *m*) was completed in 2012. Further examples of remarkable bridge innovation include the Stonecutters cable stayed bridge in Hong Kong (2009), the Normandie Bridge (1995), the East Great Belt Bridge (1998) and the Zhejiang Xihoumen Bridge in China (2009), currently the second longest suspended main span. The Hardanger Bridge in Norway, which just entered the list of the 10 longest-span suspension bridges, introduces a new era of extreme slenderness. Even by Norwegian standards, this new bridge has a daringly narrow and shallow deck for its 1310m main span, [139]. The search for slenderness is certainly economically beneficial and creates an impressive image, but ensuring that the structure remains aerodynamically stable is challenging, especially in windy environments.

Table 1.1 presents information related to the ten currently longest suspension bridges, whose aerodynamic performance is the focus of this thesis. Wind induced problems that might have been dangerous for each case as well as the adopted structural counter-measures are also presented in the table. Indeed for the five longest bridges (above approximately 1500m span length), a successful aerodynamic design necessitates the adoption of specific counter-measures. To avoid flutter instability, a central stabilizer is used for the Jiangsu Runyang Bridge and a central slot between the twin-box girders of the deck for the Zhejiang Xihoumen Bridge. Similarly, in order to suppress vortex shedding, guide vanes are implemented for the single box girder of the Great Belt Bridge [72].

The introduction of longitudinal deck slots has repeatedly been reported to enhance aerodynamic performance [203]; an additional advantage is that this configuration can simultaneously suppress the formation of large vortices in the wake [204]. The implementation of additional devices in conjunction with the slotted deck solution has also been pursued. Ueda et al. [189] investigated the effect on flutter limits when implementing vertical stabilizers (central barriers) and horizontal stabilizers (guide vanes) on very long suspension bridges, see Fig. 1.2. Wind tunnel testing following this analysis concluded

| Name | Main Span | Deck type | Aeroelastic phenomenon | Control Measure | Country | Year Built |
|---|---|---|---|---|---|---|
| Akashi Kaikyo | 1991m | Truss | Flutter | Slot & Stabilizer | Japan | 1998 |
| Zhejiang Xihoumen | 1650m | Twin-Box | Flutter | Slot | China | 2008 |
| Great Belt | 1624m | Box | Vortex | Guide vane | Denmark | 1998 |
| Yi Sun-sin | 1545m | Twin-box | Flutter | Slot | S. Korea | 2012 |
| Runyang | 1490m | Box | Flutter | Stabilizer | China | 2005 |
| Nanjing Fourth | 1418m | Box | Flutter | None | China | 2012 |
| Humber | 1410m | Box | None | None | U.K. | 1981 |
| Jiangyin | 1385m | Box | None | None | China | 1999 |
| Tsing Ma | 1377m | Twin-Box | Flutter | Slot | China | 1997 |
| Hardanger Fjord | 1310m | Box | None | None | Norway | 2013 |

Table 1.1 Ten longest span suspension bridges

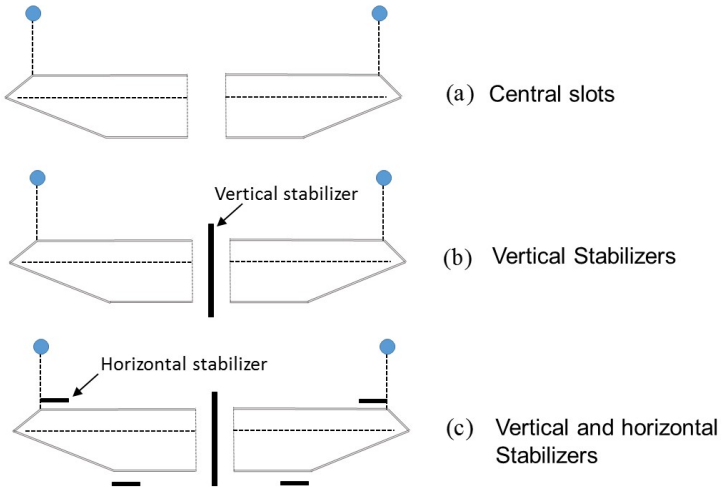


Figure 1.2 Slotted deck with vertical and horizontal stabilizers [204]

that the addition of central stabilizers increased critical flutter speed by 35% and further implementation of horizontal stabilizers resulted in a further 33% improvement. The applicability of this methodology was also investigated for the 3300*m* Messina Bridge span [29]. The effects of stabilizers is more recently investigated in [73].

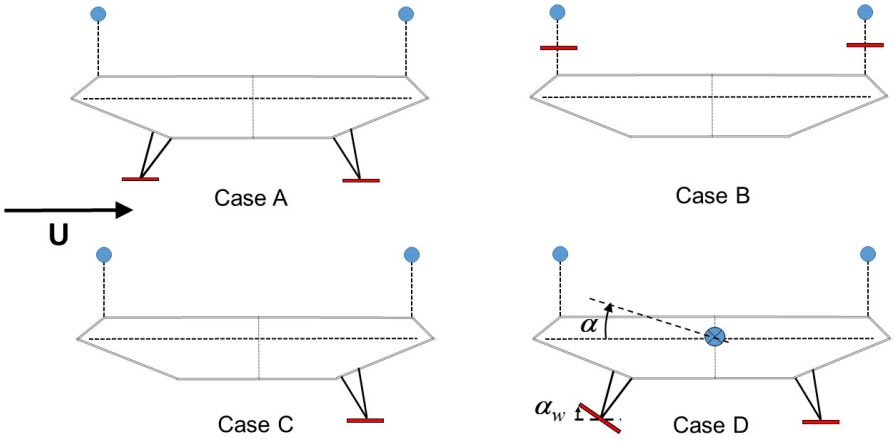


Figure 1.3 Different configurations of winglet application according to Acro and Aparicio [51].

The concept of guide vanes aims at streamlining the flow around the deck and thus suppressing the formation of Von Karman type vortices in the wake of the vibrating body. This solution is very effective against vortex-induced vibrations [107]. A logical extension of those systems is the use of winglets above or below the deck; a minimum distance between the deck and the winglets is required for the flow around the winglet to be undisturbed [79]. For the case of static winglets, if the deck is vibrating with frequency ω, the winglets are also oscillating at the same frequency. Acro and Aparicio [51] investigated four different configurations as shown in Fig. 1.3. Cases 1 and 2 were shown to increase aerodynamic damping and consequently have a positive effect on the flutter speed. Case 3 was shown to be the most advantageous one; simultaneously increasing the critical flutter and torsional divergence speed. On the other hand, cases 1 and 2 do not appear to significantly affect the point of torsional divergence instability. Case 4 corresponds to the case where the leading winglet is actively controlled, whereas the trailing flap is fixed. In the latter configuration, depending on the fixed phase controller framework adopted, care must be given to proper phase angle selection. If wrong phase delay is adopted, the bridge structure risks becoming aerodynamically unstable.

## 1.2 Wind induced vibration phenomena

It is widely appreciated that long-span bridges are prone to aerodynamic instabilities with the now iconic Tacoma Narrows Bridge disaster (1940) serving as a reminder of their importance. The Tacoma design was the immediate result of Leon Moisseiff's *deflection theory*, which replaced the less accurate *elastic theory*, which ignored cable deflections caused by live loads. This led to the use of a 2.4m deep plate girder; while this made sense statically, its poor aerodynamic performance resulted in catastrophic failure. During its four month life span, the bridge had been known to vibrate vertically, earning itself the nickname 'Galloping Gertie'. Measurements made before failure indicated a correlation between wind speed and vibrational mode: higher wind velocities favoured modes with higher frequency [67]. On the day of the collapse, a relatively modest wind speed of around 18 m/s caused a gradually growing (single-degree-of-freedom) flutter oscillation which lasted for approximately 45 minutes. Shortly before the collapse the main span abruptly began to vibrate torsionally, the magnitude quickly building up to $35^o$ from the horizontal. The transition to first torsion mode is often attributed to the loosening of the north cable, which was tied to the deck by diagonal stays.

The spectacular visual effect of the collapse, attributed to the use of the aerodynamically inappropriate squat H-section for the deck girder, had a heavy impact on the design philosophy of later suspension bridges. Subsequent designs, including the Tacoma Bridge rebuild (1950), made use of deep, open truss sections to improve torsional rigidity. In addition, many existing structures, including the Bronx-Whitestone Bridge and the Golden Gate Bridge, were strengthened [92].

While it is undoubtedly the best -known, the Tacoma Narrows Bridge was not the first suspension bridge to collapse. Several were destroyed by wind or other oscillating forces, [67], as summarised in Table. 1.2.

It is now widely accepted that wind-induced vibrations constitute the critical load case for long-span cable supported structures. Several different phenomena can result from the interaction of the structure with the surrounding fluid. Wind flow around the bridge

Figure 1.4 Collapse of Tacoma Narrows Bridge (courtesy of WSDOT).

deck is perturbed by the bridge movement, generating additional, *motion-dependent forces*. Self-excited vibrations with increasing amplitudes can result from this interaction, the most catastrophic of which is flutter. Flutter does not require flow separation and is also observed in aerofoils, which are streamlined. During flutter the aerodynamic forces act in such a way as to feed energy into the oscillating structure, which in turn responds in a divergent motion. This effect can also be thought of as negative damping, with the structure's interaction with its surroundings adding energy to the system rather than dissipating it. The flutter mode results from the coupling of at least two structural modes and it is this inter-modal interaction which allows the system to extract energy from the steady airstream.

Another aerodynamic phenomenon of common occurrence in bridges is that of *vortex shedding*. Vortex shedding is produced as a result of the turbulent wake of a bluff body in a fluid flow. A distinctive pattern of vortices can usually be seen emerging in the wake, which is carried downstream. The nature of the vortex shedding and particularly its frequency, is determined largely by the geometry of the body, the speed of the flow and the density and viscosity of the fluid. If the body is not mounted rigidly and the frequency of vortex shedding matches the modal frequency of the structure, resonance will occur driven by the energy of the flow. This phenomenon is of particular importance for oil pipes, antennas, telephone wires, submarine periscopes etc. Flexible bridges can experience vortex shedding as well, as has been often witnessed in practice. Avoidance of this type of aeroelastic

| Bridge | Designer | Length (m) | Failure |
|---|---|---|---|
| Dryburgh (Scotland) | J. and W. Smith | 79 | 1818 |
| Union (England) | Sir Samuel Brown | 137 | 1821 |
| Nassau (Germany) | Lossen and Wolf | 75 | 1834 |
| Brighton (England) | Sir Samuel Brown | 278 | 1836 |
| Montrose (Scotland) | Sir Samuel Brown | 132 | 1838 |
| Menai (Wales) | T. Telford | 177 | 1839 |
| Roche (France) | LeBlanc | 195 | 1852 |
| Wheeling (US) | C. Ellet | 308 | 1854 |
| Niagara (US) | E. Serrell | 317 | 1864 |
| Niagara (US) | S. Keefer | 384 | 1889 |
| Tacoma Narrows | L. Moisseiff | 853 | 1940 |

Table 1.2 Collapsed Suspension Bridges [67].

behaviour is usually addressed by shifting the frequency of the structure so as to avoid the *lock-in effect* or by increasing structural damping [138]. Box section girders have been known to exhibit a tendency towards larger amplitude vortex induced vibrations than truss girders.

Flutter and vortex shedding can occur under uniform flow without the presence of external disturbances. *Buffeting* on the other hand, results from the inherent wind gustiness and is mathematically treated as a stationary stochastic process. Buffeting is not an instability in the sense that it leads to divergent oscillations, but it can be problematic from the standpoints of fatigue, user discomfort, or serviceability. Air flow fluctuations can also appear due to the wake of another body located upstream, the phenomenon is then termed *wake buffeting*.

*Torsional divergence* is a very different phenomenon than the ones previously described in the sense that it is a nonconciliatory-type of instability caused by aerostatic torsional loading. It is sometimes referred to as *lateral buckling*, and represents a condition wherein, given a slight deck twist, the drag load and the self-excited aerodynamic moment will precipitate a torsional instability [56]. Simiu and Scanlan [175] presented a simple but

very accurate approach for computing the critical divergence speed, given by the following simple formula

$$U_D = \sqrt{\frac{2K_a}{\rho B^2 C'_{M0}}}, \tag{1.1}$$

where $K_a$ denotes the structure's torsional stiffness; $\rho$ is the air density; $B$ is the deck width; and $C'_{M0}$ is the pitching moment coefficient derivative with respect to zero angle of attack.

The problem of wind induced vibrations is relevant to the construction phase of the bridge as well as to the completed structure. Free standing pylons and girders during erection before closing are very flexible and their aeroelastic response can represent a more demanding load case than that of the completed structure.

Cables may also exhibit various forms of wind-induced vibrations. Incidences of large-amplitude vibrations of stay cables have been reported worldwide on a number of cable-stayed bridges. The most widely cited cause is the phenomenon of *rain-wind vibration*, driven by the formation and movement of water rivulets on the cables. The frequent occurrence of this phenomenon in cable-stayed bridges has raised considerable concern [65, 131].

Other types of wind induced vibrations of cables include *wake galloping*, which occurs in parallel cables when spaced between 3 and 5 cable diameters. Violent vibrations of this type have been observed in the suspended cables of the Akashi Bridge. *Vortex induced vibrations* of cables is also common. However, their amplitude is small and introducing a small amount of damping can often remedy the problem. To add to the complexity of the problem, motion of the cables is coupled with that of the girders and pylons, thus resulting in a non-linear interaction among the various structural components of the structure. Cables being much more flexible than the girder and pylons are more susceptible to large amplitude vibrations and their geometric non-linearity needs to be taken into account.

It is worth stressing that the mathematical description of wind-induced vibration phenomena flounders on the non-linearities of the problem at hand. Fluid non-linearities and

the complexity of the fluid-structure interaction has hindered the development of a full analytic treatment of wind induced vibrations. For many decades wind tunnel testing using full and sectional models has been the only reliable method for predicting the performance of the structure in wind flow. A parallel development in the field has been the use of computationally demanding methodologies based on *computational fluid dynamics* (CFD). CFD has made considerable progress in recent years and has been used as a supplement to experimental investigations. With continued rapid development, CFD is expected to become a powerful analysis and design tool; however it may take some time for it to form a complete replacement of wind tunnel testing due to the deck section's geometrical complexity and the three-dimensional nature of the fluid-structure interaction phenomenon.

## 1.3 A control approach to the problem

Since the Tacoma Bridge collapse, engineers have considered many possible modifications to the aeroelastic properties of new and existing bridge structures. Three different solution paradigms (which may be used in combination) are [12]:

1. Modify the deck's aerodynamic design by introducing variations in the deck cross section.

2. Modify the design of the suspension system so as to adjust beneficially the bridge's critical structural mode shapes and modal frequencies, or modify the structural system to increase bridge stability.

3. Introduce static or actively controlled devices to suppress wind-induced vibrations.

An early example of change in the aerodynamic and structural design methodology was the introduction of the deep open-truss section. This new deck form demonstrated better aerodynamic behaviour, because of the flow through the girder, as well as increased torsional stiffness. For these reasons, truss girders were used for the Tacoma Bridge Rebuild (1950) as well as for the Akashi Bridge, even though for the latter case box girders were

extensively considered. An alternative approach, first employed for the Severn Bridge, adopted the use of the trapezoidal box girder. Although the box girder was not a new invention, it would be the first time it was incorporated into the design of a long-span suspension bridge. Box girders have been known to offer significant advantages over traditional truss type decks. More specifically, the premise behind this deck system is that it simultaneously provides high torsional resistance, reduces aerodynamic drag forces, reduces deck weight and because of its streamlined character helps eliminate destabilizing vortices.

However, it is generally accepted from experience gained from record breaking projects, such as the Akashi and Great Belt East Bridge, as well as from technical insights gained from the design process of the proposed Messina Bridge, that classic aerodynamic design reaches its limit for spans approaching 2000m [54]. The third alternative aims to raise this ceiling by employing active or passive mechanical controllers. A relatively recent example of this approach, never yet implemented in practice, is the introduction of controlled aerodynamic surfaces of the type shown in Fig. 1.5. The broad methodology is to locate controllable aerodynamic surfaces above, below, or alongside the main deck in order to modify its aeroelastic loading.

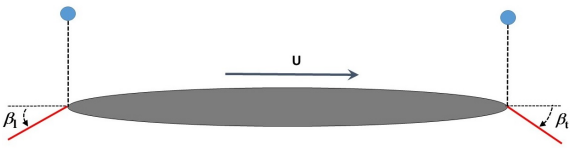


Figure 1.5 Cross section of a streamlined long-span suspension bridge with flutter suppression controllable flaps. The wind speed is denoted as $U$.

## 1.4 Scope of Study and Thesis Objectives

The work at hand will focus on flutter, the most catastrophic of aeroelastic phenomena, and will build upon an existing theoretical framework for employing actively and passively controlled leading-and trailing-edge flaps in combination. The presented analysis will

firstly cover the formulation of a reduced size finite element (FE) framework for capturing suspension bridge modal characteristics. The aerodynamic analysis will examine the implementation of thin aerofoil theory into the FE model, as well as the modification of this theory to account for the deck's bluffness using flutter derivatives. The control investigation will be based on both active and passive frameworks, and its effectiveness will be validated both using a simple sectional bridge flexible model and the FE based multi-modal model. to summarize, the major objectives of this work are the following:

- Development of a computationally efficient and reliable aeroelastic framework, which considers the full multi-modal interaction of a long-span suspension bridge.
- Comparison of different aerodynamic loading assumptions, i.e. thin aerofoil theory, experimentally obtained aerodynamic derivatives, and assessment of the resulting aeroelastic boundaries.
- Modelling of adjacent to the deck flap kinematic mechanisms and implementation of the flap aerodynamic contribution to the deck-flap system.
- Design of an active control framework controlling flap angles for system stabilization at high wind speeds.
- Examination of maximum achievable robustness margins for the controlled system and the factors which mostly affect them. This part of the analysis aims at ensuring that the proposed methodology is less susceptible to modelling errors and simplifications as well as physical uncertainties not accounted for in the design process.
- Investigation of model reduction techniques that reduce the size of the proposed aeroelastic framework in order to facilitate the design process of the control mechanisms.
- Because active schemes often result in complicated control methodologies emphasis will be placed on the development of low order mechanical networks which are

easily implementable and provide a reliable and cost-effective alternative for building longer and more slender span openings.

## 1.5 Thesis outline

This thesis is organized as follows. Chapter 2 presents a literature review of aerodynamic issues affecting cable supported bridges, and of advances in the implementation of different active and passive control techniques. Chapter 3 revisits a method for dynamic analysis of vertical, torsional and lateral free vibrations of suspension bridges based on a linearized theory and the finite element approach. The method is based on expressing the potential and kinetic energy of vibrating members and subsequently adopts finite element techniques to discretize the structure. The structural approach is validated by comparing the computed modal characteristics of the Humber and Great Belt Bridges with more computationally expensive analyses and *in situ* measurements taken from the literature. The deck erection process of the Humber bridge is also modelled, with particular importance placed on the early stages of deck assembly, when the bridge exhibits high vulnerability to flutter.

Chapter 4 presents the finite element formulation of aerodynamic forces expressed in the *Laplace domain* by using a high-fidelity rational function approximation. *Circulatory* aerodynamic forces are modelled using a feedback loop for each element and the problem is expressed in a form suitable for implementation of modern control techniques. The implementation of flutter derivatives in a similar framework is carried through. The attained aeroelastic limits for the Humber and Great Belt Bridges are compared against experimental data from the literature.

In Chapter 5 the design of actively controlled flaps is performed on the full FE model. In order to account for modelling errors and uncertainties while designing the controller, elements from *robust control* theory are invoked. The stability and robustness of the bridge when fitted with flaps controlled by *optimal and suboptimal $H_\infty$ controllers* is discussed for varying lengths of control surfaces along the suspended span, as the optimum configuration for aerodynamic performance is investigated.

Chapter 6 investigates ways to passively suppress wind-induced instabilities, such as flutter and torsional divergence. The control system design is based on a simplified sectional bridge model and two different strategies are considered separately and in combination. The first makes use of trailing and leading flaps adjacent to the bridge deck, the motion of which is triggered by the deck's movement through a combination of springs, dampers and inerters at the hinged connection. Emphasis is placed on the effect of the flap hinge location and an optimization procedure is used to determine compensator parameters that result in favourable aeroelastic properties. The second approach re-examines the efficacy and limitations of using Tuned Mass Dampers (TMDs) placed inside the bridge deck for controlling self-excited motion. It concludes by combining the two approaches and introducing a kinematic constraint between the mass of the TMD and the flaps. This combined mechanical system, referred to as the *Flap Mass Damper* (FMD), combines favourable aerodynamic properties of the flaps with a driving force provided by the vibrating mass.

Chapter 7 examines the efficacy of the first of the passive control methods on the finite element bridge aeroelastic model and particular emphasis is placed on the early stages of the deck erection process. The tuning of the mechanical network is based on a nonlinear optimization algorithm. Model reduction techniques are assessed and implemented on the model to facilitate the optimization procedure. Multimodal interaction is observed at the various erection stages and observations are made with regard to mode contributions to aeroelastic instabilities. Chapter 8 presents the conclusions of this thesis.

# Chapter 2

# Literature Review

## 2.1 Introduction

This chapter presents a concise survey of the relevant background literature. It begins by reviewing models of the key aeroelastic phenomena affecting long-span bridges, before considering the main methods of computational analysis. It then reviews the broad area of vibration control of bridge decks, before focusing on the use of control surfaces, which will be the main focus for the remainder of this thesis.

## 2.2 Aerodynamic Phenomena in Long-Span Bridges

The field of aerodynamics covers a very wide spectrum of physical phenomena, it is therefore imperative to restrict the literature review to focus on the developments which are most relevant to this work. The early $20^{th}$ century introduced deflection theory, which fuelled the interest of bridge designers to the importance of aerodynamic effects. Deflection theory enabled significant material savings by dramatically reducing deck stiffness. The most significant downside of this deck thinning trend was that it resulted in well recorded wind-induced motion phenomena in bridges of the 1930's era and eventually to the Tacoma collapse [35]. However, in many occasions the wind resistant design had already been discussed by bridge designers. Navier as early as 1823 devoted a chapter of his book to the

effects of wind. Telford's Menai bridge completed in 1826 raised extensive discussions in the engineering community of the time, after wind induced vibrations had caused extensive damage three times, which eventually led to the reconstruction of the deck and replacement of the hangers [35]. John Roebling in the United States commented on the Wheeling Bridge failure and gave a simple explanation on how wind loading produced the observed undulations on the deck [152].

In the extensive investigation, which followed the Tacoma collapse [64, 8], a wide range of technical aspects was covered, ranging from experimental techniques over aerodynamics and structural dynamics to guidelines for bridge design. The work by Maher [121], Vincent [193] and Walsche [195] added further insight into the use of wind tunnel experiments on scaled deck segments for verifying aerodynamic stability. Further versatility in wind tunnel sectional modal testing was provided by Davenport [50], who first introduced the mathematical framework for predicting buffeting response based on aerodynamic section data. Wind tunnel experiments constitute ever since a tool of paramount importance for the prediction of aeroelastic phenomena such as flutter and buffeting. A celebrated example of wind tunnel testing technology was the thorough aeroelastic investigation of a 40m long full scaled model of the Akashi-Kaikyo Bridge [136, 137].

### 2.2.1 Flutter of Bridges

The mathematical description of fluid-structure interaction phenomena originated, as would be expected, from the aeronautical field. The concept of flutter was one of the first to be studied in depth. Initially, Ludwig Prandtl developed the lifting line theory from circulation theory, which predicted lift and induced drag for finite span wings. In 1922, Prandtl's student Walter Birnbaum [22] published his thesis "The two-dimensional problem of the flapping wing". For the first time, wing flutter was described as a structural dynamic stability problem. Birnbaum considered an aerofoil which, during flight "carried out a periodic up and down movement, where, simultaneously, the angle of attack may be changed by

a rotation of an airfoil". He also used the term *reduced frequency* as a key parameter to describe *flow unsteadiness* [199].

Two years later, In 1924, Herbert Wagner introduced the *Wagner function*, [23], which describes the lift evolution acting on a theoretical flat plate given by the step change of the attack angle. in 1934, Theodorsen [186] at NASA developed the theory of lift and moment acting on a sinusoidally oscillating two dimensional airfoil. Theodorsen's seminal work laid down the theoretical foundation for treating the airfoil flutter problem and it has been up to the present time the description more extensively used [68]. Kussner, [56], later on introduced the concept of acceleration potential, formulated for three dimensional oscillating lifting surfaces. Sears [172] also derived the corresponding oscillatory lift on an airfoil.

In the bridge related aerodynamic field it was Bleich [24] who first pioneered the analytic description of the flutter problem based on Theodorsen's analysis using the thin plate assumption. Additional efforts to link bridge deck flutter to aircraft wing flutter continued by resorting to wind tunnel experiments [173]. Laboratory investigations revealed that Theodorsen's aerodynamic formulation when applied to the Tacoma Bridge deck section estimated significantly higher critical flutter speed than were found in the wind tunnel. This finding in combination with the ever more popular use of deep-truss sections at the time dismissed the applicability of aerofoil flutter coefficients for aerodynamic bluff sections such as bridge decks. It was Pugsley [170] who first suggested that experimentally determined aerodynamic coefficients rather than Theodorsen's theory may provide a more accurate description of aerodynamic phenomena.

In later years, Scanlan [169, 175, 163] played a decisive role in the adoption of flutter derivatives in bridge aerodynamics. He argued that complex deck forms preclude the use of the so-called *flat-plate derivatives*, necessitating the use of experimentally-derived derivatives instead [162]. Ironically, increasing use of streamlined shallow box girders, such as the ones used for the Severn and Great Belt Bridge, which form a modern alternative to massy truss deck sections, mitigate flow separation and allow Theodorsen's force description to

yield good aeroelastic predictions. With regard to the experimental identification of flutter derivatives it was observed that in spite of complex wind-structure interaction phenomena, bluff deck motion displayed almost pure sinusoidal or damped sinusoidal response [165]. This important finding enables the use of simple means for experimentally extracting the associated oscillating wind force coefficients. In that respect different techniques have been developed, which are usually grouped in two distinct categories. The first is based on direct measurements of aerodynamic force components using dynamometers, strain gauges and so on when the body is given a specific motion. The second category is to assess forces indirectly from the body's induced motion [169, 70].

Ukegushi et al. [190] was one of the first to apply the direct approach on deck sections. When the rigid deck section is set in harmonic motion in a wind flow which ranges in frequency and amplitude forcing in the supports is retrieved. The forced vibration process was further developed in Japan [148] to cover various aerodynamically bluff sections and also investigate related nonlinear characteristics [70]. The indirect method was introduced by Scanlan [169] and has been very popular in the bridge engineering community ever since [161]. Further development of the latter method relies on System Identification (SI) techniques which have been developed in parallel in Europe, USA and Japan [90].

The common practice of measuring aerodynamic properties is to set up the wind tunnel experiments in smooth, uniform flow. The effect of turbulence on the accuracy of the results has been traditionally regarded of secondary importance [175]. However, turbulence effects have been reported to be very significant when considering full scale models or the bridge structure itself [197]. A striking example corroborating this claim is the Lions' Gate Bridge in Vancouver Canada, which when tested in smooth flow using both a sectional and a full aeroelastic model yielded a much lower critical flutter speed than when considering atmospheric turbulence [87]. It is worth stressing that although flutter is accompanied by shed vortices, the nature of these vortices is different than the vortex shedding phenomenon. In the flutter case vortices are shed with frequency equal to the flutter frequency, in the vortex-induced oscillation case the large oscillations occur because

the frequency of alternating vortices convected in the wake matches the structure's natural frequency. In the latter case the larger amplitudes will alter the frequency of alternating vortices and the vibrations will be eventually damped out. In flutter, when the wind speed increases above the critical flutter velocity so will the oscillations of the bridge [56].

### 2.2.2 Buffeting of Bridges

Bridge aerodynamic performance is not only concerned with stability issues but also with the structure's response to gusty wind as this might cause structural fatigue and user discomfort. As opposed to flutter and torsional divergence, buffeting is not a fluid-structure interaction process in the sense that the structural motion to a first approximation does not influence the wind flow. Buffeting can be thus defined as the system's random response to wind forces associated with pressure fluctuations on the deck due to wind gustiness over the section. The analytic approach developed by Davenport [48] laid down the theoretical foundations for the first thorough investigation of this phenomenon. Davenport's spectral approach for predicting buffeting forces on a bridge deck is a statistical method, based on the earlier work by liepmann [114], in which wind loading is described as a stationary stochastic process. This procedure models the aerodynamic loading by means of power spectra of turbulent velocity components. It is usually considered that the typical size of the turbulent field at frequencies corresponding to the lowest bridge eigenmodes is much larger than deck width, which implicitly assumes that a long span bridge structure is a thin line spanning the wind field [108]. Later work by Scanlan [168, 167] considered the implementation of experimental flutter derivatives in the analysis of the buffeting response.

The original buffeting formulation was based on a series of simplifying assumptions the most important of which was the *quasi-steady* and the *strip* assumption. The quasi-steady assumption means that the instantaneous forces on the deck are considered equal to the steady forces caused by the wind flow with the same relative velocity and direction. The strip assumption means that the aerodynamic forces on one strip are only due to the incident wind fluctuation on that strip. The strip assumptions and its implications on aerodynamic

loading has been recently discussed in [128] for the case of incident turbulence buffeting. The assumption was shown to hold accurately when considering typical for long span bridge deck platform aspect ratios, wavelengths of structural modes, and length scales of incident turbulence.

A frequency-dependent correction to the steady aerodynamic forces was implemented by Sears [172] commonly referred to as *aerodynamic-admittance* and later adopted by Liepmann [114] and Davenport [49]. The concept of the *joint acceptance* function was also introduced to consider the effectiveness of the temporal and spatial cross-correlation of buffeting loading, which was assumed to be the same as that of wind turbulence [204].

The initial buffeting formulation was based on a frequency domain method, according to which the buffeting response is analyzed mode by mode. Lin et al [116] presented a time domain method using Ito's stochastic differential equations. Lin and Yang [117] further extended this method by proposing a general linear multi-mode buffeting methodology to predict deck response to turbulent wind in the time domain. Katsuchi et al. [96] reshaped the frequency domain approach and applied it to the Akashi Bridge. A fully coupled buffeting analysis of the Tsing Ma bridge in Hong Kong was performed by Xu. et al [205] with aerodynamic forces not only on the deck but also the main cable and bridge towers.

### 2.2.3 Vortex Shedding

Vortex shedding is an aeroelastic response caused by boundary layers developing along the deck surface. These produce vorticity which is shed in the form of alternating propagating downstream vortices and result in periodic crosswind forces on the deck. Vortex shedding can result in significant, but limited, amplitude vibrations on bridge decks because of the *lock-in* phenomenon. It is mostly common in low wind speed and low turbulence conditions, see Fig. 2.1. The susceptibility of a structural mode to vortex-induced resonance is indicated by the *Scruton number*, a dimensionless mass-damping parameter [133]. Modes with Scruton number lower than 15 are usually found to be problematic [59].

For slender structures such as chimneys and antennas suppression of the vortex-shedding phenomenon can be easily accomplished by using helical strakes for disrupting span-wise flow correlation. For bridges the implementation of guide vanes adjusts the flow around the deck and helps avoid the formation of a *vortex sheet* in the wake. Guide vanes of this type were fitted to the lower corners of the Great Belt Bridge in Denmark [107]. For the case of Trans-Tokyo crossing, completed in 1997, during the construction of the crossing, significant vibration due to vortex shedding was observed. Vortex shedding was also confirmed in extensive wind tunnel experiments using sectional and three dimensional models [65]. For mitigating these vibrations TMDs inside the box girder and aerodynamic flaps were installed, resulting in significant aerodynamic improvement. The analytic treatment of the vortex shedding phenomenon has not yet been properly formulated due to the complexity of the structure-fluid interaction involved [61], however the Scanlan model can be used for computing the deck forces at lock-in conditions [175].

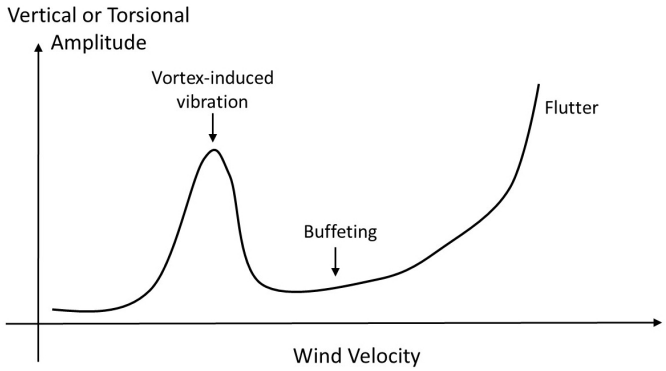


Figure 2.1 Sketch of wind-induced vibrations against wind speed. The plot shows the dominant aerodynamic effects, combinations of such phenomena can arise.

## 2.3 Computational methods in bridge aerodynamics

The analysis presented in this thesis will almost entirely focus on suppressing flutter instability. Consequently it is of importance to review computational techniques for flutter analysis on structural bridge models. Finite element based aeroelastic analysis traditionally has been expressed in the frequency domain, and demonstrated by various researchers

e.g. [7, 140, 141, 12, 178]. The procedure followed therein, with respect to modelling aerodynamic forces, is the implementation of the traditional approach, where an iterative procedure is followed both for the wind speeds as well as for the frequencies of the oscillating forces. Standard algorithms inherited from the aeronautic industry include the *k-method* and the *(p-k)-method* [83]. In terms of the bridge structural modelling using the finite element approach, the bridge structure is assumed to be divided into a system of discrete elements connected at the nodal points. The mass and stiffness matrices of the entire bridge are then formed by evaluating the properties of individual elements and superimposing them appropriately [158].

The aerodynamic loading distribution most commonly follows the strip theory assumption for long span suspension bridges. In that regard the interaction between air stream and bridge deck is to be decided in a two-dimensional section perpendicular to the longitudinal axis of the structure. Consequently, any three-dimensional effects along the longitudinal axis of the structure are assumed negligible [70]. the applicability of strip theory is however undermined at the early erection stages of a suspension bridge when the bridge deck's length is considerably smaller. Considering a mid-span to pylons erection process the open ends of the deck would inevitably introduce three-dimensional effects of air flow, which is not a negligibly small fraction [183]. An experimental investigation of this effect demonstrated that for the case of the shortest deck, typically 2 to 3 times longer than the deck width, the strip theory assumption would result in a lower critical wind speed, than in reality, by approximately 6%, [185].

The applicability of strip theory in the case of buffet by incidence turbulence is more questionable. It has been argued that the assumption is valid only when the incident gusts have much larger scales than the characteristic length of the bridge deck. Based on the strip assumption, the span-wise coherence of the aerodynamic forces can be represented by the span-wise coherence of the incident wind velocity fluctuations [108]. The span wise correlation is commonly expressed by an empirical exponential function. However, for the buffeting lift forces on modern closed-box girder bridge decks, the deck width, being

$B \simeq 20-35m$, can be close to the length scales of the vertical components of the gusts in the span-wise direction ($\simeq 30-50m$). For such cases, secondary span-wise flow could be present as well as redistribution of pressures indicating the failure of the strip assumption as originally assumed by Davenport's theory [103]. For the flutter case where smooth flow is considered, the flow perturbations, similarly to turbulence length scales, are related to the vibration mode near flutter wind speed. For the lower flutter modes, which result from the interaction of lower vibrational modes it is expected that length scales are large, comparable to the main span's length, and consequently the strip approximation works very well for predicting self-excited phenomena when the bridge is complete.

Although, the turbulence length scale effect for buffeting is very important for wind tunnel testing it was recently demonstrated by Massaro and Graham [128] that regardless of the turbulence length scales, when the structure's aspect-ratio (ratio of the cross-stream length of the body to the streamline direction) is large, three-dimensional effects are negligible on the aerodynamic admittance, provided the correlation between strips is taken into account. This is because the reduction of the sectional lift coefficient for small length scale of turbulence is balanced by its increased span-wise correlation. It is thus concluded that the importance of three-dimensional effects is aspect-ratio dependent, an aspect ratio which is very large for long-span flexible bridges and thus advocates the use of strip theory for buffeting simulation.

The afore-mentioned computational procedures aim at determining the conditions at the flutter boundary. The flutter boundary corresponds to conditions for which one of the vibrational modes has a simple harmonic time dependency. For wind speeds lower than this aeroelastic limit all modes of motion are convergent. The assumption that the solution involves simple harmonic motion is used in order to solve the equations of motion at the instability limit rather than finding a solution for the generalized equation of motion. As expected, this methodology cannot capture modal damping for arbitrary wind flow conditions but it is accurate in the vicinity of the flutter instability. The primary advantage of this procedure is that unsteady linear aerodynamic loading which corresponds

to simple harmonic motion of the surface is sufficient for this case, which demands an easier formulation than the arbitrary motion case. The flutter problem thus consists in finding the lowest wind speed and corresponding frequency at which the deck exhibits harmonic oscillation. The lowest wind speed and the associated frequency are commonly referred to as *flutter speed and frequency*. The mathematical formulation of this problem results in finding solutions of a high order polynomial equation, the *flutter determinant*, which requires a tedious, iterative process.

The previously mentioned k and (p-k) methods concentrate on providing simpler alternatives for extracting the roots of the flutter determinant and thereby identifying the stability limit. The k-method, or U-g method, introduces an artificial structural damping factor $g$, and then a root of the equation represents a point on the flutter boundary if the corresponding value of $g$ equals the assumed value of $g$ [60]. The damping force is proportional to the displacement and in phase with the velocity [83]. The k-method although popular because of its computational efficiency has received heated criticism due to the artificial damping characteristics which can in certain circumstances lead to very erroneous results. The p-k method also known as the *frequency matching method* has been the methodology most widely adopted in the aeroelasticity field. It attempts to improve upon the k-method for sub-critical and supercritical flutter conditions by allowing the reduced frequency to be complex instead of introducing the structural damping factor $g$. The p-k method is less susceptible to errors but more computationally demanding [77].

The afore-mentioned frequency approaches however, are accompanied by several disadvantages: Firstly, one must seek out the resonant frequencies one at a time. Second, one must distinguish between single- and coupled-mode cases. This becomes particularly inconvenient when large modal combinations are possible. Thirdly, during the design exercise, one cannot form a clear picture as to how design changes are influencing the aeroelastic stability of the structure as a whole, which may possibly include multiple flutter as well as multiple divergence modes [115].

The duality of the frequency and time domain formulation was initially elaborated by Garrick [69]. In the bridge aerodynamic field it was again Scanlan who first worked on solving the problem in the time domain, Scanlan et al. [166], by introducing *indicial functions*, which had preceded in the aeronautical field [23]. Bucher and Lin [34] employed an alternative formulation based on *impulse type functions* rather than indicial functions and investigated the stochastic stability of a bridge considering wind loading to be a random process. A modelling hindrance associated with the use of indicial functions is the fitting process to the experimentally obtained aerodynamic derivatives. It is only recently that much effort has been afforded to the development of efficient time domain formulations of the unsteady aerodynamic forces that can be combined with nonlinear finite element codes [70].

An example of a nonlinear aerodynamic force model would take into account the non-linear dependence of aeroelastic forces on the effective angle of incidence. Non-linear aeroelastic models become ever more necessary with the adoption of innovative bridge deck designs, which can exhibit significant sensitivity with respect to the effective angle of incidence [42]. Experimental investigation of how turbulence can affect the angle of incidence to a degree that a non-linear aerodynamic framework is significantly more realistic was given in Zasso and Curami [206]. Kovacs [100] presented a time domain approach combined with a finite element formulation geared towards buffeting response estimation based on quasi-steady aerodynamic forces. In order for the quasi-steady assumption however to be reasonable the reduced velocity should be sufficiently high such that the effect of the *unsteady fluid memory terms* is small. A control based approach based on a state-space model for buffeting response estimation was later developed by Chen and Kareem [41].

Another approach for describing self-excited aeroelastic phenomena makes use of *rational function approximations* of the Laplace variable for modelling unsteady aerodynamic forces [174]. Such rational function approximations (RFAs) allow the equations of motion to be cast in a linear time-invariant (LTI) state-space form, although the size of the

state vector increases due to the RFAs. Operational methods (and the Laplace transform) were initially introduced by Jones [91] and Sears [171] in their desire to study transient phenomena. More on high-fidelity approximations in steady state problems can be found in Peters [151]. Rational approximations of the Theodorsen function and other irrational quantities allow one to to replace techniques such as the k-method and the (p-k)-method with classical control devices and makes the iterative process redundant as was presented by Omenzetter et al. [146] and Chen et al. [43] for thin aerofoil and flutter derivatives respectively.

Diana et al. [53] developed the so-called *corrected quasi steady method* by introducing the concept of equivalent realization of force coefficients for each reduced velocity. This formulation has been proven to be adequate in many ways, except it does not consider aerodynamic memory effects and the span-wise coherence of the lift forces. More recent attempts have focused on a new approach which tries to take into account all the aerodynamic non-linear effects by means of a *rheological model* in the time domain [55].

More recent developments in the field of computational bridge aerodynamics involve probabilistic analyses in order to account for parametric uncertainty and provide confidence intervals in the aeroelastic stability estimation. Ge at al. [74] used three approaches based on first-order reliability method (FORM) to assess failure probability of bridge flutter. Pourzeynali and Datta [154] resorted to reliability theory to consider uncertainties in modelling stiffness, mass properties, damping and flutter derivatives. Cheng at al. [45] introduced a framework combining the advantages of different reliability methods which can assess the reliability of complex structures of which the limit state functions are not known explicitly. *Monte Carlo Simulations* (MCS) provide another root to estimating the likelihood of instability. This method uses randomly generated samples of input variables in a deterministic framework and records the number of time failure occurs. Failure probability is established after numerous repetitions of deterministic analysis [45]. Recent advances in the application of MCS in bridge aeroelasticity are reported in [11, 123].

## 2.4 Vibration control for bridge girders

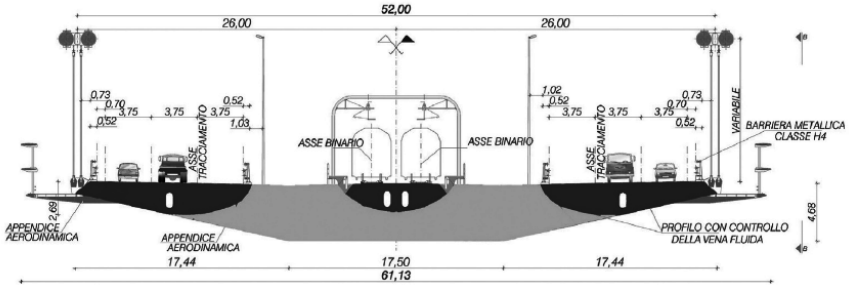


Figure 2.2 Cross section of the triple-box girder of the Messina Bridge [28].

Increasing span lengths pose a challenge to aeroelastic stability and experience gained on projects such as the Akashi Kaikyo Bridge and Great Belt East Bridge revealed that classic aerodynamic design, either in the form of deep truss girders (Akashi Bridge) or the more modern flat box girder solution (Humber, Bosporus, Great Belt), reaches its limit at span lengths approaching 2000m [54, 130]. Attempts to extend this limit can be broadly categorized in three groups. The first approach is to reduce aerodynamic forces by altering the shape of the deck section. For example, the proposed triple-girder deck solution with a total width of 60m for the 3,3km long Messina Strait Bridge, see Fig. 2.2, results in an estimation of flutter wind speed of 80m/sec [203]. Larsen has shown that improved aerodynamic performance can be achieved by *deck slotting* [109]. Other examples include vertical and horizontal stabilizers [122] and fixed winglets [119]. Static winglets were also investigated for the Messina Bridge design case [29]. Guide-vanes, see Fig. 2.3, have been proven to be an effective counter-measure against vortex shedding induced oscillations and have also been reported to increase slightly the critical flutter wind speed [107]. Appendages of this kind are enticing to engineering practise as they can be applied as a retrofiting measure to alleviate aerodynamic effects unforseen in the design stage, [143]. These methods also have the advantage of providing a passive solution to the problem. However, as span lengths increase, the economic efficiency of these methods decline due to a necessary increase in the girder separation. Additional difficulties include; the

construction of long span cross-beams between girders and the erection of tower columns appropriate for such super-long-spans [113].

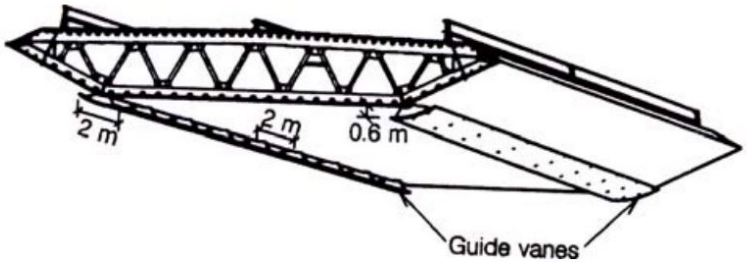


Figure 2.3 Arrangement of guide vanes along the bottom side panel joint of the Great Belt suspension bridge cross section [107].

The second approach focuses on structural modifications primarily related to the cable system for improving torsional stiffness [75]. Enhancing the structure's torsional rigidity or affecting the stiffness distribution, which aim to uncouple the lower torsional and bending modes, (or both if possible) can be achieved by adjusting the position and form of the cables and hangers [13]. Different configurations have been proposed and are usually grouped according to the number of main span cables needed: one, two, three or four. This methodology has some advantages in terms of improved stability boundaries, it requires however a much more complicated construction process and is accompanied by increased material costs.

The last category involves the installation of additional facilities for generating stabilizing forces. A passive approach implementation using tuned mass dampers (TMDs) has been investigated in depth by various researchers. This approach can be further classified in control of flutter and buffeting using single tuned mass dampers TMDs [66, 40, 118] or multiple TMDs (MTMDs) [102, 155]. The associated tuning parameters are usually derived using simplified design formulas [52, 66]. This tuning strategy seeks to calibrate the TMD degrees of freedom close to the frequencies corresponding to the structure's vertical and torsional symmetric modes, which predominately participate during flutter coupling. It is well established however, that the TMD performance is significantly degraded by off-tuning or off-optimum damping in the TMD network [102]. For this reason, a double TMD

solution was proposed in [88], without however resulting in considerable improvement in robustness. The MTMD mechanism, consisting of a large number of small TMDs, can cover a frequency band around the modes to be controlled. Despite promising results of the latter approach, there is a significant increase in complexity, which undermines the applicability of the solution. Recent applications of TMD technology can be found at the Kansai Airport Bridge, where TMDs were installed from the beginning to suppress amplitude-limited vibrations due to the wakes [65]. In the Tokyo Trans bay Crossing 16 TMDs were installed for suppressing vortex-induced vibrations of the first and second mode. TMD based aeroelastic vibration control is difficult to be implemented for an already completed structure. Other passive control strategies for improved aerodynamic stability include, placing water tanks on the deck edges, or introducing an eccentric mass on the deck windward side. The effectiveness and implications of this method were investigated by Phongkumsing et al. [153] on a full suspension bridge numerical model.

Further investigations included the use of actively or passively controlled rotatable flaps. This design methodology will be the main focus of this work as a way to generate stabilizing forces against aerodynamic loading. As shown in Fig. 2.4 these flaps can be either adjacent to the deck, or at some distance above or below it. The configuration shown in Fig. 2.4 (a) is the one considered in this thesis. In the second case, if the deck and flaps are to be assumed aerodynamically independent, a large separation is required (>1 deck width for the trailing-edge flap) that will most likely make the configuration impractical to implement [79].

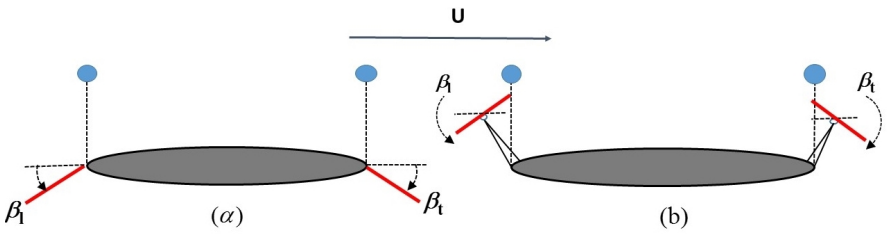


Figure 2.4 Idealized cross section of a long-span suspension bridge with a controllable leading- trailing-edge flaps. a) The flaps are adjacent to the bridge deck b) flaps detached from the deck. The wind speed is denoted by $U$, the leading-edge flap angle is denoted by $\beta_l$ and the trailing-edge flap angle by $\beta_t$.

## 2.5 Aerodynamic Control of Long Span Bridges using Auxiliary Surfaces

Flap-based flutter suppression systems have been examined both analytically and experimentally for the past twenty five years without thus far having been implemented. The control of bridge flutter using actively controlled flaps located beneath the deck was first proposed in [147]. Further examination was undertaken by Kobayashi and Nagaoka [99] and later by Hansen and Thoft-Christensen [82]. More recently Li [113] performed an active control procedure using a pair of rotatable winglets at a distance from the deck. This analysis is based on a two dimensional active control theoretical framework and geared towards achieving bridge stabilization against flutter. Optimal control strategies of this sort as well as pole placement algorithms provide a computationally viable procedure for deriving stabilizing controllers but neglect robustness properties and the assessment of the available stability margins with respect to plant uncertainties. Indeed, for a controllable and observable system the computation of a stabilizing controller is a straight forward design exercise but can result in very poor robustness margins. In the aircraft industry flutter suppression has been under development with emphasis on using actively controlled trailing edge flaps [25, 36]. Bakis et al. [17] developed a framework for investigating flap efficiency on a full bridge model while implementing an $H_\infty$ control strategy suitable for modelling uncertainties.

An important issue for an actively controlled bridge subjected to a wind storm is the compensator's reliability against failure. In this respect system redundancy of the active control strategy should be considered, if one motor fails another should become automatically effective thus resulting in a more reliable system against a destructive flutter mode. Contrary to active systems, passive flap mechanisms have the advantage of dispensing the need for an external power source, but require an elaborate mechanical network for transforming deck movement into flap rotation. Ideally, a feedback connection between deck rotational movement, pitch being the dominant mode in flutter coupling, and the flap

rotations should be established. The main practical implication of this endeavour arises due to lack of access to a ground reference frame. Omenzetter et al. [144, 145] proposed a mechanical system in which the flap rotation is linked to the deck pitch motion by means of additional cables and an auxiliary transverse beam supported by the main cables Fig. 2.5 (a). Prestressed springs are used to push the flaps since the cables only provide tensile forces. Sectional analysis of this system showed that although higher critical wind speed can be attained, large flaps are required as well as significant stiffness for the supporting beam. A subsequent 3D aeroelastic analysis [146] showed that due to kinematic coupling between the flap rotation and the sway motion of the deck and cables, the achievable improvement in the bridge critical flutter speed is limited.

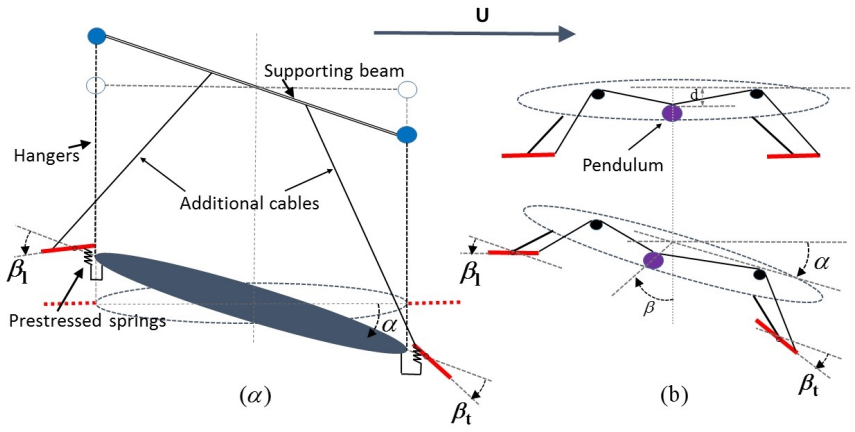


Figure 2.5 Mechanical networks for flutter suppression proposed by a) Omenzetter et al, [144] b) Wilde et al [201].

Wilde et al. [201] proposed an alternative mechanism in which the flaps are kinematically constrained by a pendulum inside the deck, Fig. 2.5(b). Analytical and experimental analyses showed that for a sectional model an increase up to 57% can be obtained. Pure gain controllers like these however forego the advantages that accrue from phase compensation, whereas fixed-phase controllers are not physically realizable. Zhao et al. [208] introduced phase compensation and used an optimization routine for determining the controller parameters. However the proposed design was only realizable under the premise that it can be connected to an inertial reference frame, which of course raises considerable practical difficulties. Similarly, in [207] the same authors revisited the problem of modelling and

validating a two-dimensional section of a suspension bridge with controllable flaps at both sides of the deck. An RFA of the unsteady aerodynamic forces was put into use and both leading and trailing flaps were used, based on a passive mechanical system assumption. [79] draws upon the conclusion that a pure gain compensation for the leading flap in combination with passive phase compensation in the trailing flap produces good results with respect to increasing the critical wind speed both for flutter and torsional divergence. Kwon [102] proposed a design based on tuned mass-dampers connected through a transmission system to aerodynamic surfaces, which oscillate through slits in the bottom flange of the deck. Starossek [180] presented preliminary results of a similar passive system in which the damper is connected to leading- and trailing-edge flaps. The feasibility of passive control schemes on the erection stage of suspension bridges for flutter and buffeting has been investigated in [16, 127]. In chapter 6 two passive mechanisms are proposed in order to overcome some of the shortcomings of the afore-mentioned control networks. The first of those mechanical designs, makes use of trailing and leading-edge flaps adjacent to the deck, passively controlled by a combination of springs, dampers and inerters at the hinge connection. The second, combines the flaps with driving forces produced by tuned masses inside the deck section. Both solutions exploit favourable aerodynamic configurations in order to increase the aeroelastic stability limits.

## 2.6 Discussion and Concluding Remarks

The presented literature review demonstrates that wind-induced vibrations are critical in the design and construction of cable supported bridges. Vibration control of aeroelastic phenomena has recently received significant attention as a means of increasing span length, reducing material or used as a retrofitting measure. The use of controllable flaps is probably the most sensible of the proposed control methodologies. It curbs the need for significant control forces as its philosophy is based on adjusting the flow field around the deck. It could also be potentially used at a later stage as a retrofitting measure or temporarily, e.g. during the erection stage of the deck.

However, the analytic and experimental investigation justifying the effectiveness of this approach needs to overcome several important issues, which have hindered its industrial implementation to date. The system's primary shortcoming relates to the conception of a reliable and relatively simple passive mechanism, which avoids external linkages and the need to be anchored to an inertial reference frame. the issue of robustness against physical uncertainties has also received very superficial attention so far and in most cases the simultaneous mitigation of flutter and torsional divergence has not been pursued. Moreover, to the best of the author's knowledge the development of a computationally efficient and reliable FE based aeroelastic model has not been properly investigated so as to be in close agreement with experimental data.

The work carried out in this thesis will address the afore-mentioned knowledge gaps and provide a holistic approach to the flap implementation procedure in suspension bridges. The next chapter will develop the structural modal framework, which will form the foundation for the subsequent implementation of the aerodynamic and control modelling elements of this work.

# Chapter 3

# Structural Modelling

## 3.1 Introduction

Suspension and cable stayed bridges are highly flexible and lightly damped structures whose eigenfrequencies are usually clustered in a narrow frequency band. Structural dynamics is a fundamental building block of bridge aeroelasticity and should be accurately modelled in order to assess wind effects on bridges. Mode shapes of cable supported bridges are usually categorized according to the dominant mode of deck motion, i.e. lateral (sway motion), vertical and torsional. In contemporary cable supported structures, which exhibit significant deck curving out of the vertical plane, mode shapes may display contributions from different directions [108], making it difficult to consider each of the three motions independently. However, the analysis presented in this work will be restricted to bridges having straight girders; which is in fact the case for the largest type of suspension bridges. The bridge mode shapes can be further divided into deck-dominated modes and modes that involve considerable cable movement but little deck motion. The second category are admittedly of little relevance to the structure's aeroelastic performance. Tower participation can vary for different modes depending on the structure. It is usually more pronounced for the lateral modes, whereas for the vertical motion the towers contribute more to the lower modes. In ambient vibration studies of the Golden Gate Bridge [6], several identified resonant

frequencies of the towers were associated with specific frequencies of the suspended structure.

In order to assess suspension bridge dynamic characteristics, 3-D and 2-D modelling has been applied by various researchers. 3-D modelling is almost exclusively based on finite element analyses, in which the suspended structure, cables and towers form an integrated system. These models are usually developed using beam and truss elements [202, 58], but more complex models using shell or plate elements for the deck have been occasionally undertaken [95, 58]. The 2-D modelling procedure has been used both for continuum and for finite element analyses. Comparison of 3-D to 2-D numerical investigations as well as numerical validation of computational models against ambient vibration measurements, has suggested that in terms of structural modal prediction the more computationally efficient 2-D analysis framework is normally sufficient [154, 5]. It has been argued however, that 3-D models are more successful in predicting torsional modal characteristics [32].

The following analysis will revisit a two dimensional mathematical framework originally proposed by Abdel-Ghaffar [1–3], in order to determine the dynamic characteristics, namely natural frequencies and corresponding modal shapes, for the cases of vertical, torsional and lateral free vibrational motion of a suspension bridge. The method is based on the so-called *linearized deflection theory* and the finite element method. The main features of the proposed methodology can be summarized as follows:

- Analytic description of the potential and kinetic energies of the vertical, torsional and lateral members (suspended structure and cables) using the continuous structure formulation. The equations of motion are then derived using Hamilton's principle. Cable extensibility and deck continuity are also addressed.

- Use of the finite element method procedure to: a) discretize the structure into equivalent systems of finite elements. b) Derive elemental and global stiffness and inertia matrices. c) Form the matrix equations of motion and the resulting eigenvalue problem.

Furthermore, the classification of the structure's modal response in independent vertical, torsional and lateral movement relies on the following physical assumptions, see Fig. 3.1. In pure vertical motion, all points on a given cross section move the same amount and remain in phase. For the torsional case the bridge section rotates about its centre point. Corresponding points on opposite sides of the centerline attain equal displacements, but in opposite directions. In pure lateral motion, each cross section swings in a pendular fashion in its own vertical plane, and therefore there is an incidental upward movement of the cables and suspended structure to the lateral sway motion.

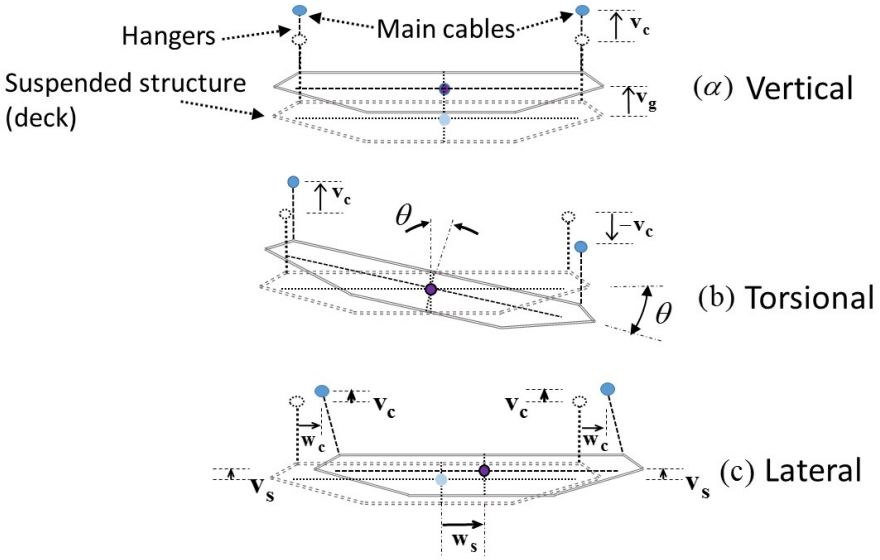


Figure 3.1 Vertical, torsional and lateral motion assumptions in suspension bridges [4].

The adopted procedure enables expression of the structural system using finite degrees of freedom upon which matrix algebra operations can be performed. The separate treatment of the the three vibration cases will eventually result in a general single element, consisting of both the suspended structure and the two main cables, which possesses six degrees of freedom per nodal point. The proposed framework will then be employed to model the dynamic characteristics of the Humber and East Great Belt Bridges. Comparisons to experimentally obtained ambient vibration data from the literature as well as other analytic investigations will cross-validate its performance. This finite element formulation will be

further used to describe the evolution of modal properties of the Humber Bridge during the deck assembly process.

For reasons of space, only the vertical formulation is presented in full. Lateral and torsional formulations follow a similar procedure.

## 3.2 Vertical Vibrations Formulation

This section will focus on presenting the mathematical framework for analyzing free vertical vibrations of suspension bridges.

### 3.2.1 General Assumptions

In consideration of the different factors affecting the dynamic analysis of a suspension bridge, the following general assumptions and approximations are made [4]:

1. All stresses in the bridge follow Hooke's law and remain within the limits of proportionality.

2. The initial dead load is carried by the main cable without causing stress in the stiffening girder (in this case box girder). If during the erection process stresses are developed in the stiffening girder, the dynamic problem formulation should be adjusted in order to consider the initial stresses involved.

3. The cable is assumed to be of a uniform cross section and of parabolic profile under dead load. The assumption of a parabolic profile requires that the sag to span ratio be kept relatively small, meaning that the cable slopes remain small. Small cable slopes ensure that the cable weight can be treated as uniformly distributed along the span rather than along the cable length. Jakkula [89] demonstrated that about 80 to 85 percent of the dead load is strictly along the horizontal and the remainder is distributed along the cable.

4. The cables are assumed to be perfectly flexible. Considering the small second moment of inertia of the cable compared to that of a stiffening structure, the assumption is expected to produce an accurate modelling description. Indeed, thorough investigations have shown that cable bending stiffness can be neglected without loss in accuracy [3].

5. The hangers are regarded as if forming a continuous sheet or wall without shearing resistance. The forces exerted by the hangers are thus regarded to be continuous and not concentrated.

6. The hangers are considered to be inextensible and to remain vertical during the vibration of the bridge, meaning that the vertical vibrational displacements of the cable $V_c(x,t)$ and that of the stiffening girder $V_g(x,t)$ are assumed equal and henceforth denoted by $V(x,t)$.

$$V_c(x,t) = V_g(x,t) = V(x,t) \tag{3.1}$$

   Steinman [182] estimated the contribution of hanger elongation to the bridge's dynamic response to be significantly less than one percent.

7. The treatment of vibrational characteristics assumes small vibrations around the position of static equilibrium in order to make use of the linear theory assumption. It has been generally accepted that a mathematical model based on the dead load state with superposition of linear elastic and geometric stiffness matrices results in good prediction of modal characteristics [32, 5].

8. The additional horizontal component, $H(t)$, of cable tension caused by the inertia forces is small in comparison with $H_w$, the dead load cable horizontal force.

$$H_w + H(t) \simeq H_w \tag{3.2}$$

   This assumption does not mean that $H(t)$ is neglected in general, rather that its effect is small when added to the dead load cable tension.

9. Furthermore, live loads on the bridge are neglected. The total mass of the bridge deck is assumed concentrated along the centreline of the deck's curvature. The curvature of the deck is assumed negligible compared to the cable curvature.

In [1], [2], and [3] two different treatments of the bridge vibration problem have been pursued: namely with and without considering the contribution of tower stiffness. In this work we will neglect the effect of towers based on the assumption that tower participation is usually limited especially for the cases of the vertical and torsional free vibration. This simplification is corroborated by ambient vibration measurements of modal characteristics [58]. In the lateral direction, tower participation is expected to be more significant mainly because the deck lateral response is an order of a magnitude weaker than in the vertical plane [33]. However, lateral modes do not play a central role in the prediction of aeroelastic phenomena such as flutter, especially for the case of streamlined box girders, which have a very low drag component.

Although, The mathematical description in this chapter will be restricted to the vertical vibration case, the most important additional assumptions pertaining to the torsional and lateral vibrational motion are given as follows.

Torsional vibration case:

1. The bridge deck cross section is assumed symmetric about the its centre.

2. Analysis is restricted to closed box girders.

3. The shape of the cross-section remains unaltered during vibrational deformation. Thus, the geometric dimensions of every plane normal to the bridge's longitudinal axis remain unchanged. However, the section may undergo out-of-plane deformation (warping).

Lateral vibration case:

1. The additional horizontal component of cable tension, $H(t)$, due to lateral vibration is negligible compared to the initial dead load horizontal cable tension $H_w$.

2. The cable supports on the top of the towers are considered infinitely rigid in the lateral direction. In reality the tower-ends will experience displacements in response to changing forces. However for reasons already stated, in this analysis supports are considered fixed.

3. Mass of the cable is considered separate from that of the suspended structure. Lateral movement is accompanied by an incidental pendular action, which results in an upward vibrational displacement of the cables and the suspended structure. The small vibration assumption facilitates the derivation of geometrical expressions describing the effect of this pendular motion [1].

### 3.2.2 Mathematical Formulation of the Vertical Vibration Problem

The finite element formulation of the vertical vibration problem will be geared towards suspension bridges with three spans, i.e. main span and two side spans, although extension to more spans is easily attainable. The variational principle here implemented requires the derivation of energy expressions for the vibrating components. The structural stiffness is derived from the potential energy of the system, which has three significant components: elastic strain energy in the deck girder, elastic strain energy in the suspension cable, and gravitational potential energy in the cable. The mass matrix is derived from the kinetic energy of the vibrating structure.

Cable tension is probably the single most important parameter influencing vertical dynamic response. In this analysis the horizontal components of cable tension, $H_w$ and $H(t)$ due to dead loads and inertial forces respectively, are assumed equal on both sides of the tower for all spans (no tower resistance assumption). This would imply that the towers are either on rockers or that the cable is mounted on saddles, which lie on rollers. Despite the fact that both of these arrangements are considered obsolete in the modern bridge construction field, the assumption can still be considered reasonable because of the high tower flexibility. Hence, tower flexural rigidity does not introduce an appreciable change in the horizontal component of cable tension between main and side spans [200].

**Potential Energy of the Suspended Structure**

Potential energy in the deck girder is in the form of strain energy resulting from bending moments, shear forces and axial forces. The vertical displacement as a function of coordinate $x$ and time $t$ has a component due to bending and one due to shear deformation [3], *Timoshenko beam model*. The slope at point $x$ can be expressed as

$$\frac{\partial \nu(x,t)}{\partial x} = \eta(x,t) + \beta(x,t), \tag{3.3}$$

where $\eta(x,t)$ is the slope of deflection due to bending and $\beta(x,t)$ is the shear angle. The well known formula relating bending deformation with bending moment reads

$$M(x,t) = E_g I_g \frac{\partial \eta(x,t)}{\partial x}. \tag{3.4}$$

where, $E_g$ is the modulus of elasticity for the girder and $I_g$ is the second moment of inertia of the box girder (or truss). The dependence between shear force, $S(x,t)$, and shear deformation on the other hand is given by

$$S(x,t) = G_g \mu_\nu(x) \beta(x,t). \tag{3.5}$$

Similarly, $G_g$ is the shear modulus of elasticity and $\mu_\nu$ is the shear resistance coefficient of the box girder or that of the vertical web system, depending on the structural system used. The potential energy due to vertical vibration can be expressed as

$$V_{g\nu}(t) = \frac{1}{2}\int_0^l E_g I_g \left(\frac{\partial \eta(x,t)}{\partial x}\right)^2 dx + \frac{1}{2}\int_0^l G_g \mu_\nu(x) \beta^2(x,t) dx. \tag{3.6}$$

The first term of Eq.( 3.6) relates to the potential energy due to bending and the second term is associated with the shear strain energy stored. In the case when the contribution of shear deformations is neglected the result is the well known *Euler-Bernoulli beam* potential

energy expression [81]

$$V_{g\nu}(t) = \frac{1}{2}\int_0^l E_g I_g \left(\frac{\partial v^2(x,t)}{\partial x^2}\right)^2 dx. \tag{3.7}$$

A similar derivation can be applied to the girder's longitudinal motion but effects of axial deformation are considered negligible in comparison with the vertical displacements. However, in some cases longitudinal motion participation is crucial for accurate modal shape derivations, as has been argued for the case of the Bosporus Bridge [58].

### Potential Energy of the Cables

Due to small, free vibrations about the equilibrium point the horizontal component of cable tension $H_w$ will change to $H_w + H(t)$ and the cable differential length will increase from $ds$ to $ds + \Delta ds$. Hence, the potential energy stored in the differential cable length is expressed by

$$dV_c(x,t) = \left\{\left[H_w + \frac{1}{2}H(t)\right]\frac{ds}{dx}\right\}\Delta ds - w^*\nu_c dx, \tag{3.8}$$

where $\Delta ds$ is the stretch of the initial differential length $ds$. $w^*$ is the per unit length cable dead weight, $w_c$, plus the per unit length weight of the stiffening girder, $w_g$. $\nu_c$ denotes the cable's vertical displacement. The first term in Eq.(3.8) describes the energy stored in the element $ds$ and equals the average force in the cable segment $[H_w + \frac{1}{2}H(t)]\frac{ds}{dx}$ multiplied by the cable stretch $\Delta ds$. The second term expresses the gravity energy change resulting from the lowered position of the dead load.

In the frame of vertical in-plane motion the resulting small free vibrations have two components. The transverse vertical motion $\nu_c$ and the longitudinal motion component $u_c$. Of course in the general vibration problem the transverse horizontal motion component should also be considered. Sway motion however, can be accurately regarded as being uncoupled from the in-plane motion because, to first order, the transverse horizontal motion involves no additional cable tension. Therefore, to first order accuracy, a disturbance which

has no in-plane component will induce only transverse horizontal motion and vice-versa [85].

Consider a cable element AB of original length $ds$, which due to an applied load moves to a new position A'B' and its length increase to $ds+\Delta ds$, see Fig. 3.2.

$$ds^2 = dx^2 + dy^2 \tag{3.9}$$

$$(ds+\Delta ds)^2 = \left(dx+\frac{\partial u_c}{\partial x}dx\right)^2 + \left(dy+\frac{\partial \nu_c}{\partial x}dx\right)^2 \tag{3.10}$$

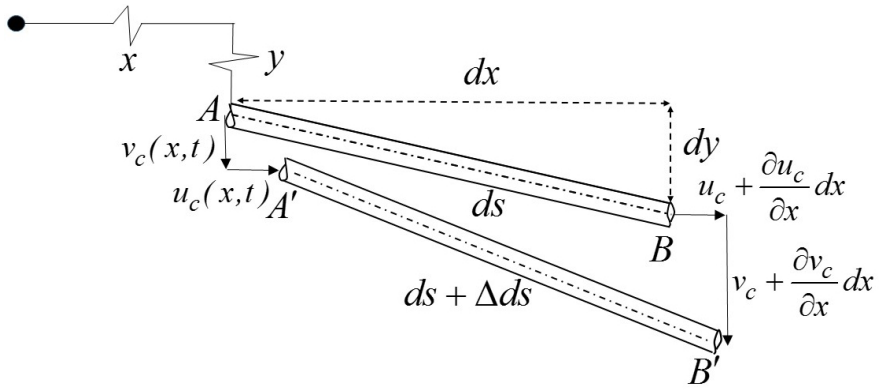


Figure 3.2 Cable element in original and deflected position.

For the case of flat-sag cables, considering that $u_c(x,t)$ is small in comparison to $\nu_c(x,t)$, the increment in length of the cable element, correct to the second order of small quantities, is

$$\Delta ds \simeq \frac{\partial u_c}{\partial x}\frac{dx}{ds}dx + \frac{\partial \nu_c}{\partial x}\frac{dy}{ds}dx + \frac{1}{2}\left(\frac{\partial \nu_c}{\partial x}\right)^2\frac{dx}{ds}dx. \tag{3.11}$$

Hooke's law applied to the element, requires that

$$\frac{H(t)}{E_c A_c}\frac{ds}{dx} = \frac{\Delta ds}{ds}, \tag{3.12}$$

where $H(t)\frac{ds}{dx}$ is the second order increment in horizontal tension exerted on the element. $E_c$ is the modulus of elasticity and $A_c$ is the effective cross-sectional area of the cable.

Consequently, the cable equation for the differential element reads

$$\frac{H(t)}{E_c A_c}\left(\frac{ds}{dx}\right)^3 = \frac{\partial u_c}{\partial x} + \frac{\partial \nu_c}{\partial x}\frac{dy}{ds} + \frac{1}{2}\left(\frac{\partial \nu_c}{\partial x}\right)^2. \tag{3.13}$$

In the case of a suspended cable, hanging between rigid supports, $u_c(0,t) = u_c(l,t) = 0$, Eq.(3.13) can be integrated to give

$$\frac{H(t)L_e}{E_c A_c} = \int_{x=0}^{x=l}\left(\frac{\partial \nu_c}{\partial x}\right)\left(\frac{dy}{dx}\right)dx + \frac{1}{2}\int_{x=0}^{x=l}\left(\frac{\partial \nu_c}{\partial x}\right)^2 dx, \tag{3.14}$$

where $L_e = \int_0^l \left(\frac{ds}{dx}\right)^3 dx$ is commonly referred to as *virtual length*. A good approximation to $L_e$ is given by [86]

$$L_e = l\left[1 + 8\left(\frac{f}{l}\right)^2\right], \tag{3.15}$$

where $l$ is the horizontal projection of the cable's length and $f$ is the cable sag at its midpoint.

Integrating Eq.(3.8) over the length of each span, while substituting equation Eq.(3.11), results in the expression of the cable potential energy as a function of time

$$V_c(t) = \left[H_w + \frac{1}{2}H(t)\right]\left[\int_0^l \frac{\partial u_c}{\partial x}dx + \int_0^l \frac{\partial \nu_c}{\partial x}\frac{\partial y}{\partial x}dx + \frac{1}{2}\int_0^l \left(\frac{\partial \nu_c}{\partial x}\right)^2 dx\right] - \int_0^l w^* v_c dx. \tag{3.16}$$

The following mathematical computations require integration by parts, use of the fact that $u_c(x,t)$ vanishes at the towers, $x = 0$ and $x = l$, and that the shape of the cable, in its free-hanging form is expressed by a parabola, whose expression is given by

$$y = \frac{w^* l^2}{2H_w}\left[\frac{x}{l} - \left(\frac{x}{l}\right)^2\right]. \tag{3.17}$$

Additionally, the cable horizontal component for an inextensible parabola is given by

$$H_w = \frac{w^* l^2}{8f}. \tag{3.18}$$

Equations Eq.(3.16) can then be simplified to

$$V_c(t) = \frac{1}{2}\left[H_w \int_0^l \left(\frac{\partial \nu_c}{\partial x}\right)^2 dx + H(t)\left[\int_0^l \frac{\partial \nu_c}{\partial x}\frac{dy}{dx}dx + \frac{1}{2}\int_0^l \left(\frac{\partial \nu_c}{\partial x}\right)^2 dx\right]\right]. \tag{3.19}$$

Substituting equation Eq.(3.14) into Eq.(3.19) the potential energy of the cable takes its final form

$$V_c(t) = \frac{1}{2}\left[H_w \int_0^l \left(\frac{\partial \nu_c}{\partial x}\right)^2 dx\right] + \frac{1}{2}\left[\frac{H^2(t)L_e}{E_c A_c}\right]. \tag{3.20}$$

The first term of Eq.(3.20) includes the constant horizontal cable tension term, $H_w$, and an integral expression of the cable length change. This term effectively expresses the potential energy resulting from the elevation of the bridge's center of gravity, while the cable is momentarily distorted under the influence of inertia forces. The second term, consisting of the horizontal cable tension variation, expresses the potential energy stored elastically in the cable due to vibrational strain variation.

An alternative way for deriving Eq.(3.20) which possibly provides a greater degree of physical intuition is the following. It can be deduced that the strain energy stored in the cable due to cable tension variations $H(t)$ equals the strain energy related to the change in tension at any cable point, $H(t)\frac{ds}{dx}$. Consequently, by integrating over the length of the span, $l$, the following expression is obtained

$$V_{ce}(t) = \int_0^l \frac{\left[H(t)\frac{ds}{dx}\right]^2}{2E_c A_c} ds = \int_0^l \frac{H^2(t)}{2E_c A_c}\left(\frac{ds}{dx}\right)^3 dx. \tag{3.21}$$

Using the definition of virtual length the above equation reads

$$V_{ce}(t) = \frac{1}{2}\frac{H^2(t)L_e}{E_c A_c}, \tag{3.22}$$

which is the same as the second term of Eq.(3.20).

The potential energy computation related to the cable's movement in the gravity field, considers that each differential element of weight $w^* dx$ loses potential energy equal to $w^* dx \nu_c$ due to vibrational displacement $\nu_c$. By integration over the span length, the total

change in potential energy is expressed by

$$V_{cg}(t) = -\int_0^l w^* \nu_c dx. \tag{3.23}$$

This is the same as the last term in Eq.(3.8). Invoking the cable inextensibility assumption it becomes evident that the vibrational elastic extension holds $\frac{H(t)L_e}{E_c A_c} = 0$. Further mathematical computations involving Eq.(3.13) result in the following identity

$$V_{cg}(t) = -\int_0^l w^* \nu_c dx = \frac{H_w}{2}\int_0^l \left(\frac{\partial \nu_c}{\partial x}\right)^2 dx, \tag{3.24}$$

which equals the first term of Eq.(3.20). This term relates to the gravity stiffness terms pertaining to the cable's vibrational formulation. This gravity term brings to the fore a type of stiffness that is not generally familiar but which helps to present the problem of the dynamics of suspension bridges in clear physical terms, in a way that brings out the type of nonlinearity present [4]. Traditional *Linearized Deflection Theory* implies that the gravity stiffness of the cable is neglected, due to omission of higher order terms in the cable equation.

**Kinetic Energy due to Vertical Vibrations - for the Deck and Cables**

The Timoshenko beam model adds the contribution of shear distortion and rotary inertia to the classical Euler-Bernoulli model [81]. Its kinetic energy can be expressed as follows

$$T_\nu(t) = \frac{1}{2}\int_0^l m^*(x)\left(\frac{\partial \nu(x,t)}{\partial t}\right)^2 dx + \frac{1}{2}\int_0^l J_g(x)\left(\frac{\partial \eta(x,t)}{\partial t}\right)^2 dx, \tag{3.25}$$

in which, $m^*(x)$ expresses the mass of the cables and suspended structure per unit length. $J_g(x)$ is the mass moment of inertia per unit length about the neutral axis passing through the centre of the girder. For the mass moment of inertia the following holds

$$J_g(x) = \rho_g I_g = \frac{m_g(x)}{A_g(x)} I_g(x) = r^2(x) m_g(x), \tag{3.26}$$

where $\rho_g$ is the mass density, $m_g$ is the mass per unit length and $r(x)$ is the radius of gyration about the neutral axis. As commonly assumed for beams where the cross sectional dimensions are small in comparison to the span, the rotatory effects can be excluded in equation (3.25), [156]. Consequently, the kinetic energy expression for the vibrating bridge again reduces to the following Euler-Bernoulli beam model. In [81] it is shown that the difference between the Euler-Bernoulli beam model and other beam model, e.g. Timoshenko beam, monotonically decreases with increasing slenderness ratio defined by the ratio of length of a beam to the radius of gyration of the cross-section. For slenderness ratios larger than 100, the Euler-Bernoulli is very accurate. Long span suspension bridges such as the Humber and the Great Belt bridges have slenderness ratios surpassing this threshold thus making this assumption appropriate for the following modal analyses.

$$T_{\mathrm{v}}(t) = \frac{1}{2}\int_0^l m^*(x)\left(\frac{\partial \mathrm{v}(x,t)}{\partial t}\right)^2 dx. \tag{3.27}$$

### 3.2.3 Finite Element Formulation for Vertical Vibrations

For establishing the vertical vibrational framework in finite element form, the bridge is discretized into connecting elements. The internal deformations in these elements are expressed in terms of the nodal displacement variables via a family of shape functions. Element stiffness and mass matrices are then derived using the potential and kinetic energy expressions presented in Section 3.2.2. Furthermore, the assumed discretization is based on horizontal elements lying on the centreline of the girder. The typical element consists of the two main cables and the girder, which are assumed rigidly connected by inextensible hangers. An explicit consequence of the hangers being assumed rigid and remaining vertical during vibrational motion, is that, for the vertical case, girder movement is identical to that of the main cable. Each element has two nodal points and each nodal point two degrees of freedom namely, vertical translation and rotation, see Fig. 3.3. The interpolation functions associated with the two nodal points, are assumed those of a uniform beam subject to the same nodal displacements. These are cubic *Hermitian polynomials* given by

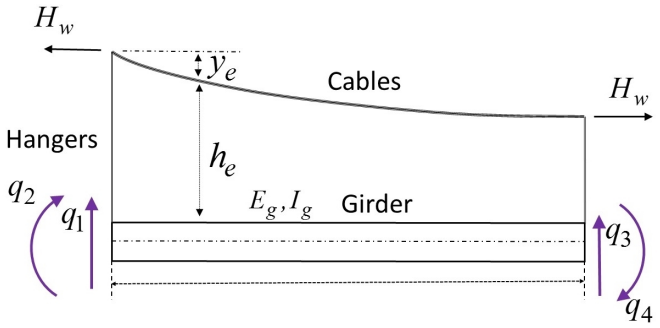


Figure 3.3 Nodal degrees of freedom of the FE element for the vertical vibration case.

$$H_1(x) = 1 - 3\frac{x^2}{L^2} + 2\frac{x^3}{L^3}, \tag{3.28}$$

$$H_2(x) = x - 2\frac{x^2}{L} + \frac{x^3}{L^2}, \tag{3.29}$$

$$H_3(x) = 3\frac{x^2}{L^2} - 2\frac{x^3}{L^3}, \tag{3.30}$$

$$H_4(x) = -\frac{x^2}{L} + \frac{x^3}{L^2}. \tag{3.31}$$

The deck displacement, within each element, is expressed as a function of its nodal displacements according to

$$\nu_e(x,t) = H_1(x)q_1(t) + H_2(x)q_2(t) + H_3(x)q_3(t) + H_4(x)q_4(t). \tag{3.32}$$

Subscript $e$ indicates the element and $q_i(t), i = 1,2,3,4$ denote the corresponding nodal degrees of freedom. Eq.(3.32) can be expressed in the following matrix form

$$\nu_e(x,t) = \mathbf{f}(x)_e^T \mathbf{q}(t)_e, \tag{3.33}$$

$$\text{where,} \qquad \mathbf{f}(x)_e^T = [H_1(x), H_2(x), H_3(x), H_4(x)]. \tag{3.34}$$

$\mathbf{q}(t)$ denotes the nodal displacement vector. Space coordinates are often expressed in the following normalized coordinate system, which facilitates polynomial integration.

$$\xi_1(x) = \left(1 - \frac{x}{L}\right) \quad \textit{and} \quad \xi_2(x) = \left(\frac{x}{L}\right) \tag{3.35}$$

The transformation allows Eq.(3.32) to be written as

$$\nu_e(\xi_1, \xi_2, t) = \mathbf{f}(\xi_1, \xi_2)_e^T \mathbf{q}(t)_e, \tag{3.36}$$

$$\mathbf{f}(\xi_1, \xi_2)_e^T = [\xi_1^2(3 - 2\xi_1) \quad -L\xi_1^2\xi_2 \quad \xi_2^2(3 - 2\xi_2) \quad L\xi_1\xi_2^2] \tag{3.37}$$

**Elastic Stiffness Matrix of the Girder**

Implementing the displacement model of Eq.(3.33) in the Euler-Bernoulli potential energy expression, Eq.(3.7), for the girder results in

$$V_{gv}(t) = \frac{1}{2} \sum_{e=1}^{N_i} E_{ge} I_{ge}(x) \{ \left(\mathbf{f}_e''\right)^T \mathbf{q}_e \}^T \{ \mathbf{f}_e'' \mathbf{q}_e \} dx, \tag{3.38}$$

where $N_i$ is the total number of bridge elements, and $E_{ge}I_{ge}$ is the flexural rigidity of the deck, assumed constant over each element. Eq.( 3.38) is evaluated over each element and results in a $4 \times 4$ elastic stiffness matrix. $\mathbf{f}_e''$ contains the curvatures of the shape functions. By consideration of Eq.(3.33) to facilitate the integration process these take the form

$$\left(\mathbf{f}_e''\right)^T = \mathbf{f}''(\xi_1, \xi_2)_e^T = \frac{1}{L^2} [(6 - 12\xi_1) \quad L(4\xi_1 - 2\xi_2) \quad (6 - 12\xi_2) \quad L(2\xi_1 - 4\xi_2)]. \tag{3.39}$$

Eq.(3.38) by means of Eq.(3.39) is then expressed as

$$V_{gv}(t) = \frac{1}{2} \sum_{e=1}^{N} \mathbf{q}_e^T \left[\mathbf{k}_{ge}\right]_e \mathbf{q}_e, \tag{3.40}$$

$$\text{in which,} \quad \left[\mathbf{k}_{ge}\right]_e = \int_0^L E_{ge} I_{ge} \mathbf{f}_e'' \left(\mathbf{f}_e''\right)^T dx \tag{3.41}$$

$\mathbf{K}_{ge}$ represents the elemental elastic stiffness matrix of the stiffening girder. the subscript $e$ again stands for "element". Eq.(3.38) is then evaluated by means of Eq.(3.39) resulting in the following matrix form

$$[\mathbf{k}_{ge}]_e = \frac{E_{ge}I_{ge}}{L^3}\begin{bmatrix} 12 & -6L & -12 & -6L \\ -6L & 4L^2 & 6L & 2L^2 \\ -12 & 6L & 12 & 6L \\ -6L & 2L^2 & 6L & 4L^2 \end{bmatrix} \tag{3.42}$$

By including the effect of shear deformations in the above used beam element we obtain the following modified matrix form

$$[\mathbf{k}_{ge}]_e = \frac{E_{ge}I_{ge}}{L^3(1+\phi)}\begin{bmatrix} 12 & -6L & -12 & -6L \\ -6L & (4+\phi)L^2 & 6L & (2-\phi)L^2 \\ -12 & 6L & 12 & 6L \\ -6L & (2-\phi)L^2 & 6L & (4+\phi)L^2 \end{bmatrix} \tag{3.43}$$

$$\text{where,} \quad \phi = \left(\frac{12E_{ge}I_{ge}}{G_{ge}\mu_{ge}L^2}\right) \tag{3.44}$$

$G_{ge}\mu_{ge}$ represents the element's shear rigidity. The finite element method procedure is based on nodal displacement compatibility, which enables the assembly of the global matrix out of individual element matrices [158]. This operation is expressed by the following expressions

$$\mathbf{K}_{GE} = \sum_{e=1}^{N} [\mathbf{k}_{ge}]_e, \tag{3.45}$$

$$\mathbf{Q} = \sum_{e=1}^{N} \mathbf{q}_e, \tag{3.46}$$

where, $\mathbf{Q}$ is a column vector matrix of the degrees of freedom of the entire structure. Similarly the FE model's strain energy due to stiffness of the girder reads

$$V_{gv}(t) = \frac{1}{2}\mathbf{Q}^T\mathbf{K}_{GE}\mathbf{Q}. \tag{3.47}$$

It is recalled that stiffness matrices of this kind are symmetric and banded about the diagonal, positive definite and consequently invertible.

### Gravity Stiffness Matrix of the Cable

The gravitational energy expression of the cable expressed in Eq.(3.24) is used to derive the gravity stiffness matrix of the element using again the interpolation function from Eq.(3.33). The gravitational energy of the cable is thus re-written as

$$V_{cg}(t) = \frac{1}{2}\sum_{i=1}^{N}\int_0^L H_w\{(\mathbf{f}'_e)^T\mathbf{q}_e\}^T\{(\mathbf{f}'_e)^T\mathbf{q}_e\}. \tag{3.48}$$

$\mathbf{f}'_e$ is the column vector representing the slope of the element nodal displacements and is expressed in terms of the generalized displacements as

$$(\mathbf{f}'_e)^T = \frac{1}{L}[6\xi_1(\xi_1-1) \quad L\xi_1(2\xi_2-\xi_1) \quad 6\xi_2(1-\xi_2) \quad L\xi_2(2\xi_1-\xi_2)]. \tag{3.49}$$

Use of Eq.(3.49) results in the following expression for the gravitational energy

$$V_{cg}(t) = \frac{1}{2}\sum_{e=1}^{N}\mathbf{q}_e^T[\mathbf{k}_{cg}]_e\mathbf{q}_e, \tag{3.50}$$

$$[\mathbf{k}_{cg}]_e = H_w\int_0^L \mathbf{f}'_e(\mathbf{f}'_e)^T dx. \tag{3.51}$$

By means of Eq.(3.49) the above equation can be cast in the following matrix form

$$[\mathbf{k}_{cg}]_e = \frac{H_w}{30L}\begin{bmatrix} 36 & -3L & -36 & -3L \\ -3L & 4L^2 & 3L & -L^2 \\ -36 & 3L & 36 & 3L \\ -3L & -L^2 & 3L & 4L^2 \end{bmatrix} \tag{3.52}$$

In the same spirit as in the previous section the global gravity-stiffness matrix can be obtained from the gravity matrices of the individual elements

$$\mathbf{K}_{CG} = \sum_{e=1}^{N}[\mathbf{k}_{cg}]_e. \tag{3.53}$$

Thus, the expression for the gravity potential energy of the FE model reads:

$$V_{cg}(t) = \frac{1}{2}\mathbf{Q}^T\mathbf{K}_{CG}\mathbf{Q}. \tag{3.54}$$

### Elastic Stiffness of the Cable

As was presented in Section 3.2.2, the strain energy stored in the cable due to vertical vibrational motion is expressed by Eq.(3.22). The cable Eq.(3.14) relates the stretching of a cable element to the geometric displacement which it undergoes. The additional elastic cable tension can thus be expressed as

$$H(t) = \frac{E_c A_c}{L_e} \int_{x=0}^{x=l} \left(\frac{\partial \nu_c}{\partial x}\right) \left(\frac{dy}{dx}\right) dx + \frac{1}{2} \int_{x=0}^{x=l} \left(\frac{\partial \nu_c}{\partial x}\right)^2 dx. \tag{3.55}$$

By linearizing the above equation it is possible to neglect the second order term, which would thus give

$$\tilde{H}(t) = \frac{E_c A_c}{L_e} \int_{x=0}^{x=l} \left(\frac{\partial \nu_c}{\partial x}\right) \left(\frac{dy}{dx}\right) dx. \tag{3.56}$$

Furthermore, due to the following identity

$$\int_{x=0}^{x=l} \left(\frac{\partial \nu_c}{\partial x}\right) \left(\frac{dy}{dx}\right) dx = \frac{w^*}{H_w} \int_{x=0}^{x=l} \nu_c dx. \tag{3.57}$$

The linearized strain energy expression is reshaped to

$$\tilde{V}_{ce}(t) = \frac{1}{2} \frac{\tilde{H}^2(t) L_e}{E_c A_c} = \frac{1}{2} \frac{L_e}{E_c A_c} \left[\frac{E_c A_c}{L_e} \frac{w^*}{H_w} \int_{x=0}^{x=l} \nu_c dx\right]^2. \tag{3.58}$$

Using the displacement model from Eq.(3.36) the above equation becomes

$$\tilde{V}_{ce}(t) = \frac{1}{2} \frac{E_c A_c}{L_e} \left[\sum_{e=1}^{N} \frac{w^*}{H_w} \int_0^L \mathbf{f}_e^T \mathbf{q}_e dx\right]^T \left[\sum_{e=1}^{N} \frac{w^*}{H_w} \int_0^L \mathbf{f}_e^T \mathbf{q}_e dx\right]. \tag{3.59}$$

Assembling the nodal displacements of the FE $\mathbf{Q} = \sum_{e=1}^{N} \mathbf{q}_e$, Eq.(3.59) is reshaped to

$$\tilde{V}_{ce}(t) = \frac{1}{2} \frac{E_c A_c}{L_e} \mathbf{Q}^T \left[\sum_{e=1}^{N} \frac{w^*}{H_w} \int_0^L \mathbf{f}_e^T dx\right]^T \left[\sum_{e=1}^{N} \frac{w^*}{H_w} \int_0^L \mathbf{f}_e^T dx\right] \mathbf{Q}. \tag{3.60}$$

By computing the following integral

$$\hat{\mathbf{f}}_e^T = \int_0^L \mathbf{f}_e^T dx = \begin{bmatrix} \frac{L}{2} & \frac{-L^2}{12} & \frac{L}{2} & \frac{L^2}{12} \end{bmatrix}, \tag{3.61}$$

and defining

$$\hat{\mathbf{f}}_N = \sum_{e=1}^{N} \mathbf{f}_e, \tag{3.62}$$

Eq.(3.60) becomes

$$\tilde{V}_{ce}(t) = \frac{1}{2}\mathbf{Q}^T \left[ \frac{E_c A_c}{L_e} \left( \frac{w^*}{H_w} \{\hat{\mathbf{f}}\}_N \right) \left( \frac{w^*}{H_w} \{\hat{\mathbf{f}}\}_N^T \right) \right] \mathbf{Q}. \tag{3.63}$$

Equivalently

$$\tilde{V}_{ce}(t) = \frac{1}{2}\mathbf{Q}^T [\mathbf{K}_{CE}] \mathbf{Q}, \tag{3.64}$$

where $\mathbf{K}_{CE}$ is derived by assembling the elemental stiffness matrices of the cable

$$\mathbf{K}_{CE} = \frac{E_c A_c}{L_e} \left[ \left( \frac{w^*}{H_w} \{\hat{\mathbf{f}}\}_N \right) \left( \frac{w^*}{H_w} \{\hat{\mathbf{f}}\}_N^T \right) \right]. \tag{3.65}$$

The procedure followed in this section leads to a well distributed matrix form, rather than a banded one as in the other cases, see Appendix B. Physically, this can be explained by considering the phenomenon of direct interaction among distant cable points caused by the variation of elastic stiffness.

### Inertia Properties

Similar to the stiffness FE formulation, the consistent mass matrices are evaluated for every element. The displacements within the element are evaluated by means of the same interpolation functions. Thus, Eq.(3.27) can be formulated as follows

$$T_{\mathrm{v}}(t) = \frac{1}{2} \sum_{e=1}^{N} m_e^* \int_0^L \{\mathbf{f}_e^T \dot{\mathbf{q}}_e\}^T \{\mathbf{f}_e^T \dot{\mathbf{q}}_e\} dx. \tag{3.66}$$

$m_e^*$ is the per metre mass of the bridge. Eq.(3.66) can be reshaped to the form

$$T_v(t) = \frac{1}{2}\left[\sum_{e=1}^{N} \dot{\mathbf{q}}_e^T \tilde{\mathbf{m}}_e \dot{\mathbf{q}}_e\right], \tag{3.67}$$

where $\tilde{\mathbf{m}}_e$ is the consistent mass matrix of the element defined as

$$\tilde{\mathbf{m}}_e = m_e^* \int_0^L \mathbf{f}_e \mathbf{f}_e^T dx. \tag{3.68}$$

The above equation by means of Eq.(3.36) results in

$$\tilde{\mathbf{m}}_e = \frac{m_e^* L}{420}\begin{bmatrix} 156 & -22L & 54 & 13L \\ -22L & 4L^2 & -13L & -3L^2 \\ 54 & -13L & 156 & 22L \\ 13L & -3L^2 & 22L & 4L^2 \end{bmatrix} \tag{3.69}$$

For the case when rotary inertia is accounted for, the consistent mass matrix takes the following form

$$\tilde{\mathbf{m}}_e = \frac{m_e^* L}{420}\begin{bmatrix} 156 & -22L & 54 & 13L \\ -22L & 4L^2 & -13L & -3L^2 \\ 54 & -13L & 156 & 22L \\ 13L & -3L^2 & 22L & 4L^2 \end{bmatrix} + \frac{m_{ge} r_e^2}{30L}\begin{bmatrix} 36 & 3L & -36 & 3L \\ 3L & 4L^2 & -3L & -L^2 \\ -36 & -3L & 36 & -31 \\ 3L & -L^2 & -3L & 4L^2 \end{bmatrix}, \tag{3.70}$$

where $m_{ge}$ is the mass of the stiffening girder per metre and $r_e$ is the radius of gyration of the element cross section. the first term in equation (3.70) corresponds to the translational inertia term ,while the second term is due to the rotatory inertia. The global mass matrix can be populated by assembling the element matrices, similarly to the case of stiffness matrices

$$\tilde{\mathbf{M}} = \sum_{e=1}^{N} \tilde{\mathbf{m}}_e, \tag{3.71}$$

and therefore the translational kinetic energy reads

$$T_v(t) = \frac{1}{2}\mathbf{Q}^T \tilde{\mathbf{M}} \mathbf{Q}. \tag{3.72}$$

**Matrix Equations of Motion and Eigenvalue Analysis**

Once the bridge model's FE mass and stiffness matrices are computed , the equations of motion for the undamped system in matrix form take the following form

$$\mathbf{M}\ddot{\mathbf{Q}} + \mathbf{K}\mathbf{Q} = 0, \tag{3.73}$$

where,

$$\mathbf{K} = \mathbf{K}_{CE} + \mathbf{K}_{CG} + \mathbf{K}_{GE} \quad \text{and} \quad \mathbf{M} = \tilde{\mathbf{M}}. \tag{3.74}$$

For calculating natural frequencies of the structure, harmonic motion is assumed for the displacements, which substituted in the equation of motion results in the classical eigenvalue problem

$$(\mathbf{K} - \omega^2\mathbf{M})\{\bar{u}\} = 0. \tag{3.75}$$

$\omega$ denotes the circular natural frequency in $rad/sec$ and $\{\bar{u}\}$ denotes the modal shape vector.

### 3.2.4 Finite Element Formulation for the Overall Vibrational Framework

The mathematical analysis followed in the preceding sections covered the case of vertical vibrations. A similar procedure, as already mentioned, can be followed for the cases of torsional and lateral vibrations, see [2, 1]. The three independent cases are combined into a single bridge element. The structural FE framework adopted provides a significant reduction of computational burden because it accounts for the effect of the main cables and hangers for each deck element indirectly. Fig. 3.4 offers an isometric representation of the geometry and nodal degrees of freedom of a typical element, which involves 12 DOFs (6 per node).

For the general FE approach the shape functions of the element based on the Hermitian cubic polynomials express the vertical $v$, lateral $l$ and torsional $t$ displacements at every

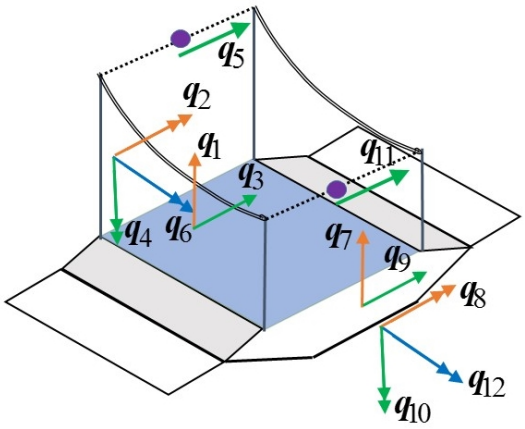


Figure 3.4 All degrees of freedom of the FE element (orange $q_1, q_2, q_7, q_8$ correspond to the vertical, green $q_3, q_4, q_5, q_9, q_{10}, q_{11}$ to the lateral and blue $q_6, q_{12}$ to the torsional.

internal point as a function of the nodal displacements $q_{1..12}$

$$\begin{Bmatrix} v(x) \\ l(x) \\ t(x) \end{Bmatrix} = \begin{bmatrix} H_1 & H_2 & 0 & 0 & 0 & 0 & H_3 & H_4 & 0 & 0 & 0 & 0 \\ 0 & 0 & H_1 & H_2 & 0 & 0 & 0 & 0 & H_3 & H_4 & 0 & 0 \\ 0 & 0 & 0 & 0 & 0 & H_5 & 0 & 0 & 0 & 0 & 0 & H_6 \end{bmatrix} \begin{Bmatrix} q_1 \\ \vdots \\ q_{12} \end{Bmatrix}. \tag{3.76}$$

where,

$$\begin{aligned} H_1(x) &= 1 - 3\tfrac{x^2}{L^2} + 2\tfrac{x^3}{L^3} & H_2(x) &= -\left(x - 2\tfrac{x^2}{L} + \tfrac{x^3}{L^2}\right) \\ H_3(x) &= 3\tfrac{x^2}{L^2} - 2\tfrac{x^3}{L^3} & H_4(x) &= -\left(-\tfrac{x^2}{L} + \tfrac{x^3}{L^2}\right) \\ H_5(x) &= 1 - \tfrac{x}{L} & H_6(x) &= \tfrac{x}{L} \end{aligned} \tag{3.77}$$

## 3.3 Modelling of Humber and Great Belt Bridges

The validation study of the developed structural vibrational framework aims at reproducing the modal characteristics of two of the longest span suspension bridges namely: the Humber Bridge and the Great Belt Bridge. For both cases comparison of the obtained modal properties will be made to experimentally obtained results or detailed finite element analyses from the literature.

### 3.3.1 Description and Structural Modelling of the Humber Bridge

The Humber Bridge in the U.K. was inaugurated in July 1981 and is now the seventh longest in its own type (single-span suspension bridge) in the world, although when it

first opened it was the longest and remained so for 17 years. The Humber Bridge, along with the contemporary Severn and Bosporus Bridge, shares a streamlined low-drag closed box-girder deck. It possesses a main span of 1410$m$ and side spans of 280$m$ and 530$m$ linking the small towns of Hessle (north) and Barton (south) and is supported by hollow concrete heavily reinforced towers. The deck girder is a streamlined steel box section 22$m$ wide and 4.5$m$ deep with approximately 3.25$m$ walkway cantilevers at each side, resulting in a main span to depth ratio of 300 to 1. The girders were prefabricated in 18$m$ long segments with transverse bulkheads, equally spaced every 4.5$m$, for improving the bridge's torsional stiffness. The main cables have a nominal sag of $f = 115.5m$ and one pair of inclined hangers per box section on each side connects the deck to the main cables via hinged sockets. Short, widened end box-sections interface to the A-frame rockers at the supports (towers), which prevent vertical and lateral movement while a rolling leaf type expansion joint provides roadway continuity while accommodating horizontal movement [31]. The A-frame supports were designed to permit longitudinal motion and rotation about the lateral axis to accommodate changes in temperature as well as wind and traffic loading.

The aerodynamic requirements for the bridge at the time were resistance to wind velocity of 47$m/s$ at deck height and up to 66$m/s$ at the top of the towers. In the design stage, wind tunnel tests were performed at British Marine Technology in order to investigate aerodynamic performance of different deck shape alternatives. Later, wind tunnel tests in Milan [63] were conducted to estimate the aerodynamic coefficients of the as-built Humber deck section. Full scale measurements in turbulent wind were also performed on the built bridge by Diana et al. [53] for identifying the real aerodynamic parameters as well as estimating their uncertainty.

### 3.3.2 Ambient Vibration Testing

Extensive ambient vibration measurements have been performed on the Humber Bridge. The original ambient vibration study performed by Brownjohn et al. [30] and the 1990/1991 extended monitoring [31] served for validating simulation software and FE modelling

procedures. Ambient excitation comes as a result of wind and traffic excitation which is regarded as a non stationary random process, and the following testing procedures and data analysis techniques serve to determine vertical, lateral and torsional vibration characteristics of the deck and towers. Such modelling also provides estimates of structural damping values for use with the models in response calculations. More recently, an ambient vibration survey was carried out in July 2008 by a combined team from the UK, Portugal and Hong Kong [33]. The purpose of the survey was again to identify vibration modes and investigate the contributions of major bridge components. A further objective of the tests was to test operational modal analysis procedures and system identification techniques using a wide range of uniaxial and triaxial accelerometers.

### 3.3.3 Model Building of the FE Model for the Humber Bridge

Figure 3.5 View of the Humber Bridge [157].

The modelling investigation based on the developed FE formulation considered a range of different element lengths, ranging from 10 to 150m. It was concluded that in terms of modal analysis $L = 100m$ long elements for both the main and side spans provide good convergence with the ambient vibration results. This discretization unavoidably leads to a slightly altered geometry than that of the real structure Fig. 3.7. It becomes apparent that the FE model results in a low order structural system comprised of about 120 degrees of freedom. Previous models of the Humber and Bosporus Bridges produced significantly

higher order modes, having up to 3500 DOFs [30]. In order to accommodate for the free rotation about the lateral axis at the tower supports, a hinge pertaining to the $q_2$ and $q_8$ DOFs was built into the model. Expansion in the longitudinal direction was not accounted for at this stage because the axial DOF is not included in the FE framework. The structural parameters implemented in the FE model are presented in Table. 3.1.

| Element | Property | Value |
|---|---|---|
| girder | Young modulus of elasticity | $E = 210 \times 10^9 N/m^2$ |
| | shear modulus of elasticity | $G = 80.8 \times 10^9 N/m^2$ |
| | element length | $L = 100m$ |
| | half chord width of the deck | $b = 14.25m$ |
| | girder mass | $m_g = 13215kg/m$ |
| | moment of inertia about horizontal axis | $I_y = 2.09m^4$ |
| | moment of inertia about vertical axis | $I_z = 41.24m^4$ |
| | torsional moment of inertia | $I_a = 4.49m^4$ |
| | mass moment of inertia (including cables) | $I_m = 1.05 \times 10^6 kgm^2/m$ |
| cables | Young modulus of elasticity | $E_c = 155.5 \times 10^9 N/m^2$ |
| | cross sectional area | $A_c = 0.362m^2$ |
| | half chord distance between cables | $b_c = 10.98$ |
| | diameter | $d_c = 0.68m$ |
| | mass of the main cables (both cables) | $m_c = \times 3000kg/m$ |
| | horizontal cable tension (both cables) | $H_w = 2 \times 3.08 \times 10^8 N$ |
| | main cable sag | $f = 115.5m$ |
| | length of shortest hanger cable | $h_{e,\min} = 17.5m$ |

Table 3.1 Structural properties of the FE model of the Humber Bridge.

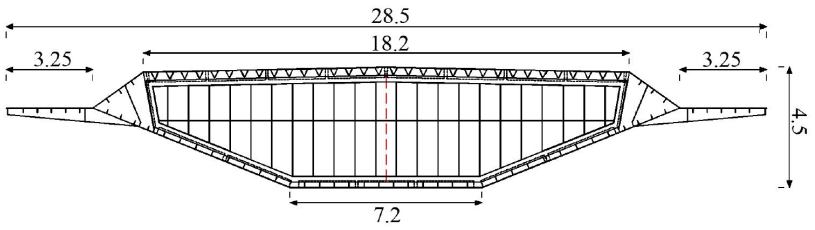


Figure 3.6 Dimensions of the Humber Bridge box girder section [157].

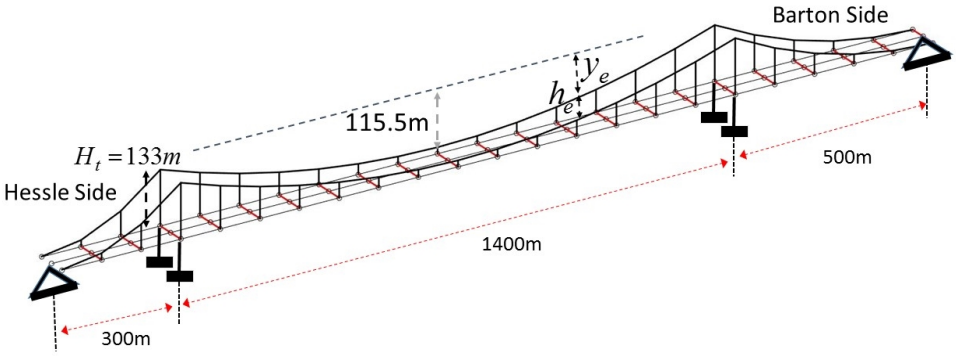


Figure 3.7 Basic dimensions of the Humber Bridge FE bridge model.

### 3.3.4 Comparison of Modal Properties for the Humber

Fig. 3.9 and Fig. 3.8 compare the natural frequencies of the vertical, lateral and torsional modes obtained from the proposed FE model analysis with the field monitoring results from Brownjohn et al. [30, 33]. For the cases of the vertical and torsional modes only the modal amplitudes on the deck are presented for plotting purposes. The 2008 testing [33] aimed at extending the original 1985 testing [30] and considered a more accurate interaction of the major bridge components (spans and towers). In terms of vertical and torsional mode shapes the results were very comparable. The lateral vibrational characteristics also exhibit very close agreement with the experimental results apart from the first mode where a deviation in the natural frequency is observed.

| Experimental torsional modes | FE torsional modes |
|---|---|
|  T. mode 1: 0.311 Hz | 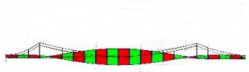 T. mode 1: 0.314 Hz |
| 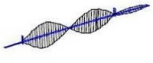 T. mode 2: 0.482 Hz |  T. mode 2: 0.458 Hz |
| 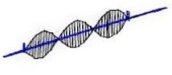 T. mode 3: 0.650 Hz |  T. mode 3: 0.696 Hz |

Figure 3.8 Comparison of experimentally identified, [33], torsional modal characteristics to FE results.

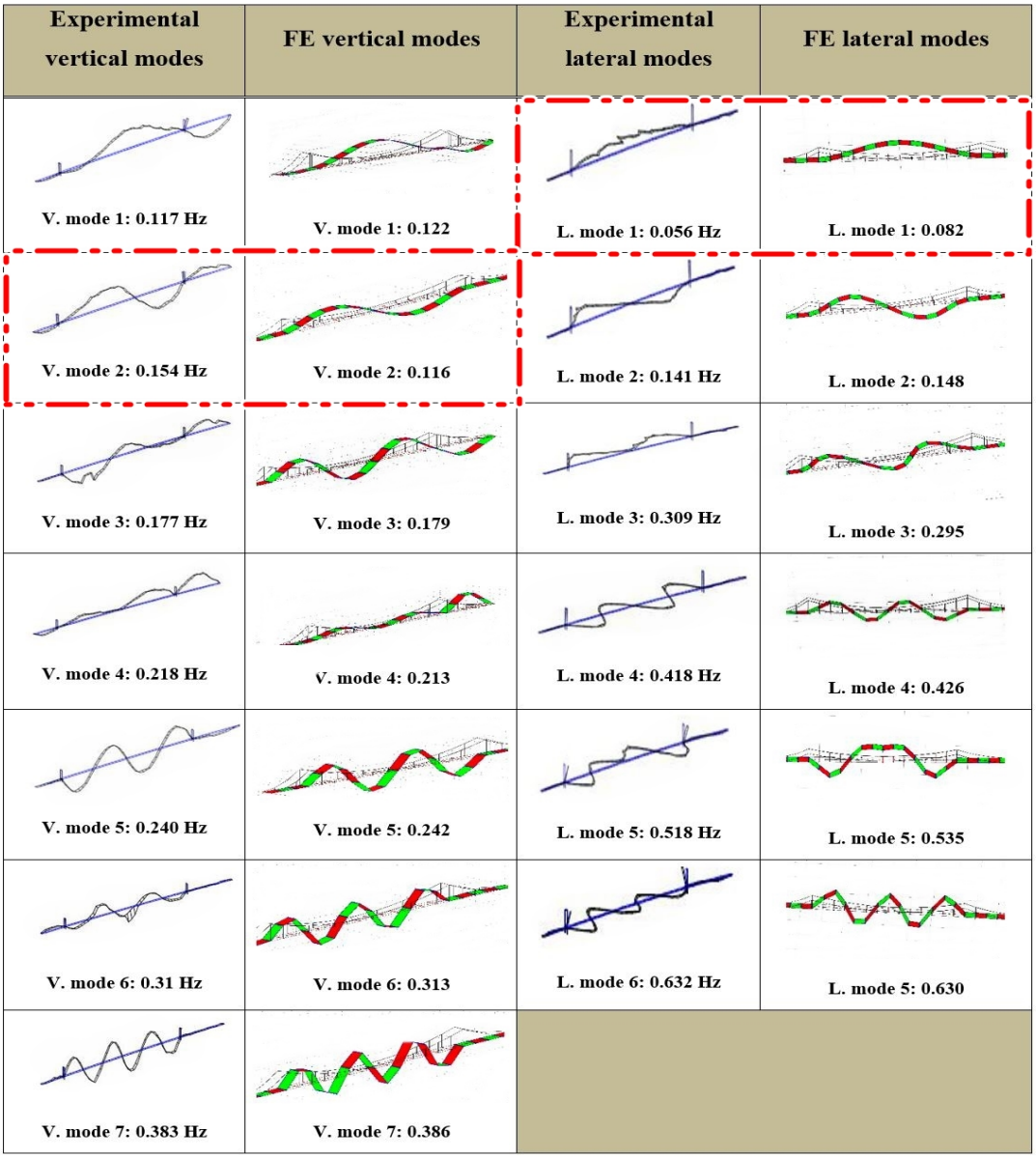


Figure 3.9 Comparison of experimentally identified, [33], vertical and lateral modal characteristics to FE results. Red boxes mark the modes for which there is deviation between experimental and FE modelling results.

Fig. 3.9 and Fig. 3.8 compare the natural frequencies of the vertical, lateral and torsional modes obtained from the proposed FE model analysis with the field monitoring results from Brownjohn et al. [30, 33]. For the cases of the vertical and torsional modes only the modal amplitudes on the deck are presented for plotting purposes. The 2008 testing [33] aimed at extending the original 1985 testing [30] and considered a more accurate interaction of the major bridge components (spans and towers). In terms of vertical and torsional

mode shapes the results were very comparable. The lateral vibrational characteristics also exhibit very close agreement with the experimental results apart from the first mode where a deviation in the natural frequency is observed.

The choice of element length at $L = 100m$ was based on a structural sensitivity analysis, in which different element lengths ranging from $L = 10m$ to $L = 500m$ were considered. Fig. 3.10 presents the natural frequencies of the first and last modes presented in Figures 3.9-3.8 dependent on the element size. It can be clearly observed that for the first vertical, torsional and lateral modes the resulting modal frequencies are quite insensitive to spatial discretization with good accordance to experimental data being attained even for element lengths of $L = 300m$. For the higher modes however, as expected, a smaller element size is required as higher mode shapes are difficult to be effectively reproduced with overly large element lengths. Using elements of length up to $L = 100m$ is clearly demonstrated to reproduce the bridge vibrational characteristics when compared to the experimental monitoring findings.

| Mode / Element length | First Vertical | First Torsional | First Lateral | Seventh Vertical | Sixth Lateral | Third Torsional |
|---|---|---|---|---|---|---|
| 10m | 0.122 | 0.314 | 0.082 | 0.385 | 0.629 | 0.689 |
| 20m | 0.122 | 0.314 | 0.082 | 0.385 | 0.629 | 0.691 |
| 30m | 0.122 | 0.314 | 0.082 | 0.385 | 0.629 | 0.692 |
| 50m | 0.122 | 0.314 | 0.082 | 0.385 | 0.629 | 0.693 |
| 75m | 0.122 | 0.314 | 0.082 | 0.385 | 0.629 | 0.694 |
| 100m | 0.122 | 0.314 | 0.082 | 0.386 | 0.630 | 0.696 |
| 150m | 0.122 | 0.315 | 0.082 | 0.388 | 0.635 | 0.728 |
| 200m | 0.122 | 0.316 | 0.082 | 0.497 | - | 0.748 |
| 300m | 0.122 | 0.317 | 0.082 | - | - | 0.79 |
| 500m | 0.294 | 0.322 | 0.085 | - | - | - |
| Experimental | 0.117 | 0.311 | 0.056 | 0.383 | 0.632 | 0.65 |

Figure 3.10 Natural frequencies in Hz of lower and higher vertical, lateral and torsional modes dependent on the structural element size.

From the comparison of modal characteristics the following observations can be drawn:

- The FE procedure results in a very good predictions of the structure's modal characteristics.

- The observed difference in the first vertical antisymmetric mode is primarily due to the coupling of that mode with the deck's longitudinal motion. It has been estimated that the mode's natural frequency ranges from 0.105 to 0.145$Hz$ depending if the axial motion is free or constrained at both ends of the deck respectively [53]. It was reported by Rahbari et al. [157] that the A-frame rocker bearings were not functioning quite as expected in allowing longitudinal motion. This causes the anti-symmetric vertical vibration mode to be at a higher frequency.

- As seen in the lowest vertical modes the center span and side spans vibrate together, but in the higher modes the center and side spans vibrate separately. This behaviour illustrates the effect of the cables during the first few modes of vibration, in which there is a more pronounced interaction between the side spans and the center span because of the cable action.

- The first lateral mode is less accurately reproduced by the structural FE framework. Possible reasons include: a) A more pronounced tower participation for lateral deck modes. b) The significant low frequency traffic-induced noise in the frequency range of that mode. c) The mathematical difficulty in expressing in phase and out of phase motion of the deck and the cables in the lateral model, given the adopted assumptions.

- Prediction of aeroelastic stability boundaries is much less dependent on the structure's sway motion. Consequently, it can be concluded that the FE model accurately captures the Humber's vibrational footprint relevant to its aerodynamic performance.

### 3.3.5 Description and Modelling of the Great Belt Bridge

The East Great Belt Bridge (1998, Denmark) crosses the East Channel of the Great Belt and consists of two multi-span beam type approach bridges leading to a long-span suspension bridge. A key structural characteristic of this system is that the resulting continuous girder deck spans over the bridge's entire length, of 2694m [104]. Suspension bridges of this type are usually hinged at the pylons, e.g. Humber Bridge, in order to accommodate

an expansion joint there. When compared to the traditional hinged configuration, the continuous girder system improves serviceability, reduces longitudinal movements due to traffic and lateral deflections due to wind.

The Great Belt suspension bridge along with the Humber Bridge (1981, UK) the Severn (1966, UK) and Bosporus Bridge (1973, Turkey) shares a streamlined flat box girder deck which reduces construction and maintenance costs while providing comparable rigidity to truss girders. Streamlined box girders resemble aerofoils in terms of aerodynamics and are expected to display a similar heave-pitch flutter mode. The hollow deck boxes are equipped with transverse trusses for improved fatigue resistance, Fig. 3.12. The bridge has a cable sag ratio 1:9, chosen to reduce sliding forces in the anchorages. The heavy main cables have an appreciable impact on the structure's dynamics. Hence, the natural frequencies for the lower modes are expected to be grouped in a much narrower frequency band compared to a simple beam structure [104]. Another interesting fact of the Great Belt Bridge is that for the two approach bridges 32 TMDs were installed for suppressing vortex shedding each having a mass of 8t (approximately 0.5% of the modal mass). In

| Element | Property | Value |
|---|---|---|
| | Young modulus of elasticity | $E = 210 \times 10^9 N/m^2$ |
| | shear modulus of elasticity | $G = 80.8 \times 10^9 N/m^2$ |
| | element length | $L = 40m$ |
| | half chord width of the deck | $b = 15.5m$ |
| girder | girder mass | $m_g = 15260kg/m$ |
| | moment of inertia about horizontal axis | $I_y = 4m^4$ |
| | moment of inertia about vertical axis | $I_z = 100m^4$ |
| | torsional moment of inertia | $I_a = 7.6m^4$ |
| | mass moment of inertia (including cables) | $I_m = 2.47 \times 10^6 kgm^2/m$ |
| | Young modulus of elasticity | $E_c = 210 \times 10^9 N/m^2$ |
| | cross sectional area | $A_c = 0.44m^2$ |
| | half chord distance between cables | $b_c = 13.5$ |
| cables | diameter | $d_c = 0.75m$ |
| | mass of the main cables (both cables) | $m_c = 2 \times 3745kg/m$ |
| | horizontal cable tension (both cables) | $H_w = 2 \times 1.92 \times 10^8 N$ |
| | main cable sag | $f = 180m$ |
| | length of shortest hanger cable | $h_{e,\min} = 10m$ |

Table 3.2 Structural properties of the FE model of the Great Belt Bridge.

the modelling investigation of the Great Belt Bridge, it was concluded that good modal

agreement is achieved using elements of approximately 40$m$ length for the main span and 50$m$ length for the side spans. This resulted in a model having approximately 350 DOFs. Basic dimensions of the FE model are presented in Fig. 3.13. In order to account for deck continuity at the tower supports, the degrees of freedom $q_2, q_5$ and $q_8, q_{10}$ respectively were considered to be free. Unconstrained degrees of freedom mean continuity, for the edge elements. The structural parameters implemented in the FE model are presented in Table 3.2.

Figure 3.11 View of the Great Belt Bridge (photo courtesy www.BRIDGEMEISTER.com).

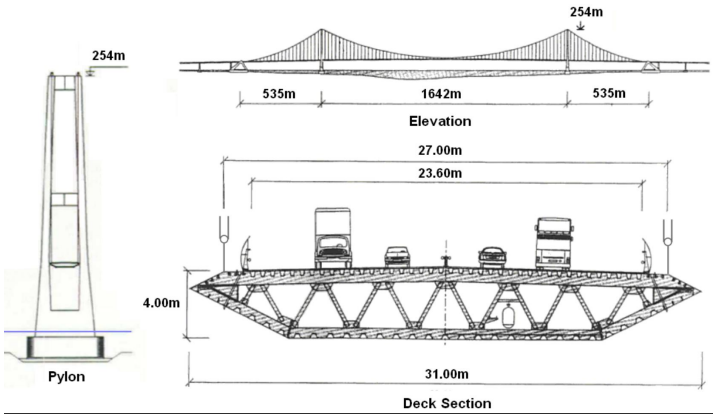


Figure 3.12 Main dimensions of the Great Belt East Bridge [198].

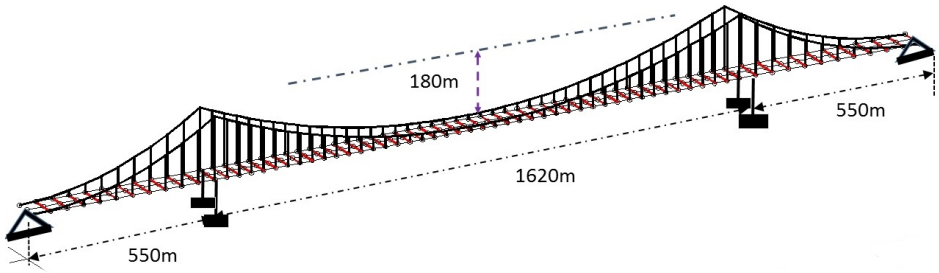


Figure 3.13 Basic dimensions of the East Great Belt FE Bridge model.

### 3.3.6 Comparison of Modal Properties for the Great Belt

Fig. 3.14 and Fig. 3.15 compare the natural frequencies and shapes of the vertical, lateral and torsional modes obtained by implementing the FE model with the measured mode shapes and natural frequencies reported in Larsen [104]. Further modal analyses of the Great Belt are given in [92]; these are the product of more detailed FE modelling using commercial packages. The proposed mathematical formulation however results in a model of considerably lower size while staying within the uncertainty scatter of more complex

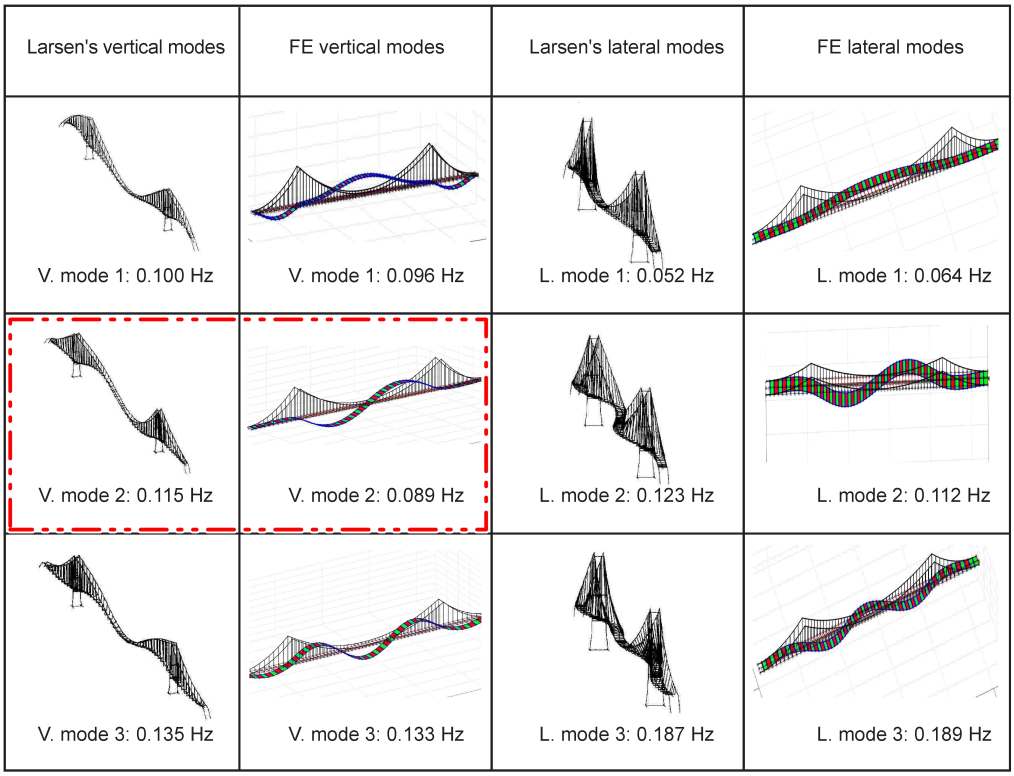


Figure 3.14 Comparison of experimentally identified vertical and lateral modes (left columns) from Larsen [104] to FE results (right columns). Red boxes mark the modes for which there is deviation between experimental and FE modelling results.

models. An equal displacement on the main cables for those cases is expected because the model assumes inextensibility of the hangers. For the lateral modes only the deck modal displacements are presented since the cable's lateral movement is of less interest. It should be stressed that the implemented linearized theory FE framework predicts no additional cable tension $H_w$ for antisymmetric deflections of the cable and the stiffening structure. This is due to the fact that for antisymmetric movement the downward movement on one side of the centreline of the centre span tends to increase the cable length, while at the same time the upward movement on the other side of the centre span tends to reduce the cable length, hence these effects balance one another. As a consequence of the lack of additional cable tension there is no interaction between the main and side spans for the antisymmetric modes due to the cables. Any movement of the side spans is because of the continuous girder assumption. Bridges however often exhibit interaction between side and main spans both for symmetric and antisymmetric modes, as well as for higher and lower modes [5]. This can potentially compromise the agreement between computed and measured results for antisymmetric modes. For the Great Belt Bridge case, the first antisymmetric mode demonstrates strong interaction between the main span and the side spans, which explains the difference when compared to Larsen's results. Given the comparison, it is concluded that the structural model approximates successfully all important modal properties, especially those crucial for aeroelastic analysis.

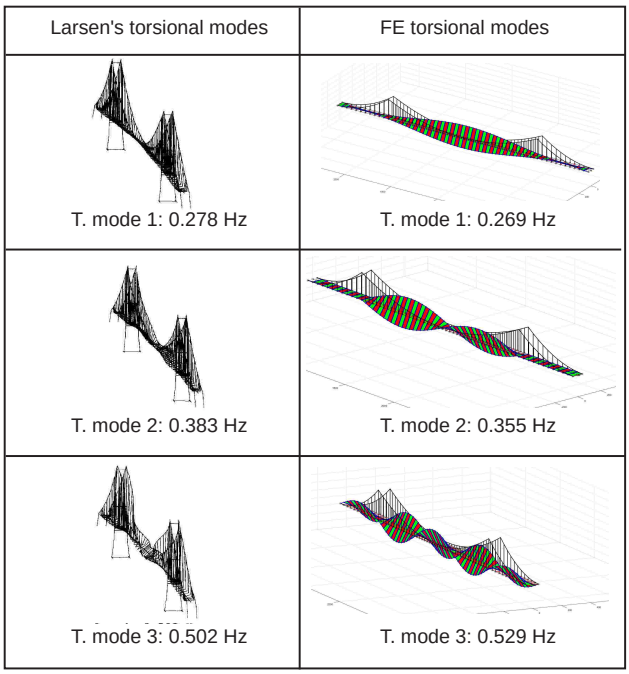


Figure 3.15 Comparison of experimentally identified torsional modes (left column) from Larsen [104] to FE results (right column).

## 3.4 Modelling of the Deck Erection Process

Early erection stages of a suspension bridge have been proven to be most vulnerable against flutter type aerodynamic instability, the main reason being the low torsional stiffness. This section will focus on implementing the modal vibrational methodology developed and validated in the previous sections in order to estimate the Humber's evolution of dynamic characteristics during the deck assembly process.

The stability during erection is determined by an interplay of frequency closeness, prominently of vertical and torsional frequencies, and of mode shape coupling, as both must reach a lock-in at the critical wind speed [27]. In that respect, the ratio of the fundamental torsional to vertical frequency has been established to be an effective indicator related to the flutter stability limit [27, 71]. As has been reported with regard to aeroelastic analyses of different suspension bridges [71] the most critical stage typically takes place when $\frac{1}{10}$ to $\frac{1}{3}$ of the deck is erected. The following are the major factors affecting the structure's modal characteristics during erection.

- The deck's contribution to torsional rigidity is greater than in vertical rigidity. Consequently, at early erection stages the torsional stiffness is much lower than the final stages, which has a direct impact on aerodynamic stability limits.

- Vertical stiffness, on the other hand, is less sensitive to the degree of deck completion and is primarily influenced by the stiffness of the main cables.

- The added inertia with increasing number of deck segments affects mostly the vertical modes because of the associated lower rotational inertia compared to that of the cables. The cable mass, at a larger distance from the centre line of the bridge, produces in fact a higher rotational inertia for the same amount of translational mass.

- Deck elements during assembly are linked by temporary connections which because of their nature result in higher deck stiffness contribution for the torsional modes than for the vertical ones.

- The towers depending on the bridge type and erection sequence may have a different impact on the modes. However, considering that the tower stiffness is much larger than that of the cables, their influence is estimated to be minimal at the early erection stages, which are the most aerodynamically interesting ones.

- Stiffness distribution during erection contributes to bringing the torsional and vertical frequencies closer together at the early stages. It is expected that when $10-20\%$ of the deck is suspended the flutter limit reaches its lowest values. At this point, the deck is long enough to pick up the aerodynamic excitation force, while torsional stiffness is low and the ratio of the fundamental torsional to vertical frequency is closer to unity.

In this part the evolution of natural frequencies during the erection stage of the Humber Bridge is modelled. The FE modelling of the erection process makes use of the same finite elements as in the full model. For the non-erected part, the deck's mass and stiffness contribution is considered negligible in the structural matrix entries. To account for

the temporary connections, whose purpose is to avoid locked-in bending stresses, we consider half the torsional rigidity for all construction stages whereas the flexural stiffness is neglected altogether [27]. For different deck completion stages, the cable horizontal force and additional displacement resulting from the added weight must be determined by solving the nonlinear cable equations [85], see Appendix A. Fig. 3.16 demonstrates the evolution of the vertical and torsional frequencies and Fig. 3.17 presents the corresponding ratio of the first torsional to vertical frequency. The ratios presented in Fig. 3.17 correspond to the cases when because of the temporary connections half or full the deck's torsional rigidity is considered. The analysis presented by Brancaleoni [27] is superimposed to the findings. Brancaleoni's analysis considered the full torsional rigidity of the deck in computing the ratio. From the modelling analysis of the Humber Bridge's erection process the following

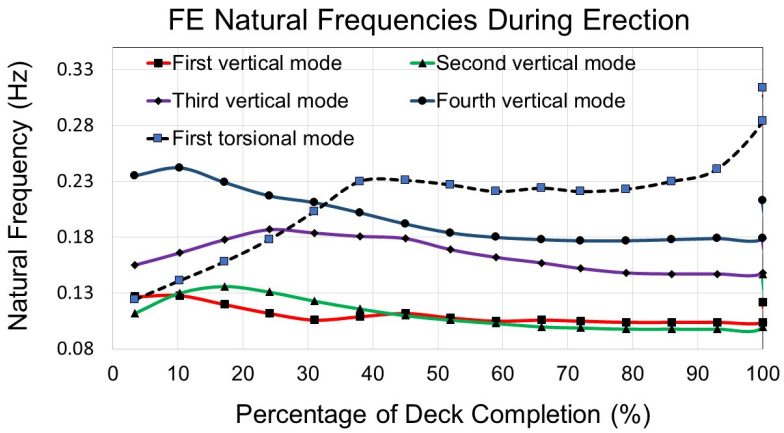


Figure 3.16 Evolution of natural frequencies of the Humber Bridge for the first four vertical and first torsional modes during deck erection process (measured as a percent of length of the main span).

observation can be drawn:

- A symmetric deck construction process for the FE modelling was adopted, with element size 50$m$, closely following the actual erection sequence.
- The natural frequencies of the vertical modes retain an approximately constant value during deck assembly as expected. The torsional stiffness increases rapidly during the initial 40% of the erection process, then remains roughly constant during intermediate

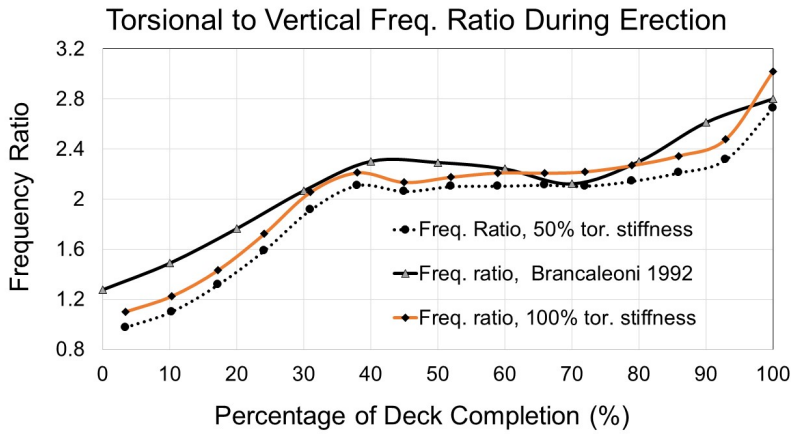


Figure 3.17 Frequency ratio for the Humber Bridge of the first torsional to the first vertical mode as a function of the deck erection stage.

stages. The stiffness increase at 100% is due to the final stiffening of the provisional deck connections.

- The frequency ratio resulting from this analysis follows a similar trend to that of Brancaleoni [27], indicating that frequency ratio is close to unity at the early stages and gradually picks up until when 40% of the main span is erected.

- When the erected deck is very short, torsional and vertical mode frequencies are very close since they effectively correspond to the in phase and out of phase movement of the cables.

- Fig. 3.18 graphically depicts the fundamental torsional mode at different erection stages. At approximately 40% there is a clear transition in mode shape because of added torsional deck inertia, which practically corresponds to a change in the modal shape of the main cables. The transition in torsional mode shape explains the flattening of the torsional natural frequency curve.

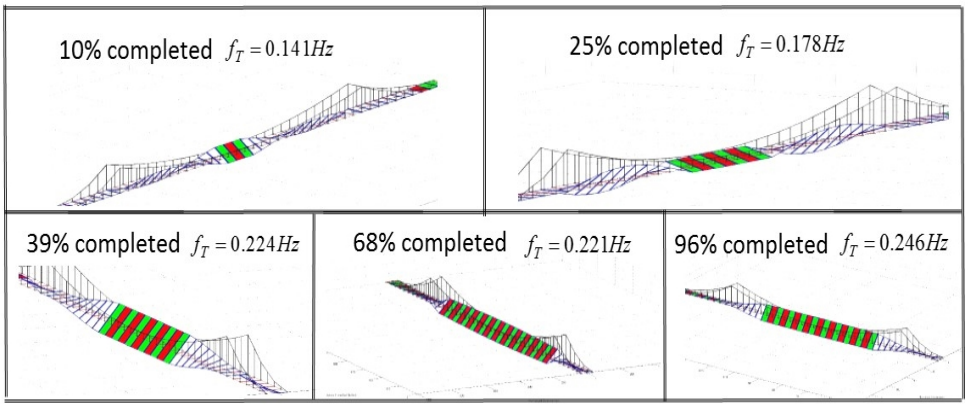


Figure 3.18 Evolution of the fundamental torsional mode at progressive construction stages. The deck torsional stiffness is assumed half its final value and the deck's flexural stiffness is neglected due to the temporary connections.

## 3.5 Discussion and Concluding Remarks

A finite element vibrational framework for capturing vertical, torsional and lateral modal characteristics of suspension bridges was presented. The most important assumption associated with the adopted methodology is that the three free vibration cases are considered independent from one another. It was shown that the adopted methodology results in a lower order system primarily because it accounts for the effect of the cables and the suspended structure in a single element. A modelling survey of the Humber Bridge and the East Great Belt Bridge and comparison to ambient vibration analysis and previous analytical investigation from the literature testify for a very good agreement in terms of modal responses. The validation analysis transitioned to the modelling of the deck erection stage under the premise that a free unbraced suspended deck is more vulnerable to flutter instability. By mimicking the deck assembly process of the Humber Bridge it was shown that the evolution of dynamic characteristics can be attained using slightly modified structural elements. The structural dynamic analysis presented here forms a fundamental building block for the multi-modal aeroelastic control investigation, which will be the focus of attention in the following chapters.

# Chapter 4

# Aeroelastic Bridge Formulation

## 4.1 Introduction

The discipline of aeroelasticity investigates phenomena in which a moving structure dynamically interacts with the surrounding fluid (airstream). From the aeroelastic phenomena described in chapters 1 and 2 the focus of the analysis presented in this thesis will narrow down to flutter instability. Flutter is a self-feeding vibrational motion leading to divergent amplitudes, assuming the system behaves linearly. If the energy input due to aerodynamic forces during a vibration cycle is larger than that dissipated by damping, the amplitude will be increased in the following cycle, which will in turn provoke amplification of aerodynamic forces thus creating a self-excited feedback.

The term flutter, stemming from the aeronautical industry, describes an aeroelastic interaction in which two degrees of freedom, torsional and vertical, couple together in a flow-driven unstable oscillation. A rigid aerofoil so constrained as to have only the flexural degree of freedom does not flutter. A rigid aerofoil with only the torsional degree of freedom can flutter only if the angle of attack is at or near the stalling angle or for some special mass distribution and elastic axis locations [68]. One degree of freedom flutter can manifest itself in long span suspension bridges as a result of complex flow separation as was indeed the case for the Tacoma Narrows collapse [21]. For the case of modern deck sections however flutter is expected to result from the coupling of different modes. Experimental

investigations on wings have shown that at critical flutter speed flexural movements at all points across the span are approximately in phase with one another and similarly the torsional movements are also in phase, but the flexural is considerably out of phase from torsional movement. This phase difference between vertical and torsional movement is an important ingredient for the occurrence of flutter instability.

This chapter will firstly describe the thin aerofoil theory and then recast these classic results from potential flow theory in a Laplace domain formulation using a rational function approximation of the circulatory fluid component. The developed aeroelastic model will then be transitioned to a finite element form so as to be combined with the structural vibrational framework presented in the preceding chapter. The resulting model allows for the estimation of the structure's aeroelastic characteristics by considering the full multi-modal interaction in a computationally efficient state space mathematical model. To account for the effect of the deck's bluff properties, the experimentally obtained flutter derivatives approach is then cast in a similar FE form and Roger's [159] approximation is then used to express the state-space system in the Laplace domain. The procedure developed is then implemented to describe the aeroelastic properties of the Humber Bridge and the Great Belt Bridge, finding very good agreement with experimental estimations. Aeroelastic instability limits are also computed during the erection stage of the Humber Bridge and the adopted framework vividly exposes the different mode contributions to the observed aeroelastic instabilities.

## 4.2 Aerodynamic Forces on Aerofoils and Bluff Bodies

This section will present the theoretical framework for computing the aerodynamic forces on a vibrating body in a smooth flow regime. In Sec. 4.2.1 Theodorsen's description of a vibrating thin plate is presented, which is a mixed description in the time and frequency domain. Sec. 4.2.2, introduces the *flutter derivatives* formulation, which forms the basis for *bluff body* aerodynamics. Theodorsen's solution is also given in flutter derivatives form. Sec. 4.2.3 presents the overall framework for the determination of the aerodynamic loading

problem entirely in the time domain. Although time domain solutions will not be further pursued in this work, this presentation provides valuable insight into the techniques involved as well as helps introduce the rational function approximation process, in Sec. 4.2.4, which will be very useful in subsequent analyses.

### 4.2.1 The Vibrating Thin Plate

Different definitions have been developed to describe the lift force '$L$' and moment force '$M$' for a thin aerofoil immersed in an incompressible fluid. Two dimensional flow results for the unsteady aerofoil problem have been formulated in both the time-domain and the frequency domain, primarily by Wagner [194], Theodorsen [186], Kuessner [101] and von Karman and Sears [94]. These results have the advantage of providing an exact analytic (closed-form) solution for the pressure distribution (hence, the forces and pitching moments). It is worth noting that although these methods are only applicable for 2-D and incompressible flow they have traditionally formed the foundations for extending to subsonic compressible flow [112], as well as providing the mathematical framework for the introduction of flutter derivatives [175].

Theodorsen's solution [186], being the most popular and widely used, is concerned with finding the aerodynamic loading on an 2-D harmonically oscillating aerofoil in inviscid, incompressible flow, under the assumption of small disturbances. The mechanics of the physical phenomenon is demonstrated in Fig. 4.1, in which both the aerofoil and its shed wake are modelled by a vortex sheet. The shed wake is regarded as a flat surface extending from the trailing edge downstream to infinity. This assumption has little influence on the results if the motion is small. The circulation in the wake consists of counteracting vortices. The bound vorticity, $\gamma_b$, is responsible for generating pressure difference and the corresponding lift force. The wake vorticity, $\gamma_w$, on the other hand must be force free with zero net pressure jump over the sheet.

Theodorsen solved the problem of obtaining the loading, $\gamma_b$, on the aerofoil subjected to harmonic forcing conditions. The equations related to the pressure distribution on the

aerofoil were solved considering the Kutta condition at the trailing edge, $\gamma_b(c,t) = \gamma_w(c,t)$, which demands that the flow separates at the trailing edge point. In the case of unsteady flow, the unsteady Kutta condition is expressed as zero pressure difference at the wake. The governing integral equation is

$$w(x,0,t) = \frac{1}{2\pi}\int_0^c \frac{\gamma_b(x,t)}{(x-x_0)}dx + \frac{1}{2\pi}\int_c^\infty \frac{\gamma_w(x,t)}{(x-x_0)}dx. \tag{4.1}$$

where, $w$ denotes the downwash on the aerofoil. The connection between change in circulation about the aerofoil and circulation shed into the wake is given by the following equation

$$\gamma_w(c,t)dx = -\frac{d\Gamma(t)}{dt}dt. \tag{4.2}$$

Assuming the vortices travel downstream with velocity $U$, this leads to

$$U\gamma_w(c,t) = -\frac{d\Gamma}{dt}, \tag{4.3}$$

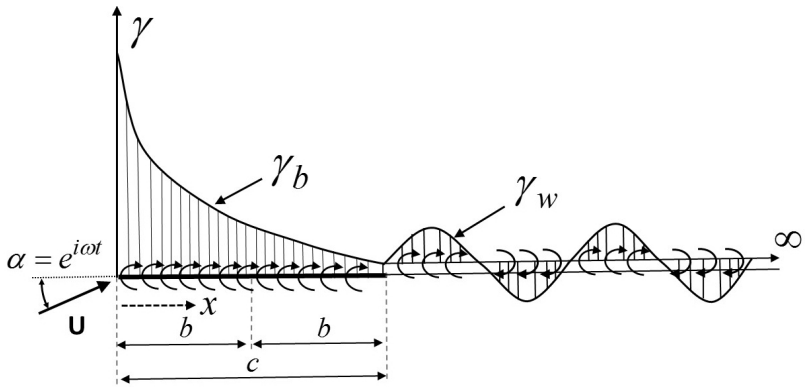


Figure 4.1 Mathematical representation of a harmonically oscillating thin aerofoil.

where, $\Gamma(t)$ is the aerofoil circulation given by

$$\Gamma(t) = \int_0^c \gamma_b(x,t)dx. \tag{4.4}$$

The changes in circulation about the aerofoil drive the circulation shed into the wake, See Kelvin's theorem regarding the conservation of circulation. The wake vorticity changes

the downwash velocity over the aerofoil and thus the corresponding pressure distribution. So long as the circulation about the aerofoil is changing with respect to time, circulation is continuously shed into the wake, being linked to the aerodynamic loads on the aerofoil. If the shed circulation abruptly stops, the forcing becomes zero and the remaining circulation in the wake convects downstream to infinity [112]. Theodorsen's mathematical treatment, [23], of the dynamic oscillating aerofoil phenomenon concentrates on forming a transfer function between the forcing (angle of attack) and the aerodynamic response (pressure distribution, lift and pitching moment). The computed closed form equations express lift and moment forces ($L$ and $M$), see Eq.(4.5) and Eq.(4.6), as linear functions of vertical displacement (heave) and rotation angle and their first and second derivatives (velocity and acceleration). These equations are derived for an aerofoil of chord $c = 2b$, in a flow stream of steady wind velocity $U$.

$$L = -\rho b^2 \left[U\pi\dot{\alpha} + \pi\ddot{h} - \pi ba\ddot{\alpha}\right] - 2\pi\rho UbC(k)\left[U\alpha + \dot{h} + b\left(\frac{1}{2} - a\right)\dot{\alpha}\right], \tag{4.5}$$

$$M = -\rho b^2\left[\pi\left(\frac{1}{2} - a\right)Ub\dot{\alpha} + \pi b^2\left(\frac{1}{8} + a^2\right)\ddot{\alpha}\right] + 2\pi\rho Ub^2\left(a + \frac{1}{2}\right)C(k)\left[U\alpha + \dot{h} + b\left(\frac{1}{2} - a\right)\dot{\alpha}\right] \tag{4.6}$$

where, the vertical motion, heave, is denoted by $h$ and rotating angle, pitch, is denoted by $\alpha$. $\rho$ is the mass of air per unit volume, $b$ is the half chord of the deck section, $U$ is the wind velocity and $ab$ is the distance from the chord midpoint to the section's rotation axis, see Fig. 4.2. Without loss of generality considering a symmetric cross section, the rotation centre coincides with the flat plate's midpoint $a = 0$. The above stated aerodynamic forcing equations then reduce to the following

$$L = -\pi\rho b^2\left[U\dot{\alpha} + \ddot{h}\right] - 2\pi\rho UbC(k)\left[U\alpha + \dot{h} + \frac{b\dot{\alpha}}{2}\right], \tag{4.7}$$

and

$$M = -\pi\rho b^2 \left[\frac{bU\dot{\alpha}}{2} + \frac{b^2\ddot{\alpha}}{8}\right] + \pi\rho U b^2 C(k) \left[U\alpha + \dot{h} + \frac{b\dot{\alpha}}{2}\right]. \tag{4.8}$$

The first set of terms in equations (4.7) and (4.8) are due to flow acceleration effects (non-circulatory or apparent mass effect). The second terms arise from the creation of circulation about the aerofoil. The circulatory term, $C(k) = F(k) + iG(k)$ is a complex valued transfer function, which accounts for the effect of the shed wake on the unsteady aerodynamic loading. $k = \frac{b\omega}{U} = \frac{B\omega}{2U} = \frac{K}{2}$ is the system's reduced frequency, where $\omega$ is the frequency of oscillation of the vibration body. The reduced frequency parameter is used to characterize the degree of unsteadiness of the problem. For $k = 0$, the flow is steady. For $0 \leq k \leq 0.05$, the flow can be considered quasi steady, meaning that unsteady effects can be considered small. When, $k \geq 0.05$, the flow is usually regarded as unsteady. Problems with reduced frequency of 0.2 and above are considered highly unsteady and the terms associated with acceleration effects begin to dominate the aerodynamic behaviour [20]. The non-circulatory or apparent mass terms are physically related to the pressure forces

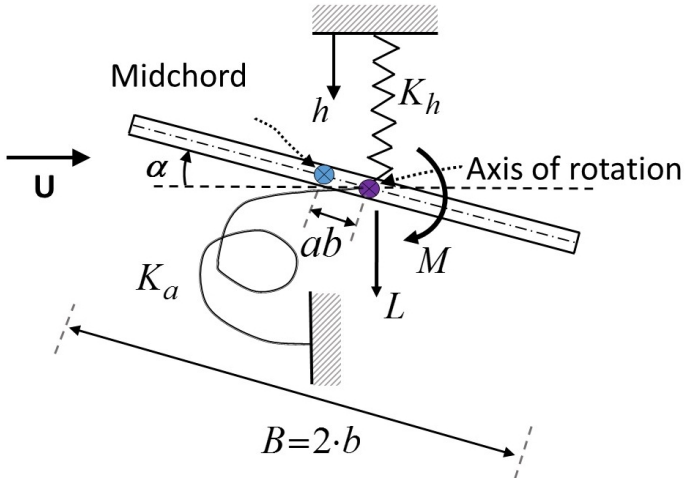


Figure 4.2 Vibrating thin plate model under perturbed deflections $\alpha$ and $h$ from static equilibrium. Springs $K_h$ and $K_a$ represent heave and pitch (bending and torsion) stiffness. $a$, according to Theodorsen's convention is measured from the midchord, $b$ is the half chord length.

required to accelerate the fluid in the vicinity of the aerofoil. The circulatory part is linked to the shed vortex wake and hence the term in square brackets in equations (4.7) and (4.8). This contribution represents the instantaneous vertical velocity of the air particle in contact

with the aerofoil at the three-quarter-chord point of the profile, towards the trailing edge.

$$U_{(3/4)C} = \left[ U\alpha + \dot{h} + \frac{b\dot{\alpha}}{2} \right] \tag{4.9}$$

Furthermore, the circulatory part of the lift $L_C = 2\pi\rho U b C(k) \left[ U\alpha + \dot{h} + \frac{b\dot{\alpha}}{2} \right]$ appears to be acting on the one-quarter-chord point, however the whole force including the non-circulatory flow contribution generally does not act there. It can thus be concluded that these two chordwise points, the one- and three-quarter-chord point, determine the aerodynamic pitching moment in the unsteady aerodynamic formulation, namely: the unsteady airfoil behaves in a quasi-steady manner with regard to the circulatory effects as if the angle of attack were defined at the three-quarter-chord point and the lift is taken at the one-quarter-chord point [20].

Theodorsen's function $C(k)$ is expressed in terms of Bessel functions

$$C(k) = \frac{J_1(k) - iY_1(k)}{(J_1(k) + Y_0(k)) - i(J_0(k) - Y_1(k))}, \tag{4.10}$$

in which $J_0(k)$, $J_1(k)$, $Y_0(k)$ and $Y_1(k)$ are Bessel functions of the first and second kind respectively. An alternative formulation uses Hankel functions defined as $H_\nu^{(2)} = J_\nu - iY_\nu$, in which gain $J_\nu$ and $Y_\nu$ are Bessel functions of the first and second kind.

$$C(k) = F(k) + iG(k) = \frac{H_1^{(2)}(k)}{H_1(k)^{(2)} + iH_0(k)^{(2)}} \tag{4.11}$$

The above stated Bessel functions receive the reduced frequency as argument. The real, or in-phase, part as well as the imaginary, or out-of-phase part, can be expressed as

$$F(k) = \frac{J_1(J_1 + Y_0) + Y_1(Y_1 - J_0)}{(J_1 + Y_0)^2 + (Y_1 - J_0)^2}, \tag{4.12}$$

and

$$G(k) = -\frac{Y_1 Y_0 + J_1 J_0}{(J_1 + Y_0)^2 + (Y_1 - J_0)^2}. \tag{4.13}$$

Theodorsen's function is plotted in Fig. 4.3 and its amplitude and phase are given by

$$|C(k)| = \sqrt{F^2 + G^2} \quad \text{and} \quad \Phi = \tan^{-1}\left(\frac{G}{F}\right). \tag{4.14}$$

respectively.

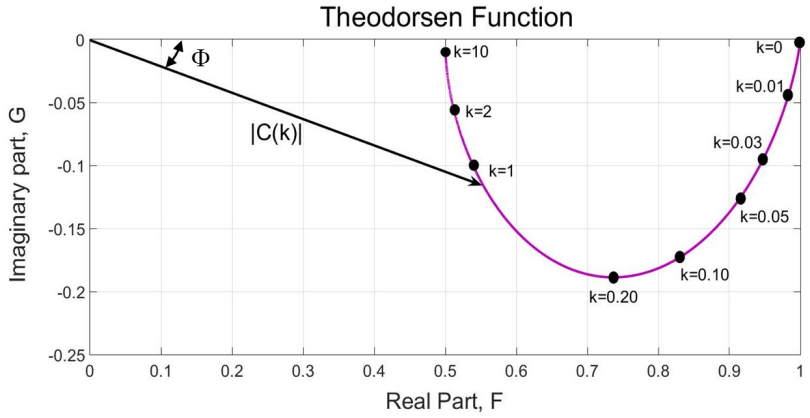


Figure 4.3 Theodorsen function plotted in terms of its real and imaginary component.

### 4.2.2 Thin Aerofoil Theory in Flutter Derivatives Form

The closed form expressions of thin aerofoil theory may result in significant errors if applied to bluff deck sections. For this reason, the flutter derivatives formulation attempts to incorporate frequency dependent parameters, more accurately related to reduced frequency, extracted from wind-tunnel testing in a mathematical framework resembling that of the classic Theodorsen approach. This alternative form of aerodynamic loading [169, 175] expresses the lift and moment forces as a linear function of the lateral, $p$, vertical, $h$, and angular, $\alpha$, displacements and their corresponding first order derivatives. In this formulation the contribution is more generally divided into in-phase and out-of-phase components of the force with respect to $p, h, a$ and their derivatives, instead of distinguishing between circulatory and non-circulatory effects, as for the aerofoil [37].

As for the thin aerofoil case, for purely sinusoidal motion with angular frequency $\omega$, the following linear relations in the frequency domain, in the spirit of equations (4.7)-(4.8),

were postulated.

$$L = \frac{1}{2}\rho U^2 B\left[KH_1^*\left(\frac{\dot{h}}{U}\right) + KH_2^* B\left(\frac{\dot{\alpha}}{U}\right) + K^2 H_3^*\alpha + K^2 H_4^*\left(\frac{h}{B}\right)\right] + \frac{1}{2}\rho U^2 B\left[KH_5^*\left(\frac{\dot{p}}{U}\right) + K^2 H_6^*\left(\frac{p}{U}\right)\right], \quad (4.15)$$

$$M = \frac{1}{2}\rho U^2 B^2\left[KA_1^*\left(\frac{\dot{h}}{U}\right) + KA_2^* B\left(\frac{\dot{\alpha}}{U}\right) + K^2 A_3^*\alpha + K^2 A_4^*\left(\frac{h}{B}\right)\right] + \frac{1}{2}\rho U^2 B^2\left[KA_5^*\left(\frac{\dot{p}}{U}\right) + K^2 A_6^*\left(\frac{p}{U}\right)\right], \quad (4.16)$$

$$D = \frac{1}{2}\rho U^2 B\left[KP_1^*\left(\frac{\dot{p}}{U}\right) + KP_2^* B\left(\frac{\dot{\alpha}}{U}\right) + K^2 P_3^*\alpha + K^2 P_4^*\left(\frac{p}{B}\right)\right] + \frac{1}{2}\rho U^2 B\left[KP_5^*\left(\frac{\dot{h}}{U}\right) + K^2 P_6^*\left(\frac{h}{B}\right)\right], \quad (4.17)$$

where $H_i^*, A_i^*, P_i^*$ are the dimensionless flutter derivatives, which are functions of the reduced frequency $K = \omega B/U$, $\omega$ is the circular frequency and $B = 2b$ is the deck width. In this format the sway of the drag forces is included, see Fig. 4.4. In the flutter derivative context as in Theodorsen's flutter theory, linear superposition of small effects, such as angle of attack, is assumed. For the case of bridge decks this assumption must be considered as an approximation only [165].

For a sinusoidally oscillating body the heave and pitch motion can be expressed in the following form

$$h = h_o e^{i\omega t} \quad \text{and} \quad \alpha = \alpha_o e^{i(\omega t+\phi)}. \quad (4.18)$$

In Eq.(4.18) the vertical and torsional motion have the same frequency thus indicating incipient flutter instability. The following identities result as a consequence of Eq.(4.18).

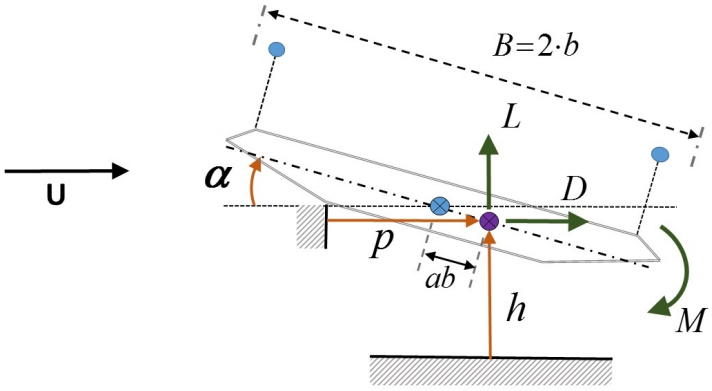


Figure 4.4 Aerodynamic forces in the context of the Flutter Derivatives framework.

$$\frac{\dot{h}}{\omega} = ih \qquad \frac{\dot{\alpha}}{\omega} = i\alpha \qquad \ddot{h} = -\omega^2 h \qquad \ddot{\alpha} = -\omega^2 \alpha \tag{4.19}$$

Through substitution of Eq.(4.19) in the thin aerofoil forcing expressions given in Eq.(4.7) and Eq.(4.8) the following can be written

$$L = -\pi\rho b^2 \left[U\dot{\alpha} - \omega^2 h\right] - 2\pi\rho U b[F(k) + iG(k)] \left[U\alpha + \dot{h} + \frac{b\dot{\alpha}}{2}\right], \tag{4.20}$$

$$M = -\pi\rho b^2 \left[\frac{bU\dot{\alpha}}{2} - \frac{\omega^2 b^2 \alpha}{8}\right] + \pi\rho U b^2 [F(k) + iG(k)] \left[U\alpha + \dot{h} + \frac{b\dot{\alpha}}{2}\right]. \tag{4.21}$$

In equations (4.20)-(4.21) the following substitutions were made: $\frac{\dot{h}}{\omega} \rightarrow ih$, $\frac{\dot{\alpha}}{\omega} \rightarrow i\alpha$, $-\omega h \rightarrow i\dot{h}$ and $-\omega\alpha \rightarrow i\dot{\alpha}$. The resulting equations are in the form of the flutter derivatives framework.

$$L = \frac{1}{2}\rho U^2 B \left[KH_1^{*T}\left(\frac{\dot{h}}{U}\right) + KH_2^{*T} B\left(\frac{\dot{\alpha}}{U}\right) + K^2 H_3^{*T}\alpha + K^2 H_4^{*T}\left(\frac{h}{B}\right)\right], \tag{4.22}$$

$$M = \frac{1}{2}\rho U^2 B^2 \left[KA_1^{*T}\left(\frac{\dot{h}}{U}\right) + KA_2^{*T} B\left(\frac{\dot{\alpha}}{U}\right) + K^2 A_3^{*T}\alpha + K^2 A_4^{*T}\left(\frac{h}{B}\right)\right], \tag{4.23}$$

where $H_i^{*T}$ and $A_i^{*T}$ are the theoretical flutter derivatives corresponding to the Theodorsen vibrating aerofoil problem. The drag related terms are of course zero for this case.

$$\begin{array}{cc} H_1^{*T} = -\frac{2\pi F(k)}{K} & A_1^{*T} = \frac{\pi F(k)}{2K} \\ H_2^{*T} = -\frac{\pi}{2K}\left[1+\frac{4G(k)}{K}+F(k)\right] & A_2^{*T} = -\frac{\pi}{2K^2}\left[\frac{K}{4}-G(k)-\frac{KF(k)}{4}\right] \\ H_3^{*T} = -\frac{\pi}{K^2}\left[2F(k)-\frac{G(k)K}{2}\right] & A_3^{*T} = \frac{\pi}{2K^2}\left[\frac{K^2}{32}+F(k)-\frac{KG(k)}{4}\right] \\ H_4^{*T} = \frac{\pi}{2}\left[1+\frac{4G(k)}{K}\right] & A_4^{*T} = -\frac{\pi G(k)}{2K} \end{array} \tag{4.24}$$

Equations (4.22)-(4.23) express self excited forces in real number format. An alternative approach is based on using complex arithmetic [179]. In complex notation, the physical displacement and force quantities, by convention, equal the real part of the corresponding complex quantity. The aerodynamic forces in complex notation are written as

$$L = \omega^2 \pi \rho b^2 (C_{Lh} h + b C_{L\alpha} \alpha), \tag{4.25}$$

$$M = \omega^2 \pi \rho b^2 (b C_{Mh} h + b^2 C_{M\alpha} \alpha). \tag{4.26}$$

Similarly to $H_i^*$ and $A_i^*$, the four new complex coefficients $C_{mn}$ are functions of the reduced frequency and by comparing the corresponding force equations the following identities can be established.

$$\begin{array}{cc} C_{Lh} = \frac{2}{\pi}(H_4^* + iH_1^*) & C_{L\alpha} = \frac{2}{\pi}(H_3^* + iH_2^*) \\ C_{Mh} = \frac{4}{\pi}(A_4^* + iA_1^*) & C_{M\alpha} = \frac{8}{\pi}(A_3^* + iA_2^*) \end{array} \tag{4.27}$$

It has been argued [179] that although the real value notation has been traditionally used in the bridge aerodynamic field, the corresponding complex expressions are more compact because they can express the phasing internally. In real notation, the velocity terms $\dot{h}$ and $\dot{\alpha}$ need to be added in order to properly account for the phasing. In terms of expressing the thin plate problem in the complex derivatives form, the following equivalences among the

complex coefficients and the Theodorsen circulation function are presented.

$$\begin{aligned} C_{Lh}^{T} &= 1 - \tfrac{2i}{k}C(k) \quad & C_{L\alpha}^{T} &= -\tfrac{1}{k}\left[i(C(k)+1) + \tfrac{2}{k}C(k)\right] \\ C_{Mh}^{T} &= \tfrac{i}{k}C(k) \quad & C_{M\alpha}^{T} &= \tfrac{i}{2k}(C(k)-1) + \tfrac{1}{k^2}C(k) + \tfrac{1}{8} \end{aligned} \tag{4.28}$$

### 4.2.3 Extension of Aerodynamic Loading into the Time Domain

The previous approach to the aerodynamic instability problem is based on a frequency domain framework. However, expressing aerodynamic forces in the time domain is strictly speaking a more general solution because it can account for non-linear geometrical behaviour as well as non-linear behaviour of acting forces. In the aeronautic field, Wagner [194] first obtained the solution for the so-called indicial lift on a thin aerofoil undergoing a transient step change in the angle of attack in an incompressible flow. The effective angle of attack on a thin aerofoil linked to Eq.(4.9) is given by Eq.(4.29), located at the rearward three-quarter-chord point.

$$\alpha_{3/4} = \left[\alpha + \frac{\dot{h}}{U} + \frac{b}{2}\frac{\dot{\alpha}}{U}\right] \tag{4.29}$$

It can be observed that for the thin aerofoil the terms $\frac{\dot{h}}{U}$, $\alpha$ and $\frac{b}{2}\frac{\dot{\alpha}}{U}$ have equal contributions to the effective angle of attack. In Wagner's time domain form the step change in the effective angle of attack can be expressed as

$$\alpha_{3/4} \rightarrow \begin{cases} 0, & t < 0 \\ \alpha_0, & t > 0 \end{cases} \tag{4.30}$$

The instantaneous circulatory lift because of this change is then given by the following equation

$$L(s) = -\frac{1}{2}\rho U^2 B(2\pi)\alpha_0 \Phi(s), \tag{4.31}$$

where $s = \frac{2Ut}{B}$ is a dimensionless parameter representing the distance travelled by the aerofoil in semi-chords. $\Phi(s)$ is referred to as the Wagner function and has an exact analytic

expression [68]. In analogy with the Theodorsen function, Wagner's function accounts for the effect of the shed wake. The function builds up asymptotically from one half to a final value as $s \to \infty$. In Wagner's problem, the aerodynamic centre is at mid-chord at $s = 0$ and moves immediately to $\frac{1}{4}$-chord for $s > 0$. If the indicial response is known, Eq.(4.31), the unsteady circulatory loads to arbitrary changes in the angle of attack can be obtained through the superposition of indicial aerodynamic responses by means of Duhamel's superposition integral. Finally, Eq.(4.32) and Eq.(4.33) express the self excited lift and moment around the midchord of an aerofoil considering both circulatory and added mass effects.

$$L(t) = -\frac{1}{2}\rho U^2 B(2\pi)\left(\frac{b\dot{\alpha}}{2U} + \int_{-\infty}^{t} \Phi(t-\tau)\dot{\alpha}_{3/4}(\tau)d\tau\right) \tag{4.32}$$

$$M(t) = -\frac{1}{2}\rho U^2 B(\frac{\pi}{2})\left(-\frac{b\dot{\alpha}}{2U} + \int_{-\infty}^{t} \Phi(t-\tau)\dot{\alpha}_{3/4}(\tau)d\tau\right) \tag{4.33}$$

Where,

$$\dot{\alpha}_{3/4} = \frac{d}{ds}\alpha_{3/4}(s) \tag{4.34}$$

Although the Wagner function is known exactly, it is not in a convenient analytic form. Therefore, simple exponential or algebraic approximations have been used for its approximation. Garrick [69] proposed the following rational approximation, which agrees with the exact solution within 2% accuracy.

$$\Phi(s) \simeq \frac{s+2}{s+4} \tag{4.35}$$

Other more accurate approximations, include the R.T. Jones approximation [91], which agrees within 1% to the exact solution.

$$\Phi(s) \simeq 1.0 - 0.165e^{-0.0455s} - 0.335e^{-0.3s} \tag{4.36}$$

Furthermore, The Wagner function and the Theodorsen function are related via the Fourier transform presented in the following equation

$$C(k) = (ik)\int_0^\infty \Phi(\tau)e^{-ik\tau}d\tau. \tag{4.37}$$

For the case of bluff sections the time domain formulation can be expressed in terms of impulse response functions [34, 42, 111, 117], which are in turn associated with the previously introduced flutter derivatives, Eq.(4.15)-Eq.(4.17). Eq.(4.38)-Eq.(4.40) describe the general form of aerodynamic self excited forces in terms of convolution integrals of the uncorrelated impulse response functions.

$$L(t) = \frac{1}{2}\rho U^2 \int_{-\infty}^{t} [I_{Lh}(t-\tau)h(\tau) + I_{La}(t-\tau)\alpha(\tau) + I_{Lp}(t-\tau)p(\tau)]\, d(\tau), \tag{4.38}$$

$$M(t) = \frac{1}{2}\rho U^2 \int_{-\infty}^{t} [I_{Mh}(t-\tau)h(\tau) + I_{Ma}(t-\tau)\alpha(\tau) + I_{Mp}(t-\tau)p(\tau)]\, d(\tau), \tag{4.39}$$

$$D(t) = \frac{1}{2}\rho U^2 \int_{-\infty}^{t} [I_{Dh}(t-\tau)h(\tau) + I_{Da}(t-\tau)\alpha(\tau) + I_{Dp}(t-\tau)p(\tau)]\, d(\tau), \tag{4.40}$$

where, $I_x(x = Lh, La, Lp, Mh, Ma, Mp, Dh, Da, Dp)$ are the aerodynamic impulse response functions. The next step consists in introducing the Fourier transform to Eq.(4.38) which results in the following expression

$$\frac{2F[L(t)]}{\rho U^2} = F[I_{Lh} * h + I_{L\alpha} * \alpha + I_{Lp} * p] = F[I_{Lh}] * F[h] + F[I_{L\alpha}] * F[\alpha] + F[I_{Lp}] * F[p]. \tag{4.41}$$

Repeating the process for equations (4.39) and (4.40), the following matrix form can be written

$$\begin{Bmatrix} F[L(t)] \\ F[M(t)] \\ F[D(t)] \end{Bmatrix} = \frac{1}{2}\rho U^2 \begin{bmatrix} F[I_{Lh}] & F[I_{L\alpha}] & F[I_{Lp}] \\ F[I_{Mh}] & F[I_{M\alpha}] & F[I_{Mp}] \\ F[I_{Dh}] & F[I_{D\alpha}] & F[I_{Dp}] \end{bmatrix} \begin{bmatrix} F[h(t)] \\ F[\alpha(t)] \\ F[p(t)] \end{bmatrix} \tag{4.42}$$

Similarly, by using the Fourier transformation on the flutter derivative equations, (4.15)-(4.17), the following expression in matrix form is concluded.

$$\begin{Bmatrix} F[L(t)] \\ F[M(t)] \\ F[D(t)] \end{Bmatrix} = \frac{1}{2}\rho U^2 \begin{bmatrix} K^2(H_4^*+iH_1^*) & K^2B(H_3^*+iH_2^*) & K^2(H_6^*+iH_5^*) \\ K^2B(A_4^*+iA_1^*) & K^2B^2(A_3^*+iA_2^*) & K^2B(A_6^*+iA_5^*) \\ K^2(P_4^*+iP_1^*) & K^2B(P_3^*+iP_5^*) & K^2(P_6^*+iP_5^*) \end{bmatrix} \begin{bmatrix} F[h(t)] \\ F[\alpha(t)] \\ F[p(t)] \end{bmatrix} \tag{4.43}$$

Comparing matrix forms (4.42) and (4.43) the following relationships between flutter derivatives and impulse response functions is obtained

$$\begin{aligned} F[I_{Lh}] &= \tilde{I}_{Lh} = K^2(H_4^*+iH_1^*) & F[I_{L\alpha}] &= K^2B\tilde{I}_{La} = (H_3^*+iH_2^*) \\ F[I_{Lp}] &= \tilde{I}_{Lp} = K^2(H_6^*+iH_5^*) & F[I_{Mh}] &= \tilde{I}_{Mh} = BK^2(A_4^*+iA_1^*) \\ F[I_{M\alpha}] &= \tilde{I}_{Ma} = B^2K^2(A_3^*+iA_2^*) & F[I_{Mp}] &= \tilde{I}_{Mp} = BK^2(A_6^*+iA_5^*) \\ F[I_{Dh}] &= \tilde{I}_{Dh} = K^2(P_4^*+iP_1^*) & F[I_{D\alpha}] &= \tilde{I}_{D\alpha} = K^2B(P_3^*+iP_2^*) \\ F[I_{Dp}] &= \tilde{I}_{Dp} = K^2(P_6^*+iP_5^*), \end{aligned} \tag{4.44}$$

where, $\tilde{I}_x$ $(x = Lh, La, Lp, Mh, Ma, Mp, Dh, Da, Dp)$ is given by

$$\tilde{I}_x = \int_0^\infty I_x(t)e^{-i\omega t}dt. \tag{4.45}$$

Self excited forces for bluff sections can also be expressed in terms of indicial response functions, $\Phi_r$, equivalently to equations (4.32) and (4.33) for the thin aerofoil. Equivalences of the form similar to Eq.(4.44) can also be derived, see [42, 164].

### 4.2.4 Rational Function Approximation for Time Domain Analysis

In order to compute unsteady aerodynamic forces in the time domain the impulse functions must be identified. A direct determination of these functions for bluff bridge sections is laced with difficulties, and the techniques based on wind tunnel testing have not been well established [42]. The alternative would be to rely on attainable flutter derivatives data in the frequency domain and derive the impulse functions using Eq.(4.44) equivalences. A related technical issue however, is that flutter derivatives are determined at discrete

values of reduced frequency and in order to reverse-transform the Fourier form and cast the equations in the time domain some sort of continuity approximation needs to take place. A common procedure suitable for complex couples is based on an approximation using rational functions [174, 159].

Taking the example of the Fourier transformed lift response to vertical motion, $h$, the used form of rational approximation reads

$$\tilde{I}_{Lh}(iK) = K^2(H_4^* + iH_1^*) = A_{Lh,0} + iK(A_{Lh,1}) + (iK)^2(A_{Lh,2}) + \sum_{j=3}^{N} \frac{A_{Lh,j} iK}{iK + \gamma_{j-2}}. \quad (4.46)$$

Grouping together the real and imaginary parts of both sides of Eq.(4.46) the following equivalences are obtained

$$\text{Real part:} \quad K^2 H_4^* = A_{Lh,0} + A_{Lh,2}(iK)^2 + \sum_{j=3}^{N} \frac{A_{Lh,j} K^2}{K^2 + \gamma_{j-2}^2}, \quad (4.47)$$

$$\text{Imaginary part:} \quad K^2 H_1^* = A_{Lh,1}(iK) + \sum_{j=3}^{N} \frac{A_{Lh,j} \gamma_{j-2}(iK)}{K^2 + \gamma_{j-2}^2}. \quad (4.48)$$

In Eq.(4.46) the terms $A_{Lh,0}, A_{Lh,1}, A_{Lh,2}, A_{Lh,j}$ and $\gamma_{j-2}$ are frequency independent coefficients. The first and second terms represent non-circulatory static-aerodynamics and the aerodynamic damping, respectively; the third term represents the added aerodynamic mass terms and can be usually thought as a negligible quantity. The rational terms represent the unsteady component of the flow and approximate the time delay. The additional number of aerodynamic poles determines largely the accuracy of approximation as well as the number of the extra states. The rational function approximation can be reformatted in the Laplace domain by substituting $s$ for $i\omega$, then the inverse Laplace transform will yield the lift force in the time domain according to the following equation

$$L_h(t) = \frac{1}{2}\rho U^2 \left( A_{Lh,0} h(t) + A_{Lh,1} \frac{B}{U} \dot{h}(t) + A_{Lh,2} \left( \frac{B}{U} \right)^2 \ddot{h}(t) + \sum_{j=3}^{N} \Gamma_{Lh,j-2}(t) \right). \quad (4.49)$$

where,

$$\Gamma_{Lh,j-2} = \int_{-\infty}^{t} A_{Lh,j-2} \cdot e^{\left[-\frac{\gamma_{j-2}U}{B}(t-\tau)\right]} \cdot \dot{h}(\tau) d\tau. \tag{4.50}$$

Alternatively, $\Gamma_{Lh,j-2}$ can be defined as the solution to the following differential equation [43]

$$\dot{\Gamma}_{Lh,j-2}(t) = -\frac{\gamma_{j-2}U}{B}\Gamma_{Lh,j-2}(t) + A_{Lh,j}\dot{h}(t). \tag{4.51}$$

The memory term representation of equation Eq.(4.50) depends on the entire time history of $\dot{h}(t)$ and, similarly to the Wagner function for the thin aerofoil, depends on the shed vortices convected downstream. Because of the difficulty in computing the integral of Eq.(4.50) simplifying formulae for approximate integration have been proposed [26].

## 4.3 Aeroelastic Stability on a Sectional Bridge Model

In this section the aeroelastic modelling framework of a simple 2-DOF sectional model is presented. Special attention is given to deriving a high fidelity rational approximation of the Theodorsen function and expressing the system's stability as a generalized eigenvalue problem. The introduction of control tools, such as the root-locus diagram, prove very effective in the system's aeroelastic stability examination.

### 4.3.1 Sectional Bridge Model with Thin Aerofoil Theory

In this section the focus is placed on describing the aeroelastic modelling of a simple sectional representation of the bridge using thin aerofoil-theory. This model typically represents the lowest-frequency heave (bending) and pitch (torsional) modes of the structure. The heave and pitch dynamic equations are given by equations (4.52) and (4.53) respectively

$$m\ddot{h} + 2m\omega_h\zeta_h\dot{h} + K_h h = L, \tag{4.52}$$

$$I_a\ddot{\alpha} + 2I_a\omega_\alpha\zeta_\alpha\dot{\alpha} + K_\alpha\alpha = M. \tag{4.53}$$

$L$ and $M$ represent the aerodynamic lift and moment forces, which for a symmetric aerofoil can be described by equations (4.7) and (4.8) respectively. $\omega_h, \omega_a$ are the natural frequencies of the heave and pitch modes and $\zeta_h, \zeta_a$ are the corresponding critical damping ratios. The equivalent spring stiffness is computed by considering the equivalences $K_h = m\omega_h^2$ and $K_\alpha = I_a\omega_\alpha^2$. Algebraic manipulation of the preceding formulae leads to the expression of the aeroelastic problem in the following state space form

$$\begin{bmatrix} 0 & \mathbf{M}-\mathbf{M}_{nc} \\ \boldsymbol{I} & 0 \end{bmatrix} \begin{bmatrix} \dot{\mathbf{q}} \\ \dot{\mathbf{q}}_v \end{bmatrix} = \begin{bmatrix} -\mathbf{K} & -\mathbf{C}+\mathbf{C}_{nc} \\ 0 & \boldsymbol{I} \end{bmatrix} \begin{bmatrix} \mathbf{q} \\ \mathbf{q}_v \end{bmatrix} + \Xi_C, \tag{4.54}$$

where $\Xi_C$ represents the circulatory terms and

$$\mathbf{M} = \begin{bmatrix} m & 0 \\ 0 & I_a \end{bmatrix}, \quad \mathbf{C} = \begin{bmatrix} 2m\omega_h\zeta_h & 0 \\ 0 & 2I_a\omega_a\zeta_a \end{bmatrix}, \quad \mathbf{K} = \begin{bmatrix} m\omega_h^2 & 0 \\ 0 & I_a\omega_a^2 \end{bmatrix}, \tag{4.55}$$

$$\mathbf{M}_{nc} = \begin{bmatrix} -\pi\rho b^2 & 0 \\ 0 & -\frac{\pi\rho b^4}{8} \end{bmatrix}, \qquad \mathbf{C}_{nc} = \begin{bmatrix} 0 & -\pi\rho b^2 U \\ 0 & -\frac{\pi\rho b^3 U}{2} \end{bmatrix}. \tag{4.56}$$

By denoting $\mathbf{q} = \{h, \alpha\}^T$ the position vector and $\mathbf{q}_v = \{\dot{h}, \dot{\alpha}\}^T$ the velocity vector as well as introducing the state vector notation $\mathbf{x} = \{\mathbf{q}, \mathbf{q}_v\}^T$, Eq.(4.54) can be expressed in the following compact form

$$\mathbf{E}_c\dot{\mathbf{x}} = \mathbf{A}_c\mathbf{x} + \Xi_C. \tag{4.57}$$

where,

$$\mathbf{E}_c = \begin{bmatrix} 0 & \mathbf{M}-\mathbf{M}_{nc} \\ \boldsymbol{I} & 0 \end{bmatrix} \qquad \mathbf{A}_c = \begin{bmatrix} -\mathbf{K} & -\mathbf{C}+\mathbf{C}_{nc} \\ 0 & \boldsymbol{I} \end{bmatrix}. \tag{4.58}$$

Matrices $\mathbf{M}_{nc}, \mathbf{C}_{nc}$ contain the non-circulatory terms, added mass and added damping, of the aerodynamic thin aerofoil expressions.

### 4.3.2 Rational Approximation of the Theodorsen Function

The circulatory term $\Xi_C$ depends on the irrational function $C(k)$ and therefore on the oscillatory frequency, $\omega$, and hence cannot be expressed directly in a state space form. As a consequence the traditional approach to aeroelastic stability analysis is based on finding iteratively wind speed(s) for which sinusoidal solutions to Eq.(4.57) (or alternatively Eq.(4.54)) exist. For reasons delineated in Chapter 2 this approach is laced with several disadvantages. However, a rational approximation of the Theodorsen function enables one to formulate the aeroelastic problem in a state-space form and use analytic devices such as the root-locus and Nyquist diagrams to assess the stability of the fluid-structure coupled system without iterative calculations.

By invoking linear least squares approximation methods, an accurate quartic rational approximation to $C(k)$ was found, whose numerator and denominator coefficients are given in Table 4.1. More on high-fidelity approximations in unsteady flow problems can be found in [151]. The poles and zeros of this approximation are given in Table 4.2 and show that this function is stable, minimum phase and with poles and zeros that interlace along the negative real axis. It is well known in passive circuit theory that such functions can be realized as the impedance function of resistor-capacitor networks [79]. The traditionally

| numerator terms | denominator terms |
|---|---|
| 0.99592 | 1 |
| $57.01896\,\hat{s}$ | $62.30441\,\hat{s}$ |
| $623.78848\,\hat{s}^2$ | $807.78489\,\hat{s}^2$ |
| $1895.46328\,\hat{s}^3$ | $3060.67868\,\hat{s}^3$ |
| $1523.24700\,\hat{s}^4$ | $3033.76379\,\hat{s}^4$ |

Table 4.1 Numerator and denominator coefficients of a quartic approximation to the Theodorsen function.

used rational approximation to the steady-sate Theodorsen function is attributed to Jones [91], in which $\hat{s} = \frac{sb}{U}$ is the reduced Laplace transform variable, Eq.(4.59). The Nyquist diagrams of the Theodorsen, Jones and quartic approximation are shown in the left-hand part of Fig. 4.5. It is self evident that the quartic approximation is very accurate with the

| poles | zeros |
|---|---|
| −0.64340 | −0.77893 |
| −0.24852 | −0.33125 |
| −0.09530 | −0.11143 |
| −0.02162 | −0.02274 |

Table 4.2 Poles and zeros of the quartic approximation to the Theodorsen function.

lower order Jones function somewhat less so. If one considers the quartic approximation to be a system, then its step response, shown on the right-hand of Figure 4.5 [23], is the well known Wagner step response curve.

$$J(\hat{s}) = \frac{1}{2\pi}\left\{2\pi - \frac{0.330\pi\hat{s}}{0.0455+\hat{s}} - \frac{0.670\pi\hat{s}}{0.3+\hat{s}}\right\}, \tag{4.59}$$

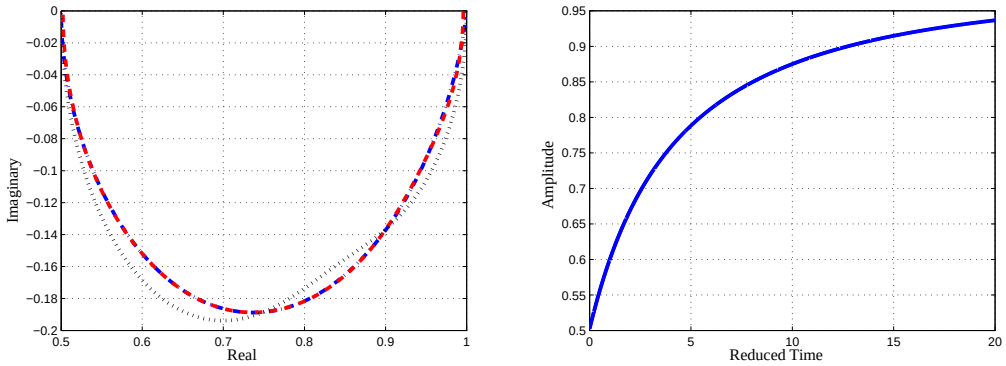


Figure 4.5 The Theodorsen function and its rational approximations. In the left-hand diagram the Theodorsen function [186] is the (blue) dot-dash curve, the quartic approximation the (red) dashed curve, and the Jones [91] function the (black) dotted curve. The right-hand diagram is the step response of the quartic approximation - this is the Wagner step response curve [23].

The circulatory component of the flow for this sectional bridge model is modelled by a feedback loop, see Fig.4.6, in which the approximation of the circulation function $C(s)$ is regarded as a transfer function receiving input the velocity at the three-quarter-chord point $y = U_{(3/4)C} = \left[U\alpha + \dot{\alpha} + \frac{b\dot{\alpha}}{2}\right]$ and generating output $\tilde{y}$, which is finally translated into lift and moment by the column vector **B**. The procedure enables introducing aerodynamic loading on the sectional model and simultaneously performing a rational function approxi-

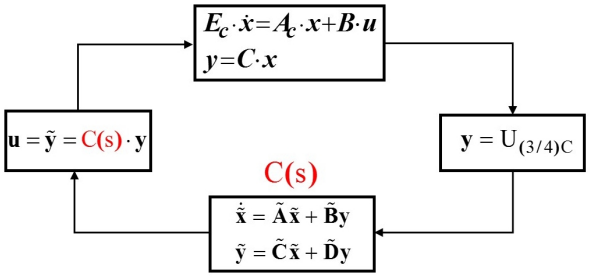


Figure 4.6 Block diagram of the open loop aeroelastic sectional bridge model. The circulatory component of aerodynamic loading is modelled by a feedback loop with the Theodorsen function, $C(s)$ as a transfer function; "$s$" represents the Laplace variable.

mation of the Theodorsen function. An equivalent state space realization $\tilde{\mathbf{A}}$,$\tilde{\mathbf{B}}$,$\tilde{\mathbf{C}}$,$\tilde{\mathbf{D}}$ of $C(s)$ is derived using standard techniques. The number of additional (aerodynamic) states is four, according to the order of the $C(s)$ approximation used.

The open loop system dynamics for the sectional model are reshaped in the following generalized eigenvalue form, Eq.(4.60), by augmenting the state space in Eq.(4.57) to include the aerodynamic states related to the circulatory function

$$\mathbf{E}\dot{\hat{\mathbf{x}}} = \mathbf{A}\hat{\mathbf{x}}. \tag{4.60}$$

where,

$$\mathbf{E} = \begin{bmatrix} \mathbf{E}_c & 0 \\ 0 & \boldsymbol{I} \end{bmatrix}, \quad \mathbf{A} = \begin{bmatrix} \mathbf{A}_c + \mathbf{B}\tilde{\mathbf{D}}\mathbf{C} & \mathbf{B}\tilde{\mathbf{C}} \\ \tilde{\mathbf{B}}\mathbf{C} & \tilde{\mathbf{A}} \end{bmatrix}, \quad \mathbf{B} = \begin{bmatrix} -2\pi\rho U b \\ \pi\rho U b^2 \\ 0 \\ 0 \end{bmatrix}, \quad \mathbf{C} = \begin{bmatrix} 0 & U & 1 & b/2 \end{bmatrix}. \tag{4.61}$$

Matrices $\mathbf{B}$ and $\mathbf{C}$ are explicitly derived from Eqns.(4.7), (4.8) and $\hat{\mathbf{x}}$ consists of the four structural (heave, pitch, and related velocities) plus the four added aerodynamic states $(C_1, C_2, C_3, C_4)$, $\hat{\mathbf{x}} = [h, \alpha, \dot{h}, \dot{\alpha}, C_1, C_2, C_3, C_4]^T$. The system of Eq.(4.60) depends solely on the wind speed $U$ and its stability for each wind speed can be assessed by computing the corresponding eigenvalues, as will be explained in subsection, Sec. 4.3.3. More specifically, the wind speed at which the real part of an eigenvalue becomes positive signifies the onset of unstable motion.

The real and imaginary parts of the eigenvalues of Eq.(4.60) are conveniently presented by a root-locus diagram in which the wind speed $U$ is the varied parameter. Such a diagram is presented in Fig. 4.7 for the sectional representation of the Humber Bridge, which considers the first heave and first pitch natural frequencies of the structure according to Figs. 3.9 and 3.8. As wind speed increases, the heave mode damping is increased and the corresponding complex pair of eigenvalues moves further into the stable left-half plane. Although the pitch mode is stabilized by moderate winds, it becomes unstable when the wind speed reaches $65m/s$. There is also a real structural mode that represents pitching of the bridge deck due to steady-state aerodynamic moment, this is the torsional divergence mode. When wind speed exceeds $72m/s$ the bridge deck assuming linear behaviour will monotonically diverge in a pitching motion due to loss of torsional rigidity. In mechanical terms its torsional stiffness will be cancelled out by the pitch-related aerodynamic moment.

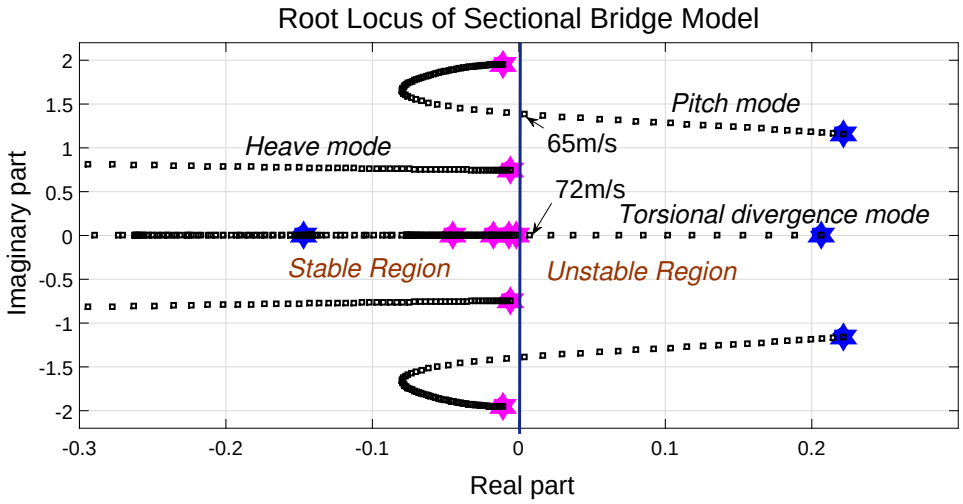


Figure 4.7 Root-loci of the Humber Bridge sectional model. The wind speed is swept from $0m/s$ to $85m/s$, with the low-speed ends of the root loci marked with 'red' hexagons and the high-speed ends with 'blue' hexagons. The pitch mode goes unstable at approximately $65m/s$ and the torsional divergence mode goes unstable at approximately $72m/s$.

### 4.3.3 Solution of the State Space Equation by a Modal Approach

Eq.(4.57), in general, can be used to describe the equations of motion for the general damping case, when the modal matrix cannot diagonalize the damping matrix, i.e. the non-proportional damping case. The analytic solution in this case inevitably follows the

state space approach. Considering matrix $\mathbf{E}$ in Eq.(4.57) as invertible, which is indeed the case for the system described in Sec.(4.3.1), Eq.(4.57) can be expressed in the standard state space form.

$$\dot{\hat{\mathbf{x}}} = \mathbf{A}_k \hat{\mathbf{x}} \quad \text{where,} \quad \mathbf{A}_k = \mathbf{E}^{-1}\mathbf{A} \tag{4.62}$$

Because Eq.(4.62) represents a homogeneous set of ordinary differential equations with constant coefficients, a solution of exponential form can be postulated.

$$\mathbf{x}(t) = e^{\lambda t}\mathbf{x} \tag{4.63}$$

$\lambda$ and $\mathbf{x}$ are in this case a constant scalar and vector respectively for every wind speed $U$. Introducing Eq.(4.63) in Eq.(4.62) the following well-known algebraic eigenvalue problem is obtained

$$\mathbf{A}_k \mathbf{x} = \lambda \mathbf{x}. \tag{4.64}$$

For this case, because of the introduction of aerodynamic damping, matrix $\mathbf{A}_k$ is non-symmetric. The eigenvalues and eigenvectors can be real or complex quantities and the eigenvectors are not orthogonal, as for the standard undamped case [134]. Because $\mathbf{A}_k$ is real, if $\lambda_\nu$ is a complex eigenvalue the complex conjugate $\lambda_\nu^*$ is also an eigenvalue. Furthermore, the eigenvector $\mathbf{x}_\nu$ associated with $\lambda_\nu$ is also complex and the eigenvector $\mathbf{x}_\nu^*$ associated with $\lambda_\nu^*$ is the complex conjugate of $\mathbf{x}_\nu$. Moreover, the adjoint eigenvalue problem is defined as

$$\mathbf{A}_k^T \mathbf{y} = \lambda \mathbf{y}. \tag{4.65}$$

Because $\det\mathbf{A}_k = \det\mathbf{A}_k^T$, the eigenvalues of $\mathbf{A}_k^T$ are identical to the eigenvalues of $\mathbf{A}_k$. However the eigenvectors of $\mathbf{A}_k$ and $\mathbf{A}_k^T$ are not the same. The transpose of Eq.(4.65) is

$$\mathbf{y}^T \mathbf{A}_k = \lambda \mathbf{y}^T. \tag{4.66}$$

The right eigenvectors $\mathbf{x}$ are not mutually orthogonal nor are the left eigenvectors $\mathbf{y}$. However, the two sets of eigenvectors satisfy a ceratin type of bi-orthogonality which is useful.

Some algebraic manipulations of Eq.(4.64) and Eq.(4.66) leads to the following identities [135].

$$\mathbf{Y}^T\mathbf{X} = \boldsymbol{I}, \quad \mathbf{Y}^T\mathbf{A}_k\mathbf{X} = \Lambda, \quad \mathbf{A}_k = \mathbf{X}\Lambda\mathbf{Y}^T \tag{4.67}$$

where, $\Lambda = \text{diag}[\lambda_1 \ \ \lambda_2 \ \ ...\lambda_n]$ is the eigenvalue matrix. $\mathbf{X} = [\mathbf{x}_1 \ \ \mathbf{x}_2 \ ...\mathbf{x}_n]$ is the matrix of right eigenvectors and $\mathbf{Y} = [\mathbf{y}_1 \ \ \mathbf{y}_2 \ ...\mathbf{y}_n]$ the matrix of left eigenvectors. Eq.(4.67) indicates that matrices $\mathbf{A}_k$ and $\Lambda$ are related through a similarity transformation. In the general case, in which the eigenvalues are not distinct, the matrix $\mathbf{A}_k$ is similar to a triangular matrix, where the triangular matrix is known as the Jordan form, [14].

A solution to the state equations (4.62) can be expressed as a linear combination of right eigenvectors multiplied by modal coordinates as follows

$$\mathbf{x}(t) = \xi_1(t)\mathbf{x}_1 + \xi_2(t)\mathbf{x}_2 + .... + \xi_n(t)\mathbf{x}_n = \sum_{\nu=1}^{\nu=n} \xi_\nu(t)\mathbf{x}_\nu = \mathbf{X}\boldsymbol{\xi}(t). \tag{4.68}$$

Inserting Eq.(4.68) in Eq.(4.62) and premultiplying by $\mathbf{Y}^T$ the following is attained

$$\mathbf{Y}^T\mathbf{X}\dot{\boldsymbol{\xi}}(t) = \mathbf{Y}^T\mathbf{A}_k\mathbf{X}\boldsymbol{\xi}(t). \tag{4.69}$$

using the bi-orthogonality relationships from Eq.(4.67) we obtain the following

$$\dot{\boldsymbol{\xi}}(t) = \Lambda\boldsymbol{\xi}(t). \tag{4.70}$$

Eq.(4.70) can alternatively be written as a set of independent modal equations of the form

$$\dot{\xi}_\nu(t) = \lambda_\nu\xi_\nu(t), \quad \nu = 1,2,...,n. \tag{4.71}$$

Furthermore, taking the Laplace transform on both sides of Eq.(4.71) yields the following

$$s\Xi_\nu(s) - \xi_\nu(0) = \lambda_\nu\Xi_\nu(s). \tag{4.72}$$

where $\Xi_\nu(s) = \mathscr{L}\xi_\nu(t)$ is the Laplace transform of $\xi_\nu(t)$, and $\xi_\nu(0)$ is the initial modal coordinate. The latter can be obtained by setting $t = 0$ in Eq.(4.68) and premultiplying by $\mathbf{y}_\nu^T(t)$ as well as using the identities of Eq.(4.67).

$$\xi_\nu(0) = \mathbf{y}_\nu^T \mathbf{x}(0), \quad \nu = 1,2,...,n \tag{4.73}$$

Where $\mathbf{x}(0)$ is the initial state vector. From Eq.(4.72) it is obtained

$$\Xi_\nu(s) = \frac{1}{s-\lambda_\nu}\xi_\nu(0) \rightarrow \xi_\nu(t) = \mathscr{L}^{-1}\Xi_\nu(s) = e^{\lambda_\nu t}\xi_\nu(0), \tag{4.74}$$

which can also be written in the following matrix form

$$\boldsymbol{\xi}(t) = e^{\Lambda t}\boldsymbol{\xi}(0) \rightarrow \mathbf{x}(t) = \mathbf{X}e^{\Lambda t}\boldsymbol{\xi}(0). \tag{4.75}$$

Moreover, because $\boldsymbol{\xi}(0) = \mathbf{Y}^T\mathbf{x}(0)$ Eq.(4.75) becomes

$$\mathbf{x}(t) = \mathbf{X}e^{\Lambda t}\mathbf{Y}^T\mathbf{x}(0). \tag{4.76}$$

Because $\Lambda$ is diagonal then $e^{\Lambda t} = \text{diag}[e^{\lambda_i t}]$. Consequently the convergence of the solution to the original state space equations (4.62) dependents on the convergence of every $e^{\lambda_i t}(i = 1,2,..,n)$ term. If an eigenvalue has a positive real part this would translate to divergent motion. The root locus diagram as presented in Fig. 4.7 is a useful tool for assessing stability. The eigenvalues of the system are a function of the wind speed and consequently the wind speed at which an eigenvalue becomes positive determines the aeroelastic instability boundary.

## 4.4 Aeroelastic Stability on the Finite Element Model

The analysis presented in this section extends the preceding sectional aeroelastic formulation to the FE bridge model, developed in Chapter 3. Sec. 4.4.1 presents the FE aeroelastic

framework based on Theodorsen's aerodynamic theory. Sec. 4.4.2 extends the latter approach for the more general flutter derivative case. These mathematical descriptions are cross-validated using models for the Humber and Great Belt Bridges. The computed numerical aeroelastic predictions from the model are compared against experimental and analytical results from the literature.

### 4.4.1 Finite Element Model with Thin Aerofoil Theory

In order to include the aeroelastic forcing in a general FE procedure, distributed lift and moments are considered for every element. The procedure followed here assumes lumping of the distributed forces at the nodes of the element, Fig. 4.8. The aerodynamic mass and damping matrices, in comparison to Eq.(4.56) are of dimensions $12 \times 12$, and have the following form.

$$\mathbf{M}_{nc,e} = \frac{\ell}{2}\begin{pmatrix} \overbrace{\begin{bmatrix} \underbrace{-\pi\rho b^2}_{\text{vertical}} & & 0 \\ & \ddots & \\ 0 & & \underbrace{-\frac{\pi}{8}\rho b^4}_{\text{torsional}} \end{bmatrix}}^{StartNode} & \\ & \underbrace{\begin{bmatrix} \underbrace{-\pi\rho b^2}_{\text{vertical}} & & 0 \\ & \ddots & \\ 0 & & \underbrace{-\frac{\pi}{8}\rho b^4}_{\text{torsional}} \end{bmatrix}}_{EndNode} \end{pmatrix}, \mathbf{C}_{nc,e} = \frac{\ell}{2}\begin{pmatrix} \overbrace{\begin{bmatrix} 0 & \dots & \underbrace{-\pi\rho b^3 U}_{\text{vertical}} \\ & \ddots & \\ 0 & & \underbrace{-\frac{\pi}{2}\rho b^3 U}_{\text{torsional}} \end{bmatrix}}^{StartNode} & \\ & \underbrace{\begin{bmatrix} 0 & \dots & \underbrace{-\pi\rho b^3 U}_{\text{vertical}} \\ & \ddots & \\ 0 & & \underbrace{-\frac{\pi}{2}\rho b^3 U}_{\text{torsional}} \end{bmatrix}}_{EndNode} \end{pmatrix}$$

The non-zero entries correspond to the heave and pitch related degrees of freedom, 1, 6, 7 and 12 according to Fig. 3.4. Matrices $\mathbf{M}_{nc,e}$ and $\mathbf{C}_{nc,e}$ can be added at the corresponding degrees of freedom similarly to the structural matrices. This results in the global aerodynamic mass and damping matrices $\mathbf{M}_a$ and $\mathbf{C}_a$

$$\mathbf{M}_a = \sum_{e=1}^{N} \mathbf{M}_{nc,e}, \qquad \mathbf{C}_a = \sum_{e=1}^{N} \mathbf{C}_{nc,e}. \tag{4.77}$$

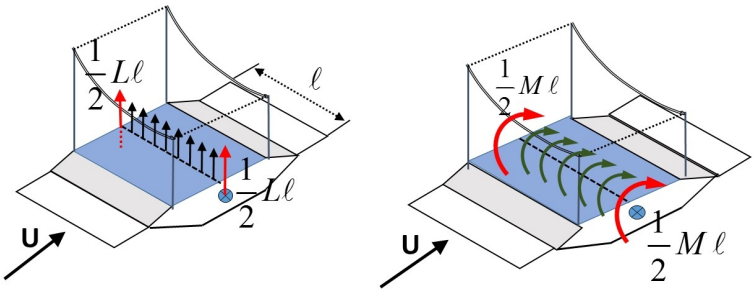


Figure 4.8 Lumped aerodynamic lift and moment forces. L is the aerodynamic lift and M is the aerodynamic moment. $\ell$ is the element length.

Consequently the equations of motion in a FE format, in correspondence to the sectional case Eq.(4.54), take the following form

$$\overbrace{\begin{bmatrix} 0 & \mathbf{M}-\mathbf{M}_a \\ \boldsymbol{I} & 0 \end{bmatrix}}^{\mathbf{E}_{cg}} \begin{bmatrix} \dot{\mathbf{Q}} \\ \dot{\mathbf{Q}}_v \end{bmatrix} = \overbrace{\begin{bmatrix} -\mathbf{K} & -\mathbf{C}+\mathbf{C}_a \\ 0 & \boldsymbol{I} \end{bmatrix}}^{\mathbf{A}_{cg}} \begin{bmatrix} \mathbf{Q} \\ \mathbf{Q}_v \end{bmatrix} + \Xi_C, \tag{4.78}$$

where $\mathbf{Q}$ is a vector containing the degrees of freedom of the bridge structure and $\mathbf{Q}_v$ the related velocities. The corresponding state vector is defined as $\mathbf{x}_g = \{\mathbf{Q}, \mathbf{Q}_v\}^T$. In order to model the non-circulatory part of aerodynamic forces, as an extension to the sectional case presented in Fig. 4.6, a feedback system is devised with as many feedback loops as elements of the FE model bridge model, Fig. 4.9.

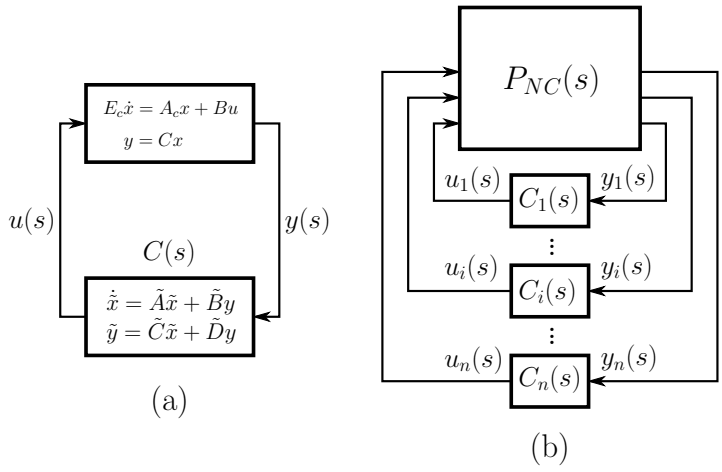


Figure 4.9 (a) Block diagram of the sectional open-loop aerodynamic system. (b) Block diagram of the open-loop FE model. $P_{NC}(s)$ is the aeroelastic model without the circulatory terms, and $C_i(s)$ are Theodorsen function approximations for each deck element.

Similarly to the sectional case the dynamic equations of motion for the finite element system can be expressed in the form

$$\mathbf{E}_g \dot{\hat{\mathbf{x}}}_g = \mathbf{A}_g \hat{\mathbf{x}}_g, \tag{4.79}$$

where,

$$\mathbf{E}_g = \begin{bmatrix} \mathbf{E}_{cg} & 0 \\ 0 & \boldsymbol{I} \end{bmatrix}, \qquad \mathbf{A}_g = \begin{bmatrix} \mathbf{A}_{cg} + \mathbf{B}_g \widetilde{\mathbf{D}}_g \mathbf{C}_g & \mathbf{B}_g \widetilde{\mathbf{C}}_g \\ \widetilde{\mathbf{B}}_g \mathbf{C}_g & \widetilde{\mathbf{A}}_g \end{bmatrix}. \tag{4.80}$$

in which $\tilde{\mathbf{A}}_g = \text{diag}(\tilde{\mathbf{A}})$, $\tilde{\mathbf{B}}_g = \text{diag}(\tilde{\mathbf{B}})$, $\tilde{\mathbf{C}}_g = \text{diag}(\tilde{\mathbf{C}})$, $\tilde{\mathbf{D}}_g = \text{diag}(\tilde{\mathbf{D}})$. $\hat{\mathbf{x}}_g$ consists of the structural states, their velocities as well as the aerodynamic states related to the approximation of circulatory functions (namely there are four aerodynamic related states for every element, because of the fourth order approximation of the Theodorsen circulation function).

$$\mathbf{C}_e = \begin{bmatrix} \overbrace{\underbrace{0 \quad \cdots \quad \frac{U}{2}}_{start\ node} \; \underbrace{0 \quad \cdots \quad \frac{U}{2}}_{end\ node}}^{\mathrm{X}} & \overbrace{\underbrace{\frac{1}{2} \quad \cdots \quad \frac{b}{4}}_{start\ node} \; \underbrace{\frac{1}{2} \quad \cdots \quad \frac{b}{4}}_{end\ node}}^{\dot{\mathrm{X}}} \end{bmatrix}, \quad \mathbf{B}_e = \frac{\ell}{2} \begin{bmatrix} -2\pi\rho U b \\ \vdots \\ \pi\rho U b^2 \\ \hdashline -2\pi\rho U b \\ \vdots \\ \pi\rho U b^2 \end{bmatrix} \begin{matrix} \left.\vphantom{\begin{matrix} a \\ b \\ c \end{matrix}}\right\} \text{start node} \\ \left.\vphantom{\begin{matrix} a \\ b \\ c \end{matrix}}\right\} \text{end node} \end{matrix} \tag{4.81}$$

Matrices $\mathbf{C}_g$ and $\mathbf{B}_g$ are derived explicitly from the aerodynamic loading of the Theodorsen equations. The $C_i(s)$ transfer functions, same for every element, receive structural response $y_i(s)$ as input and generate outputs $\tilde{y}_i(s) = u_i(s)$. Matrix $\mathbf{C}_g$ reconstructs these structural responses in the FE framework. The $u_i(s)$ components are translated into lift and moment node loading by means of the $\mathbf{B}_g$ matrix. Eq.(4.81) presents the elemental form of $\mathbf{C}_g$ and $\mathbf{B}_g$, $\mathbf{C}_e$ and $\mathbf{B}_e$ respectively. $\mathbf{C}_e$ has both displacement and velocity terms. For the $\mathbf{B}_e$ case, the velocity related part is zero.

### 4.4.2 Finite Element Model considering the Flutter Derivatives Approach

The flutter derivatives based FE aerodynamic formulation neglects the drag associated terms, in order to be comparable to thin aerofoil theory. Hence equations (4.22) and (4.23) are used, which can be expressed in the following matrix form

$$\left\{ \begin{array}{c} L \\ M \end{array} \right\} = \frac{1}{2}\rho U^2 B \left[ \begin{array}{cc} \frac{KH_1^*}{U} & KH_2^*\frac{B}{U} \\ \frac{BKA_1^*}{U} & BKA_2^*\frac{B}{U} \end{array} \right] \left\{ \begin{array}{c} \dot{h} \\ \dot{\alpha} \end{array} \right\} + \frac{1}{2}\rho U^2 B \left[ \begin{array}{cc} \frac{K^2H_4^*}{B} & K^2H_3^* \\ K^2A_4^* & K^2A_3^*B \end{array} \right] \left\{ \begin{array}{c} h \\ \alpha \end{array} \right\} \tag{4.82}$$

Assuming purely oscillatory motion, the following substitution can be made in Eq.(4.82): ($\dot{h} = i\omega h$ , $\dot{\alpha} = i\omega\alpha$), in the spirit of Eq.(4.19). The reduced frequency terms are denoted by: $K = 2k = \frac{2\omega b}{U}$. Given these substitutions the following expressions are attained

$$\begin{aligned} \left\{ \begin{array}{c} L \\ M \end{array} \right\} &= \frac{1}{2}\rho U^2 \left[ \begin{array}{cc} K^2H_4^* + iK^2H_1^* & B[K^2H_3^* + iK^2H_2^*] \\ B[K^2A_4^* + iK^2A_1^*] & B^2[K^2A_3^* + iK^2A_2^*] \end{array} \right] \left\{ \begin{array}{c} h \\ \alpha \end{array} \right\} \\ &= U^2 \cdot \mathbf{Q}(iK) \cdot \left\{ \begin{array}{c} h \\ \alpha \end{array} \right\}. \end{aligned} \tag{4.83}$$

The following step consists of employing Roger's approximation [159], for approximating the $\mathbf{Q}(iK)$ matrix. Roger's expression is of the form

$$\hat{\mathbf{Q}}(iK) = \mathbf{P}_0 + \mathbf{P}_1 \cdot iK + \mathbf{P}_2 \cdot (iK)^2 + \sum_{j=3}^{N} \frac{\mathbf{P}_j \cdot iK}{iK + \gamma_{j-2}}. \tag{4.84}$$

Matrices $\mathbf{P}_0, \mathbf{P}_1, \mathbf{P}_2, \mathbf{P}_j$ as well as the coefficients $\gamma_{j-2}$ are frequency independent, and for the sectional model case have dimensions $2 \times 2$. These can be computed by fitting against wind tunnel experimental data, for the associated deck section, for a finite number of frequencies for which tabular data are available. Note that $\mathbf{P}_0, \mathbf{P}_1, \mathbf{P}_2$ are related to the non-circulatory stiffness, damping and inertia (added-mass) respectively. On the other hand, $\mathbf{P}_j$ and $\gamma_{j-2}$ are related to the circulatory component of aerodynamic forces. $N-2$ is the number of

poles used in order to fit the circulatory component. In this work four poles are used for consistency with the order of approximation of the Theodorsen function. The poles $\gamma_{j-2}$ are usually preselected in the range of reduced frequencies of interest. The fitting process in our case follows a least squares process. More details on this procedure can be found in [174]. However, the pole parameters can alternatively be selected through an optimization process for minimizing the total least-squared error summed over a range of frequencies. In our case, the inclusion of the poles in the optimization process resulted in marginal improvement in fitting the data with disproportionate requirements in computational efforts. Hence the following analysis considered the poles to be fixed parameters, adjusted through trial and error.

The preceding rational function approximation of the aerodynamic transfer function can be extended in the Laplace domain by substituting $s$ for $i\omega$ [43]. The expression of forces as functions of $s$ means that aerodynamic forcing holds not only for sinusoidal motion, but for arbitrary motions as well ($s$ not on the $i\omega$ axis). This logical leap is founded on the notion of analytic continuation. The process effectively seeks to find analytic functions which agree with the aerodynamic forcing functions at all values of frequency [174]. However, there are only a finite number of frequencies at which tabular data are available; hence the process is an approximation. The validity of this assumption lies in the fact that phenomena such as flutter occur for points in the complex $s-$plane which lie along the $i\omega$ axis. The equations of motion for the sectional model in the Laplace domain can be written as follows

$$\begin{aligned}(\mathbf{M}s^2+\mathbf{C}s+\mathbf{K})\mathbf{q}(s) &= U^2\hat{\mathbf{Q}}(s)\mathbf{q}(s) \\ &= U^2\left(\mathbf{P}_0+\mathbf{P}_1 s\frac{B}{U}+\mathbf{P}_2 s^2\left(\frac{B}{U}\right)^2+\sum_{j=3}^{N}\frac{\mathbf{P}_j\cdot s\frac{B}{U}}{s\frac{B}{U}+\gamma_{j-2}}\right)\mathbf{q}(s)\end{aligned} \tag{4.85}$$

. Eq.(4.85) can be cast in a standard state space form by employing the inverse Laplace transform. In this process the resulting augmented aerodynamic states are defined by $\mathbf{X}_{aj}(s)$ in the Laplace domain. Their final form is attained through the following manipulation

$$\mathbf{X}_{aj}(s)=\frac{s\frac{B}{U}}{s\frac{B}{U}+\gamma_{j-2}}\mathbf{q}(s)\xrightarrow{\mathscr{L}^{-1}}\dot{\mathbf{X}}_{aj}(t)=\dot{\mathbf{q}}(t)-\frac{U}{B}\gamma_{j-2}\mathbf{X}_{aj}(t). \tag{4.86}$$

The final state space formulation reads as follows

$$\begin{Bmatrix} \dot{\mathbf{q}} \\ \ddot{\mathbf{q}} \\ \dot{\mathbf{X}}_{a3} \\ \dot{\mathbf{X}}_{a4} \\ \dot{\mathbf{X}}_{a5} \\ \dot{\mathbf{X}}_{a6} \end{Bmatrix} = \begin{bmatrix} 0 & I & 0 & 0 & 0 & 0 \\ -\bar{\mathbf{M}}^{-1}\bar{\mathbf{K}} & -\bar{\mathbf{M}}^{-1}\bar{\mathbf{C}} & U^2\bar{\mathbf{M}}^{-1}\mathbf{P}_3 & U^2\bar{\mathbf{M}}^{-1}\mathbf{P}_4 & U^2\bar{\mathbf{M}}^{-1}\mathbf{P}_5 & U^2\bar{\mathbf{M}}^{-1}\mathbf{P}_6 \\ 0 & \boldsymbol{I} & -\left(\frac{U}{B}\right)\gamma_1\boldsymbol{I} & 0 & 0 & 0 \\ 0 & \boldsymbol{I} & 0 & -\left(\frac{U}{B}\right)\gamma_2\boldsymbol{I} & 0 & 0 \\ 0 & \boldsymbol{I} & 0 & 0 & -\left(\frac{U}{B}\right)\gamma_3\boldsymbol{I} & 0 \\ 0 & \boldsymbol{I} & 0 & 0 & 0 & -\left(\frac{U}{B}\right)\gamma_4\boldsymbol{I} \end{bmatrix} \begin{Bmatrix} \mathbf{q} \\ \dot{\mathbf{q}} \\ \mathbf{X}_{a3} \\ \mathbf{X}_{a4} \\ \mathbf{X}_{a5} \\ \mathbf{X}_{a6} \end{Bmatrix} \tag{4.87}$$

where the following definitions apply: $\bar{\mathbf{M}} = \mathbf{M} - U^2\mathbf{P}_2\left(\frac{B}{U}\right)^2$, $\bar{\mathbf{C}} = \mathbf{C} - U^2\mathbf{P}_1\left(\frac{B}{U}\right)$ and $\bar{\mathbf{K}} = \mathbf{K} - U^2\mathbf{P}_0$.

The extension of the flutter derivatives approach to a FE format follows a similar procedure to the thin aerofoil case. Equations (4.22) and (4.23) are lumped at the end nodes of each element, as shown in Fig. 4.8. In this case matrices $\mathbf{P}_{0,e}, \mathbf{P}_{1,e}, \mathbf{P}_{2,e}$ associated to the non-circulatory aerodynamic terms have dimensions $12 \times 12$. The corresponding global matrices can be added similarly to the structural matrices.

$$\mathbf{P}_{0G} = \sum_{e=1}^{N} P_{0,e} \qquad \mathbf{P}_{1G} = \sum_{e=1}^{N} P_{1,e} \qquad \mathbf{P}_{2G} = \sum_{e=1}^{N} P_{2,e} \tag{4.88}$$

The summation operation again follows the FE sense. Because the added aerodynamic states $\mathbf{X}_{aj}, j = 3..6$ are associated with only the heave and pitch degrees of freedom at each node, matrices $\mathbf{P}_{j,e}, j = 3..6$ have size $12 \times 4$, see Eq.(4.89).

The preceding formulation following Roger's approximation introduces 8 extra aerodynamic states per node, four heave-related and four pitch-related following the number of poles used. In the thin aerofoil FE framework four additional aerodynamic states per element were used, related to the four poles for the approximation of the Theodorsen function. Thus, in the latter case the aerodynamic state dimension is halved when compared

to the flutter derivatives approach.

$$\mathbf{P}_j = \begin{pmatrix} \mathbf{P}_j^{11} & \mathbf{P}_j^{12} \\ \mathbf{P}_j^{21} & \mathbf{P}_j^{22} \end{pmatrix} \xrightarrow{FE\ \ extension} \mathbf{P}_{j,e} = \frac{\ell}{2} \begin{pmatrix} \underbrace{\mathbf{P}_j^{11}}_{heave} & \mathbf{P}_j^{12} & 0 & 0 \\ \vdots & \vdots & \vdots & \vdots \\ \mathbf{P}_j^{21} & \underbrace{\mathbf{P}_j^{22}}_{pitch} & 0 & 0 \\ 0 & 0 & \underbrace{\mathbf{P}_j^{11}}_{heave} & \mathbf{P}_j^{12} \\ \vdots & \vdots & \vdots & \vdots \\ 0 & 0 & \mathbf{P}_j^{21} & \underbrace{\mathbf{P}_j^{22}}_{pitch} \end{pmatrix} \tag{4.89}$$

### 4.4.3 Aeroelastic Boundary Predictions for the Humber and Great Belt Bridges

#### Humber Bridge

Considering the framework developed in Section 4.4.1 the stability of the open-loop system of the Humber Bridge FE model is assessed. Fig. 4.10 shows the corresponding root-locus diagram, similarly to Fig. 4.7 for the associated sectional case, in which the wind speed $U$ is again the swept parameter. In this analysis the structural damping matrix is derived assuming a Rayleigh proportional damping model $C = a_M M + a_K K$. The parameters $a_M, a_K$ are chosen so as to result in a 1% critical damping ratio for the first vertical and torsional mode in the completed stage.

It can be observed that as wind speed increases, the damping of the heave modes increases and the corresponding complex pair of eigenvalues moves further into the stable left-half plane. The first torsional mode, although stabilized at moderate winds becomes unstable when wind speed reaches $65 m/s$. Similarly, the second torsional mode reaches the flutter boundary at $99 m/s$. There is also a real structural mode that represents pitching of the bridge deck due to steady-state aerodynamic moment, this is the torsional divergence

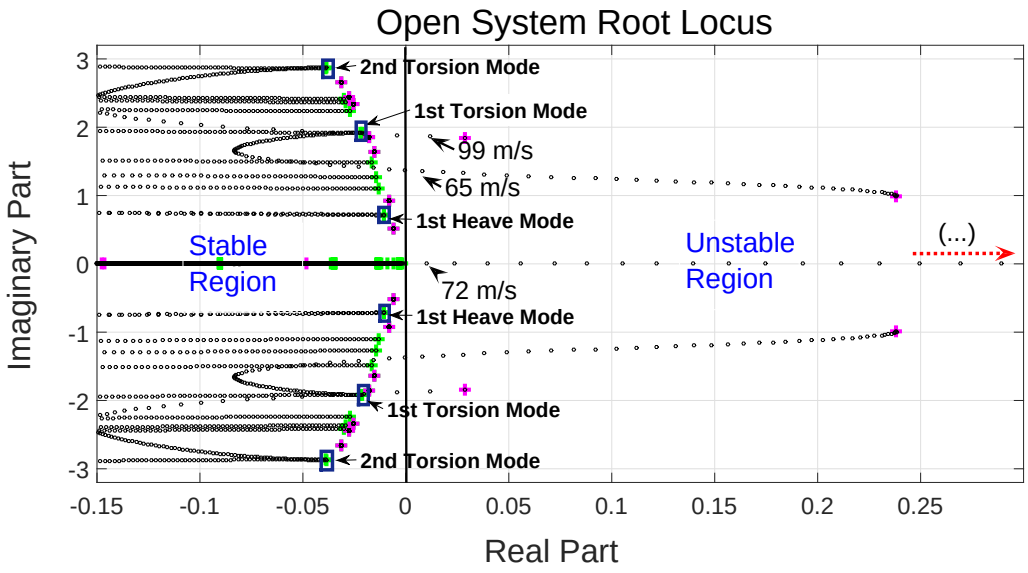


Figure 4.10 Root locus of the Humber Bridge. The wind speed is swept from 0 m/s to 100 m/s, with the low-speed end marked with a green plus and the high-speed end with a magenta plus. The first flutter mode, starting at 0 m/s as the 1st torsion mode, becomes unstable at 65 m/s. Torsional divergence instability occurs at 72 m/s.

mode. When wind speed exceeds $72m/s$ the bridge deck assuming linear behaviour will monotonically diverge in a pitching motion. In mechanical terms the bridge's torsional stiffness is 'cancelled out' by the pitch-related aerodynamic moment. The critical flutter speed estimation using thin aerofoil theory is in agreement with the experimental investigation given by Diana et al. [53], in which the flutter speed is estimated at $57m/s$ with an accumulated error of $12\%$.

Fig. 4.11 presents the evolution of the natural frequencies and damping ratios for the first two torsional modes and the first four vertical modes. It can be observed that at in the vicinity of the first flutter speed at $65m/s$ the natural frequencies of the first vertical symmetric, the first torsional symmetric and the second vertical symmetric converge in value. It is however the damping ratio of the first torsion mode that becomes negative at the critical flutter wind speed, whereas the damping of the vertical modes increases with increased wind speed. Similarly for the second flutter mode it is seen that the natural frequencies of the second torsion mode, the first vertical antisymmetric mode and the first symmetric vertical mode converge in value near the second critical flutter speed.

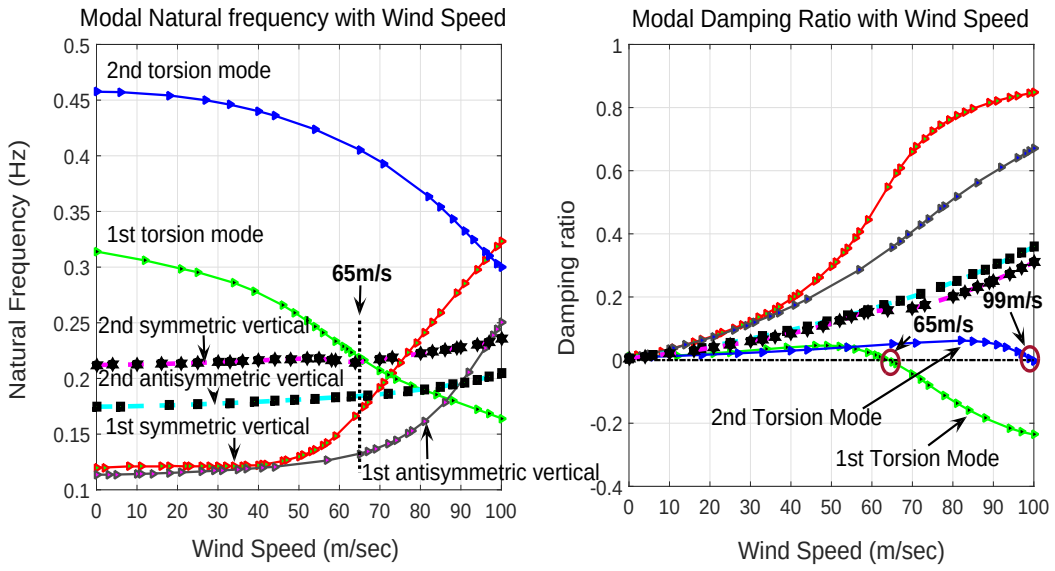


Figure 4.11 Evolution of the natural frequencies and damping ratios for the first two torsional modes and the first four vertical modes with the wind speed swept from 0 m/s to 100 m/s.

### Humber Bridge during Erection

A similar procedure is followed during erection the of the Humber Bridge. Fig. 4.12 shows the modes shape of the first vertical symmetric mode during the erection process with reference to the completed Humber Bridge. As a result of modelling assumptions, the vertical displacement of the deck is assumed equal to the vertical displacement of the cables. For visualisation purposes, the cable displacement at locations where the deck is yet to be erected is shown as a deck displacement in Fig. 4.12. This symmetric erection process mimics the actually deck construction as reported in [27] and [142]. The flutter and torsional divergence stability limits are shown in Fig. 4.13 for the adopted erection process. The Rayleigh damping parameters $a_M, a_K$ are chosen so as to result in a 0.5% critical damping ratio for the first vertical and torsional mode, recalculated at every stage of the erection process. The flutter limits reported in Brancaleoni [27] are superimposed on the figure for comparison.

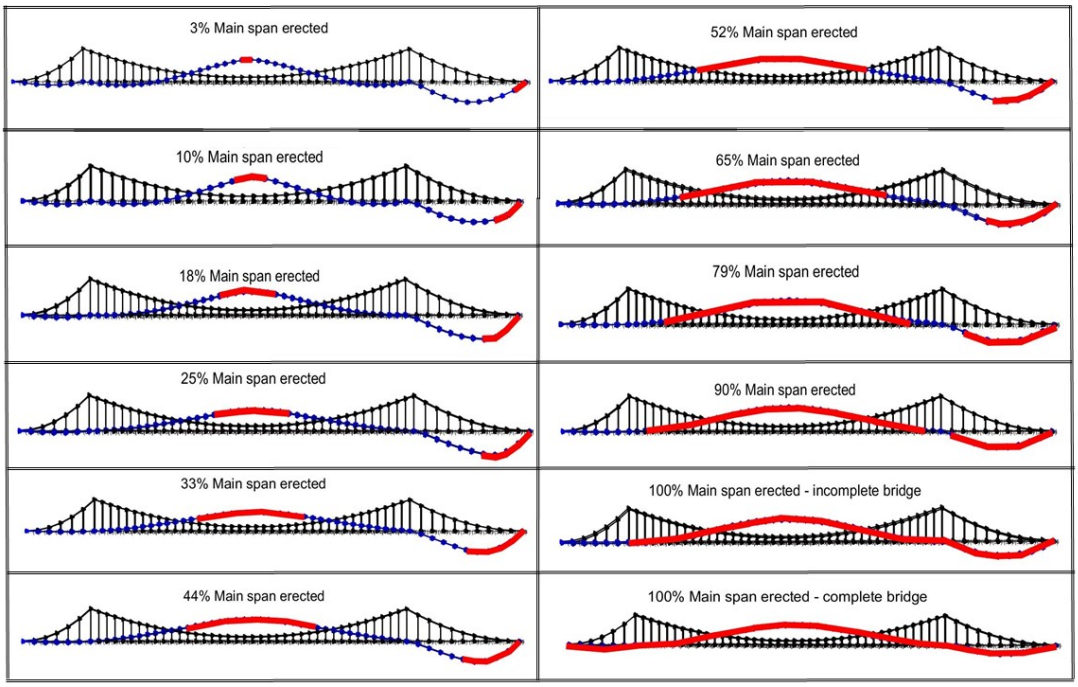


Figure 4.12 Humber Bridge, mode shape evolution of first symmetric vertical mode for different erection stages. Erected deck segments denoted by red solid line.

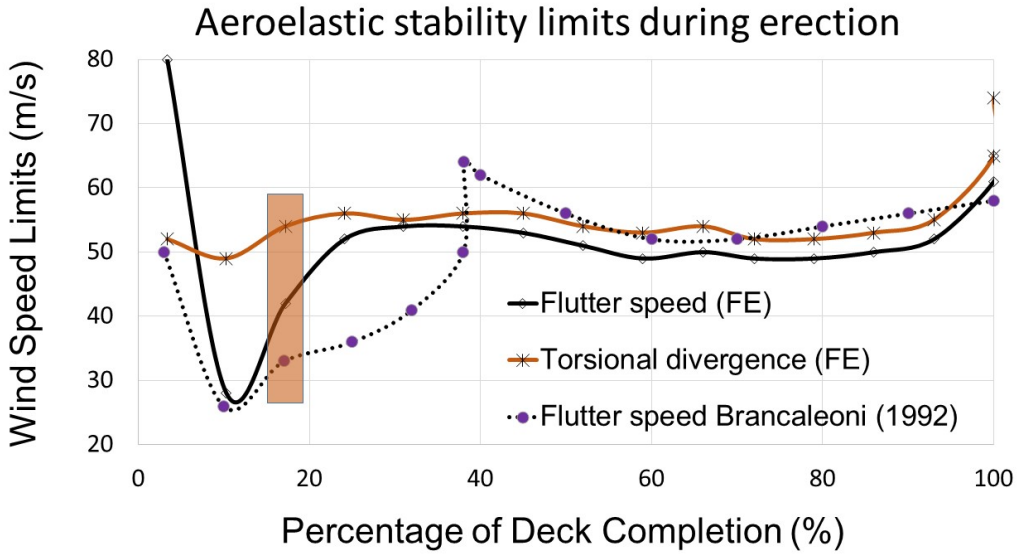


Figure 4.13 Aeroelastic stability limits as a function of deck percentage completion.

During the erection process the evolution of the bridge's stability characteristics is related to the interplay between the critical modal frequencies and their mode shapes. It has become evident that there is a strong correlation between the torsion/heave frequency ratio,

as shown in Figures 3.16 and 3.17, and the first flutter mode stability limits presented in Fig. 4.13. The abrupt change in the flutter curve of Fig. 4.13 is associated with the change in the first torsional mode illustrated in Fig. 3.18; this change is apparently a result of increased deck inertia. The distinct peak reported in Brancaleoni [27] is not reproduced by the present aeroelastic model, which recognises the full-bridge multimodal interactions, and consequently, results in a more realistic and accurate prediction of the stability limits. The results do, however, show that the Humber Bridge exhibits low critical flutter speed at 10-20% completion. When the partially erect deck is short, the oscillating mass is large because of the mass of the cables and a large structural inertia results. Also, a short deck section results is relatively small aerodynamic forces, which explains why the flutter speed is high in the early stages of construction. At reduced torsional stiffness the vertical and torsional vibration frequencies are close together. As the aerodynamic forces increase with increased deck length the flutter speed drops drastically. It has been suggested that a favourable erection sequence can improve the bridge's aeroelastic performance during erection, as has been examined in [71]

### 4.4.4 Great Belt Bridge

The aeroelastic modelling of the Great Belt Bridge was pursued both using thin aerofoil theory of Section 4.4.1 and the flutter derivatives approach of Section 4.4.2. Again the Rayleigh damping model is used with the $a_M, a_K$ parameters resulting in 1% critical damping ratio for the first vertical and torsional mode. The experimental data used for the flutter derivatives approach were obtained at the water channel of the University of Hamburg, first reported in Starossek et al. [181] and later in [120]. The graphs in Fig. 4.14 represent the four flutter derivatives $H^*$ and $A^*$ , according to equations (4.22) and (4.23). The corresponding thin aerofoil derivatives for the equivalent deck section based on equations (4.24) are also presented in the graphs. The horizontal axis is expressed in reduced velocity which is related to reduced frequency quantity according to the relationship $\frac{U}{fB} = \frac{2\pi}{K}$.

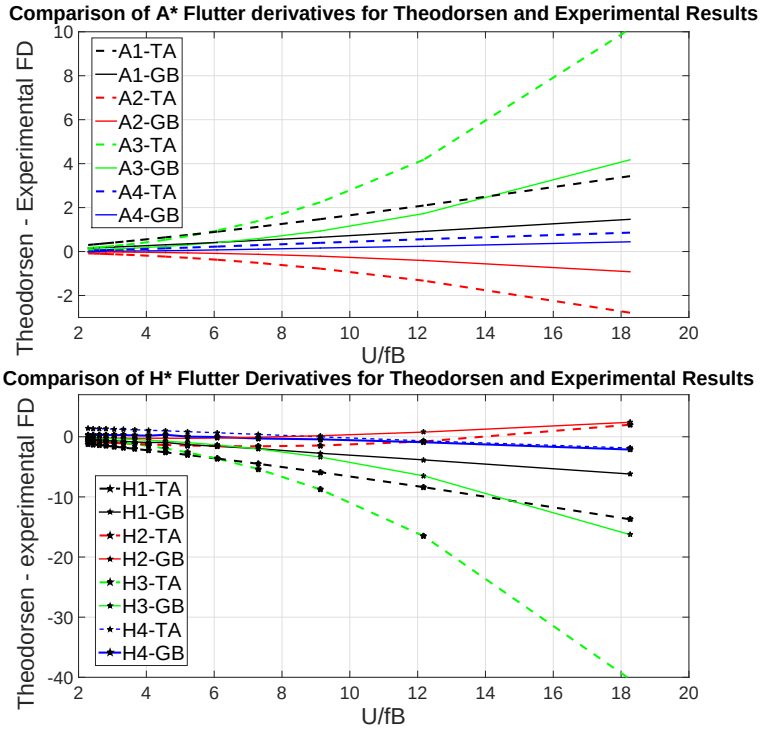


Figure 4.14 Comparison of $H^*$ and $A^*$ flutter derivatives based on thin aerofoil formulation with the experimentally obtained data from the Great Belt Bridge [120].

Fig. 4.15 demonstrates the effectiveness of the fitting process for the $\hat{Q}$ matrix, Eq.(4.84), terms. The comparison is made when the thin aerofoil derivatives and the experimentally derived derivatives are used. The rational function approximation process results in a very accurate fit for the thin aerofoil case. This is because the data points, following closed form analytical expressions, fall into smooth lines. As expected, the more irregular experimental data are more difficult to fit, however as seen in Fig. 4.15 the approximation error is reasonably small. Further improvement can be attained by increasing the number of aerodynamic poles, however this would in turn increase the order of the state space equations. Comparing the shape of the terms in the **Q** matrix when using thin airfoil theory and flutter derivatives, it can be noticed that $Q_{21}$ demonstrates a different slope in the two cases. $Q_{11}, Q_{12}, Q_{22}$ on the other hand follow a similar pattern although values can be quite different.

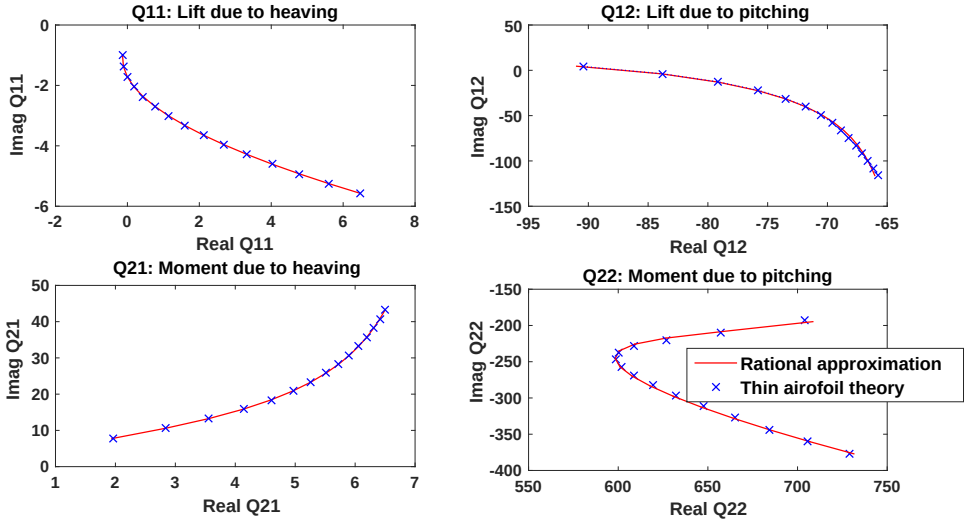


(a) Thin aerofoil

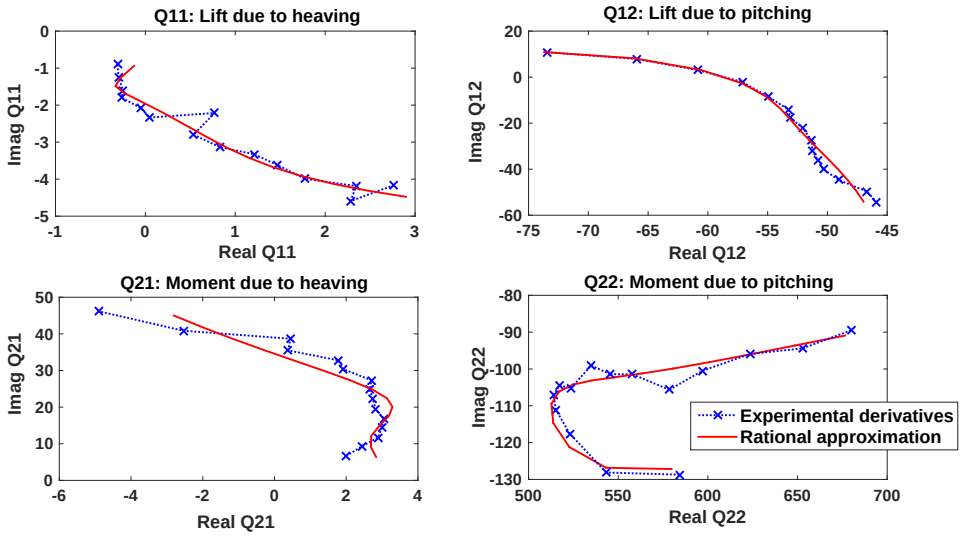


(b) Flutter derivatives

Figure 4.15 Roger's approximation for the four terms of $\hat{Q}$ when thin aerofoil (a) and experimental flutter derivatives (b) are implemented.

Fig. 4.16 presents a comparison of the root-loci of the full bridge when using thin aerofoil theory and flutter derivatives approach. The similarity of aerodynamic behaviour and the assumption that the streamlined box girder under investigation resembles the behaviour of a thin aerofoil is apparent. Both thin aerofoil theory and the use of flutter derivatives are very close in their prediction of the flutter critical wind speed ($82m/s$ vs. $81m/s$). Torsional divergence is estimated at $90m/s$ using thin aerofoil theory and $104m/s$ using flutter derivatives. The latter discrepancy is because in the actual Great Belt bridge

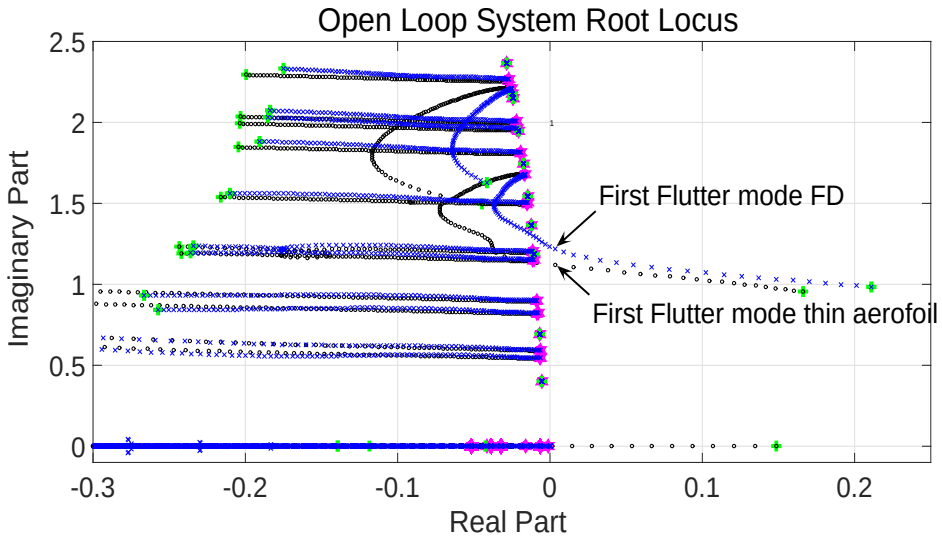


Figure 4.16 Comparison of root-loci for the Great Belt Bridge using thin aerofoil theory and flutter derivatives. The wind is swept from 0 (magenta hexagon) to $100m/s$ (green cross). The black circles correspond to the use of thin aerofoil theory and the blue crosses to the use of flutter derivatives. Thin aerofoil theory predicts flutter at $82m/s$ and flutter derivatives at $81m/s$.

section $C'_{M0}$ in Eq.(1.1) is lower than the theoretical value for a thin plate, which is $\pi/2$. Furthermore, in flutter conditions the reduced frequency was estimated to be about $k = 0.24$. As mentioned already, for $k > 0.2$ the conditions are considered strongly unsteady [112]. It was estimated in this case that using quasi steady aerodynamic theory [42], would result in an error for the prediction of flutter limits of about 20%.

Fig. 4.17 presents the transient response of the main span's midpoint due to an initial vertical perturbation for different wind speeds. For wind speeds below the flutter speed the motion gets damped very quickly. For wind speeds above the flutter speed one can observe an exponentially growing oscillatory motion and for wind speeds above the divergence limit the systems becomes unstable in a both divergent and oscillatory manner.

| Reference | Flutter Velocity |
|---|---|
| [92]: numerical, flutter derivatives, 2 modes | $90m/s$ |
| [92]: numerical, flutter derivatives, 18 modes | $62m/s$ |
| [46]: numerical, flutter derivatives, 2 modes | $83m/s$ |
| [46]: numerical, flutter derivatives, 6 modes | $97m/s$ |
| [104]: wind tunnel section model | $70-74m/s$ |
| [104]: wind tunnel taut strip model | $72m/s$ |
| [104]: wind tunnel full bridge model | $70-75m/s$ |
| [104]: numerical, flutter derivatives from section model | $75m/s$ |
| [104]: numerical, flutter derivatives from taut strip model | $79m/s$ |
| this work: numerical, flutter derivatives, all modes | $81m/s$ |
| this work: numerical, thin aerofoil, all modes | $82m/s$ |
| this work: numerical, flutter derivatives, 2 modes | $75m/s$ |
| this work: numerical, thin aerofoil, 2 modes | $75m/s$ |

Table 4.3 Estimation of flutter velocities of the Great Belt Bridge from literature.

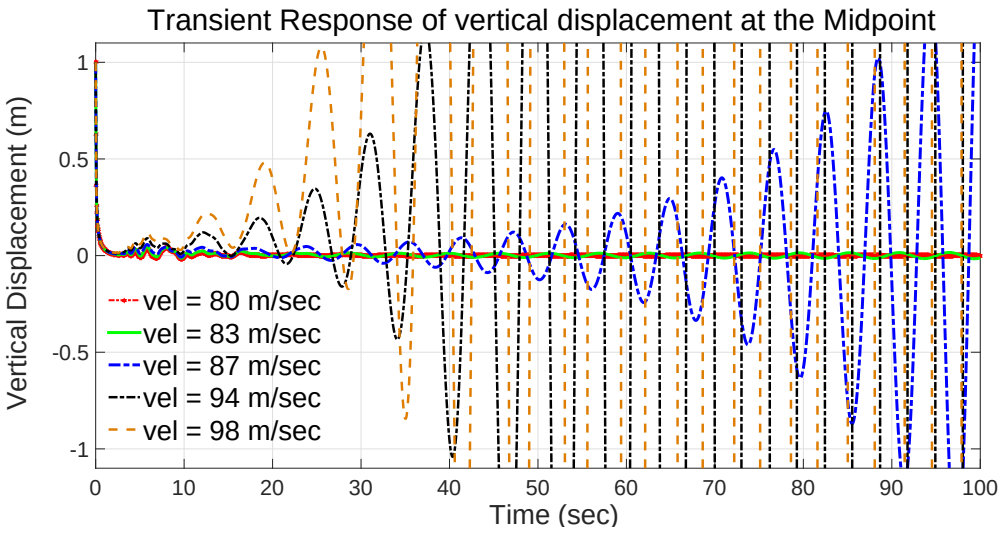


Figure 4.17 Mid-span vertical transient behaviour due to initial vertical displacement in different wind conditions. The initial perturbation has its maximum of 1m at the Mid-span point.

Flutter speed estimates for the Great Belt Bridge have been reported elsewhere [92] but these predictions have a large scatter, ranging from 62 to $97m/s$, see Table 4.3. The table gives a summary of these results as well as the values predicted by the proposed analytical framework. Flutter speeds based on an equivalent 2-DOF, heave-pitch model, both using thin aerofoil theory and flutter derivatives are included. The predicted flutter speed using the 2-DOF model is the same as Larsen's analytic flutter prediction using flutter derivatives (measured on a sectional model)[104], which was based on a two mode routine

with allowance for the mode shapes of the basic symmetric bending and torsion mode. The higher critical wind speeds obtained with the full structural modes can be attributed to multimodal behaviour with higher vertical modes participating in the first flutter mode as will be discussed in the next chapter.

### 4.4.5 Discussion on the Applicability of the Theodorsen Model

In the preceding sections aeroelastic stability limits were evaluated both using the Theodorsen model and the Scanlan model, Flutter Derivatives approach. For the case of the Great Belt Bridge it was demonstrated that although the experimentally derived flutter derivatives deviate quantitatively than the ones predicted by thin aerofoil theory, the aeroelastic flutter limits are very close for the two cases. In the following chapters the Theodorsen model will be exclusively used in order to account for the aerodynamic influence of the flaps for controlling deck motion, because of the choice of the Theodorsen-Garrick transformation [187] to model leading and trailing flap contributions, which is based on thin aerofoil theory.

The question however of quantitatively assessing the streamlined performance of bridge decks is a long standing one. In their pioneering work Scanlan and Tomko [169] tested 20 deck forms and obtained their aerodynamic derivatives, which were also graphically compared to the thin plate performance. From their analysis is becomes evident that truss-stiffened cross sections and similar to the Tacoma bridge H-sections have a fundamentally different performance than the one predicted by the Theodorsen model. In most of the cases however, when box girder deck sections are employed the flutter derivatives trend mimics quite effectively thin plate behaviour. In this analysis it was also revealed that the most striking difference between aerofoil and bridge deck response is due to the $A_2^*$ derivative, which while differing among bridges, will differ drastically for certain types of bridge decks when compared to an aerofoil. The single most outstanding effect is the $A_2^*$ sign reversal presented in a variety of bridge decks, which determines their intrinsic proclivity towards single-degree torsional instability similar to the Tacoma destructive mode. This

phenomenon is not possible for unstalled aerofoils and for streamlined deck forms such as the ones used for the Humber and the Great Belt Bridges.

More recently several researchers have examined the applicability of stability indices [98, 18], defined as the ratio between the critical flutter speed of a given experimental section and the critical flutter speed using the equivalent thin plate model. The stability index is normally within the range (0.4-0.8) for bluff bodies and (0.8-1.1) for streamlined sections; larger values up to 1.25 can be reached for streamlined slotted profiles [18, 75]. Furthermore, Matsumoto [129] proposed an iterative "step-by-step" method to predict flutter instability, which has the advantage of highlighting the stabilizing role of each flutter derivative individually. In particular for coupled flutter the destabilizing effect of $A_1^*$ and $H_3^*$ derivatives is shown. On the other hand, $H_1^*$ and $A_2^*$ are of importance for heaving-branch and torsional-branch instabilities respectively. Matsumoto also examines the bluffness effect on 2-D rectangular prisms with various side ratios $\frac{B}{D}$, $B$ is the longitudinal length of the prism and $D$ is its height, in relation to torsional flutter and coupled flutter.

Chen at al. [44] showed that flutter derivatives are only slightly dependent on amplitude and frequency under small vibrations. Nonlinear characteristics of aerodynamic forces were also investigated. Results indicate that the response of a thin plate and streamlined sections are close to linear behaviour, however the response of bluff sections contains a relatively large contribution from higher order harmonics even at small amplitudes. More recently Gouder et al. [78] compared the aerodynamic derivatives of an experimental box section having $B/D \simeq 11$ and confirmed a relatively good agreement with the Theodorsen model predictions.

## 4.5 Discussion and Concluding Remarks

This chapter placed emphasis on recasting classical results from potential flow theory in a form suitable for control analysis and design in the Laplace domain. The procedure is extended to a finite element framework and implemented to the case of the Humber Bridge finding good agreement compared to previous experimental and analytic studies.

The aeroelastic finite element procedure was also modified to consider experimentally obtained flutter derivatives. The analysis revealed that for bridges having streamlined deck girders, such as the Great Belt Bridge, the system's aerodynamic behaviour is similar to that predicted by thin aerofoil theory, thus supporting the validity of the latter for all the following control analysis. Considerable attention was given in the aeroelastic modelling of the deck erection process of a suspension bridge. For the case of the Humber Bridge, aeroelastic limits during erection are in agreement with prior analyses based on sectional models, but also suggest that higher-order modes have a beneficial effect on the critical flutter wind speed. The combination of the developed structural and aerodynamic framework allows for a full bridge aeroelastic analysis by considering the structure's full multi-modal behaviour in a computationally efficient manner. This framework is also advantageous for the subsequent active and passive control analyses.

# Chapter 5

# Active Aeroelastic Control with moving Flaps

## 5.1 Introduction

The current chapter employs the previously developed aeroelastic bridge modelling framework in order to investigate an active control scheme for flutter and torsional divergence suppression. In order to account for modelling errors and uncertainties while designing the controller, elements from robust control theory are invoked. The stability and robustness of the bridge when fitted with flaps controlled by optimal and suboptimal $H_\infty$ controllers is discussed for varying lengths of control surfaces along the suspended span as the optimum configuration for aerodynamic performance is investigated. More specifically, the process aims at optimizing the closed-loop system's robustness to uncertainties, which can be interpreted as uncertainty in modal characteristics or aerodynamic parameters. The goal is to establish an active control strategy that results in a minimum area of control surfaces along the span while attaining good robustness characteristics. It will be shown that although this approach significantly improves the structure's aerodynamic response, there is a clear loss in uncertainty tolerance for wind speeds higher than the torsional divergence boundary. The controller effectiveness is also demonstrated through time domain simulations following the

application of displacement initial conditions. Experimental work carried in conjunction with this analysis is presented in [78].

## 5.2 Flap Aerodynamic Modelling

### 5.2.1 Flap Aerodynamic Contribution on a Sectional Model

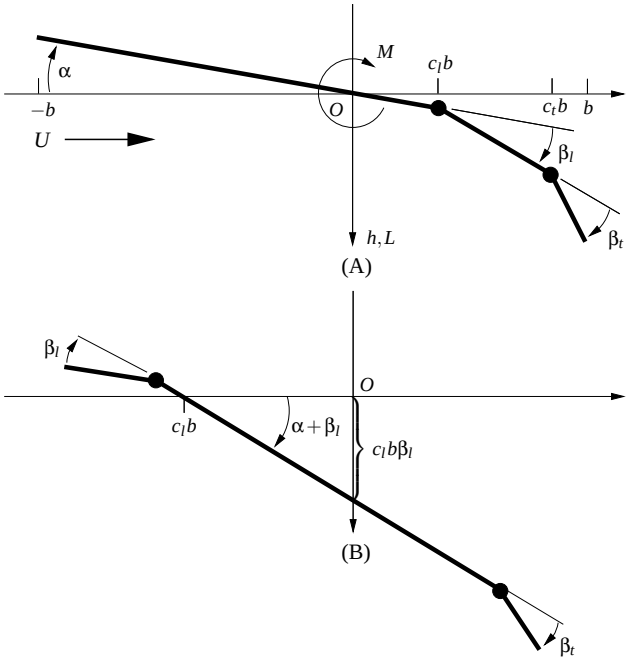


Figure 5.1 Transformation of the Theodorsen-Garrick wing-aileron-tab configuration into a controlled bridge deck. (a): The wing pitch angle is $\alpha$, the aileron angle is $\beta_l$ and the tab angle is $\beta_t$, $U$ denotes the wind speed. (b): The leading flap angle is $\beta_l$, the deck angle is $\alpha$ and the trailing-edge flap angle is $\beta_t$.

The sectional aeroelastic model described in Section 4.3 is here extended to account for the aerodynamic contributions of leading-and trailing-edge flaps. The analytic procedure is based on the transformation of the wing-aileron-tab configuration originally proposed by Theodorsen and Garrick [187]. This transformation is graphically depicted in Fig. 5.1. In the new configuration the aileron becomes the bridge deck, the wing the leading-edge flap and the tab becomes the trailing-edge-flap.

The presented transformation is considered in combination with equations (22) and (23) in [187], in which $l$ and $m$ are set to zero. The general aerodynamic expressions are

presented in Chapter 6 for a more general case. In order to re-level the bridge, and return its mass centre to the correct position, pitch and heave correction must be applied. The first step involves the use of a negative value of $c_l$ to replace $c_t$, which transforms the wing into the leading-edge flap and the flap into the main deck. This change leaves the main deck at an inclination of $\alpha + \beta_l$ and with a heave offset of $c_l b \beta_l$ in the mass centre. In order to correct the heave and pitch offsets, the whole assembly must be rotated through $-\beta_l$ and elevated through a vertical distance of $c_l b \beta_l$ [79]. For the system depicted in Fig. 5.1 the inertial properties of the flaps were neglected and only their aerodynamic influence on the lift and moment applied on the deck was considered. This simplifying assumption is based on the premise that the mass of the flaps should be kept considerably smaller that the mass of the deck in order to minimize the additional dead load. Furthermore, because the following analysis will focus on active control it is expected that the controller motors have sufficient power to adjust the flaps angles $\beta_l$ and $\beta_t$.

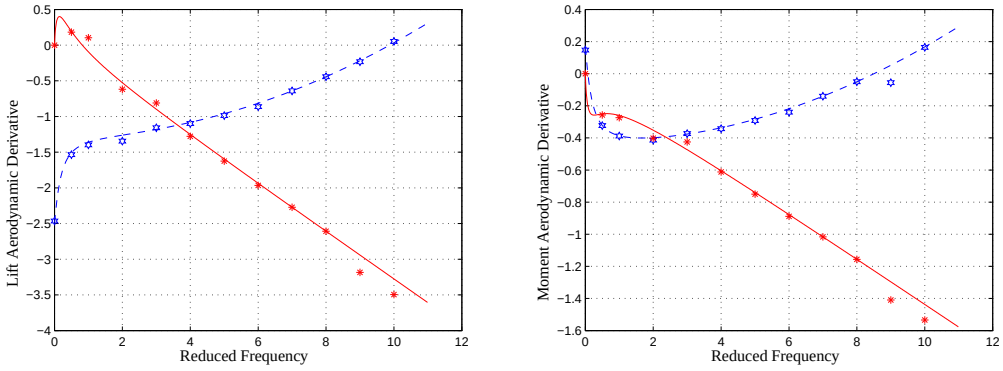


Figure 5.2 Aerodynamic derivatives for the trailing-edge flap. The blue dashed curves (red solid) correspond to the real (imaginary) parts of the aerodynamic derivatives computed using thin aerofoil theory. The (red) stars and (blue) hexagons were computed using a discrete vortex panel code [79].

The aerodynamic derivatives using Theodorsen's theory were computed in [79] with a two-dimensional discrete vortex panel code, which implies the assumption of thin aerofoil theory. The results are presented in figures 5.2 and 5.3. It should be noted that these plots have been scaled by $k^2$ so that the illustrated quantities are properly defined in the steady

state ($k = 0$). Good agreement between thin aerofoil and the vortex panel code can be observed.

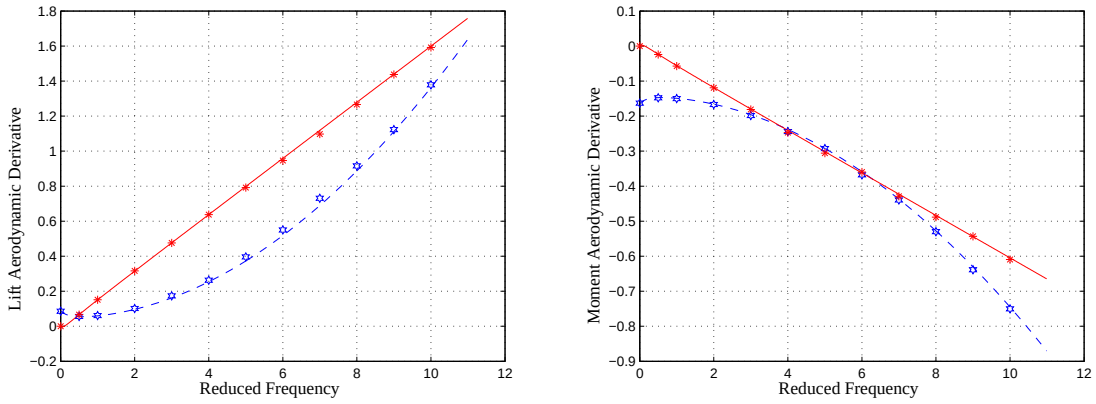


Figure 5.3 Aerodynamic derivatives for the leading-edge flap. The blue dashed curves (red solid) correspond to the real (imaginary) parts of the aerodynamic derivatives computed using Theodorsen-Garrick potential theory. The (red) stars and (blue) hexagons were computed using a linear discrete vortex code [79].

Similarly to the deck case the fluid-structure stability can be expressed in the generalized eigenvalue form, Eq.(4.60). The $4 \times 4$ aerodynamic mass, damping and stiffness matrices are now formed as follows

$$\mathbf{M}_{ncF} = \begin{bmatrix} -\pi\rho b^2 & 0 & M_{ncF}^{1,3} & M_{ncF}^{1,4} \\ 0 & -\frac{\pi\rho b^4}{8} & M_{ncF}^{2,3} & M_{ncF}^{2,4} \\ 0 & 0 & 0 & 0 \\ 0 & 0 & 0 & 0 \end{bmatrix} \tag{5.1}$$

$$\mathbf{C}_{ncF} = \begin{bmatrix} 0 & -\pi\rho b^2 U & C_{ncF}^{1,3} & C_{ncF}^{1,4} \\ 0 & -\frac{\pi}{2}\rho b^3 U & C_{ncF}^{2,3} & C_{ncF}^{2,4} \\ 0 & 0 & 0 & 0 \\ 0 & 0 & 0 & 0 \end{bmatrix} \tag{5.2}$$

$$\mathbf{K}_{ncF} = \begin{bmatrix} 0 & 0 & K_{ncF}^{1,3} & K_{ncF}^{1,4} \\ 0 & 0 & K_{ncF}^{2,3} & C_{ncF}^{2,4} \\ 0 & 0 & 0 & 0 \\ 0 & 0 & 0 & 0 \end{bmatrix} \tag{5.3}$$

where,

$$M_{ncF}^{1,3} = \rho b^3 T_1(c_t) \tag{5.4}$$

$$M_{ncF}^{1,4} = \rho b^3 (T_1(c_l) - \pi c_l) \tag{5.5}$$

$$M_{ncF}^{2,3} = \rho b^4 (T_7(c_t) + c_t T_1(c_t)) \tag{5.6}$$

$$M_{ncF}^{2,4} = \rho b^4 (T - T_7(c_l) + c_l T_1(c_l) + \frac{\pi}{8}) \tag{5.7}$$

$$C_{ncF}^{1,3} = \rho U b^2 T_4(c_t) \tag{5.8}$$

$$C_{ncF}^{1,4} = \rho U b^2 (T_4(c_t) + \pi) \tag{5.9}$$

$$C_{ncF}^{2,3} = -\rho b^3 U \left[ T_1(c_t) - T_8(c_t) - c_t T_4(c_t) + T_{11}\left(\frac{c_t}{2}\right) \right] \tag{5.10}$$

$$C_{ncF}^{2,4} = -\rho b^3 U \left[ T_1(c_l) - T_8(c_l) - c_l T_4(c_l) + T_{11}\left(\frac{c_l}{2}\right) - \frac{\pi}{2} \right] \tag{5.11}$$

$$K_{ncF}^{1,3} = K_{ncF}^{1,4} = 0 \tag{5.12}$$

$$K_{ncF}^{2,3} = -\rho b^2 U^2 (T_4(c_t) + T_{10}(c_t)) \tag{5.13}$$

$$K_{ncF}^{2,4} = -\rho b^2 U^2 (T_4(c_l) + T_{10}(c_l)) \tag{5.14}$$

The terms $T_{ij}$ are given in [187], see Appendix C. In the above matrices, the two additional columns are related to the flap angles $\beta_t, \beta_l$ (note that the upper left $2 \times 2$ sub-matrices are exactly those reported in Eq.(4.56), whereas the two additional zero rows correspond to the equations of motion related to the flap angles. The structural matrices $\mathbf{M}, \mathbf{C}, \mathbf{K}$ are accordingly enlarged to $4 \times 4$ size, and are denoted $\mathbf{M}_F, \mathbf{C}_F, \mathbf{K}_F$ to indicate the extra flap degrees of freedom. For this case the additional rows/columns are all comprised of zero terms, because of the massless flap assumption.

Matrices $\mathbf{B}_F, \mathbf{C}_F$ are in this case used in place of $\mathbf{B}$ and $\mathbf{C}$, presented in Eq.(4.61).

$$\mathbf{B}_F^T = \begin{bmatrix} -2\pi\rho U b & \pi\rho U b^2 & 0 & 0 & 0 & 0 & 0 & 0 \end{bmatrix} \tag{5.15}$$

$$\mathbf{C}_F = \begin{bmatrix} 0 & U & T_{10}(c_t)\frac{U}{\pi} & T_{10}(c_l)\frac{U}{\pi} - U & 1 & \frac{b}{2} & T_{11}(c_t)\frac{b}{2\pi} & T_{11}(c_l)\frac{b}{2\pi} + b\left(c_l - \frac{1}{2}\right) \end{bmatrix} \tag{5.16}$$

The aeroelastic model of the deck-flap assembly is thus brought into a state space form in accordance with Eq.(4.60). The corresponding $8\times 8$ $\mathbf{E}_{cF},\mathbf{A}_{cF}$ matrices are as follows

$$\mathbf{E}_{cF}=\begin{bmatrix} 0 & \mathbf{M}_F-\mathbf{M}_{\text{ncF}} \\ \boldsymbol{I} & 0 \end{bmatrix} \qquad \mathbf{A}_{cF}=\begin{bmatrix} -\mathbf{K}_F+\mathbf{K}_{\text{ncF}} & -\mathbf{C}_F+\mathbf{C}_{\text{ncF}} \\ 0 & \boldsymbol{I} \end{bmatrix}. \tag{5.17}$$

The state vector is now $\mathbf{x}=\{h,\alpha,\beta_t,\beta_l,\dot{h},\dot{\alpha},\dot{\beta}_t,\dot{\beta}_l\}^T$.

With regard to the implementation of flap dynamics in the FE model, the system is similarly expressed in the form of Eq.(4.79) and Eq.(4.80) with the state vector now augmented to include the flap rotations and the flap rotation velocities, $\hat{\mathbf{x}}=\{\mathbf{Q},\mathbf{F},\mathbf{Q}_v,\mathbf{F}_v\}^T$. $\mathbf{F}$ and $\mathbf{F}_v$ denote the flap angles and their derivatives respectively. Depending on the control strategy implemented a number of elements will consist of just the deck with the flaps frozen, meaning $M^{i,i}_{ncF}=C^{i,i}_{ncF}=K^{i,i}_{ncF}=0$ and $\mathbf{C}_F=[0,U,0,0,1,b/2,0,0]$, while elements including movable flaps are formulated as indicated in this section.

### 5.2.2 Active Feedback Design Framework

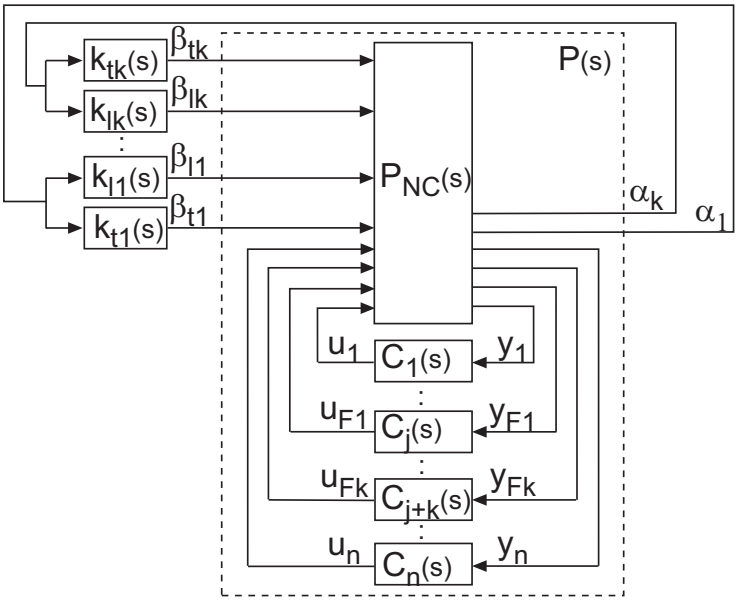


Figure 5.4 Block diagram of the system: $P_{NC}(s)$ is the aeroelastic model without the circulatory terms, $P(s)$ is the aeroelastic model (the $C_i(s)$ feedbacks are for the inclusion of the circulatory terms), $k_{li}(s)$ and $k_{ti}(s)$ are the compensators of the leading and trailing flaps, $\alpha_i$ are the pitch angles, $\beta_{li}$ and $\beta_{ti}$ are the leading- and trailing-edge flap angles.

In the design of feedback design framework, the general case of bridge-flap system is presented. $n$ segments are assumed in place from which $k$ are equipped with trailing- and leading-edge flaps, see Fig. 5.4. The uncontrolled (open loop) system is described by the aeroelastic model $P(s)$ (corresponding to the state space matrices $\mathbf{E}_{gF}, \mathbf{A}_{gF}, \mathbf{B}_{gF}, \mathbf{C}_{gF}$ ) and the leading- and trailing-edge flaps controllers are denoted as $k_{li}(s)$ and $k_{ti}(s)$. Both controllers receive the pitch angle $\alpha_i$ of the corresponding element as their input, and generate the flap angles $\beta_{li}, \beta_{ti}$ as outputs. The use of flap angles as control inputs to the system, instead of flap torques, simplifies computations involved in the control design. This is because although the flap related degrees of freedom and their velocities appear in the states of the system the modelling of the flap dynamics is omitted. Furthermore, because the flap controllers receive an angle as input and produce angles as outputs the control law computation is easier than when the output consists of control torques, in which case proper scaling must be introduced. In contrast, When a passive mechanical network control implementation is followed, see Chapter 6, rather than power based active control, the more realistic flap torques should be considered. This is because the passivity component constraint necessitates the identification of across variables such as forces and torques and through variables such as displacements and velocities [62, 177].

The generalized state-space model is given by

$$\begin{cases} \mathbf{E}_{gF}\dot{\hat{\mathbf{x}}} = \mathbf{A}_{gF}\hat{\mathbf{x}} + \mathbf{B}_{gF}\mathbf{u} \\ \mathbf{z} = \mathbf{C}_{gF}\hat{\mathbf{x}} \end{cases} \tag{5.18}$$

where, $\mathbf{u} = \{\beta_{t1}, \beta_{l1}, ..., \beta_{tk}, \beta_{lk}\}^T$ and $\mathbf{z} = \{\alpha_1, ...\alpha_k\}^T$. Since the controlled inputs are the flap angles rather than torques to massy flap bodies, the model given in equations (5.18) must generate the first and second derivatives of the flap angles internally; these derivatives are required by the aerodynamic model. This is achieved using a generalized state space system of the form [79]

$$\begin{bmatrix} 0 & 0 \\ 1 & 0 \end{bmatrix} \begin{bmatrix} \dot{x}_1 \\ \dot{x}_2 \end{bmatrix} = \begin{bmatrix} 1 & 0 \\ 0 & 1 \end{bmatrix} \begin{bmatrix} x_1 \\ x_2 \end{bmatrix} + \begin{bmatrix} -1 \\ 0 \end{bmatrix} \beta. \tag{5.19}$$

In which, $\beta$ represents each flap angle. It follows immediately that

$$x_1 = \beta, \qquad x_2 = \dot{\beta}, \qquad \dot{x_2} = \ddot{\beta}. \tag{5.20}$$

Note that these equations are introduced in the state space model at the rows corresponding to the flap angles $\beta_{ti}, \beta_{li}$ (first row of Eq.(5.19)) and their derivatives $\dot{\beta}_{ti}, \dot{\beta}_{li}$ (second row of Eq.(5.19)). Since Eq.(5.19) has both its eigenvalues at infinity the system will have $4k$ eigenvalues there. These eigenvalues are not associated with 'real' system dynamics, or system stability properties and are thus ignored throughout this analysis.

## 5.3 The $H_\infty$ Framework

### 5.3.1 Active Control Methodologies

Control applications to civil engineering structures have been gaining in popularity thanks to novel advances in the field [19] with a particular emphasis to bridge structures [38]. In recent years there has been growing interest in control design of structural systems under the presence of structured or unstructured uncertainties. In [188] for example the vibration control of a tensegrity structure was considered using $H_\infty$ robust control theory and $\mu$ synthesis.

The most important objective in control system design is stability. It is however unavoidable that the system model will differ in behaviour from the actual system. Differences between the actual plant and the nominal model, system model to be compensated, are generally referred to as *modelling errors* or *system uncertainty* [132]. The nature of uncertainty can arise from different sources. A successful model should be simple enough to facilitate design, yet complex enough to provide confidence that it is representative of the true plant. Most models are for example a linearized version of a more mathematically involved non-linear physical system, as is the case for the structural FE bridge model, see Chapter 3. Further sources of uncertainty include; inaccurate determination of model

parameters and variation in the structural and aerodynamic loading. For the aeroelastic bridge model it is well known that modal frequencies vary with temperature [47] and that structural damage inflicts changes, although usually modest, in the mechanical parameters. The effect of aerodynamic parameter variations in the flutter boundary has been investigated in [53], whereas wind turbulence is expected to also effect the flutter stability limits.

Given such uncertainties, a practical approach would be to design a controller that not only stabilizes the nominal model, but also stabilizes a family of systems which exist in the *uncertainty region* around the nominal model. The concept of *robust stability* is thus geared towards stabilizing the closed-loop system in the presence of modelling errors. The $H_\infty$ optimal control framework is a frequency-domain optimization and synthesis theory developed in response to the need of a synthesis procedure that explicitly addresses questions of modelling errors [80]. It is also worth mentioning that techniques stemming from the *modern control* area, as has been used for the bridge aeroelastic stabilization in [82], fall short in the assurance of stability margins for the closed loop system. This might seem surprising because the linear quadratic regulator (LQR) framework, which has a prominent place in optimal control theory, is known to exhibit impressive robust stability properties including at least $60^o$ of phase margin, an infinite gain margin and a 50% gain-reduction tolerance. This practically means that a phase shift of up to $60^o$ can be tolerated in each of the input channels simultaneously and the gain in each channel can be increased indefinitely without loss of stability. Because LQ controllers are based on full state feedback it is often the case that the states need to be reconstructed by an optimal compensator, Kalman filters, thus forming the linear quadratic gaussian (LQG) optimal controllers. The resulting framework however does not ensure stability robustness and its practical impact is thus undermined.

Error modelling can take the form of either structured or unstructured uncertainties. *Structured uncertainty* is uncertainty about which structural information is available. It is thus a way to express variations in specific model parameters based on the *structured singular values*, $\mu$, framework designed using DK iterations [149, 176]. Although, this

is an attractive and non-conservative way of modelling uncertainty it comes with a high computational cost and difficulty in convergence of the DK-iteration method for high state models. *Unstructured uncertainty* is uncertainty about which no information is available about its effects on a process, except that an upper bound on its size or magnitude as a function of frequency can be estimated [132]. The unstructured uncertainty is usually defined as a full complex perturbation matrix $\mathbf{\Delta}$, usually with dimensions compatible with those of the plant. The design of feedback controllers in the presence of non-parametric unstructured uncertainty is the main focus of the $H_\infty$ design method, which will be applied in the following sections for determining the flap compensators.

### 5.3.2 Uncertainty Modelling

Several unstructured uncertainty models can be defined. Let $\mathbf{G}$ and $\mathbf{G}_\Delta$ be the transfer functions of the nominal and perturbed plant models respectively. For example, by denoting $\mathbf{\Delta}_A$ the perturbation due to additive uncertainty and $\mathbf{\Delta}_M$ due to multiplicative uncertainty, the resulting perturbed plants are $\mathbf{G}_\Delta = \mathbf{G} + \mathbf{\Delta}_A$ and $\mathbf{G}_\Delta = (\boldsymbol{I} + \mathbf{\Delta}_M)\mathbf{G}$ respectively [80, 176]. In these uncertainty representations the nominal and perturbed models must have the same number of right half plane poles - a somewhat artificial restriction. An attractive way of representing the uncertainty perturbation is also by means of the coprime factorization of the plant.

In that respect, The normalized left coprime factorization of the transfer function, $\mathbf{G}$, of the plant, see Fig. 5.5, is defined as

$$\mathbf{G} = \mathbf{M}^{-1}\mathbf{N}, \tag{5.21}$$

where, $\mathbf{M}, \mathbf{N} \in H_\infty$ and

$$\mathbf{M}\mathbf{M}^{\sim} + \mathbf{N}\mathbf{N}^{\sim} = \boldsymbol{I}. \tag{5.22}$$

$(\cdot)^\sim$ means adjoint. The perturbed plant is

$$\mathbf{G}_\Delta = (\mathbf{M}+\mathbf{\Delta}_M)^{-1}(\mathbf{N}+\mathbf{\Delta}_N): \quad [\mathbf{\Delta}_M,\ \mathbf{\Delta}_N] \in H_\infty, \ \left\| \mathbf{\Delta}_M \quad \mathbf{\Delta}_N \right\|_\infty < \gamma^{-1}. \tag{5.23}$$

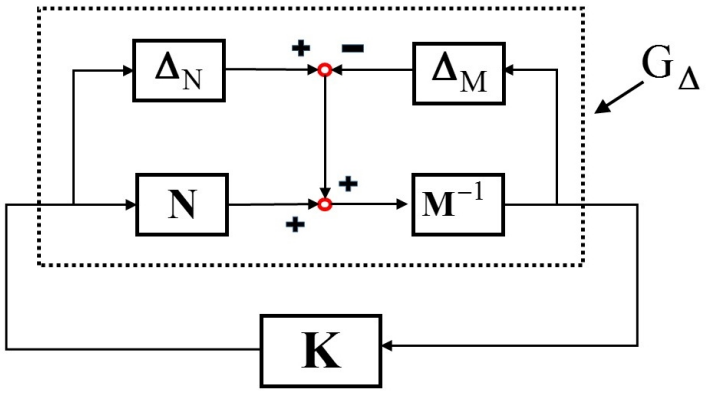


Figure 5.5 Left coprime factor perturbations.

$\mathbf{N}_\Delta = \mathbf{N}+\mathbf{\Delta}_N$, and $\mathbf{M}_\Delta = \mathbf{M}+\mathbf{\Delta}_M$, represent the left coprime factorization of $\mathbf{G}_\Delta$.

Because in such cases the uncertainty is assumed unstructured, the only information available about the perturbation is that a bound on its magnitude over frequency can be estimated. In the case where $\mathbf{\Delta}$ is a multivariable transfer function then an approximate magnitude measure is the maximum singular value, denoted $\bar{\sigma}(\mathbf{\Delta})$. The perturbations $\mathbf{\Delta}_N$ and $\mathbf{\Delta}_M$ must always be stable.

The perturbation modelling in the normalized coprime representation of the plant combines advantages from several robustness criteria [80, 176, 192], it can for example account for uncertainty on lightly damped natural frequencies, which play a pivotal role in the system's dynamics. It has been established that the representation of model errors as stable perturbations to the normalized coprime factors of the nominal plant model provides a more general description of the robust stability problem. This is because this formulation also provides a bound on the infinity norm of other transfer function matrices of interest in assessing closed-loop performance and robustness. Optimizing for additive perturbation on the plant $\mathbf{P}$ is known to give controllers with poor gain margins but places a favourable

explicit limit on the high-frequency gain of the resulting controller. On the other hand, an index related to multiplicative perturbation on **P** is known to give good robustness margin, but may have an unbounded high-frequency gain.

### 5.3.3 The $H_\infty$ Control Framework

The $H_\infty$ control framework is presented in Fig. 5.6, where $\mathbf{P}(s)$ shows the system to be controlled and $\mathbf{K}(s)$ the compensator to be determined. **P** is called the standard plant containing the nominal plant, **G**, and connections. It is assumed that the plant **P** is assumed to be time-invariant. By **K** we denote the class of causal, linear, time-invariant and finite-dimensional controllers that internally stabilize **P**. The pair $(\mathbf{A}, \mathbf{B}_2)$ is assumed *stabilizable* and the pair $(\mathbf{A}, \mathbf{C}_2)$ *detectable*, see Eq.(5.24). The latter assumptions are necessary and sufficient for the existence of admissible controllers [80]. The system outputs available for control are denoted by **y** and **z**, the latter being referred to as the *objective signal*. The objective of the control design is to minimize the effect of the exogenous input **w** on the objective signal, through acting of the control signal **u**. It should be noted that the optimal $H_\infty$ controllers are generally not unique for multi-input multi-output (MIMO) systems [209]. Furthermore, finding an optimal $H_\infty$ controller is often numerically and theoretically complicated.

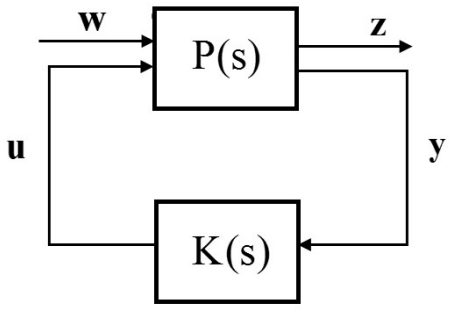


Figure 5.6 Scheme of robust control.

The effect of exogenous inputs including disturbances on the objective signal can be represented by the transfer function $T_{zw}(s)$. The $H_\infty$ norm is a measure for the size of this

transfer function. The $H_\infty$ framework consists in determining the compensator $\mathbf{K}(s)$ which stabilizes the system in Fig. 5.6 while guaranteeing $\|T_{zw}\|_\infty \leq \gamma$.

The state space equations of the system $\mathbf{P}(s)$ in the $H_\infty$ control scheme are given by

$$\begin{cases} \mathbf{x} = \mathbf{A}\mathbf{x} + \mathbf{B}_1\mathbf{w} + \mathbf{B}_2\mathbf{u}, \\ \mathbf{z} = \mathbf{C}_1\mathbf{x} + \mathbf{D}_{11}\mathbf{w} + \mathbf{D}_{12}\mathbf{u}, \\ \mathbf{y} = \mathbf{C}_2\mathbf{x} + \mathbf{D}_{21}\mathbf{w} + \mathbf{D}_{22}\mathbf{u}, \end{cases} \tag{5.24}$$

in which $\mathbf{w}$ is an l-dimensional exogenous input, $\mathbf{u}$ is an m-dimensional control signal, $\mathbf{y}$ is a q-dimensional measurement and $\mathbf{z}$ is a p-dimensional objective signal. The state vector $\mathbf{x}$ has dimensions n. The uncertainty $\mathbf{\Delta}(s)$ is modelled as a transfer function from $\mathbf{z}$ to $\mathbf{w}$. Furthermore, by introducing an ULFT (*upper linear fractional transformation*), $F_U$, the uncertainty plant $\boldsymbol{G}_\Delta$, shown in Fig. 5.5, can be expressed as

$$\mathbf{G}_\Delta = F_U(\mathbf{P}, \mathbf{\Delta}). \tag{5.25}$$

The standard plant associated with the coprime uncertainty description is given as

$$\mathbf{P} = \left(\begin{array}{c|c} P_{11} & P_{12} \\ \hline P_{21} & P_{22} \end{array}\right) = \left(\begin{array}{c|c} 0 & \boldsymbol{I} \\ \tilde{\boldsymbol{M}}^{-1} & \mathbf{G} \\ \hline \tilde{\boldsymbol{M}}^{-1} & \mathbf{G} \end{array}\right); (\mathbf{\Delta} = [\mathbf{\Delta}_N, -\mathbf{\Delta}_M]). \tag{5.26}$$

Let $\mathbf{\Delta} \in \mathscr{D}$, where $\mathscr{D}$ is a class of possible uncertainties including $\mathbf{\Delta} = 0$. The system's robust stabilization thus results in finding the feedback controller which enables the largest attainable perturbation $\mathbf{\Delta}$, in a $L_\infty$ sense, such that the closed-loop stability is maintained. The $L_\infty$ norm of the largest allowable perturbation is referred to as *maximum stability margin*. $L_\infty$ is the class of systems for which the supremum is finite.

$$L_\infty = \{\mathbf{G} : \|\mathbf{G}\|_\infty < \infty\} \tag{5.27}$$

In which the $L_\infty$-norm is defined as

$$\|G\|_\infty = \sup_\omega \bar{\sigma}(\boldsymbol{G}(i\omega)). \tag{5.28}$$

The following theorem provides a definition for robust stability.

**Theorem 1** *$\boldsymbol{K}$ stabilizes $F_U(\boldsymbol{P},\boldsymbol{\Delta})$ for all $\boldsymbol{\Delta} \in \mathscr{D}$, and any standard plant $\boldsymbol{P}$ if and only if:*

1. *$\boldsymbol{K}$ stabilizes $F_U(\boldsymbol{P},0)$ ;*
2. *$\|F_L(\boldsymbol{P},\boldsymbol{K})\|_\infty \leq \gamma = \frac{1}{\varepsilon}$;*

Where $\mathbf{G} = F_U(\mathbf{P},0)$ is the nominal plant and $F_L$ denotes the *lower fractional transformation*. for the case of coprime factor uncertainty the above theorem translates to the following corollary. For proof see [132].

**Corollary 1.1** *$\boldsymbol{K}$ stabilizes $\boldsymbol{G}_{\boldsymbol{\Delta}} = (\tilde{\boldsymbol{M}} + \boldsymbol{\Delta}_M)^{-1}(\tilde{\boldsymbol{N}} + \boldsymbol{\Delta}_N)$ for all $[\boldsymbol{\Delta}_N, \boldsymbol{\Delta}_M] \in \mathscr{D}$, if and only if:*

1. *$\boldsymbol{K}$ stabilizes $\boldsymbol{G}$;*
2. $$\left\| \begin{array}{c} \boldsymbol{K}(I-\boldsymbol{G}\boldsymbol{K})^{-1}\tilde{\boldsymbol{M}}^{-1} \\ (\mathbf{I}-\boldsymbol{G}\boldsymbol{K})^{-1}\tilde{\boldsymbol{M}}^{-1} \end{array} \right\|_\infty \leq \gamma = \frac{1}{\varepsilon}$$

The robust stabilization problem thus results in finding a controller that minimizes the achievable value of $\gamma$ or equivalently maximizes $\varepsilon$. From Theorem 1 it follows that

$$\gamma_{min} = \varepsilon_{max} = \left( \inf_{\mathbf{K}} \|F_L(\mathbf{P},\mathbf{K}\|_\infty \right)^{-1}. \tag{5.29}$$

Eq.(5.29) expresses the robust stabilization problem as an $H_\infty$ optimization problem, where the controller $\mathbf{K}$ is chosen so as to minimize the $H_\infty$ norm of the closed loop transfer function, under the constraint that it must also stabilize the nominal plant. $F_L(\mathbf{P},\mathbf{K})$ represents the transfer function from an exogenous input $\mathbf{w}$ to an output signal $\mathbf{z}$, and $\mathbf{P}$ is the standard plant associated with a particular combination of objectives.

Minimizing the $H_\infty$ norm of a transfer function is equivalent to minimizing the energy in the output signal due to inputs of unit energy [132]. As already mentioned determining $\gamma_{min}$ or equivalently $\varepsilon_{max}$ might be very challenging computationally and an iterative procedure is employed alternatively. This procedure for estimating $\gamma_{min}$ is outlined in Doyle et. al [57]. It is however often the case that a sub-optimal controller is sought after, such that $\gamma > \gamma_{min}$, with $\|F_L(\mathbf{P},\mathbf{K})\|_\infty < \gamma$.

When considering the case of the coprime factor plant description, Fig. 5.5, it can be shown that the robust stabilization problem has a particularly simple solution, which dispenses the need for iterative calculations [176].

Given the following coprime factor uncertainty

$$\left\| \boldsymbol{\Delta}_M \quad \boldsymbol{\Delta}_N . \right\|_\infty < \varepsilon = \gamma^{-1} \tag{5.30}$$

Then the largest positive stability margin $\varepsilon = \varepsilon_{max}$, such that $\mathbf{G}_\Delta = (\tilde{\mathbf{M}} + \boldsymbol{\Delta}_M)^{-1}(\tilde{\mathbf{N}} + \boldsymbol{\Delta}_N)$ can be stabilized by a controller $\mathbf{K}$, is given by

$$e_{max} = (\gamma_{min})^{-1} = \left\| \inf_{\mathbf{K}} \begin{bmatrix} \mathbf{K} \\ \boldsymbol{I} \end{bmatrix} (\boldsymbol{I} - \mathbf{GK})^{-1} \tilde{\mathbf{M}}^{-1} \right\|_\infty = \left\| \inf_{\mathbf{K}} \begin{bmatrix} \boldsymbol{I} \\ \mathbf{K} \end{bmatrix} (\boldsymbol{I} - \mathbf{GK})^{-1} \begin{bmatrix} \boldsymbol{I}, \mathbf{G} \end{bmatrix} \right\|_\infty$$
$$= \sqrt{\left(1 - \left\|[\tilde{\mathbf{N}}, \tilde{\mathbf{M}}]\right\|_H^2\right)}. \tag{5.31}$$

where $\|\cdot\|_H$ denotes the Hankel norm.

In Eq.(5.29) note that $\gamma \geq 1$. It is worth pointing out that minimizing $\gamma$ also results in the bounded $\infty$-norm for the contribution of objectives; $\mathbf{S}, \mathbf{KS}, \mathbf{SG}, \mathbf{KSG}$. Where, $\mathbf{S} = (\boldsymbol{I} - \mathbf{GK})^{-1}$ is the sensitivity function. This finding results from expanding the sub-matrices in Eq.(5.31). In particular $||\mathbf{KS}||_\infty$ is related to the robustness against additive perturbation on the plant $\mathbf{P}$, $||\mathbf{S}||_\infty$ is related to the robustness against additive perturbation on the loop transfer function $\mathbf{PK}$, $||\mathbf{KSP}||_\infty$ is related to the robustness against multiplicative perturbation on the controller $\mathbf{K}$ and $||\mathbf{SP}||_\infty$ is related to the robustness against additive perturbation on controller $\mathbf{K}$.

### 5.3.4 $H_\infty$ Control for the Bridge Aeroelastic Model

The robust stabilization of the Bridge-flap aeroelastic model presented in Fig. 5.4 is based on the left coprime factor plant description $H_\infty$ framework. The resulting active controller produces the maximum/best stability robustness margins for the given bridge-flap configuration and will serve in subsequent analyses as a reference for simpler, lower-order networks. The computed $H_\infty$ optimal controller has a size reduced by at least one compared to the original plant. An $H_\infty$ sub-optimal controller, $\gamma > \gamma_{min}$, has the same order as that of the plant. As already pointed out, although sub-optimal controllers are of higher order they demonstrate significant advantages, because they are easier to derive, can produce lower gains and often result to smoother system behaviour.

For the bridge feedback system assuming $k$ the number of elements equipped with flaps, the resulting controller matrix $\mathbf{K}$, will be of dimension $2k \times k$. Where the inputs are the trailing and leading flap angles for those elements and the outputs are the related deck rotations for each element. The $H_\infty$ framework as explained results to high order controller matrices both for the optimal and suboptimal cases. By employing model reduction techniques the number of states can be significantly reduced. However, the number of inputs and outputs of the system remains unaltered [80].

## 5.4 Control Design Example

The control aeroelastic performance is based on a model of the Great Belt Bridge discussed in Chapters 3 and 4. The flutter and torsional divergence boundaries of the structure are already very high because of the deck's favourable aerodynamic characteristics. In order to provide a meaningful investigation, a longer and more flexible version of the bridge was created. In this respect, the structure's properties presented in Table 3.2 remain unaltered but the main span length was elongated to $L_m = 2400m$ (instead of $1620m$ of the actual bridge). The length of the shortest hanger $h_{e,\min} = 10m$ also remains the same but in order to keep the span to sag ratio constant the cable sag is increased to $f = 260m$ (instead of

180$m$ of the actual structure). In essence, this example assumes upscaling of the main span and towers by 50%, while the deck structural and aerodynamic properties remain constant. The controllable flaps are assumed concentrated about the midpoint of the main span so as to work towards suppressing the critical first flutter mode, which mainly results from the contribution of symmetric vertical and torsional modes. The flaps are considered to be an integral part of the deck as shown in Fig.5.7.

The choice of locating the flap controllers symmetrically about the main span's midpoint aims to target the span-wise locations for which the magnitude of the critical aeroelastic eigenvector near the flutter boundary is maximized. For the first flutter mode, as mentioned, this is expected to be about the mid-span location. In order to validate this assumption, aeroelastic flap performance was compared for the cases when flaps are located in the central span region and when they are placed at alternative locations (e.g. near the supports). The former solution exhibits improved flutter suppression efficiency. A more detailed analysis could potentially treat flap locations as optimization parameters, at of course a higher computational cost. An alternative approach for optimal flap placement could potentially be founded on determining span-wise power-in and power-out regions, as has been demonstrated for the case of vortex induced vibrations on flexible cylinders [191].

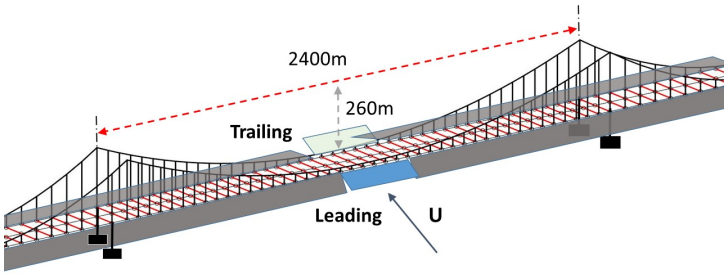


Figure 5.7 Bridge with flaps considered to be an integral part of the deck.

For the investigated bridge case the flutter and divergence speed using the FE thin aerofoil theory framework is estimated at 57$m/s$ and 68$m/s$ respectively, as shown in Fig. 5.8(a). It is also observed that there is a second flutter mode reaching instability at

$73m/s$. Each point on the root-locus diagram corresponds to a system's mode, which can be complex or real, for a given wind speed. Fig.5.8 presents the natural frequency and the damping ratio at selected points along the first instability path.

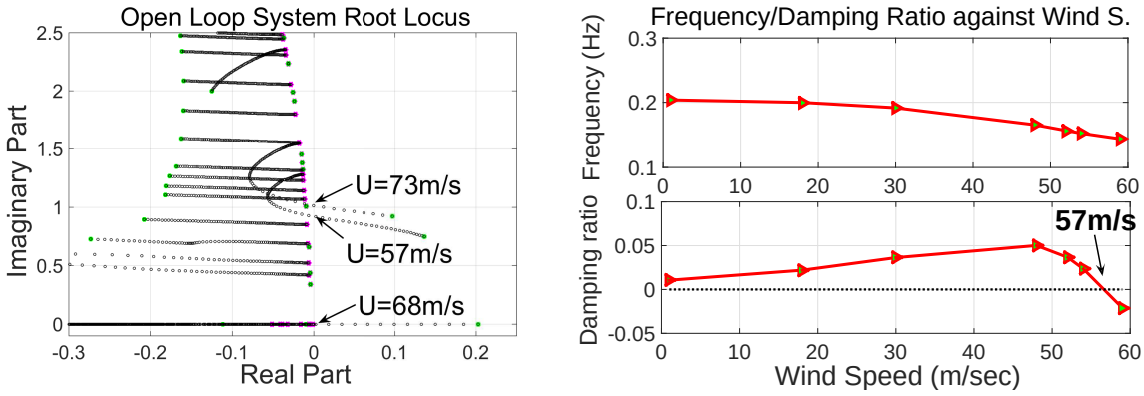


(a) (b)

Figure 5.8 (a) Root locus of the 2400$m$ main span bridge example. The first flutter mode becomes unstable at $57m/s$ and the second one at $73m/s$. The torsional divergence mode reaches instability at $68m/s$. (b) Natural frequency (Hz) and damping ratio for different wind speeds along the first flutter instability path. The system becomes unstable when overall damping becomes negative.

in Fig. 5.8(b) Negative overall damping means that the oscillating structure draws energy from the environment thus resulting to flutter divergent motion, the corresponding wind speed is indicated on the graph. At zero wind speed when aerodynamic contributions are negligible, but not zero due to the non vanishing aerodynamic added mass part, the natural frequency and damping ratio is found to be effectively that of the first torsion mode. Following points in the root locus, for $U > 0m/s$, do not correspond to a pure structural mode due to the airflow effect. By examination of the complex eigenvectors along the instability paths physical insight can be gained with regard to the flutter contributing modes. Fig. 5.9 presents the normalized real part of the torsional and vertical components along the first two flutter paths. It becomes apparent from Fig. 5.9(a) that higher vertical modes contribute near the flutter boundary. The aim of this design exercise is to determine the minimum flap area needed, stretching from the midpoint of the main span symmetrically towards the tower supports, for restoring the stability limits to those of the original structure. The effect of the flap length on the system's robustness margins is also investigated, for

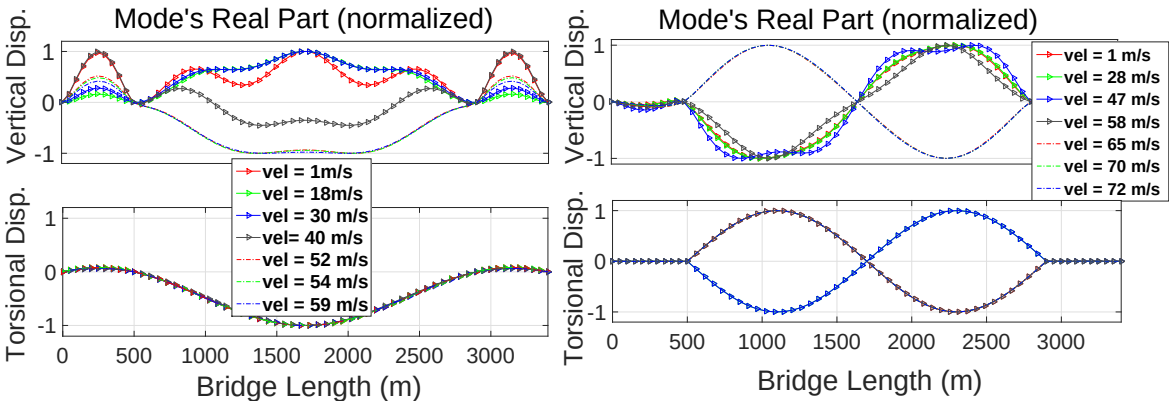


(a) (b)

Figure 5.9 Normalized real part of complex mode shape along the first flutter path (a) and the second flutter path (b).

wind speeds up to $80m/s$. The initial control design investigation follows a simplified procedure. In this case, The structure's equivalent pitch-heave sectional model is used, see Fig. 5.11, and the stabilizing controllers which seek to maximize the system's closed loop coprime robustness are computed. Fig. 5.10(a) presents the robustness index $\gamma$ of the sectional model as a function of wind speed; for the case of the open loop system (no control) as well as for three different control strategies. In all cases, the trailing-and leading edge flap width is chosen to be $3m$ long. The blue crosses correspond to the optimal $H_\infty$ controller, optimized for coprime robustness at every wind speed (adaptive). The resulting controllers are of $9^{th}$ order, size slightly smaller than the $12^{th}$ order plant. Green hexagons indicate the robustness index for suboptimal controllers, designed to have a 10% larger $\gamma$ than the optimal $\gamma$. Again for this case controller computation is performed for each wind speed. To illustrate the system's response to variations, the performance of a low order flap compensator is superimposed in the previous graphs. The assumed control law assumes a first order leading and a second order trailing flap compensator. Although this strategy results to root loci much leftward in the complex plane the associated robustness properties are significantly degraded. It is thus concluded that the distance from the imaginary axis is not a good robustness indicator, as has been suggested in previous studies.

Fig. 5.10(a) demonstrates that, as expected, the robustness index approaches infinity, corresponding to zero robustness, when flutter occurs at $57m/s$ for the open loop system.

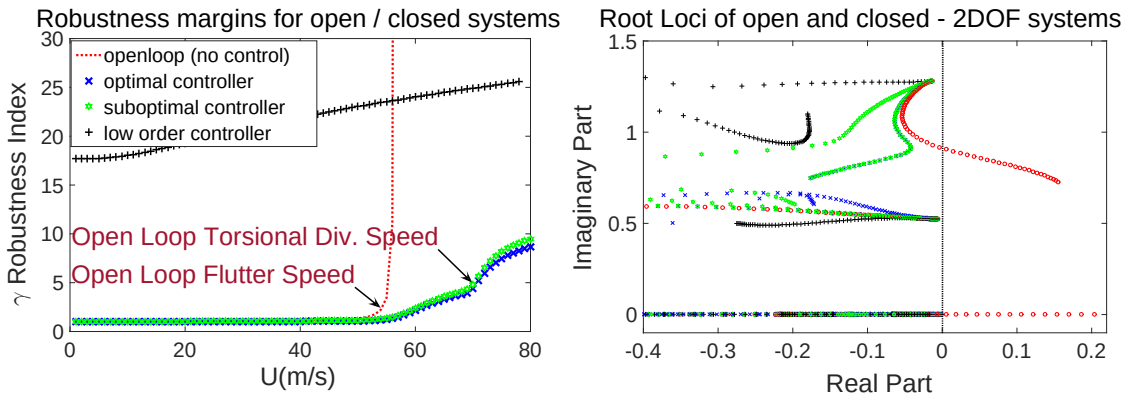


(a) Robustness margins (b) Root loci

Figure 5.10 (a) Robustness index as a function of wind speed for the open loop system and three alternative active control strategies. (b) Corresponding root loci diagrams for the examined control strategies.

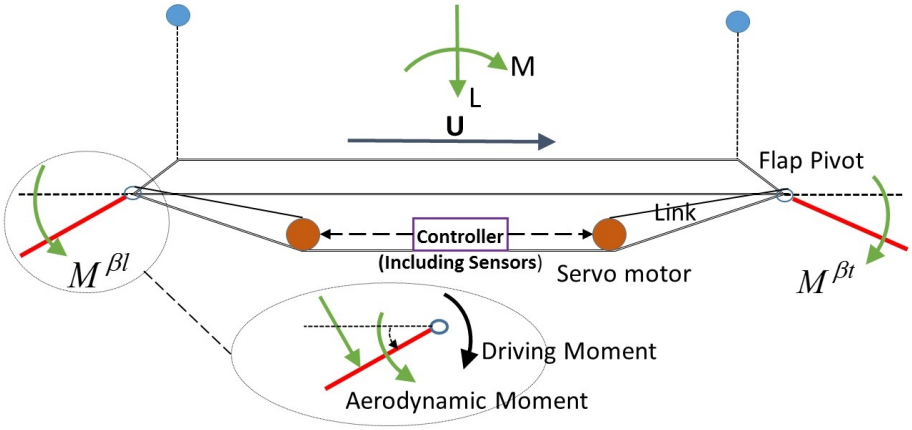


Figure 5.11 Sketch of the practical implementation of the active control system to the bridge deck. The pitch of the deck is monitored and the control signals are transmitted to the servo motors which determine the rotation angles of the leading and trailing flaps.

Moreover, the performance of the optimal and suboptimal controllers is very similar and both control approaches achieve good margins up to $67-68m/s$, before the torsional divergence aerostatic boundary is reached. However, system stabilization above the torsional divergence critical wind speed inflicts a significant toll on robustness performance. The corresponding root-loci indicate that all closed loop systems are stable up to the designed wind speed of $80m/s$, but simultaneously achieving good robustness margins appears to be a much more challenging objective.

Following the sectional analysis, the simplified control law is implemented into the FE bridge aeroelastic model. In this form, the controller matrix has a diagonal structure and

the same control law is applied to all the leading and trailing edge flaps respectively. The system outputs are the rotations of deck elements and the system inputs are the pitches from the associated flaps. Fig. 5.12(a) presents the robustness indices of the FE bridge model with flaps along the full length, half-length and quarter-length of the 2400$m$ main span. It is easily observed that the controller designed on the section model exhibits poor robustness margins when applied to the full bridge. It is evident that the system loses robustness rapidly for the case when only the 25% of the span is equipped with flaps, while for longer flap surfaces an abnormal spike is observed indicating poor behaviour at specific wind speeds.

The closed loop system robustness investigation using the sub-optimal sectional control law is presented in Fig. 5.12(b). In this case much smoother behaviour is attained, while deviation from strict optimality yields no significant loss in performance. Moreover, sub-optimal controller design is less computationally demanding. Flaps along 50% of the span's length have closely comparable performance to the case when flaps are placed along the entire length. When the wind speed approaches the second flutter instability boundary, $73m/s$, the control law based on a sectional model becomes highly ineffective (robustness index becomes infinite). This is not surprising as the second flutter mode results from the contribution of modes absent from the controller design sectional analysis, only including the first heave and pitch modes. Following the above simplified analysis, a more rigourous control investigation is followed, in which the design procedure is applied directly on the FE model. Different flap length variations extending from the bridge's midpoint are considered. Fig. 5.12(c) presents the coprime robustness indices for those cases. In this modelling example the main span is modelled using 37 elements (about 65$m$ width each). It is worth stressing that Fig. 5.12(c) summarizes the best achievable results for enhancing the aeroelastic performance for the chosen model, and quantifies the effectiveness of using trailing/leading-edge flaps while retaining good coprime robustness margins. The control law is re-computed for every wind speed, which in conjunction with the system's high state dimension makes the analysis a time consuming endeavour. The bridge-flap configuration

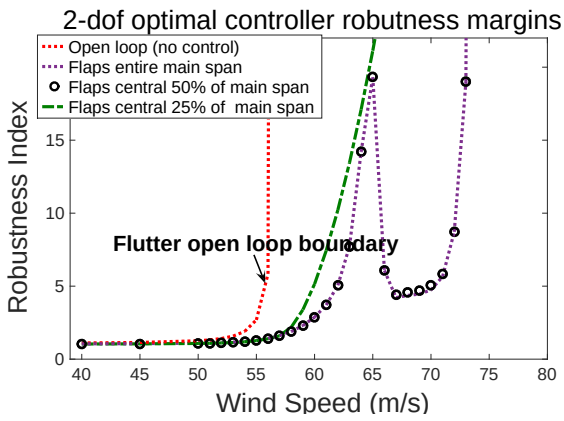


(a) Sectional model

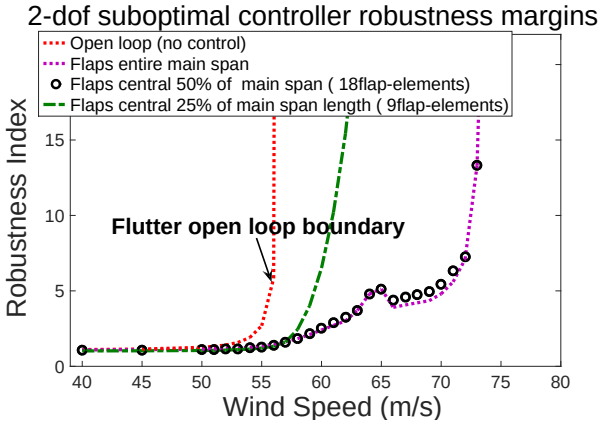


(b) Sectional model

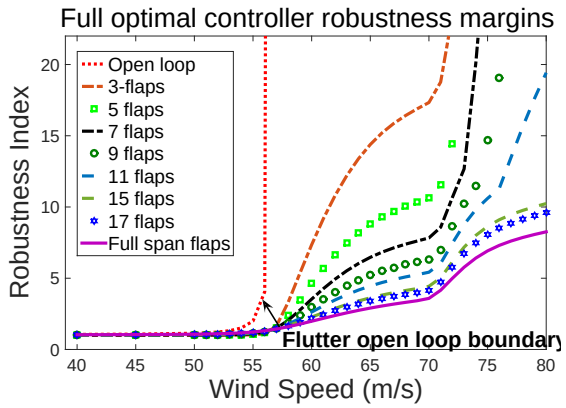


(c) FE model

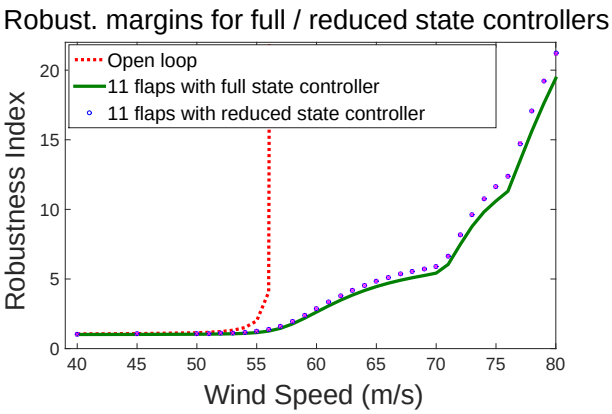


(d) FE model

Figure 5.12 Coprime robustness index of the full FE model as a function of wind speed. (a) Optimal controller designed on the sectional model. (b) 10%-suboptimal controller designed on the sectional model. (c) Optimal controller designed on the full FE model. (d) Reduced order optimal controller designed on the full FE model.

involving 11 flaps, approximately 30% of the main span length, appears to be a reasonable choice as the aerodynamic instability limit is increased up to $70m/s$ with a robustness index $\gamma \approx 5$. Achieving good robustness above the open loop divergence speed and the second flutter mode proves to be very difficult, with a reasonable flap width, even when the entire span length is covered with such controllable surfaces.

The FE based controller design procedure results in a very high order control law, which would no doubt prove difficult to implement in practice. It is thus of important to implement a reduced order approximation, preferably with little sacrifice in performance. Several reduction procedures exist and for the task at hand we perform a truncation operation to the balanced realization of the state space representation of the optimal controller matrix,

[80, 176]. Given the chosen reduction procedure the controller size can be substantially reduced, (from 400+ to 20 states), while achieving a negligible loss in performance; Fig. 5.12(d) makes a comparison of the closed-loop system robustness when full state and reduced order controllers are used.

## 5.5 Frequency and Time Domain Simulations

In the frame of this design exercise time simulations at different wind speeds are performed for the case when approximatively 30% of the main span is controlled (11 leading and 11 trailing edge flaps). Consequently, the resulting controller matrix size is 11 by 22, 11 deck pitch inputs and 22 flap angle outputs. Fig. 5.13 presents the magnitudes of the frequency response, bode plots, for 4 of the 242 entries of the control matrix; more specifically these are related to the leading- and trailing-edge flap motion from the pitch of the leftmost element, and to the leading- and trailing-edge flap motion from the pitch of the middle element. Different wind speeds are considered for presentation namely: $55m/s$ (below the first open loop critical flutter speed), $62m/s$ (above the first critical flutter speed and below the torsional divergence speed), $70m/s$ (above the torsional divergence and below the second critical flutter speed) and $77m/s$ (above the second critical flutter speed). The $20^{th}$ state, reduced order, controller is superimposed to the full size controller, showing once again that the two are almost identical in the spectrum of frequencies of interest.

Fig. 5.14 presents the maximum magnitudes of the controller matrix for the two highest wind speeds considered: $70m/s$ and $77m/s$. It is interesting to note that at $70m/s$ the flaps in the middle have slightly higher gains than the flap in the edges. Also the magnitudes of the trailing flaps are larger than those of the leading flaps, translating to larger maximum pitch angles for the trailing flaps. On the contrary at wind speed $U = 77m/s$ one can observe an asymmetric distribution of magnitudes. This behaviour can be attributed to the flap controller effort to simultaneously suppress the first and second flutter modes, which result from the first symmetric and first antisymmetric torsional modes respectively.

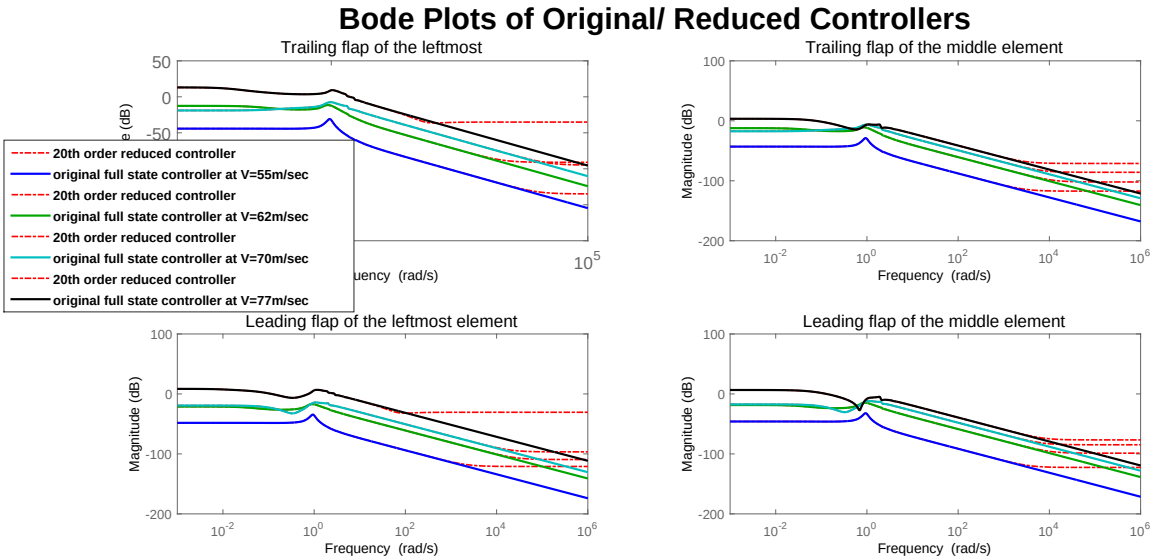


Figure 5.13 Transfer functions related to four of the $22 \times 11$ entries of the control matrix: leftmost leading- and trailing-edge flap motion from the pitch of the leftmost element, and middle leading- and trailing-edge flap motion from the pitch of the middle element.

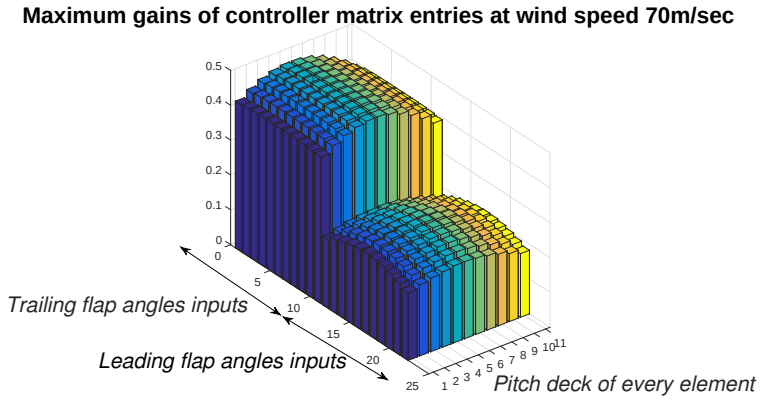


(a) $70m/s$

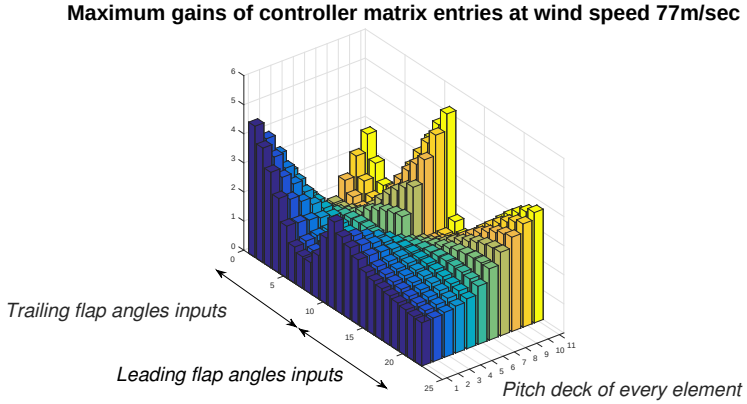


(b) $77m/s$

Figure 5.14 Maximum magnitudes of the $22 \times 11$ transfer functions of the reduced order controller matrix for wind speeds of $70m/s$ (a) and $77m/s$ (b)

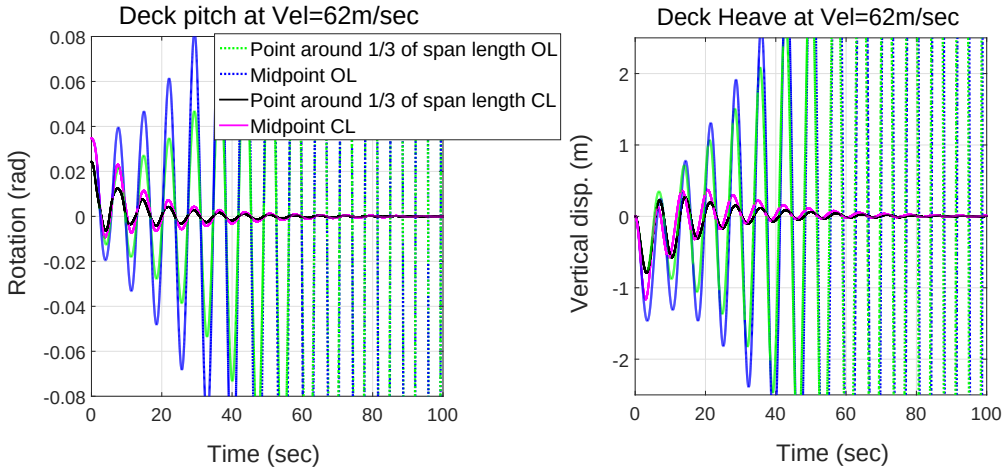


(a) $62m/s$

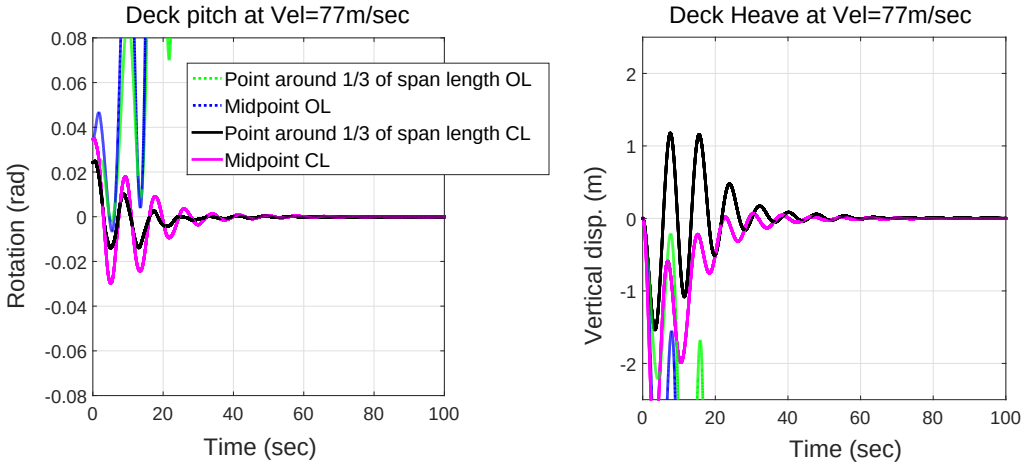


(b) $77m/s$

Figure 5.15 Deck's Pitch and Heave transient response at wind speed of $62m/s$ (a) and $77m/s$ (b) for the open-loop (no controller) and closed-loop system, case 11 flaps around the middle (30% of the whole span), reduced order controller.

Fig. 5.15 presents the flap control effectiveness in the time domain at wind speeds $U = 62m/s$ and $U = 77m/s$. The bridge-flap system's initial motion is triggered by an initial displacement condition of sinusoidal twisting/pitch of the main span. The maximum value of this displacement snapshot is assumed at the midpoint having a rotation angle of $2^o = 0.035rad$. The transient response of the deck's heave and pitch is presented at two locations (middle and one third span) for the case of the open-loop system (flaps are frozen), and the closed-loop controlled system. The controlled system as before assumes 11 active flaps around the span's midpoint (30% of the whole span). For $U = 62m/s$ the uncontrolled bridge diverges by exhibiting an oscillatory motion, characteristic of flutter instability. For

$U = 77m/s$ the uncontrolled system demonstrates a more violent instability behaviour, culminating from the combination of flutter and torsional divergence. It should be stressed that this fictitious simulation produces the worst case scenario, because it assumes that the flap controllers are switched on at a high wind speed given the assumed initial condition. In reality the controllers would already be functioning at lower wind speeds thus preventing the deck pitch from reaching large values.

The movement of the flaps with regard to the deck pitch is shown in Fig. 5.16, for the same wind speeds and initial conditions as in the previous simulation case. Rotations of the leading and trailing flaps at three different locations are presented (leftmost edge flap, middle flap, midway flap on the right). The presented time history graphs give insight into the flap behaviour for suppressing deck motion. At $U = 62m/s$ (and in general for all wind speeds lower than the second flutter speed) a comparable behaviour between the movement of the trailing and leading flaps can be observed, showing that potentially the same control law can be applied for all flaps along the span without considerable loss in performance. On the other hand, for $U = 77m/s$ this is not the case when differences in flap responses can be observed.

The flap response simulation as well as the presented controller magnitude plots indicate that flap rotations are restricted below $10^o$. Of course the magnitude of the flap response depends on the chosen initial conditions selected. However, from the transfer function magnitudes it can be concluded that for wind speeds up to $80m/s$ the flap rotation does not exceed $15^o$ given a maximum deck pitch initial condition of $2^o$. This consists of an important observation because larger flap rotations would be responsible for causing flow separation, which would threaten the theoretical foundation of thin aerofoil theory. Deck bluffness can however lead to a further complication associated with the use of trailing edge flaps. This is associated with the flow separation caused by the deck affecting the performance of the trailing flaps. In [78] it was indeed concluded that a 2 to 3 times larger flap pitch magnitude is required than the one computed by thin aerofoil theory. This

behaviour however, did not undermine the controller's effectiveness as the flap pitch never exceeded $6^o$ in the experimental investigation.

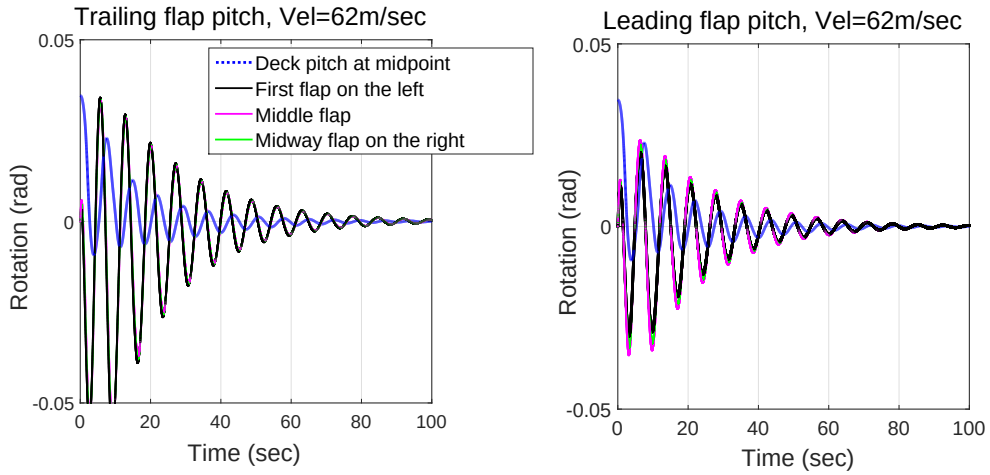


(a) $62m/s$

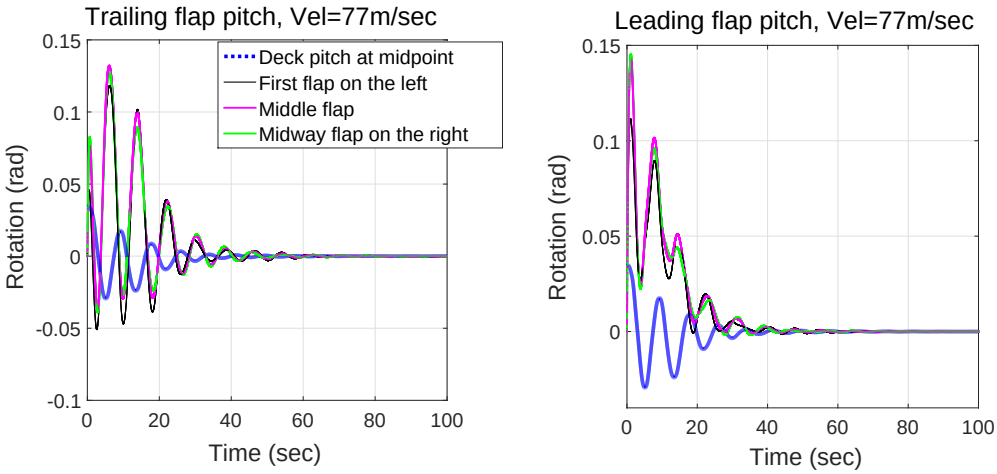


(b) $77m/s$

Figure 5.16 Flap angles transient response at wind speed of $62m/s$ (a) and $77m/s$ (b) at three different locations, case 11 flaps around the middle (30% of the whole span). The reduced order controller's were used in this computation.

## 5.6 Discussion and Concluding Remarks

This chapter addressed the issue of employing the developed finite element bridge aeroelastic framework to examine the effectiveness and limitations of the proposed active bridge-flaps system. The adopted approach makes use of a transformation from the wing-aileron-tab to the flap-deck-flap configuration in order to express the aerodynamic influence on

the deck resulting from flap angle rotations. The feedback control configuration assumes the flap angles as inputs, whereas the rotations at the corresponding deck elements are the system outputs. This approach dispenses the need of physically modelling the flap surfaces or considering the aerodynamic loading on them.

In the control part of this work $H_\infty$ control theory was employed to tackle the robust stabilization of the unstable bridge at high wind velocities. This novel approach successfully quantifies structural and aerodynamic uncertainty and answers questions related to the applicability of a control strategy based on controllable winglets. It was demonstrated that, although the stabilization of the system can be achieved in a straight forward manner, the controlled system loses robustness rapidly for wind speeds above the torsional divergence aerostatic boundary. This is an important result that sets a qualitative limit for the performance of all flap-controllers. For the chosen bridge example however, based on the Great Belt Bridge, it was shown that a significant increase in the structure's aeroelastic limits with good robustness margins can be achieved when 30% of the main span's total length is controlled.

The presented framework however is laced with drawbacks undermining its implementation in real applications; firstly power driven motors and sensors are required. Secondly, the effective control use is based on an adaptive scheme where controller matrix is recomputed at each wind speed. Thirdly, the resulting controller transfer functions are of very high order, although automatic model reduction techniques can significantly reduce their order. The remaining chapters will focus on addressing these issues by proposing low order mechanical flap compensators, which based on an optimization approach will provide viable alternatives.

# Chapter 6

# Passive Control of a Sectional Model with Tuned Mass Dampers and Movable Flaps

## 6.1 Introduction

The analysis presented in this chapter will focus on ways to passively suppress flutter and torsional divergence. The main characteristic of a passive mechanical feedback is that the flaps can be powered by the deck's motion rather than an external power source. The advantages of this approach is that they are realizations of simpler low-order controllers, when compared to active control strategies. In principle, passive systems should be easily implementable and require little to no servicing. However most importantly, they eliminate the need for a powered computer control system; a commodity that is likely to fail during stormy weather conditions when aeroelastic instabilities are most likely to occur.

The analysis presented here will make a step backwards in terms of structural complexity to concentrate on a sectional heave-pitch bridge model interacting with a constant velocity airstream. This will aid in examining in depth the effectiveness and applicability of the proposed control mechanisms before progressing to their implementation in a full mode aeroelastic model. Two different strategies are considered, separately and in combination.

The first makes use of trailing and leading flaps adjacent to the bridge deck, the motion of which is triggered by the deck's movement through a combination of springs, dampers and inerters at the hinged connection. Emphasis is placed on the effect of the flap hinge location and an optimization procedure is used for determining the compensator parameters that result in favourable aeroelastic properties. The second approach reexamines the efficacy and limitations of using tuned mass dampers (TMDs) placed inside the bridge deck for controlling self-excited motion. We conclude the investigation by combing these two approaches through the introduction of a kinematic constraint between the TMD masses and the flaps. This combined mechanical system, referred to as the flap mass damper (FMD), combines favourable aerodynamic properties of the flaps with a driving force provided by the vibrating mass. This approach has the advantage of not requiring complex and often impractical linkages for transmitting deck motion to the flaps. Special attention is given to ensuring that the passive control system attains optimum robustness properties and maximizes tolerance to uncertainties. Uncertainties are quantified in a series of simulations showing how the alteration of the bridge's natural frequencies affect the stability of the closed loop system. The Humber Bridge in the U.K. is chosen as an example for the numerical simulations.

The chapter is organized as follows: The first part of the analysis examines the aerodynamic modelling of a bridge deck section with leading- and trailing-edge flaps, four degrees of freedom in total. As opposed to the preceding analysis, an unavoidable difficulty in modelling a passive mechanism is that flap torques rather than flap angles are the control inputs to the system. Hence, flap degrees of freedom need to be independently incorporated in the model. The system's aerodynamic modelling is again based on thin aerofoil theory and the transformation of the Theodorsen-Garrick wing-aileron-tab mechanism, the difference to the aerodynamic model of Chapter 5 being that aerodynamic forces on the flaps are also included. The mechanical feedback control system, described in section 6.3, determines the torques acting on the flaps by a configuration of springs, dampers and inerters for different hinge positions. Section 6.4 examines the effectiveness of using a single TMD for

improving the aeroelastic boundaries, whereas section 6.5 introduces the flap mass damper mechanism and examines its effectiveness in achieving robust stabilization of the system.

## 6.2 Dynamic Model of the Deck-Flap Passive System

This section will formulate the deck-flaps system structural dynamics and derive the aerodynamic moments on the deck and flaps. The components of the system model are described as follows.

### 6.2.1 Deck-Flap Structural Model

The kinematic model of the deck-flap system is assumed to have four degrees of freedom, Fig. 6.1. These freedoms include the deck's pitch angle $\alpha$, the deck's heave $h$ with respect to the elastic centre, and the leading-and trailing-edge flap angles $\beta_l$ and $\beta_t$. Sway motion of the deck and main cables as well as changes in the hanger length are neglected. Given

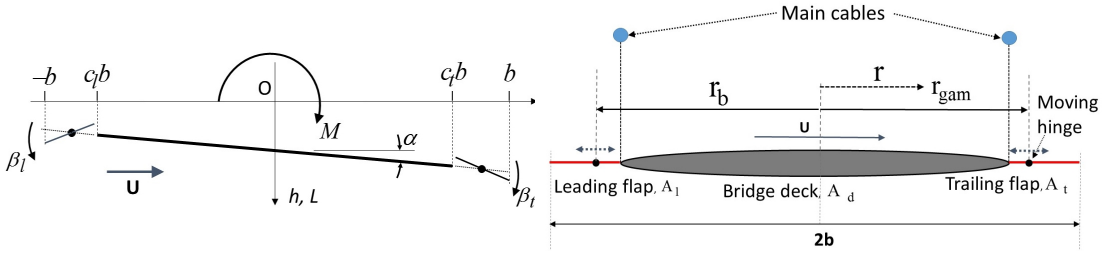


(a) (b)

Figure 6.1 (a) Kinematic model of the bridge deck. The wind velocity $U$ is assumed positive to the right, the heave $h$ and lift force $L$ are assumed positive downwards, the moment $M$ is positive clockwise, as are the pitch and trailing-edge flap angles $\alpha$ and $\beta_t$ respectively. The leading-edge flap angle $\beta_l$ is positive anti-clockwise. The deck chord (including the flaps) is $2b$. The leading- and trailing-edge flap chords are $(1+c_l)b$ and $(1-c_t)b$ respectively; note that $c_l$ is a negative quantity. (b) Bridge deck-flap system notation.

the introduced notation of Fig. 6.1 the kinetic energy of the system, $T$, can be derived from the separate contributions of the deck, the leading and the trailing flaps. These are denoted as $T_d$, $T_l$ and $T_t$ respectively.

$$T = T_d + T_l + T_t \tag{6.1}$$

where,

$$T_d = \frac{1}{2}\int_{A_d}\left(\dot{h}+r\dot{\alpha}\right)^2 dm \tag{6.2}$$

$$T_l = \frac{1}{2}\int_{A_l}\left[\dot{h}+r\dot{\alpha}-(r-r_b)\dot{\beta}_l\right]^2 dm \tag{6.3}$$

$$T_t = \frac{1}{2}\int_{A_t}\left[\dot{h}+r\dot{\alpha}+(r+r_{gam})\dot{\beta}_t\right]^2 dm \tag{6.4}$$

$A_d$, $A_l$, $A_t$ are the cross section areas of the deck, leading and trailing flap respectively. The above integral computations are carried through by means of defining the following identities

$$S_\alpha = \int_{A_d+A_l+A_t} r dm, \quad S_\beta = -\int_{A_l}(r-r_b)dm \text{ and } S_\gamma = \int_{A_t}(r-r_{gam})dm. \tag{6.5}$$

The subscripts $\alpha, \beta, \gamma$ designate the whole deck, and the leading- and trailing-edge flaps respectively.

$$I_\alpha = \int_{A_d+A_l+A_t} r^2 dm, \quad I_\beta = \int_{A_l}(r-r_b)^2 dm, \text{ and } I_\gamma = \int_{A_t}(r-r_{gam})^2 dm. \tag{6.6}$$

$m$ is the total mass, $S_\alpha$ the first order moment of inertia of the deck-flap system, $S_\beta$ and $S_\gamma$ are the first order moments of inertia of the leading and trailing flaps about their hinges. $I_\alpha$ is the second order moment of inertia of the deck-flap system about the deck elastic center, $I_\beta$ and $I_\gamma$ are the second order moments of inertia of the leading and trailing flaps about their hinges, respectively. Similarly the potential energy of the system can be expressed as follows

$$V = \frac{1}{2}K_h h^2 + \frac{1}{2}K_\alpha \alpha^2 + \frac{1}{2}K_\beta \beta_l^2 + \frac{1}{2}K_\gamma \beta_t^2. \tag{6.7}$$

Where, $K_h$, $K_\alpha$, $K_\beta$ and $K_\gamma$ are the stiffness coefficients of the associated degrees of freedom. Also the damping forces depending on the velocities can be expressed through the following dissipation function

$$F = \frac{1}{2}C_h \dot{h}^2 + \frac{1}{2}C_\alpha \dot{\alpha}^2 + \frac{1}{2}C_\beta \dot{\beta}_l^2 + \frac{1}{2}C_\gamma \dot{\beta}_t^2. \tag{6.8}$$

Given the above quantities, Lagrange's generalized coordinate framework can be adopted to derive the system's equation of motion. More details in this procedure can be found in books such as [135].

$$\text{Deck-lift} : m\ddot{h} + S_\alpha \ddot{\alpha} + S_\beta \ddot{\beta}_l + S_\gamma \ddot{\beta}_t + C_h \dot{h} + K_h h = L \tag{6.9}$$

$$\text{Deck-moment} : S_\alpha \ddot{h} + I_\alpha \ddot{\alpha} - (I_\beta - bc_l S_\beta)\ddot{\beta}_l + (I_\gamma + bc_t S_\gamma)\ddot{\beta}_t + C_\alpha \dot{\alpha} + K_\alpha \alpha = M \tag{6.10}$$

$$\text{Leading-flap moment} : S_\beta \ddot{h} - (I_\beta - bc_l S_\beta)\ddot{\alpha} + I_\beta \ddot{\beta}_l + C_\beta \dot{\beta}_l + K_\beta \beta_l = M^{\beta_l} + M_c^{\beta_l} \tag{6.11}$$

$$\text{Trailing-flap moment} : S_\gamma \ddot{h} + (I_\gamma + bc_t S_\gamma)\ddot{\alpha} + I_\gamma \ddot{\beta}_t + C_\gamma \dot{\beta}_t + K_\gamma \beta_t = M^{\beta_t} + M_c^{\beta_t} \tag{6.12}$$

$\zeta$ is the damping ratio per unit length, and the subscripts $h$ and $\alpha$ designate the heave and torsional motions respectively. The flap break points are at $c_l$b and $c_t$b, where $c_l < 0$ and $c_t > 0$. For a given bridge, the heave and torsional resonant frequencies $\omega_h$ and $\omega_\alpha$ are assumed known. The corresponding stiffnesses are computed as $K_h = m\omega_h^2$ and $K_a = I_\alpha \omega_\alpha^2$. The flap frequencies $\omega_\beta$ and $\omega_\gamma$ are similarly computed using $K_\beta = I_\beta \omega_\beta^2$ and $K_\gamma = I_\gamma \omega_\gamma^2$. Similarly, the damping terms are computed by: $C_h = 2\zeta_h \omega_h m$, $C_a = 2\zeta_\alpha \omega_a I_a$, $C_\beta = 2\zeta_\beta \omega_\beta I_\beta$ and $C_\gamma = 2\zeta_\gamma \omega_\gamma I_\gamma$. The aerodynamic lift and moment on the bridge deck are given by $L$ and $M$ respectively. The aerodynamic moments $M^{\beta_l}$ and $M^{\beta_t}$ act, respectively, around the leading- and trailing-edge flap hinges. The flap control torques are given by $M_c^{\beta_l}$ and $M_c^{\beta_t}$. The per unit span masses of the flaps are computed as follows

$$m_\beta = b(1 + c_l)\rho_f d_f, \quad m_\gamma = b(1 - c_t)\rho_f d_f. \tag{6.13}$$

The modelling presented in this chapter is based on a sectional model of the Humber Bridge. The parameters used in conjunction with Section 3.3.3 are presented in Table 6.1. $\rho_f$ and $d_f$ are the flaps density and thickness respectively.

| Parameters | Values |
|---|---|
| $b$ | $14.25\,m$ |
| $m$ | $13215\,kg$ |
| $I_a$ | $1.05\times10^6\,kg\,m^2$ |
| $\omega_\alpha$ | $1.973\,rad/s$ |
| $\omega_h$ | $0.767\,rad/s$ |
| $\rho$ | $1.23\,kg/m^3$ |
| $\rho_f$ | $7850\,kg/m^3$ |
| $d_f$ | $0.025\,m$ |
| $\zeta_h$ | 0.01 |
| $\zeta_\alpha$ | 0.01 |

Table 6.1 Parameters of the Humber Bridge sectional model including flaps.

### 6.2.2 Deck-Flap Aerodynamic Model

Following the thin aerofoil theory assumption, the aerodynamic lift ($L$) and aerodynamic moments $M$, $M^{\beta_l}$ and $M^{\beta_t}$ in equations (6.9)-(6.12) are based on the Theodorsen and Garrick expressions [187]. The transformation presented in the preceding chapter, Fig. 5.1, is again employed for the computation of the lift and moments acting on the deck and flaps. These can be expressed in the following matrix form

$$\mathbf{F}_{se} = \mathbf{M}_{nc}\ddot{q} + \mathbf{C}_{nc}\dot{q} + \mathbf{K}_{nc}q + \Xi_C. \tag{6.14}$$

where, $\mathbf{q}$ is the position vector defined as $\mathbf{q} = \{h, \alpha, \beta, \gamma\}^T$. The equations of motion of the sectional model (4-DOF deck-flap assembly), given by equations (6.9)-(6.12) combined with the aerodynamic forces given in Eq.(6.14) can be expressed in the following state space form

$$\begin{bmatrix} 0 & \mathbf{M}-\mathbf{M}_{nc} \\ \boldsymbol{I} & 0 \end{bmatrix} \begin{bmatrix} \dot{\mathbf{q}} \\ \dot{\mathbf{q}}_v \end{bmatrix} = \begin{bmatrix} -\mathbf{K} & -\mathbf{C}+\mathbf{C}_{nc} \\ 0 & \boldsymbol{I} \end{bmatrix} \begin{bmatrix} \mathbf{q} \\ \mathbf{q}_v \end{bmatrix} + \Xi_C. \tag{6.15}$$

where, $\mathbf{q}_v$ is the velocity vector defined as $\mathbf{q}_v = \{\dot{h}, \dot{\alpha}, \dot{\beta}, \dot{\gamma}\}^T$. Eq.(6.15) is of the same form as Eq.(4.54) with the difference being that because of the flap modelling, the structural and aerodynamic expressions are more complicated. Also in this case, the flap hinge locations are not fixed at the flaps break points (edge of the deck), but are free to move within the

length of the flaps, see Fig. 6.1. Similarly to the 2-dof case by introducing the state vector $\mathbf{x} = \{\mathbf{q}, \mathbf{q}_v\}^T$, Eq.(6.15) can be expressed in the form

$$\mathbf{E}_c \dot{\mathbf{x}} = \mathbf{A}_c \mathbf{x} + \Xi_C. \tag{6.16}$$

$\Xi_C$ represents the circulatory aerodynamic loading depending on the irrational function $C(k)$, [79]. The derivation of the non-circulatory matrices $\mathbf{M}_{nc}, \mathbf{C}_{nc}, \mathbf{K}_{nc}$ for the deck-flap system is based on the wing-flap-tab combination proposed in [187]. The non-circulatory aerodynamic loading of the latter is presented in the following compact matrix form.

$$\boldsymbol{M}_a = \rho b^4 \begin{bmatrix} -\frac{\pi}{b^2} & \frac{\alpha\pi}{b} & \frac{-T_4(c_l)l + T_1(c_l)}{b} & \frac{-T_4(c_t)m + T_1(c_t)}{b} \\ & \pi\alpha^2 - \frac{\pi}{8} & -T_{24}(c_l)l - 2T_{13}(c_l) & -T_{24}(c_t)m - 2T_{13}(c_t) \\ sym & & \frac{l^2 T_5(c_l) - 2lT_2(c_l) + T_3(c_l)}{\pi} & \frac{mY_1(c_l,c_t) - lY_3(c_l,c_t) - Y_4(c_l,c_t) + Y_6(c_l,c_t)}{\pi} \\ & & & \frac{m^2 T_5(c_t) - 2mT_2(c_t) + T_3(c_t)}{\pi} \end{bmatrix} \tag{6.17}$$

$$\boldsymbol{C}_a = \rho b^3 U \begin{bmatrix} 0 & -\frac{\pi}{b} & \frac{2l\sqrt{-c_l^2+1} + T_4 c_l}{b} & \frac{2m\sqrt{-c_t^2+1} + T_4 c_t}{b} \\ 0 & \alpha\pi - \frac{\pi}{2} & -T_{23}(c_l)l - T_{16}(c_l) & -T_{23}(c_t)m - T_{16}(c_t) \\ 0 & -T_{25}(c_l)l - T_{17}(c_l) & \frac{-T_{29}(c_l)l^2 - T_{27}(c_l)l - T_{19}(c_l)}{\pi} & \frac{-Y_{16}(c_l,c_t)lm - Y_{12}(c_l,c_t)l - Y_{14}(c_l,c_t)m - Y_{10}(c_l,c_t)}{\pi} \\ 0 & -T_{25}(c_t)m - T_{17}(c_t) & \frac{Y_{24}(c_l,c_d)m - Y_{22}(c_l)l - Y_{20}(c_l,c_t)m - Y_{18}(c_l,c_t)}{\pi} & \frac{-T_{29}(c_t)m^2 - T_{27}(c_t)m - T_{19}(c_t)}{\pi} \end{bmatrix} \tag{6.18}$$

$$\boldsymbol{K}_a = \rho b^2 U^2 \begin{bmatrix} 0 & 0 & 0 & 0 \\ 0 & 0 & -T_{22}(c_l)l - T_{15}(c_l) & -T_{22}(c_t)m - T_{15}(c_t) \\ 0 & 0 & \frac{-T_{28}(c_l)l^2 - T_{26}(c_l)l - T_{18}(c_l)}{\pi} & \frac{-Y_{15}(c_l,c_t)lm - Y_{11}(c_l,c_t)l - Y_{13}(c_l,c_t)m - Y_9(c_l,c_t)}{\pi} \\ 0 & 0 & \frac{-Y_{23}(c_l,c_t)lm - Y_{21}(c_l,c_t)l - Y_{19}(c_l,c_t)m - Y_{17}(c_l,c_t)}{\pi} & \frac{-T_{28}(c_t)m^2 - T_{26}(c_t)m - T_{18}(c_t)}{\pi} \end{bmatrix} \tag{6.19}$$

$T_{ij}(\cdot)$'s and $Y_{ij}(\cdot,\cdot)$'s are presented in Appendix C. The parameters $l, m$ determine the position of the leading and trailing flap hinges respectively within the flaps[187]. Conver-

sion of this aerodynamic framework to the leading flap-deck-trailing flap combination is accomplished though the following transformation matrix $\mathbf{V}$

$$\mathbf{M}_{nc} = \mathbf{V}^T\mathbf{M}_a\mathbf{V},\ \ \mathbf{C}_{nc} = \mathbf{V}^T\mathbf{C}_a\mathbf{V},\ \ \mathbf{K}_{nc} = \mathbf{V}^T\mathbf{K}_a\mathbf{V},\ \ \mathbf{V} = \begin{bmatrix} 1 & 0 & c_l b & 0 \\ 0 & 1 & -1 & 0 \\ 0 & 0 & 1 & 0 \\ 0 & 0 & 0 & 1 \end{bmatrix}. \tag{6.20}$$

The inputs $\Xi_C$ as described in Section 4.3.2 can be approximated by a rational function [17, 15, 79]. In this framework $C(s)$ is a transfer function that receives structural responses $y = \mathbf{Q}_T$ as inputs, and generates an output $\tilde{y}$, which is translates into lift forces and moments by the matrix $\mathbf{B}$, Fig. 4.6. The same fourth order approximation is used for the Theodorsen function.

$$\mathbf{Q}_T = \dot{h} + Ua + \frac{1}{2}b\dot{a} + (\frac{1}{\pi}T_{10}(c_l)U - U)\beta + (\frac{1}{2\pi}T_{11}(c_l)b + c_l b - \frac{1}{2}b)\dot{\beta} + \frac{1}{\pi}T_{10}(c_t)U\gamma + \frac{1}{2\pi}T_{11}(c_t)b\dot{\gamma} \tag{6.21}$$

$$\mathbf{B} = \begin{bmatrix} -2\pi\rho Ub & \pi\rho Ub^2 & -(\pi + T_{12}(c_l) + 2\pi c_l)\rho Ub^2 & -T_{12}(c_t)\rho Ub^2 & 0 & 0 & 0 & 0 \end{bmatrix}^T \tag{6.22}$$

## 6.3 Deck-Flap Mechanical Feedback System

This section formulates the feedback control configuration of the deck-flaps system. Because this is constrained to be comprised solely from passive components, modelling the flap mass is necessary in order to satisfy the passivity constraint. In this configuration the flap torques are the controllable inputs to the system. The controller objective is again to maximize the system's closed loop robustness to coprime factor perturbation, as presented in Chapter 5. To this end, two controller configurations are considered; the first consists of a simple spring and damper on the deck-flap hinged connection. The second, assumes an additional mechanical network in parallel to these retention components. It is found that

the location of the deck-flap hinge, when accompanied by an optimization of the retention components, greatly improves the controlled system's stability properties. in Sec. 6.3.6, the passive flap mechanism's performance in the time domain is compared to the active control framework, as presented in Chapter 5.

### 6.3.1 Feedback Configuration

The block diagram of the bridge control system shown in Figure 6.2 demonstrates the interconnection of structural dynamics, fluid dynamics and the flap control system. The uncontrolled system is described by the plant $P_{NC}(s)$ which contains the structural dynamics and the non-circulatory part of the fluid mechanics, while the Theodorsen function approximation $C(s)$ generates the circulatory flow. The controllers for the leading- and trailing- edge flaps are $K_l(s)$ and $K_t(s)$ respectively and generate the flap torques, $M_c^{\beta_l}$ and $M_c^{\beta_t}$, from flap velocities, $\dot{\beta}_l$ and $\dot{\beta}_t$. Diagrams of this type are standard in control systems and can be used to asses both nominal and robust stability; more detail on linear fractional representations of control systems is available in books such as [80].

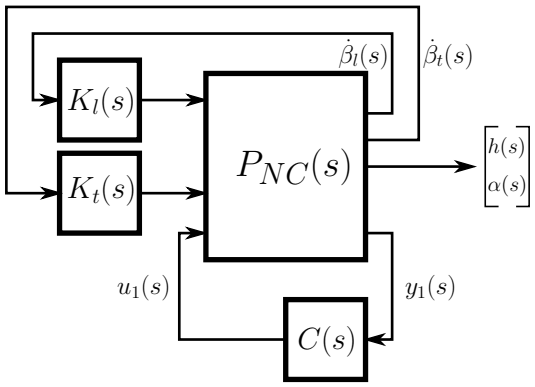


Figure 6.2 Block diagram of the aeroelastic control system. The dynamics of the bridge and non-circulatory fluid mechanics are represented by the plant $P_{NC}(s)$, with the Theodorsen circulation function approximation is given by $C(s)$. The controllers for the leading- and trailing- edge flaps are given by $K_l(s)$ and $K_t(s)$ respectively, and generate the flap torques. The bridge deck's heave and pitch response are given by $h(s)$ and $\alpha(s)$ respectively.

The initial feedback control investigation will implement a standard mechanical layout, comprising of a spring and a damper at the hinged connection of the leading and trailing

flaps. Initially, three flap pivot configurations are considered, shown schematically in Fig. 6.3. The flap width is considered constant, $2.75m$, and an internal part of the walkways, with width of $3.25m$, Fig. 3.6.

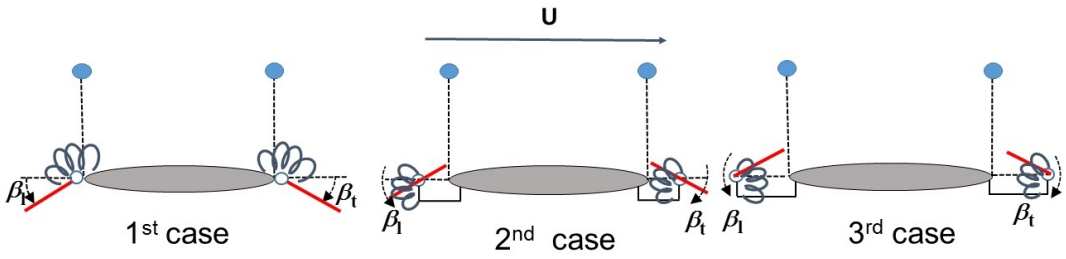


Figure 6.3 Three configurations of flap hinge location.

The procedure for designing the mechanical elements at the flap pivot is based on a constrained optimization procedure. The objective of the process is to maximize the robust stability margins in a sense to be described. The higher the stability robustness margin, the larger the uncertainties (e.g. variations in the model and/or in its parameters) under which the controlled system can maintain stable. A key assumption in modelling of the feedback system is that the uncertain part of the process is considered separate from the known nominal model of the process. This is referred to as unstructured uncertainty and does not relate to specific mechanical components or system parameters [132]. In this analysis we will again make use of the left normalised coprime factor description of the plant [132, 80] as the basis for the robust stability optimisation process for the reasons delineated in Chapter 5.

The objective of the design process is to generate controllers that guarantee a level of robust stability in the closed-loop system. The robust stabilization problem at hand is expressible as an $H_\infty$ optimization problem, where the controller matrix $\mathbf{K}$ is designed to minimize the $H_\infty$ norm of a closed-loop transfer function [76]. For the normalized left coprime factorization of $\mathbf{P}$ the largest positive stability margin attainable $\varepsilon = \varepsilon_{max}$ is given by Eq.( 6.23), [80]. In practise the objective is to find a stabilizing feedback controller which maximizes $\varepsilon$ according to Section 5.3.3. Eq.(6.23) restates the maximum stability

margin when using a left coprime factor uncertainty for the plant **P** [80, 176].

$$\varepsilon_{max} = (\gamma_{min})^{-1} = \left\{ \inf_{\mathbf{K}} \left\| \begin{bmatrix} \mathbf{K} \\ \boldsymbol{I} \end{bmatrix} (\boldsymbol{I} - \mathbf{PK})^{-1} \begin{bmatrix} \boldsymbol{I} & \mathbf{P} \end{bmatrix} \right\|_{\infty} \right\}^{-1} = \sqrt{\left(1 - \|\tilde{\mathbf{M}}\,\tilde{\mathbf{N}}\|_H^2\right)} \quad (6.23)$$

In order to ensure that the compensator synthesis optimization problem is properly posed, a number of constraints must also be put in place:

1. The closed-loop eigenvalues must be constrained to have negative real parts; meaning that the controlled system is stable.

2. The compensators' gains may be constrained so that high-ratio gearboxes and large flap angles are avoided.

3. The flap compensators are constrained to be passive so that they can be synthesized using passive mechanical components.

For the deck-flap system at hand the overall state dimension of the plant, **P**, is 12. 4 states relate to the position vector, 4 states to the velocity vector and 4 states to the approximation of the Theodorsen function. The plant has 2 inputs, being the 2 flap torques, and 2 outputs, being the flap angle rates. The controller matrix **K** is thus of dimension $2 \times 2$. Since the leading and trailing flaps are considered independent, the off-diagonal elements are assumed zero. The normalized coprime stability margin associated with Eq.(6.23) is computed for the system at increasing wind speeds, until it reaches instability (stability margin becomes zero).

### 6.3.2 Optimization I: Spring-Damper on Flap Hinges

An optimization process is next performed for each of the three cases of Fig. 6.3. The stiffness and damping at the flap hinges are the sought after optimization parameters, whereas the optimization objective is the minimization of $\gamma$ in Eq.(6.23), constraint to closed-loop system stability. A fully symmetric configuration is assumed, i.e. same values

of spring/damper and hinge location for the windward and leeward sides. The optimization results demonstrate that case 3 exhibits the most favourable aeroelastic characteristics, with both the critical flutter speed and divergence speed significantly increased. For case 1 the optimized retention components yield an effectively rigid connection between the flaps and deck; consequently, softening of the springs results in lower critical wind speeds. The comparison of the stability behaviour for the three cases is presented by their root-loci diagrams in Fig. 6.4. The associated results are summarized in Table 6.2. Case 1, having the flaps rigidly attached to the deck effectively produces an identical root locus to the the open-loop case, see Fig. 4.7.

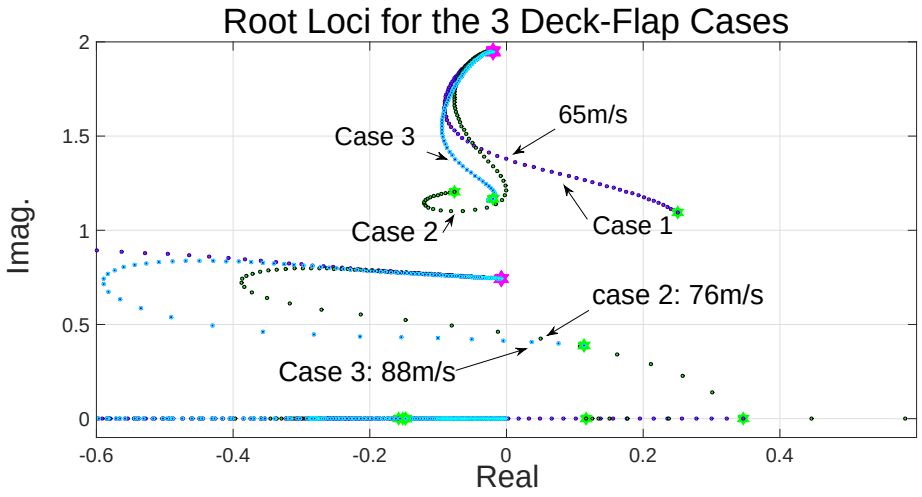


Figure 6.4 Root-loci for the deck-flap assembly connected with springs and dampers for the 3 hinge positions. The wind speed is swept from 0 m/s to 90 m/s, with the low-speed end of the root loci marked with (magenta) hexagons and the high-speed ends marked with (green) hexagons. The onset of aeroelastic instabilities for these cases are summarized in Table 6.2

| Cases | Flutter Speed | Divergence Speed | Rob. Index($\gamma$) | Stiffness $K_\beta = K_\gamma$ | Damping ratio |
|---|---|---|---|---|---|
| 1 | $65m/s$ | $72m/s$ | 31.33 | $1.05 \times 10^6 kNm/m$ $(\omega_\beta = \omega_\gamma = 14\omega_\alpha)$ | 2.11% |
| 2 | $76m/s$ | $82m/s$ | 90.85 | $1.84 \times 10^5 kNm/m$ $(\omega_\beta = \omega_\gamma = 11.78\omega_\alpha)$ | 10.1% |
| 3 | $88m/s$ | $108m/s$ | 4.12 | $2.41 \times 10^5 kNm/m$ $(\omega_\beta = \omega_\gamma = 6.75\omega_\alpha)$ | 3.52% |

Table 6.2 Aeroelastic limits and robustness indexes for the 3 cases of Deck-Flap configurations, values of stiffness and damping about the flap connections.

As was highlighted in Chapter 5 the choice of the robustness index based on the coprime realization of the system is founded on the premise that this is related to the system's physical properties. Consequently, it is anticipated that the deck-flap configuration of case 3, having a smaller robustness index or equivalently a larger stability margin index, will be less sensitive to variations when compared to case 2. However, it should be stressed that the equivalence between robustness index and allowable tolerance in parametric variations is not proportional. This should be expected since the modelling follows an unstructured representation for the uncertainty process. To further illustrate this point, cases 2 and 3 are examined in terms of the closed loop system's stability while reducing the torsional natural frequency in a vacuum. The choice of torsional frequency as the varied parameter is due to its dominant contribution to the flutter mode. Fig. 6.5 demonstrates that case 3 can in fact sustain a slightly larger reduction in the bridge's torsional stiffness. Both cases however exhibit a type of soft flutter behaviour when relatively minor changes to the deck's torsional stiffness are introduced.

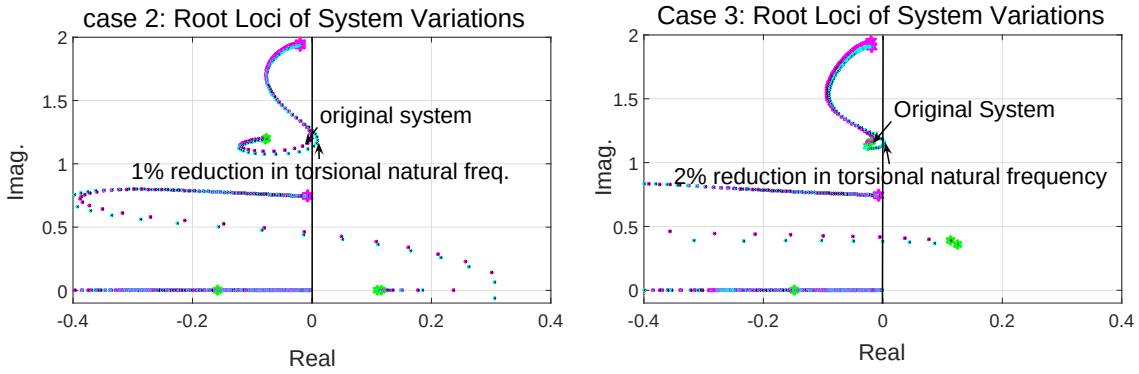


(a) (b)

Figure 6.5 (a) Root loci of the deck-flap system corresponding to case 2 for 1% variation in the zero wind speed torsional natural frequency. (b) Root loci of the deck-flap system corresponding to case 3 for 2% variation in the zero wind speed torsional natural frequency.

### 6.3.3 Network Synthesis using Inerters

#### The Inerter

The inerter is a two-terminal, one port, mechanical device introduced in [177] such that equal and opposite forces applied at the terminals are proportional to the relative acceleration between them. Consequently, $F = b(\dot{U}_2 - \dot{U}_1)$, see Fig. 6.6. The constant of proportionality $b$ is referred to as the *inertance* and is measured in kilograms. The applicability of the inerter device is dependent on its small dimensions and mass (relative to its inertance) as well as independence from spatial orientation. Furthermore, the inertance should be adjustable independently of the mass and should support adequate linear travel [62]. There

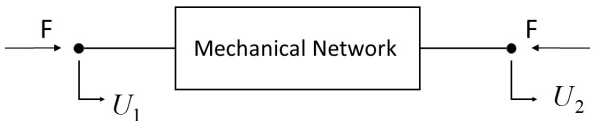


Figure 6.6 A-free-body diagram of a one-port (two-terminal) mechanical element or network with force velocity pair $(F, \upsilon)$ where $\upsilon = U_2 - U_1$.

are several ways in which the inertance can be realized, depending on how the device is built. Three types of inerters have been proposed namely; mechanical geared inerters; hydraulic inerters and electromagnetic inerters. In this work only the mechanical system alternative is considered. Schematics of two mechanical realizations of an inerter component are shown in Fig. 6.7.

For devices such as the ones presented in Fig. 6.7 the value of the inertance is easy to compute [39, 110]. In general, if the device gives rise to a flywheel rotation of $\alpha$ radians per metre of relative displacement between terminals, then the inertance is given by $b = J\alpha^2$, where $J$ is the flywheel's moment of inertia. Alternatively, considering a gear of radius $r_g$, then $b = \frac{J}{r_g^2}$. A key feature of the inerter is that the inertance can be adjusted through gearing, without significantly increasing the inerter's physical mass. Devices weighting approximately 1kg have been reported to produce inertance of the order of 60 to 240kg, depending on the gearing [39].

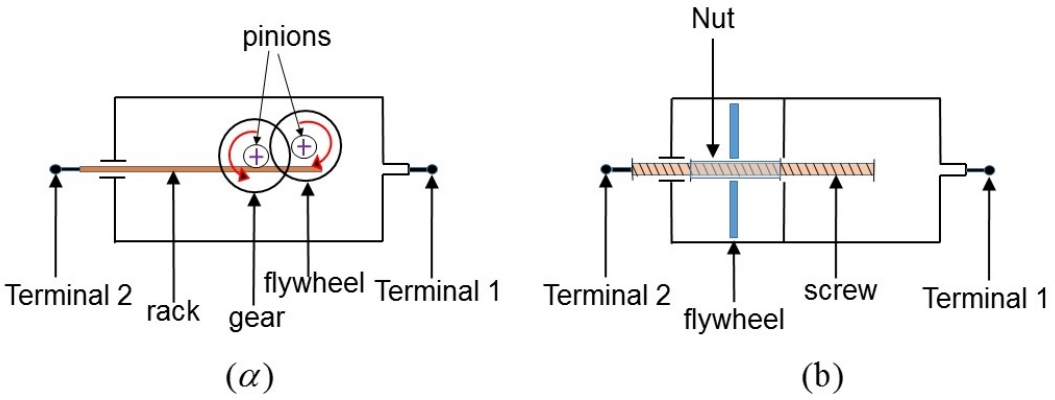


Figure 6.7 Inerter schematics (a) Rack and pinion mechanism (b)Ball screw inerter. These drawings were reproduced from [177] and [39].

### Passive Circuit Synthesis

One of the principal motivations for the introduction of the inerter [177] is the synthesis of passive mechanical networks. It has been pointed out that simple masses together with spring and damper components are insufficient in establishing an electrical-mechanical analogy, which would allow the full implementation of the electrical circuit synthesis theory for mechanical systems. In the afore-mentioned analogy the spring is the equivalent of the inductor and the damper is the resistor equivalent. The mass element however, cannot be used as the capacitor equivalent because it has one terminal connected to the ground. It is thus necessary to replace the mass element by a genuine two-terminal element. The inerter bridges this gap.

The theory of passive networks has been widely studied in the electrical engineering literature [9] and is based on the idea of through and across variables. Through variables require one point of measurement, e.g. forces, while the across variables need to be measured at the extremities of an element, e.g. velocities. For mechanical networks in rotational form, the through and across variables are torque and angular velocity, respectively.

The concept of passive electrical circuits can be translated explicitly to mechanical networks as follows: A mechanical one-port network with a force-velocity pair $(F, \upsilon)$, see Fig. 6.6, is considered passive if for all admissible $F$ and $\upsilon$, square integrable over$(-\infty, T)$,

Eq.(6.24) is satisfied.

$$E(T) = \int_{-\infty}^{T} F(t)\upsilon(t)dt \geq 0 \tag{6.24}$$

The above integral equation effectively represents the energy supplied to the mechanical network [62]. A network is thus passive if it cannot supply energy to the environment. The *impedance* of a network, $Z(s)$, is defined as the ratio of the across to the through variable. For a mechanical network it is effectively, $Z(s) = \frac{\mathscr{L}\upsilon}{\mathscr{L}F}$ (where $\mathscr{L}$ denotes the laplace transform, $\upsilon$ is the relative velocity across the element and $F$ is the force). The *admittance*, $Y(s)$, is defined as the reciprocal of the impedance, $Y(s) = \frac{1}{Z(s)}$. If a one-port mechanical network has impedance $Z(s)$, which is a real rational function then the network is passive if and only if $Z(s)$ is analytic and $Z(s) + Z^*(s) \geq 0$ in $Re(s) \geq 0$. The following theorem [9] is an equivalent way to define network passivity.

**Theorem 2** *Let $Z(s)$ be the real rational impedance function of a linear time invariant two-terminal network. Then the network is passive if and only if*

1. *$Z(s)$ has no pole in $Re(s) > 0$ ;*
2. *$Re[Z(i\omega)] \geq 0$ for all real $\omega$ with $i\omega$ not a pole of $Z(s)$;*
3. *Poles on the imaginary axis and infinity are simple and have non-negative residues.*

Real positive functions satisfying the above conditions are termed positive real. If $Z(s)$ is positive real, there exists a two-terminal mechanical network whose impedance equals $Z(s)$, which consists of a finite interconnection of springs, dampers and inerters [62, 177]. With regard to its practical implementation, this means that by imposing a passivity constraint on the impendence of the controller transfer function, which is to be designed, a mechanical realization of this controller, out of pure passive components, can be subsequently pursued. This strategy provides a considerable advantage compared to the standard techniques when the mechanical network layout is selected before hand.

### Applications

The inerter, although a relatively new discovery has found its way in many engineering applications. Smith [177] initially outlined the potential use of some inerter-based systems. These include: i) the simulation of a mass element without the need of a large mass. ii) a methodology for absorbing vibration without the need for mounting an additional mass. This is also advantageous in the sense that it avoids the problem of setting limits of travel for the added mass. iii) Implementation in vehicle suspension systems. In traditional suspension problems, the suspension system makes use of springs and dampers for connecting together the sprung and unsprung elements of the vehicle. This approach is restricted because it is unable to reproduce the full breadth of impedances. The inerter allows the broadening of impedances [62]. The inerter component was first used in Formula 1 racing car suspension systems, under the name *J-damper* [39] for the McLaren team.

In the civil engineering field, the inerter device was first introduced for suspension control of buildings in [196]. The focus therein was on earthquake and traffic loading. The performance of different inerter-based layouts was compared to traditional suspension systems comprising of springs and dampers. Similarly, Ikago et. al [84] proposed a tuned viscous mass damper (TVMD) for building systems. In their work they propose an inerter-based ball screw mechanism, which translates linear motion to high-speed rotational motion, thus resulting in significant additional apparent mass. In other words, the ball screw mechanism amplifies the apparent effect of a relatively small mass, enabling effective control of the seismic response of building structures. In [124] the inerter mass-amplification mechanism was used for forming the tuned-mass-damper inerter (TMDI), building upon the conventional tuned-mass-damper (TMD). It was analytically shown that an optimally designed TMDI outperforms the classical TMD in minimizing displacement variance of single-degree-of-freedom systems under stochastic excitation. The study was then extended to multi-degree-of-freedom structures. More recently, Lazar et. al [110] proposed an inerter-based system, modelled inside a multi-storey building, located in braces between adjacent stories, aiming at reducing vibrations due to base excitation.

The following analysis will focus on combining the mass amplification effect of the inerter with the aerodynamic flap effect for flutter stabilization. It will be demonstrated that the added mass effect has a beneficial impact on the closed-loop system robustness. Furthermore, as opposed to previous analyses, in the structural field, the mechanical layout of the mechanical compensators is not predefined but constructed from the associated positive real transfer function.

### 6.3.4 Optimization II: Mechanical Compensator in parallel to Flap Retention Components

The control investigation of the previous section demonstrated that a significant increase in aeroelastic boundaries can be achieved through the combination of optimized flap retention components and appropriate deck-flap pivot location. The spring and damper elements optimized are effectively the structural parameters $K_\beta$, $K_\gamma$ and $C_\beta$, $C_\gamma$ appearing in equations (6.9)-(6.12). The location of the flap hinges is implemented in the model by computing the structural quantities in equations (6.5)-(6.6) as well as adjusting the $l$ and $m$ parameters in equations (6.17)-(6.19). The main disadvantage of this relatively simple feedback mechanism is the resulting poor robustness properties. The following examination seeks to improve the stability margins, while retaining the increased critical flutter and divergence speeds, by introducing control networks $K_l(s)$ and $K_t(s)$ in parallel to the retention components.

In this study we confine our attention to passive control systems that do not require power supply. Consequently the added feedback systems should be realized by the interconnection of passive mechanical components. It should be stressed that the network layout is not preselected. Instead, a passivity constraint is assigned to the controller transfer function and a mechanical realization is then derived based on springs, dampers and inerters [177].

In the examined deck-flap system, whose block diagram is presented in Fig. 6.2, the through variables are the flap torques $M_c^{\beta_l}$, $M_c^{\beta_t}$, see equations (6.11)-(6.12), and the cross variables are the flap angle rates $\dot{\beta}_l, \dot{\beta}_t$. Consequently the leading and trailing flap

compensator admittance functions are defined as $K_l(s) = M_c^{\beta_l}/\dot{\beta}_l$ and $K_t(s) = M_c^{\beta_t}/\dot{\beta}_t$ respectively. In a further narrowing of the problem, emphasis is placed on the synthesis of first order compensators that seek to maximize the robustness index $\varepsilon$ in Eq.(6.23). Higher order compensators were examined, but the additional benefits were found to be minimal. The class of first-order compensators considered here are of the following form

$$K(s) = \frac{As+B}{Cs+D}, \tag{6.25}$$

where $A \geq 0$, $B \geq 0$, $C \geq 0$ and $D \geq 0$, with at least one of $C$ and $D$ positive. for this class of compensators this condition is sufficient to ensure the positive realness of the admittance function, in accordance with Eq.(6.24).

The design results of this procedure for cases 2 and 3, see Fig. 6.3 are presented in Table 6.3. The final flap controllers consist of a spring and a damper in parallel to the mechanical realization of $K_l(s)$ and $K_t(s)$. The overall system admittance is denoted as $Y_{gl}(s)$ and $Y_{gt}(s)$ for the leading and trailing flaps respectively. Case 1 is not reported because no improvement was obtained when using an additional compensator. For case 3 a trade-off between the maximum critical flutter speed and the allowable robustness is presented (cases 3a and 3b). Clearly, by introducing a first order compensator at the deck-flap hinges we can significantly raise the system's tolerance to parametric uncertainty in the torsional frequency. Similar results are attained for variations in aerodynamic parameters.

| Cases | Flutter Speed | Max. Tor. Variation | Stiffness $K_\beta = K_\gamma$ (kNm/m) | Damp. Ratio $C_b = C_\gamma$ | Leading Flap | Trailing Flap |
|---|---|---|---|---|---|---|
| 2 | $78m/s$ | 5% | $1.97 \times 10^5$ | 2.77% | $\frac{1.43\times10^6 s+363000}{11.97s+45.69}$ | $\frac{0.78\times10^6 s+72440}{7.87s+34.58}$ |
| 3*a* | $89m/s$ | 3% | $2.48 \times 10^5$ | 0.16% | $\frac{762500s+75}{13.92s+83.01}$ | $\frac{1.27\times10^6 s+120}{33.87s+301.5}$ |
| 3*b* | $86m/s$ | 5% | $2.33 \times 10^5$ | 1.34% | $\frac{922500s+90}{16.71s+81.97}$ | $\frac{1.46\times10^6 s+145}{44.41s+300}$ |

Table 6.3 Flutter critical wind speeds and maximum allowable variations in the zero wind speed torsional natural frequency for deck-flap configuration 2 and two variations of deck-flap configuration 3 (3a,3b).

In order to synthesise the controller, one recalls that the admittance (the ratio force/velocity) of a damper is constant, say $c$. The admittance of a spring is $k/s$ and the admittance of an inerter is $bs$ [177]. Therefore, if one were to consider a damper and spring connected in parallel, the admittance of the combination would be $c+k/s$. Applying the basic rules associated with series and parallel combinations of mechanical elements, the admittance is the sum of the admittances for a parallel combination of elements, while the inverse of the sum of the inverses is used for a series combination. In the case of the first-order compensator (6.25), one observes that when $AD-BC>0$:

$$\begin{aligned} K(s) &= \frac{As+B}{Cs+D} = \left(\frac{Cs+D}{As+B}\right)^{-1} = \left(\frac{C}{A}+\left(\frac{A(As+B)}{AD-BC}\right)^{-1}\right)^{-1} = \\ &= \left(\frac{1}{A/C}+\left(\frac{A^2 s}{AD-BC}+\frac{AB}{AD-BC}\right)^{-1}\right)^{-1} = \left(\frac{1}{c_1}+(bs+c_2)^{-1}\right)^{-1} \end{aligned} \tag{6.26}$$

which represents a damper $c_1 = A/C$ connected in series with the parallel combination of a damper $c_2 = AB/(AD-BC)$ and an inerter $b = A^2/(AD-BC)$; see Fig. 6.8[1]. When $A \gg B$, the transfer function $K(s)$ can be approximated by an inerter and a damper in series.

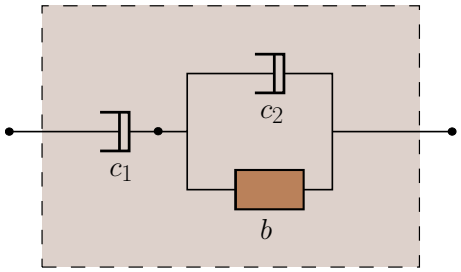


Figure 6.8 Realization of the first-order mechanical compensator (6.26).

[1] When $AD-BC<0$ there holds

$$\begin{aligned} K(s) = \frac{As+B}{Cs+D} &= \frac{A}{C}+\frac{BC-AD}{C(Cs+D)} = \frac{A}{C}+\left(\frac{C^2 s}{BC-AD}+\frac{CD}{BC-AD}\right)^{-1} \\ &= \frac{A}{C}+\left(\frac{1}{\frac{BC-AD}{C^2 s}}+\frac{1}{\frac{BC-AD}{CD}}\right)^{-1} = c_1+\left(\frac{1}{\frac{k}{s}}+\frac{1}{c_2}\right)^{-1} \end{aligned} \tag{6.27}$$

which consists of a damper $c_1 = A/C$ in parallel with the series connection of a spring $k = (BC-AD)/C^2$ and a damper $c_2 = (BC-AD)/CD$.

The physical parameters of the networks for the different transfer functions presented in Table 6.3 are shown in Table 6.4. It is observed that the magnitude of the damper $c_2$ is considerably smaller than that of $c_1$, so without significant loss in performance the transfer function can be realized by solely an inerter and a damper in series.

| Cases | Flutter Speed | Max. Torsion Variation | Leading Flap Network | Trailing Flap Network |
|---|---|---|---|---|
| 2 | $78m/s$ | 5% | $c1 = 54777.3Nmsec/rad$<br>$c2 = 0.9Nmsec/rad$<br>$b = 9185.8kgm^2$ | $c1 = 37584.9Nmsec/rad$<br>$c2 = 0.398Nmsec/rad$<br>$b = 4222.3kgm^2$ |
| $3a$ | $89m/s$ | 3% | $c1 = 119632.4Nmsec/rad$<br>$c2 = 8509.9Nmsec/rad$<br>$b = 33571.1kgm^2$ | $c1 = 99047Nmsec/rad$<br>$c2 = 2140.4Nmsec/rad$<br>$b = 23029kgm^2$ |
| $3b$ | $86m/s$ | 5% | $c1 = 55206.5Nmsec/rad$<br>$c2 = 1.1Nmsec/rad$<br>$b = 11254.3kgm^2$ | $c1 = 32864.2Nmsec/rad$<br>$c2 = 0.48Nmsec/rad$<br>$b = 4865.1kgm^2$ |

Table 6.4 Mechanical network parameters for the first order compensators presented in Table 6.3

### 6.3.5 Investigation of the Optimum Flap Pivot Position

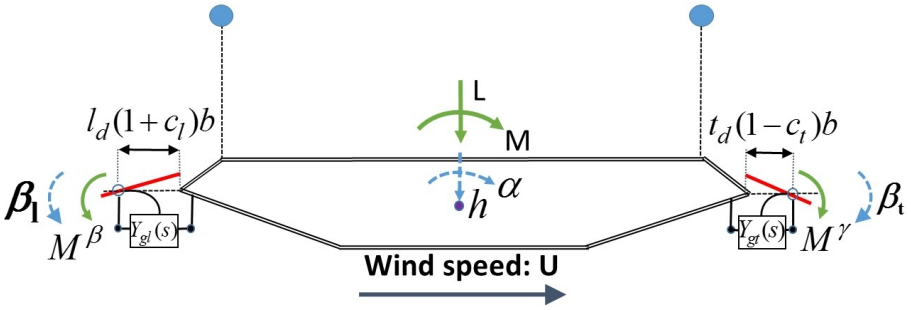


Figure 6.9 Sketch of the practical implementation of the passive deck-flaps configuration system. $Y_{gl}(s)$ and $Y_{gt}(s)$ are the passive networks attached at the hinges of the leading and trailing flaps respectively. They are composed by a spring and a damper in parallel with the mechanical realization of a first order compensators $K_l(s)$ and $K_t(s)$.

In the previous sections three different flap pivot locations were investigated, Fig. 6.3. It was demonstrated that when the pivot points are on the outer edges of the flaps significantly better aeroelastic performance can be attained. To further examine this point the general

case where the location of the flap pivot is considered as an optimization parameter is considered. In Fig. 6.9 parameters $l_d$ and $t_d$ ranging from 0 to 1 determine the location of the hinges. The sectional Humber Bridge example was used again to assess the performance of the mechanical feedback system. Fig. 6.10 (b), presents the stability performance after the optimization procedure of the flap retention components $K_\beta$ and $K_\gamma$, and $C_\beta$ and $C_\gamma$ in (6.11) and (6.12), the optimal locations of the flap pivots in Fig. 6.9 and the added mechanical network, Fig. 6.8, placed in parallel to the retention elements. The aeroelastic stability properties of the uncontrolled deck are shown in Fig. 6.10 (a), where the flaps are considered rigidly attached to the deck.

Similarly to the previous sections the design of the mechanical compensators $Y_{gl}$ and $Y_{gt}$ and the determination of the deck-flap system configuration, presented in Table 6.5, results in significantly increased flutter and torsional divergence speeds of $89\,m/s$ and $101\,m/s$ respectively. When only the retention components were implemented it was again observed that the robustness properties were poor, which was remedied by the implementation of control networks $K_l(s)$ and $K_t(s)$. Since this added robustness is required at high wind speeds, the chosen design wind speed is $89\,m/s$, being the highest wind speed for which the open-loop system, only retention components, is stable. The design optimisation focuses on determining the four parameters in each of $K_l(s)$ and $K_t(s)$, so as to maximise $\varepsilon_{max}$ in (6.23). Since we impose a first-order passivity constraint on the controller, the parameter optimisation is achieved using a nonlinear programming algorithm rather than the standard linear optimal coprime-factor robustness theory associated with (6.23). The optimal compensators are also given in Table 6.5 with $\varepsilon_{max} = 0.2770$.

The system's robustness properties when subjected to reduction of its in vacuum torsional deck stiffness is presented in Fig. 6.11. Reducing the deck's torsional frequency by more than 3% results in a *soft flutter* type instability having a resonant frequency of approximately 0.175 Hz. From this analysis, given the optimized values for $l_d$ and $t_d$ as well as the stability results it can be concluded that the flap pivots can be positioned at the outer edges for construction simplicity.

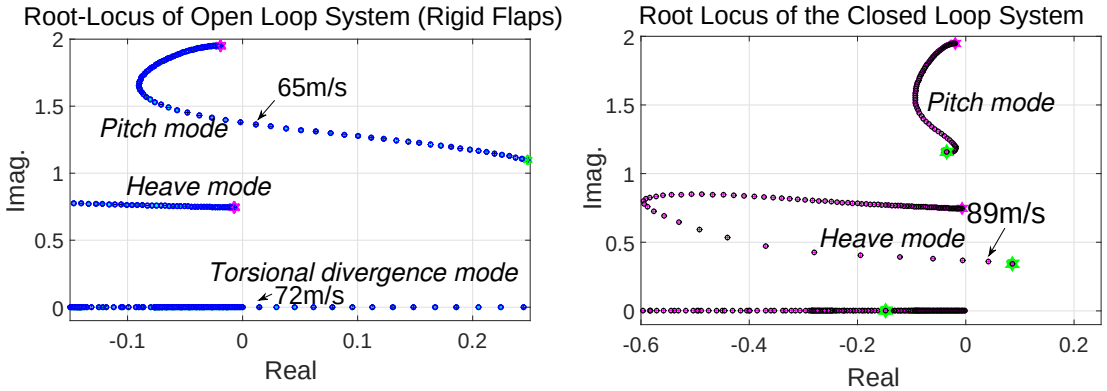


(a) Uncontrolled (b) Controlled

Figure 6.10 (a) Root-loci of the uncontrolled section model of the Humber Bridge. (b) Root-loci of the controlled section model of the Humber Bridge. The wind speed is swept from $0\,m/s$ to $90\,m/s$.

| Flutter Speed | Tor. Diverg. Speed | Rob. Index | Max. Torsion Variation | Stiffness $K_\beta$ kNm/m | Stiffness $K_\gamma$ kNm/m |
|---|---|---|---|---|---|
| 89m/s | 101m/s | 3.61 | 3% | $3.72 \times 10^5$ | $1.67 \times 10^5$ |
| Damp. Ratio $\zeta_\beta$ | Damp. Ratio $\zeta_\gamma$ | Pivot Position LF | Pivot Position TF | Transfer Function LF | Transfer Function Function TF |
| 1.4% | 1.6% | $l_d = 0.98$ | $t_d = 0.91$ | $\frac{1.34\times10^6 s+135}{18.46s+141.2}$ | $\frac{4.51\times10^6 s+460}{69.16s+305.7}$ |

Table 6.5 Aeroelastic limits, robustness properties and flap compensator properties of the sectional deck-flap system. Notation, LF: Leading Flap, TF: Trailing Flap.

### 6.3.6 Time Response - Comparison to Active Control

The time response of the previously optimized deck-flap system is investigated in this section. The aim is to examine the effectiveness of the passive flap mechanism in suppressing divergent pitching and heaving motion of the deck at different wind speeds. The corresponding flap movement is also observed. Furthermore, the response of the passive system is compared to the implementation of an active $H_\infty$ control framework, as was described in Chapter 5; the active control treatment is also presented in [17]. Since, an active control scheme relies on the availability of a power source and results in high order compensators, the flap pivot points were considered adjacent to the deck, case 1. Two different conceptual strategies are effectively compared, the first is based on a passive

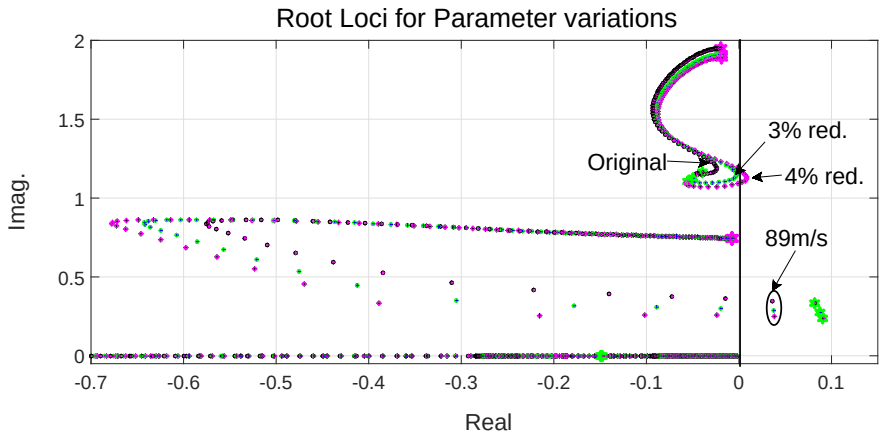


Figure 6.11 Root loci of the section deck-flap system for the nominal system, and for systems with 3% and 4% reductions in the (zero wind speed) structural torsional frequency.

system with optimized aerodynamic configuration and the second relies on a brute force high order compensator implementation.

Fig. 6.12 presents the deck's transient response related to an initial condition of a twisting/pitch of $2^o = 0.035rad$. Four different configurations are considered, namely: the uncontrolled deck with flaps rigidly attached to the deck, the passive networks presented in cases 2 and 3b of Table 6.4 and the active $H_\infty$ control. Because the chosen wind speed is above the critical flutter limit ($65m/s$) of the open loop system, but below the torsional divergence limit $72m/s$, the deck diverges in an oscillatory mode. The passive networks, cases 2 and 3b, exhibit similar behaviour whereas the active control results in larger magnitude oscillations but has a faster settling time. Note that this fictitious simulation is the worst case condition, as it assumes that the controllers are switched on at the chosen wind speed under the given initial condition. In reality the flap controllers would already be functioning at lower wind speeds thus preventing the deck from reaching such large amplitude values.

The deck's pitch transient response as well as the associated flap rotation is presented in Fig. 6.13 for wind speeds of $75m/s$ and $85m/s$. Both the passive network case 3b and the active $H_\infty$ control case are included. For the lower wind speed the behaviour of the two systems is comparable in terms of rotation magnitudes. For the wind speed of

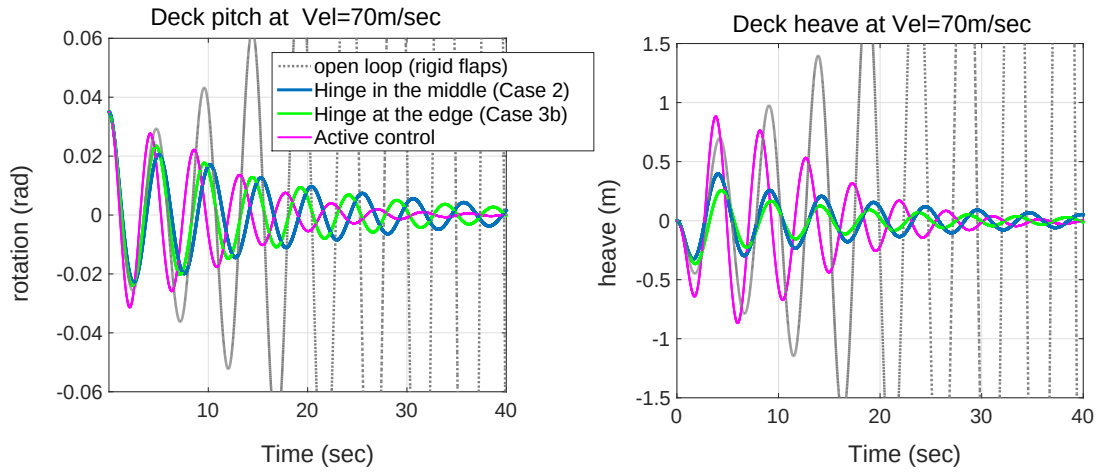


Figure 6.12 Deck's pitch and heave transient response at a wind speed of 70m/s. 4 cases are considered: The uncontrolled deck with the flaps rigidly attached, the passive networks of cases 2 and 3b and the active $H_\infty$ control.

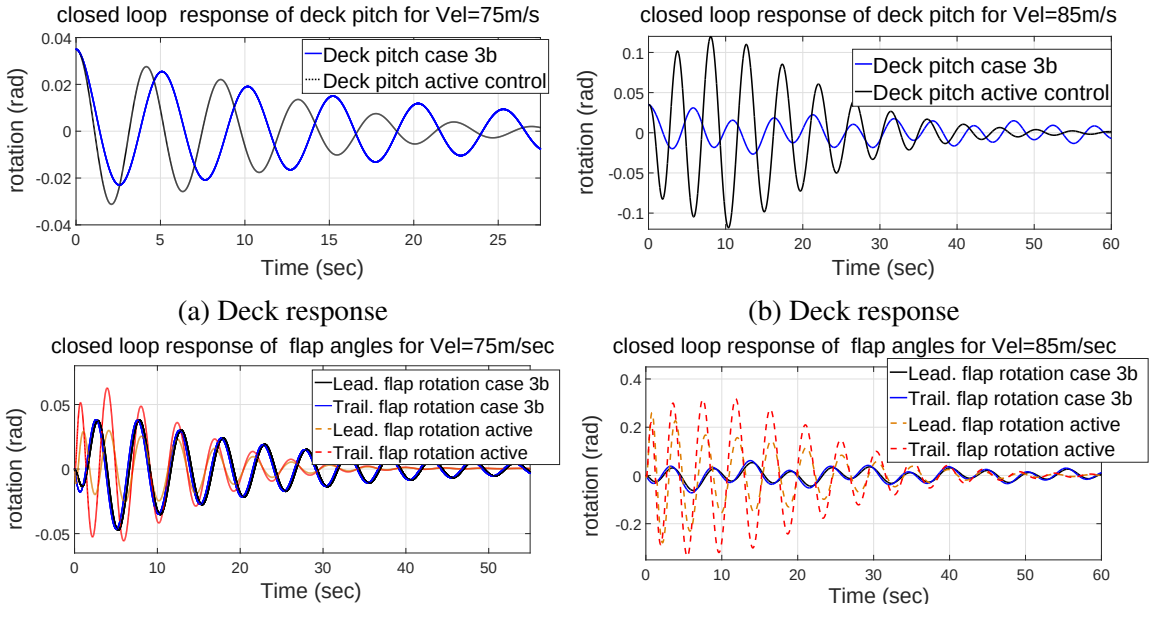


(a) Deck response

(b) Deck response

(c) Flap response

(d) Flap response

Figure 6.13 Transient response of deck pitch and flap rotations for the configuration of passive network case 3b and actively controlled flaps. Initial condition is a $2^o$ pitch of the deck and considered wind speeds are $75m/sec$ and $85m/s$.

$85m/s$ however it is shown that active control provokes significantly larger flap movement. Magnitude of this size, $0.3rad$, can provoke flow separation. This behaviour is not entirely surprising if its considered that for the active control case, flap compensator need to stabilize the deck against torsional divergence, at $U = 72m/s$. Because torsional divergent behaviour is effectively a static instability, larger counteracting moments are required which in turn provoke significantly larger flap rotations. The passive deck-flap design on the other hand, by optimizing the system kinematics in an aerodynamic favorable manner attains a higher divergence critical wind speed. Hence, the passive configuration has a positive impact both on performance and flap amplitude limitation.

The following part examines the leading edge flap contribution in terms of stability and performance. Deck-flap configuration 3b is once more chosen for comparing the system's response when the leading flap is controlled, see previous analysis, or fixed. For the latter case the afore-mentioned described optimization procedure is carried through and the mechanical compensators are re-tuned in order to consider the leading flap fixed. Fig. 6.14(a) compares the root loci of the two configurations whereas Fig. 6.14(b) presents the time response due the previous imposed initial condition for the 2 systems. In terms of stability analysis employing just the trailing-edge flap proves sufficient in suppressing flutter instability, however the divergence speed limit is now decreased to $81m/s$, compared to $108m/s$ when both flaps are employed.

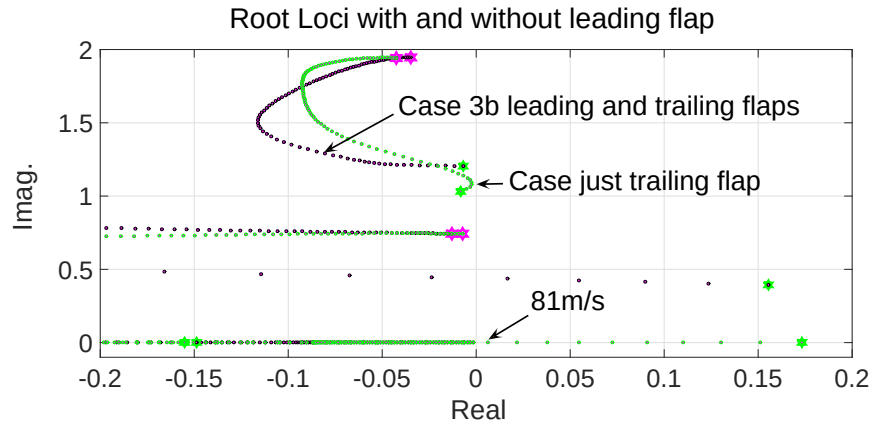


(a)

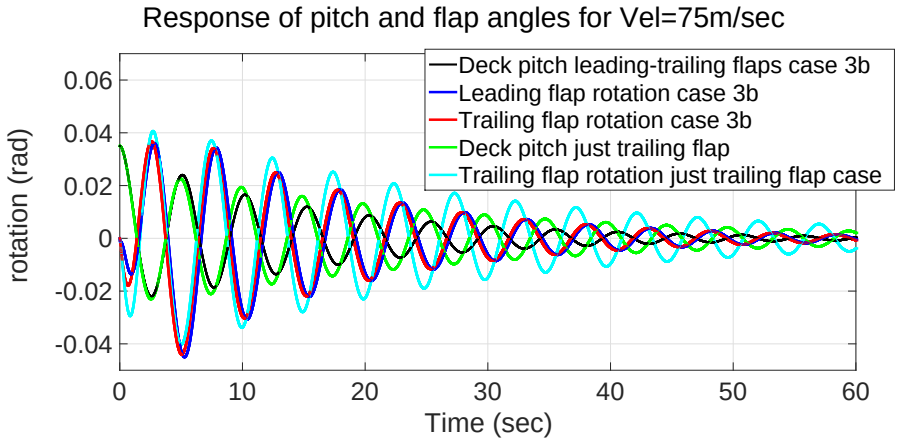


(b)

Figure 6.14 (a) Root Loci of the closed loop system with the leading flap active, case 3b, and inactive. (b) transient response of the deck pitch and flap rotations with the leading flap active and inactive.Initial condition is a $2deg$ pitch of the deck and the demonstrated wind speeds is $75m/sec$

It is recalled that employing flap controllers to achieve stability above the torsional divergence limit results in a steep robustness loss. Consequently, a leading flap is mostly beneficial in cases where the flutter and divergence boundaries are in proximity. In special circumstances however, e.g. during the deck erection process, when flutter aeroelastic boundaries are much lower than divergence boundaries, Fig. 4.13, the contribution of the leading flap might be small. Furthermore, dynamic response simulations for this case demonstrate that when the leading flap is active the settling time for the deck pitch is slightly faster and the trailing flap rotation magnitudes are somewhat smaller.

### 6.3.7 Section summary

This section addressed the problem of stabilizing aeroelastic instabilities in a bridge-section model using a passive control scheme. An optimization process is proposed for tuning the values of the mechanical components, which connect the flaps to the deck. Best results in terms of stability and robustness are achieved when the connection is at the outer edge of the flaps, case 3. In the case where the optimization parameters are only a spring and a damper at the connection, significant improvement in the critical flutter speed and divergence speed is gained but the robustness of the system is poor. We are able to improve robustness properties of the system by introducing a first order compensator in parallel with the spring-damper. The mechanical realization of these compensators also introduces the use of the Inerter, which appears to have a considerable impact on system properties. Transient response simulations show that flap magnitudes for the case of the passive system are smaller than when using active control and thus less likely to cause flow separation problems. The proposed mechanical configuration is also quite simple to implement in real bridge structures as it avoids the use of additional structural components such as supporting beams or pendulums.

## 6.4 Tuned Mass Dampers for Suppressing Aerodynamic Instabilities

This section reviews some of the characteristics and shortcomings of using an eccentric mass or a tuned mass damper (TMD) for suppressing aeroelastic instabilities. It also provides the fundamental background for the next section, which will introduce a kinematic link between the oscillating tuned masses and the movable flaps. More specifically, in Sec. 6.4.2 the effect of a windward eccentric mass on reducing aerodynamic moment is investigated. In Sec. 6.4.3 the additional masses are considered suspended. Tuning of the mechanical components for those oscillators results in improved aeroelastic performance. However, the latter method is laced with significant drawbacks, which will be pointed out.

### 6.4.1 Deck-TMD Structural Model

The sectional model of the Humber Bridge is used for the stability investigation, which in this case considers the flaps to be rigidly attached to the deck, see Fig. 6.15. Following a similar energy approach to Sec. 6.2.1, the equations of motion for the combined system of the deck with the two symmetrically placed masses of Fig. 6.15 are as follows

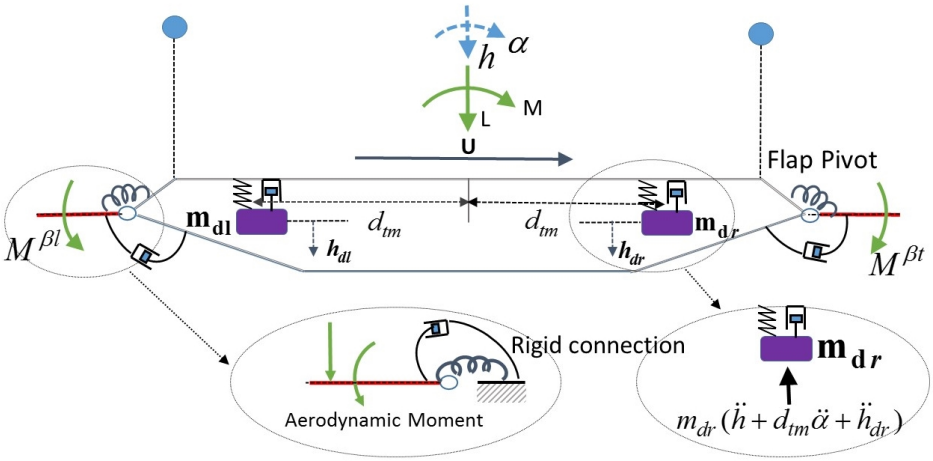


Figure 6.15 Sketch of a practical implementation of a TMD control system. The TMD consists of 2 masses symmetrically placed about the section's elastic center. The flaps are assumed rigidly attached to the deck.

$$m_g\ddot{h} + (S_\alpha - m_{dl}d_{tm} + m_{dr}d_{tm})\ddot{\alpha} + m_{dl}\ddot{h}_{dl} + m_{rl}\ddot{h}_{dr} + C_h\dot{h} + K_h h = L, \tag{6.28}$$

$$(S_\alpha - m_{dl}d_{tm} + m_{dr}d_{tm})\ddot{h} + I_g\ddot{\alpha} - m_{dl}d_{tm}\ddot{h}_{dl} + m_{dr}d_{tm}\ddot{h}_{dr} + C_\alpha\dot{\alpha} + K_\alpha\alpha = M, \tag{6.29}$$

$$m_{dl}\ddot{h} - m_{dl}d_{tm}\ddot{\alpha} + C_{dl}\dot{h}_{dl} + K_{dl}h_{dl} = 0, \tag{6.30}$$

$$m_{dr}\ddot{h} + m_{dr}d_{tm}\ddot{\alpha} + C_{dr}\dot{h}_{dr} + K_{dr}h_{dr} = 0. \tag{6.31}$$

For a given bridge, in this case the Humber Bridge, the heave and torsion resonant frequencies $\omega_h$ and $\omega_a$ are assumed known, and are related to the corresponding stiffness by $K_h = m_g\omega_h^2$ and $K_a = I_g\omega_a^2$ where $m_g = m_d + m_{dl} + m_{dr}$ and $I_g = I_a + m_{dl}d_{tm}^2 + m_{dr}d_{tm}^2$. Similarly $C_h = 2\zeta_h\omega_h m_g$, $C_a = 2\zeta_\alpha\omega_a I_g$, $C_{dl} = 2\zeta_{dl}\omega_{dl}m_{dl}$ and $C_{dr} = 2\zeta_{dr}\omega_{dr}m_{dr}$, where

$\omega_{dl} = \sqrt{\frac{K_{dl}}{m_{dl}}}$ and $\omega_{dr} = \sqrt{\frac{K_{dr}}{m_{dr}}}$. $L$ and $M$ are the aerodynamic lift and moment on the bridge deck, which are effectively identical to those of the previous section.

### 6.4.2 Eccentric Mass

The first examined case is that of a simple eccentric mass, placed on the windward side of the bridge deck. This is of course a special case of the general deck-TMD system. Equations (6.28)-(6.31) are modified by making the substitutions: $K_{dl} \to \infty$ and $m_{dr} = 0$. The underlying physical principle in flutter control by using an eccentric ballast is the reduction of aerodynamic moment, acting on the deck's centre of rotation [105].

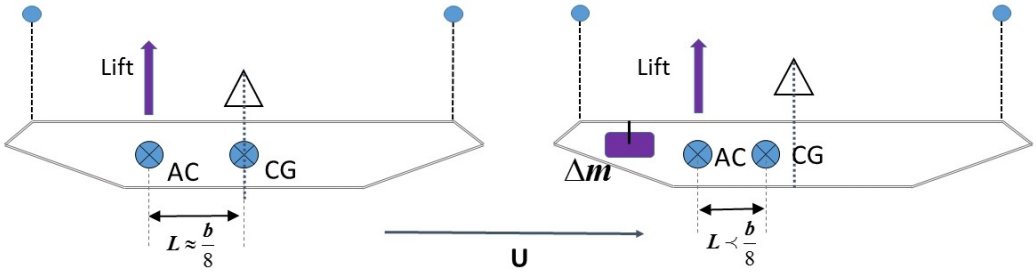


Figure 6.16 Sketch of eccentric mass implementation on a sectional deck. The additional mass $\Delta m$ moves the centre of gravity on the windward side thus reducing the lever arm of the aerodynamic lift [105].

As presented in Fig. 6.16, when an additional mass is introduced at the windward edge of the deck the *centre of gravity* (CG) shifts towards the *aerodynamic centre* (AC), which in turn results in a smaller lever arm ($L < \frac{b}{8}$) and thus a smaller aerodynamic moment. The following numerical investigation presents the aerodynamic stability limits for increasing added mass ratio defined as $\mu = \frac{\Delta m}{m_d}$. The distance of the mass is assumed constant at $d_{tm} = 10m$; other parameter values for the Humber Bridge are given in Table 6.1. Fig. 6.17 presents the root-loci with the wind speed $U$ being the varied parameter for a range of mass ratios $\mu$, as well as the corresponding instability mode. For example, in the case of an added mass ratio of $\mu = 0.1$, which corresponds to an eccentric mass of $1.32tn/m$, the flutter boundary is raised from $65m/s$ to $75m/s$. It is apparent that this methodology, although simple, provides only modest improvement to the critical flutter speed and fails

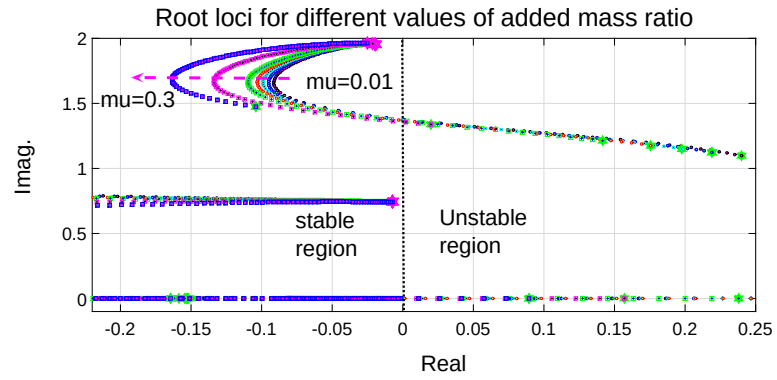


(a)

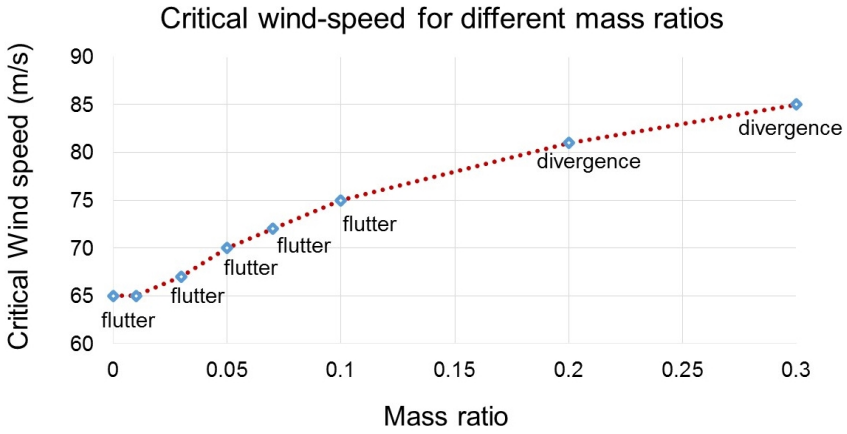


(b)

Figure 6.17 (a) Root loci for different added mass ratios, of the system shown in Fig. 6.16. Mass ratio of eccentric to deck mass ranges from $\mu = 0.01$ to $\mu = 0.3$. (b) Corresponding critical wind-speeds and associated instability type.

to substantially raise the critical divergence speed. In addition our analysis showed that the achieved stability margins are very small. Phongkumsing et al. [153] reported that by considering the structure's multi-modal behaviour, through a FE aeroelastic model, much better results can be attained, e.g. a 70% increase in the critical wind speed with a 5% mass ratio distributed along the full bridge. The finding was attributed to changes in the mode coupling resulting to flutter, however this analysis is not pursued further in this work.

### 6.4.3 Deck-TMD System Stability and Robustness Analysis

Returning to the twin-TMD arrangement, Fig. 6.15, the following investigation will concentrate on implementing a non-linear optimization process for tuning the physical parameters

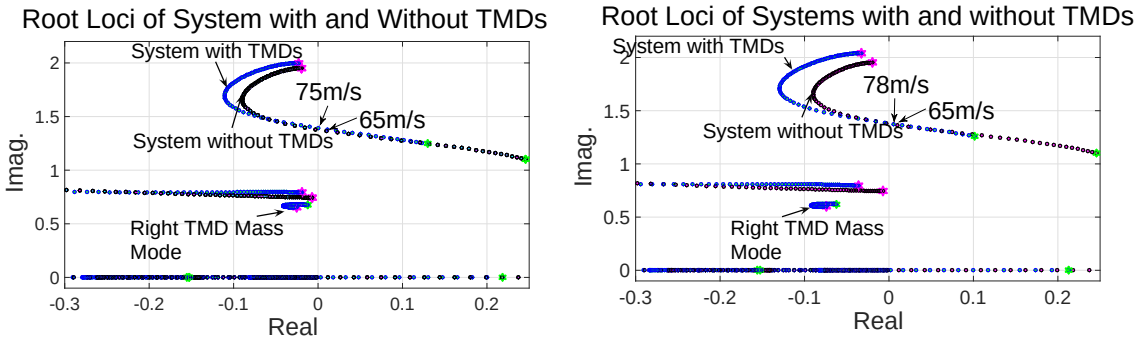


(a) TMD1 (b) TMD2

Figure 6.18 Root Loci for the sectional Humber Bride deck model with and without TMDs. (a) Case TMD1: Left TMD mass 7% of deck mass, right TMD mass 3.5% of deck mass . (b) Case TMD2: Left TMD mass 7% of deck mass, right TMD mass 7% of deck mass.

of the two tuned masses. Simplified design formulas, from the literature [52, 118], are also used and compared to the optimization approach. Tolerance to system uncertainties is also discussed based on the results. The system presented in Sec. 6.4.1 has four degrees of freedom, namely: deck heave, deck pitch and the two vertical displacements of the two TMD masses relative to the deck, $h_{dl}$ and $h_{dr}$. The optimization parameters are the mass, stiffness and damping of each TMD: $m_{dl}$, $K_{dl}$, $\zeta_{dl}$, $m_{dr}$, $K_{dr}$ and $\zeta_{dr}$. Two cases are examined; the first, case TMD1, allows a maximum left mass ratio index of $\mu_{l,max} = \frac{m_{dl}}{md} = 0.07$ and maximum right mass ratio of $\mu_{r,max} = \frac{m_{dr}}{md} = 0.035$. The second case, case TMD2, considers both $\mu_{l,max} = \frac{m_{d\_l}}{md} = 0.07$ and $\mu_{r,max} = \frac{m_{d\_r}}{md} = 0.07$. The optimization objective, similarly to the previous case is to maximize the normalized coprime stability margin. Large movements of the tuned mass are also penalized by introducing weighting coefficients for minimizing the TMDs natural periods, $T_{dl}$ and $T_{dr}$. Hence, the optimization objective reads

$$\min_{m_{dl/r},K_{dl/r},\zeta_{dl/r}} \{0.5\|\gamma\|_\infty + 0.25T_{dl} + 0.25T_{dr}\}. \tag{6.32}$$

Fig. 6.18 presents the root loci for the two deck-TMD system configurations. Table 6.6 lists the obtained aerodynamic stability boundaries for flutter and torsional divergence as well as the optimised TMD mechanical parameters. In Fig. 6.19 the transient response to an initial deck pitch of $2^o$ is presented for cases TMD1 and TMD2. It is easily observed that when using double the right mass, the settling time is faster and the vertical movement of the tuned

masses is slightly smaller. However, in both cases the vertical displacement amplitudes of the TMDs are large, which calls into question the method's practical applicability when considering a shallow deck girder.

| Cases | Flutter Speed | Div. Speed | $m_{dl}$ (kg/m) | $K_{dl}$ (kN/m) | $\zeta_{dl}$ % | $m_{dr}$ kg/m | $K_{dr}$ kN/m | $\zeta_{dr}$ % |
|---|---|---|---|---|---|---|---|---|
| TMD1 | $75m/s$ | $77m/s$ | 945 | 39000 | 19.4 | 473 | 222 | 5.2 |
| TMD2 | $78m/s$ | $78m/s$ | 945 | 45900 | 19.4 | 945 | 373 | 15.6 |

Table 6.6 Aerodynamic limits for deck-TMD configuration associated with cases TMD1 and TMD2, and corresponding optimized mechanical TMD components.

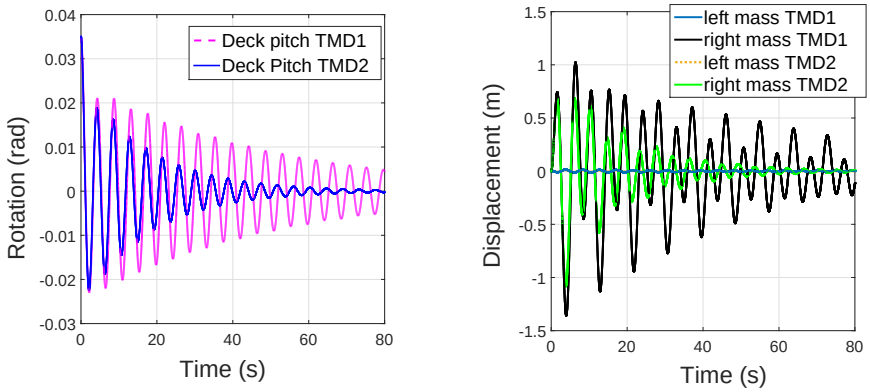


Figure 6.19 (a) Transient response of the deck pitch (b) transient response of the tuned mass movement, for cases TMD1 and TMD2, presented in Table 6.6.

The optimization framework implemented resulted, in this case, in a mechanical deck-TMD configuration, in which the windward mass is static. The windward mass consequently performs a function similar to that of an eccentric mass, described in Sec. 6.4.2, whereas the leeward mass exhibits considerable oscillatory motion.

The more widely-used approach for tuning the TMD characteristics however, is based on the use of simplified formulas derived from first principles. Fujino and Abe [66] suggest the following tuning approach for suppressing self-excited motion.

$$\gamma = \frac{1}{\sqrt{1+\mu}} \tag{6.33}$$

$$\xi_t = \sqrt{\frac{\sqrt{1+\mu}-1}{2\sqrt{1+\mu}}} \approx \frac{\sqrt{\mu}}{2} \tag{6.34}$$

$$(\xi_s)_{max} = \sqrt{\frac{(1+\mu)-\sqrt{1+\mu}}{2}} - \approx \frac{\sqrt{\mu}}{2} \tag{6.35}$$

where $\mu = \frac{m_t}{m_d}$ is the mass ratio, $m_t$ being the total TMD mass. $\gamma = \frac{\omega_t}{\Omega_d}$ is the tuning frequency ratio. Usually, the vertical mass ratio is preselected and then the corresponding optimum damping ratio is evaluated using Eq.(6.34). For tuning the TMD frequency, $\omega_t$, one can set $\omega_d$ to be the effective frequency of the first torsional mode or the bridge's flutter frequency, when TMDs are not included [118]. It should be stressed that the afore-mentioned formulae result in optimal performance when the negative damping related to the self-excited motion equals the maximum damping $(\xi_s)_{max}$ for the chosen TMD ratio. The TMD parameters are thus chosen to convert the structure's negative damping to zero at a specific wind speed. It was pointed out in [40] that this approach is a very limiting case because in practical applications the designed TMD mass ratio, tuning frequency and damping ratio would be expected to achieve the maximum positive damping, for the deck-TMD system. Alternative formulas to overcome this issue have been proposed by Chen and Kareem [40], however in every case the TMD performance appears to be very sensitive to the tuning frequency and damping ratio. Multiple TMDs which cover a wider frequency band offer a plausible alternative which can improve robustness but as expected is laced with implementation difficulties. It is also possible to use a higher than optimal damping ratio but the associated downside is that performance is compromised.

For comparing the two tuning approaches mentioned, the mass ratio of case TMD2 is used, $\mu = 0.14$, and the TMD damping ratio is evaluated at $\xi_t = 18.7\%$. The optimal tuning frequency is computed at $\gamma = 0.937$ and assuming $\omega_d = \omega_{flutter} = 1.38 rad/s$ we calculate the frequency of each TMD at $\omega_t = 1.293 rad/s$. Fig. 6.20 presents the stability analysis for these parameters and also compares the dynamic response of the deck-TMD system for the two tuning approaches. Tuning1, is based on simplified formulas, and Tuning2 follows the optimization framework. From the root locus diagram it is shown that there is a strong coupling between the deck and the leeward suspended mass, which results into

a self-excited instability. From the dynamic behaviour it is observed that vertical motion amplitudes are comparable for both tuning strategies, the difference being that for the Tuning1 case the windward mass oscillates as well. In both cases however, large motion amplitudes of the masses are observed, being more prevalent in the leeward side. It should also be stressed that auxiliary tuned mass dampers appear to be unsuccessful in raising the static divergence speed. In essence, the increase in the critical divergence limit from $72m/s$ to $78m/s$ is due to the increased mass moment of inertia resulting from the additional masses at a distance from the centre of rotation.

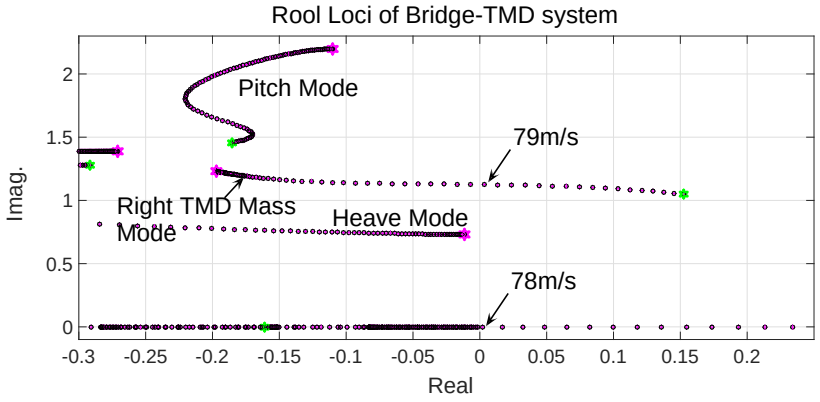


(a)

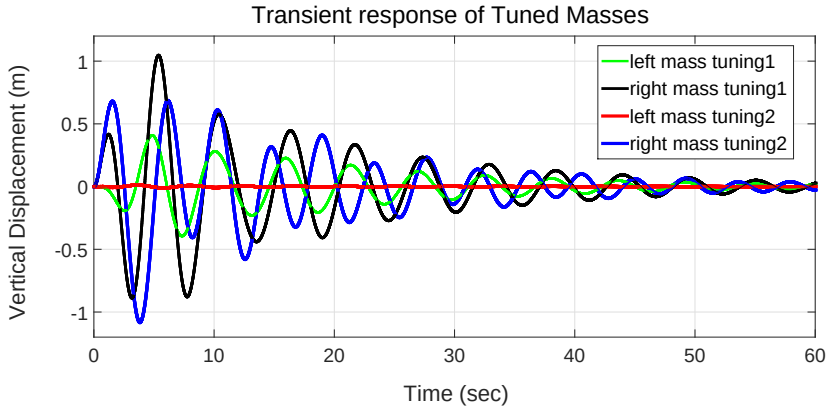


(b)

Figure 6.20 (a)Root loci of the section deck-TMD system with tuning parameters resulting from equations (6.33)-(6.35). Wind speed is swept from 0-95m/s (b) Transient response of mass dampers for the 2 tuning procedures. Initial condition assumes pitch of $2^o$ at t=0s

Fig. 6.21 demonstrates the TMD stabilization performance against self-excited instabilities and torsional divergence in a range of frequencies. It should be noticed that the mass

damper optimum frequency is estimated around $\omega_t = 1.1 rad/s$, which is different than the one estimated before. Use of explicit formulae, based on a single degree of freedom formuation, is thus not very accurate for determining optimal TMD parameters for controlling the coupled flutter phenomenon. This can be attributed to the fact that the frequency, damping ratio and complex mode shape of the target mode branch vary with increasing wind speed, which in turns affects the performance of the TMD [40]. For achieving more accurate tuning parameters one should rely on parametric studies or use of an optimization based framework, as was undertaken in the preceding analysis.

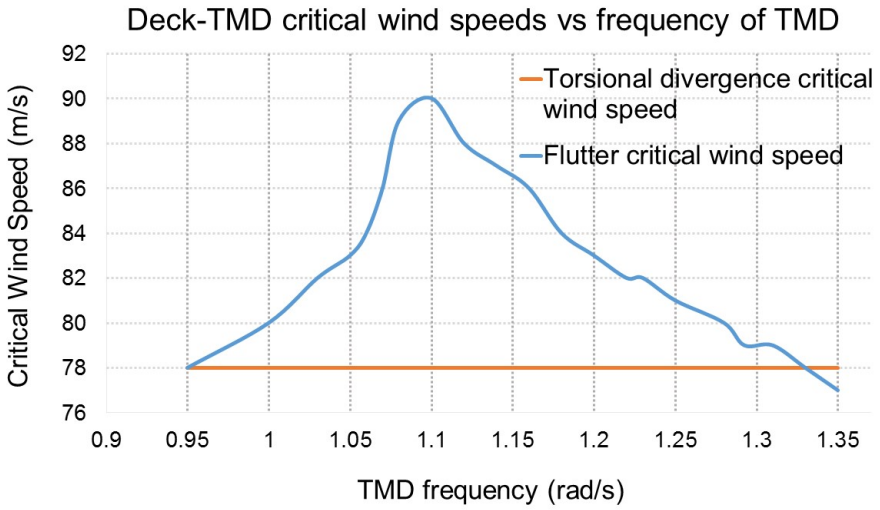


Figure 6.21 Effectiveness of TMDs versus frequency of TMD for TMD damping ratio $\xi_t = 18.7\%$

### 6.4.4 Section Summary

This section serves as a review of TMD implementation in controlling self-excited motion. It was demonstrated that the use of an eccentric mass and tuned mass dampers contributes only to a minor degree to the improvement of aeroelastic limits. The analysis presented was restricted to thin airfoil theory for the description of aerodynamic loading and the structure was modelled by a sectional model, which neglects intermodal coupling among structural modes and dampers. Foregoing studies have investigated the dependence of TMDs on bridge aeroelastic characteristics. The distinction between hard-type and soft-type flutter

has been introduced and it has been shown that for the latter case tuned dampers have a considerable impact on the flutter critical wind speed. TMD performance has also been proven to be sensitive to design parameter tuning around their optimal values, which poses a severe limitation in terms of the system's robustness. This work also showed that TMDs are unsuccessful in increasing the bridge's torsional divergence speed. This is an important drawback as it is often the case that flutter critical wind speed is close to the divergence limit, e.g. Humber Bridge. Finally the TMDs experience large displacements, *TMD stroke*, relative to the deck, particularly on the leeward side. The presented design will serve as a building block for the next section, in which a kinematic constraint between the mass dampers and flaps is introduced. It was demonstrated that passive flaps can favorably modify the system's aerodynamic characteristics, allowing a hard-type flutter to become a soft-type flutter, whereas the auxiliary damped masses control the flap movement and provide additional damping.

## 6.5 A Nexus Between Tuned Mass Dampers and Flaps

In this section the Tuned Mass Damper's (TMD) properties are exploited in order to control aerodynamic surfaces adjacent to the deck. The combined system is referred to as the *flap mass damper* (FMD). It is shown that this novel approach can significantly improve the aeroelastic limits while achieving good robustness margins, as well as limiting rotations of the flaps and vertical movement of the suspended masses. The function of the tuned mass in this case is twofold. Firstly, the motion of the masses is related to the deck's heaving and pitching movement and consequently it consists of an indirect way of sensing the input signal for the flap controllers. The proposed linkage between the tuned masses and the flaps relates to the inherent problem of passive systems based on flaps associated with lack of access to a ground reference point. Consequently, flap rotation cannot be explicitly linked to deck movement. The tuning procedure of the TMD in essence establishes the feedback relationship between the two components, flaps and TMDs, and a virtual ground connection is achieved. Secondly, the oscillating masses provide driving forces for controlling flap

rotation. In general it is expected that the flap which attracts greater aerodynamic force will require a larger mass connected to it.

### 6.5.1 Passive Control with Movable flaps and a linked TMD (Flap Mass Damper)

Similarly to previous sections, application of classical mechanics to the combined system of the deck with two symmetrically placed suspended masses and leading and trailing flaps, Fig. 6.22, results in the following equations of motion. The four independent degrees of freedom are the deck heave, pitch and the leading and trailing flap angles.

$$m_f\ddot{h}+(S_\alpha-m_{dl}d_{tm}+m_{dr}d_{tm})\ddot{\alpha}+(S_\beta+m_{dl}r_l)\ddot{\beta}_l+(S_\gamma-m_{dr}r_t)\ddot{\beta}_t+C_h\dot{h}+K_hh=L, \tag{6.36}$$

$$(S_\alpha-m_{dl}d_{tm}+m_{dr}d_{tm})\ddot{h}+I_f\ddot{\alpha}-(I_\beta-bc_lS_\beta+m_{dl}r_ld_{tm})\ddot{\beta}_l+(I_\gamma+bc_tS_\gamma-m_{dr}r_td_{tm})\ddot{\beta}_t+ \\ +C_\alpha\dot{\alpha}+K_\alpha\alpha=M, \tag{6.37}$$

$$(S_\beta+m_{dl}r_l)\ddot{h}-(I_\beta-bc_lS_\beta+m_{dl}r_ld_{tm})\ddot{\alpha}+(I_\beta+m_{dl}r_l^2)\ddot{\beta}_l+ \\ +(C_\beta+r_l^2C_{dl})\dot{\beta}_l+(K_\beta+r_l^2K_{dl})\beta_l=M_l^\beta+M_c^{\beta_l}, \tag{6.38}$$

$$(S_\gamma-m_{dr}r_t)\ddot{h}+(I_\gamma+bc_tS_\gamma-m_{dr}r_td_{tm})\ddot{\alpha}+(I_\gamma+m_{dr}r_t^2)\ddot{\beta}_t+ \\ +(C_\gamma+r_t^2C_{dr})\dot{\beta}_t+(K_\gamma+r_t^2K_{dr})\beta_t=M^{\beta_t}+M_c^{\beta_t}, \tag{6.39}$$

where $m_f=m_d+m_\beta+m_\gamma+m_{dl}+m_{dr}$ and $I_f=I_a+m_{dl}d_{tm}^2+m_{dr}d_{tm}^2$. The expressions for aerodynamic lift $L$ and the aerodynamic moments $M$, $M^{\beta_l}$, $M^{\beta_t}$ follow the same formulation developed in section 6.2.2.

The kinematic constraint between the tuned mass and the flap angle can be realized in different ways, for example through a rack, pinion and belt mechanism or by a connection using levers and a gear box. A conceptual realization of the proposed mechanism is graphically presented in Fig. 6.22. In this design, the TMD movement is transmitted through a rack-pinion-belt linkage. For the leading-edge flap a single pinion of radius

$r_o$ is used and for the trailing flap two pinions are needed in order to reverse the angle. Assuming radii of the pinions at the flap pivots $r_l$ and $r_t$, it is computed that $h_{dl} = \beta_l \times r_l$ and $h_{dr} = -\beta_t \times r_t$. The sign for the latter expressions was determined after preliminary numerical investigations and showed to exhibit optimum performance. For the current analytic investigation, however, it is only of essence to determine the kinematic relationship between the mass's vertical movement and the flap's rotation.

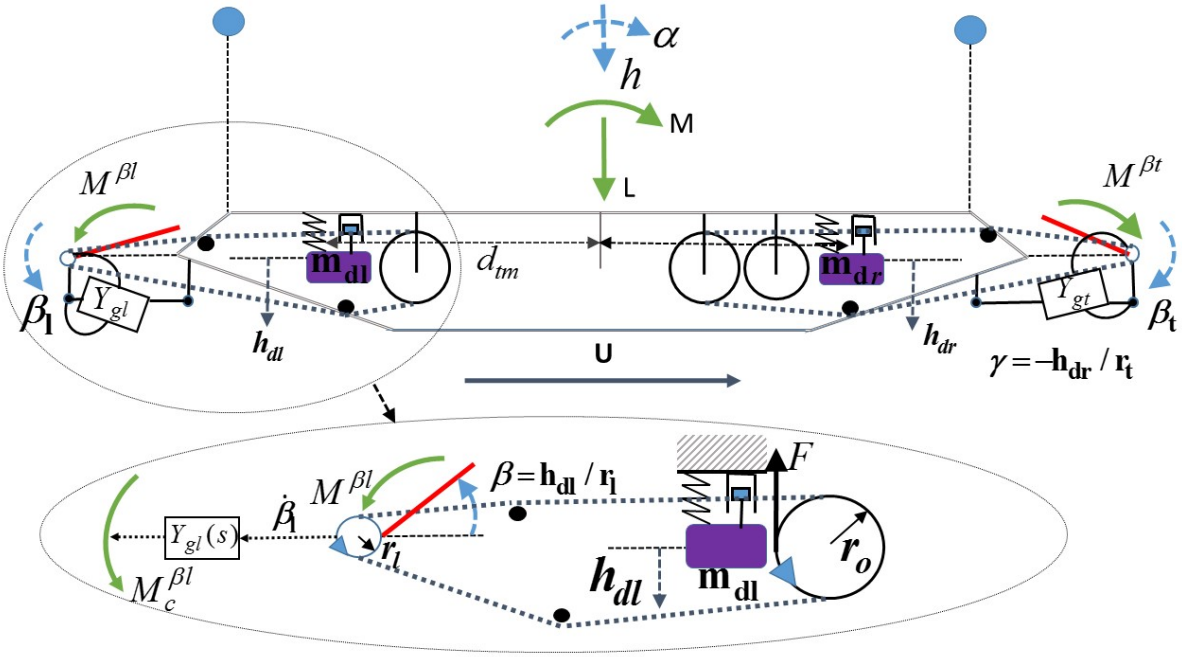


Figure 6.22 Conceptual mechanical configuration of the Flap Mass Damper mechanism.

In terms of the mechanical network at the flap pivot point, different alternatives of increasing complexity were investigated. It was again observed that using a first order compensator in parallel to structural flap retention components resulted in the simplest network with marginally worse performance when compared to higher order compensators. Referring to Fig. 6.2 the flap angular rates $\dot{\beta}_l, \dot{\beta}_t$ are the inputs to the compensators, which in turn produce the flap torques $M_c^{\beta_l}$ and $M_c^{\beta_t}$ as outputs. in Fig. 6.22 the overall compensator mechanical structures are denoted by $Y_{gl}(s)$ and $Y_{gt}(s)$ for the leading and trailing flap respectively. The number of optimization parameters is 14, $2 \times 4$ for the compensators at the flap pivot plus 6 parameters for the mechanical components of the mass dampers.

Similarly to section 6.3.4, the objective is to minimize the robustness index and $Y_{gl/gt}(s)$ are constrained to be passive. Table 6.7 summarizes the mechanical components of the FMD for 3 hinge locations whereas Table 6.8 presents the key findings related to aeroelastic stability limits and robustness properties.

| Cases | $m_{dl}$ $(kg/m)$ | $\zeta_{dl}$ % | $K_{dl}$ $(kN/m)$ | $m_{dr}$ $(kg/m)$ | $\zeta_{dr}$ % | $K_{dr}$ $(kN/m)$ | Leading Flap Controller | Trailing Flap Controller |
|---|---|---|---|---|---|---|---|---|
| 1 | 945 | 19.2 | 141300 | 828 | 4.8 | 16510 | $\frac{-7.35\times10^6 s-1620}{95.68s+147.8}$ | $\frac{-1.89\times10^6 s-1.73\times10^6}{18.18s+68.91}$ |
| 2 | 914.9 | 11.1 | 169280 | 803.7 | 8.3 | 28280 | $\frac{-1.03\times10^7 s-1460}{86.21s+233.3}$ | $\frac{-8.172\times10^6 s-1245}{70.73s+208.3}$ |
| 3 | 936.6 | 7.6 | 110740 | 267.2 | 9.5 | 43390 | $\frac{-883000s-80}{101.5s+32.26}$ | $\frac{-285000s-30}{10.36s+52.62}$ |

Table 6.7 Optimized mechanical FMD components for the 3 hinge locations cases depicted in Fig. 6.3. Damping ratios are defined as: $\zeta_{dl} = \frac{C_{dl}}{2\omega_{dl}m_{dl}}$ and $\zeta_{dr} = \frac{C_{dr}}{2\omega_{dr}m_{dr}}$ .

| Cases | Flutter Speed | Div. Speed | Rob. Index | Max. Tor. Variation |
|---|---|---|---|---|
| 1 | $110m/s$ | $81m/s$ | 2.58 | 2% |
| 2 | $117m/s$ | $86m/s$ | 3.62 | 3% |
| 3 | $93m/s$ | $104m/s$ | 2.7 | 5% |

Table 6.8 Aeroelastic performance limits for optimized mechanical FMD components for the 3 hinge locations depicted in Fig. 6.3.

Comparing the results in Table 6.8 with those of Table 6.3, it is shown that aeroelastic performance is improved when an auxiliary TMD is kinematically connected to the flaps. For cases 1 and 2 the aeroelastic limit is posed by the torsional divergence speed. When the flap pivot points are places at the outer edge of the flaps, the divergence speed is increased significantly making it possible to achieve better performance. Moreover, when the limit is posed by the divergence, smaller tolerance to torsional stiffness variations is attained. The improved closed-loop stability properties of the FMD can be shown by comparing the root loci of case 3b, Table 6.3, with that of case 3, Table 6.8.

Fig. 6.25 presents the transient response of the deck heave, deck pitch and flap rotations for the three methodologies described in this chapter, for a wind speed $U = 76m/s$. The transient response is comparable in all cases, however the FMD exhibits slightly smaller

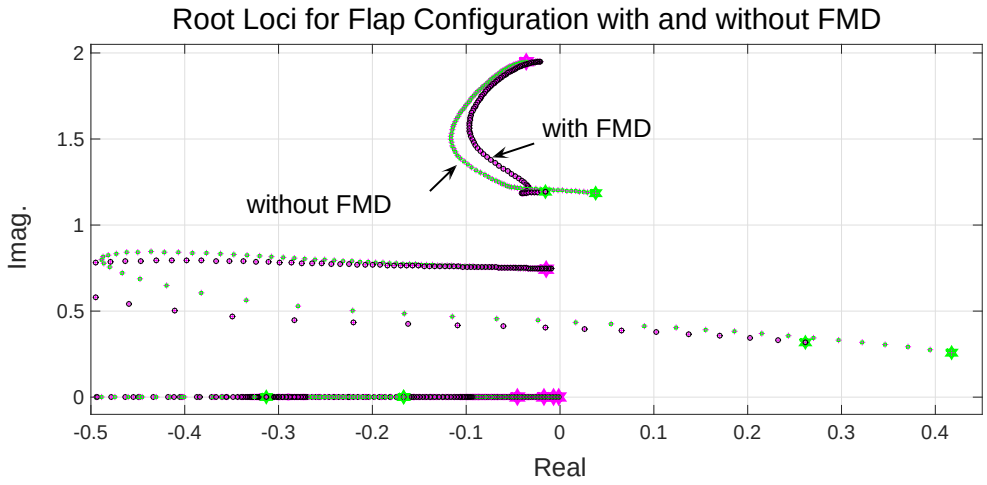


Figure 6.23 Root Loci of case 3b of Table 6.3 and case 3 of Table 6.8. The wind velocities are swept from 0 to 100m/s.

flap rotations compared to the case when only movable flaps are present. It is recalled that it is important to restrict flap movement so as to avoid flow separation and bluff body behaviour in general, in order to abide with the thin aerofoil assumption. In Fig. 6.24 the suspended mass movement is presented for the TMD2 case and for case 3, Table 6.8. It becomes apparent that the FMD provokes much less mass vertical movement compared to when only the TMD is implemented.

As already stressed, TMD parametric tuning sensitivity poses a serious reliability issue. Fig. 6.26 presents the FMD's effectiveness over tuning frequency variations of the leeward suspended mass, which is the most important. Compared to the equivalent TMD graph of Fig. 6.21 it is clearly illustrated that the FMD's performance is much less sensitive to optimal tuning of mechanical components. The presented optimization framework determined the tuning frequency of the right mass to be $\omega_{dr} \approx 12.75 rad/s$. From the following figure it is seen that this value is a trade-off between achieved performance and robustness. The loss in robustness is explained by the steep drop in flutter boundaries at frequencies greater than $\omega_{dr} \approx 13.75 rad/s$. This behaviour is due to a change in the flutter mode which becomes unstable for this choice of tuning parameters.

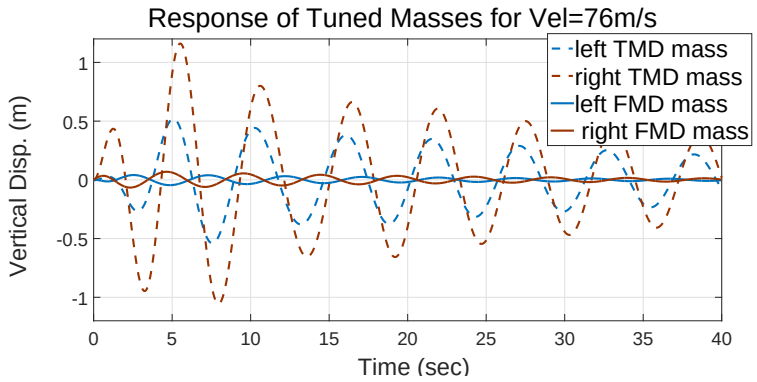


(a)

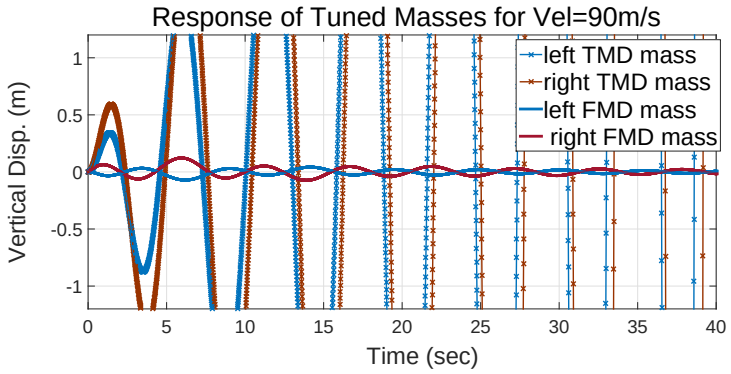


(b)

Figure 6.24 Vertical mass movement of the mass dampers for cases TMD2 from Table 6.6 and Case 3 from Table 6.8 and for wind speeds (a) 76m/s, both TMD and FMD stable, (b) 90m/s, FMD stable and TMD unstable.

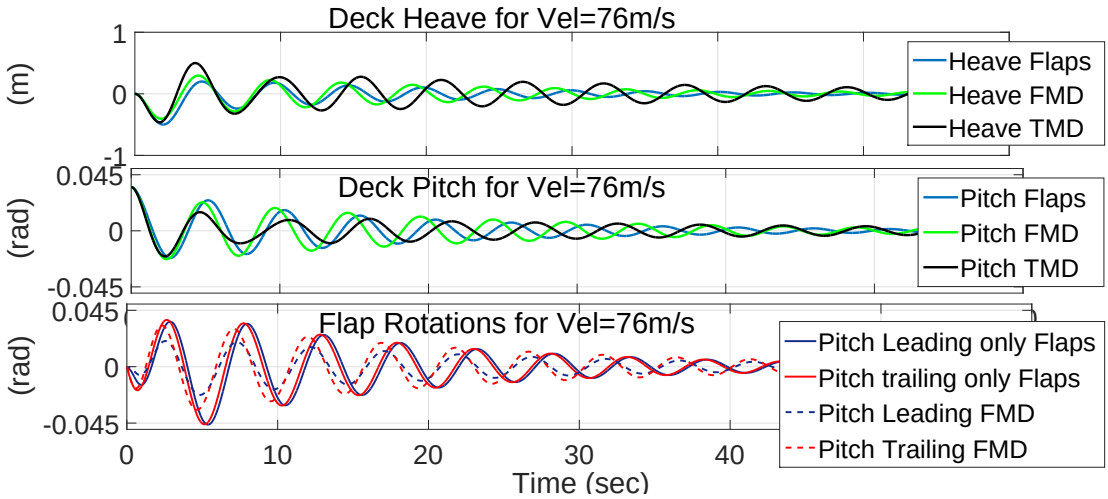


Figure 6.25 Transient response of deck heave, deck pitch and flap rotations for the following cases: i)case 3b from Table 6.3, ii) case 3 from Table 6.8 and iii) case TMD2 from Table 6.6.

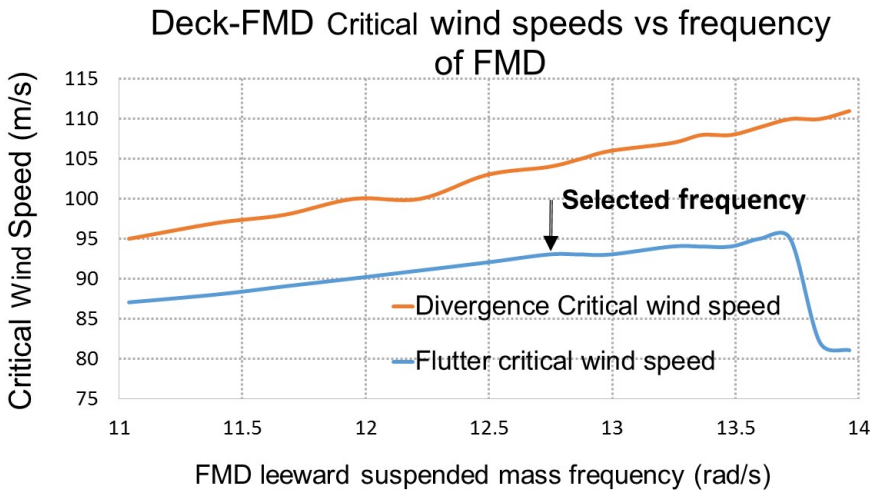


Figure 6.26 Effectiveness of FMD against tuning frequency of the right mass.

## 6.6 Discussion and Concluding Remarks

This chapter analytically investigated the improved aeroelastic performance of three passively controlled mechanical networks. It was shown that the implementation of single tuned mass dampers is laced with problems associated to poor robustness margins and large movement of the suspended masses. On the contrary, solutions based on movable flaps, show great promise. The first approach is based on a kinematic deck-flap arrangement, where an optimization process is used for tuning the mechanical components at the flap pivot points as well as the connection location between the deck and flaps. It was shown that locating the flap hinges at the flap outer edges while optimizing for the flap retention components increases aeroelastic stability. Addition of a passive first order compensator, including inerter components, helps achieve better robustness properties.

The second approach focused on combining the benefits of tuned mass dampers systems with that of optimum flap kinematics. A transmission system designed out of purely passive components (spring, dampers and inerters) aims at achieving maximum robustness margins to structural and aerodynamic uncertainties. The proposed design avoids the inherent shortcomings of TMDs while increasing flap effectiveness by providing additional structural

damping. An advantage of both procedures is that the network layout is not preselected, but determined through an optimization process. The FMD leads to a more more complicated design, but avoids external structural linkages which can pose serious technical difficulties as well as altering the deck's aerodynamic properties. Passive arrangements of this sort are not only appealing because of their practical simplicity and reliability but can even exhibit advantages when compared to active control schemes. The reason is largely based on the fact that the optimal arrangement of deck-flap kinematics raises the divergence boundary and thus helps avoid large flap angle magnitudes and associated large torques as controller outputs.

# Chapter 7

# Passive Aeroelastic Control of a Suspension Bridge during Erection

## 7.1 Introduction

This chapter will extend the analytic investigation of the previously proposed passive control mechanisms on the FE aeroelastic model. Particular emphasis is placed on the early stages of the deck erection process, where the structure's vulnerability to flutter has been established. In the following FE implementation the focus will be on the first passive deck-flap network examined in Chapter 6 because of its construction simplicity and promising aeroelastic performance exhibited on the sectional investigations. It is however expected that implementation of the flap mass damper mechanism will yield better results, due to the additional structural damping provided by the auxiliary TMD. Its performance remains to be revealed in future examination.

The practical use of nonlinear optimization algorithms in a high mode aeroelastic model necessitates the use of reduced order models. The techniques here employed relate to the determination of the dominant poles, and the corresponding dominant modes of the system transfer function, which are specific eigenvalues and eigenvectors of the state matrix. The eigensolution methods for computing dominant poles and modes are briefly reviewed and their effectiveness is demonstrated on the bridge aeroelastic model. The overall framework

for tuning the passive feedback components on the full model is reviewed. Multimodal interactions are observed at the various erection stages and conclusions are drawn with regard to contribution of various vibration modes to aeroelastic instabilities. The Humber Bridge is again the chosen example for numerical simulations.

## 7.2 Implementation of Flap Dynamics in the FE model

The deck-flap kinematic model presented in Fig. 6.1 is incorporated in the FE structural element, as presented in Fig. 3.4. The flap additional terms related to their kinematic and potential energy contribution are added to the corresponding bridge terms as expressed in [1–3]. These quantities are given in (7.1) and (7.2) respectively.

$$T_l = \frac{1}{2}\int_{A_l}[-(r-r_b)\dot{\beta}_l]^2 dm \quad T_t = \frac{1}{2}\int_{A_t}[(r-r_{gam})\dot{\beta}_t]^2 dm \tag{7.1}$$

$$V_f = \frac{1}{2}K_\beta(\beta_l)^2 + \frac{1}{2}K_\gamma(\beta_t)^2 \tag{7.2}$$

The full structural matrices including the flap terms are given in Appendix B.

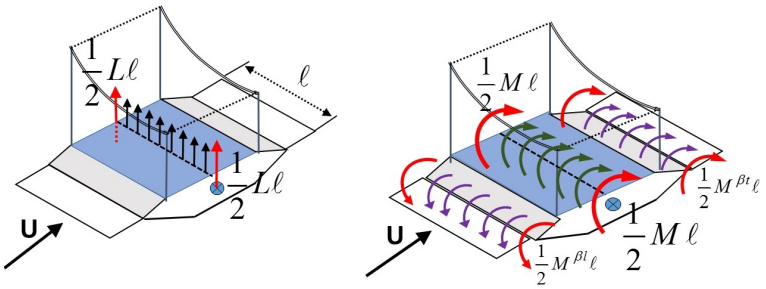


Figure 7.1 Relating the aerodynamic forces to the element nodes.

The aerodynamic force modelling follows a similar lumping approach to Chapter 4, Fig. 4.8. The aerodynamic moments on the flaps $M^{\beta l}$ and $M^{\beta t}$ acting about the leading-and trailing-edge flap hinges respectively are also lumped at the end nodes of each element, see Fig. 7.1.

## 7.3 Model Reduction of Aeroelastic Model

This section presents an algorithm for computing the dominant eigenvalues and corresponding eigenvectors of a large scale dynamical system. This procedure seeks to dispense with the less important characteristics of the model and thus reduce the size of the state-space. Because almost all of the quantities in this chapter are either matrices or vectors, boldface notation is omitted.

### 7.3.1 Dominant Poles and Modal Equivalent

The flap controller design optimisation process requires the use of a nonlinear programming algorithm, which can be expensive to run in terms of computing resources. Given that the system model has hundreds of states, significant practical design benefits derive from the use of a reduced-order system model.

The model reduction framework adopted here follows the following framework. Assume a stable $n^{th}$ order time invariant descriptor multi-input multi-output system (MIMO) $(E_f, A_f, B_f, C_f)$ of the form

$$\begin{cases} E_f \dot{x}_f = A_f x_f + B_f u \\ z = C_f x_f, \end{cases} \tag{7.3}$$

where, $E_f, A_f \in \mathbb{R}^{n\times n}$, $B_f \in \mathbb{R}^{n\times m}$, $C_f \in \mathbb{R}^{p\times n}$, $x_f \in \mathbb{R}^n$, $u \in \mathbb{R}^m$ and $z \in \mathbb{R}^p$. The descriptor matrix $E_f$ may be singular. If $E_f$ is non-singular, the system can be transformed to a regular state-space form $(E_f^{-1}A_f, E_f^{-1}B_f, C_f)$ although this might not always be computationally efficient [160]. The model reduction problem consists in finding a stable $k^{th}$ order system $(\tilde{E}_f, \tilde{A}_f, \tilde{B}_f, \tilde{C}_f)$:

$$\begin{cases} \tilde{E}_f \dot{\tilde{x}}_f = \tilde{A}_f \tilde{x}_f + \tilde{B}_f u \\ \tilde{z} = \tilde{C}_f \tilde{x}_f, \end{cases} \tag{7.4}$$

where $k \ll n$, and $\tilde{E}_f, \tilde{A}_f \in \mathbb{R}^{k\times k}$, $\tilde{B}_f \in \mathbb{R}^{k\times m}$, $\tilde{C}_f \in \mathbb{R}^{p\times k}$, $\tilde{x}_f \in \mathbb{R}^k$, $u \in \mathbb{R}^m$ and $\tilde{z} \in \mathbb{R}^p$. The number of inputs and outputs are hence the same as for the original system. The reduced order model should satisfy the following requirements [160]:

- The approximation error must be small, meaning that that the output error $||z(t) - \tilde{z}(t)||$ should be minimized for some or all the inputs $u(t)$.
- The order of the reduced system should be much smaller than the order of the original system $k \ll n$.
- The reduced model must preserve the structure of the original model especially in terms of stability and passivity.
- The reduced model must be physically realizable.

The model reduction methods implemented in this work are based on the premise that the reduced-order model is constructed via a Petrov-Galerkin projection

$$(\tilde{E}_f, \tilde{A}_f, \tilde{B}_f, \tilde{C}_f) = (Y^* E_f X, Y^* A_f X, Y^* B_f, X^* C_f), \tag{7.5}$$

where $X, Y \in \mathbb{R}^{n \times k}$ are matrices whose columns form the bases of relevant subspaces in the state-space. The procedure adopted in this paper is that of the dominant pole algorithm (DPA) first proposed by Martins et al. [125]. The transfer function $G(s)$ of the system in Eq.(7.3) is given by

$$G(s) = C_f (sE_f - A_f)^{-1} B_f, \tag{7.6}$$

where $s$ is the Laplace variable. The poles of the transfer function (7.6) are the eigenvalues $\lambda_i \in \mathbb{C}$ of the matrix pencil $(A_f, E_f)$, some of which might be at infinity. An eigentriplet $(\lambda_i, v_i, w_i)$ contains an eigenvalue as well as the right and left eigenvectors $v_i, w_i \in \mathbb{C}^n$

$$\begin{cases} A_f v_i = \lambda_i E_f v_i, \;\; v_i \neq 0 \\ w_i^* A_f = \lambda_i w_i^* E_f \;\; w_i \neq 0. \end{cases} \tag{7.7}$$

If the pencil has a simple eigenstructure, non repeated eigenvalues, then the transfer function can be expressed as a sum of residue matrices $R_j \in \mathbb{C}^{p \times m}$ over the first order poles [93, 125]

$$G(s) = R_\infty + \sum_{j=1}^{\tilde{n}} \frac{R_j}{s - \lambda_j}, \tag{7.8}$$

where, $\tilde{n} \leq n$ is the number of finite poles (eigenvalues), and $R_\infty$ is the contribution due to poles at infinity. It can be therefore concluded that $G(s)$ can be effectively approximated by the sum of $k < \tilde{n}$ terms, which have the largest residue magnitudes $|R_j|$. The reduced sum of $k$ terms determine the so called *effective* transfer function [125]. Large residue magnitudes translate to good observability and controllability for the associated pole, thus signifying *pole dominance*. This means that the peaks of the Bode magnitude plots occur at frequencies close to the imaginary parts of the dominant poles of $G(s)$. Hence, an approximation of $G(s)$ consisting of $k$ terms with the largest $|R_j|$ defines the approximation, which a *modal equivalent* of the original system as the poles are preserved.

$$G_k(s) = \sum_{j=1}^{k} \frac{R_j}{s - \lambda_j} \tag{7.9}$$

In general, dominant poles can be located anywhere in the $(A_f, E_f)$ spectrum. The proposed algorithm in [125] converges to the dominant poles of a single-input single-output system (SISO) using initial guesses as starting points, referred to as shifts. The exact definition of dominance therein, is given as follows.

**Definition 7.3.1** *Dominant Pole. A pole $\lambda_i$ of $G(s)$ with corresponding right and left eigenvectors $v_i$ and $w_i$ $(w_i^* v_i = 1)$ is called dominant if $\hat{R}_i = \frac{|R_i|}{|Re(\lambda_i)|} = \frac{|(C_f v_i)(w_i^* B_f)|}{|Re(\lambda_i)|}$ is relatively large compared to $\hat{R}_j, i \neq j$.*

A modal equivalent that consists of the most dominant terms determines the effective transfer function behaviour. iF $X \in \mathbb{C}^{n \times k}$ and $Y \in \mathbb{C}^{n \times k}$ contain the right and left eigenvectors $v_i$ and $w_i$ of $(A_f, E_f)$ as column vectors, such that $Y^* A X = \Lambda = diag(\lambda_1, ..., \lambda_k)$ and $Y^* E_f X = I$, then the reduced system can be derived as follows by setting $x = X\tilde{x}$ and left multiplying by $Y^*$.

$$\begin{cases} \dot{\tilde{x}}_f(t) = \Lambda \tilde{x}_f(t) + (Y^* B_f) u(t) \\ \tilde{z}(t) = (C_f X) \tilde{x}_f(t) \end{cases} \tag{7.10}$$

For stable systems, the error in the modal equivalent can be quantified as follows [80]

$$\|G-G_k\|_\infty = \left\| \sum_{j=k+1}^{n} \frac{R_j}{s-\lambda_j} \right\|_\infty \leq \sum_{j=k+1}^{n} \frac{\|R_j\|}{|Re(\lambda_j)|}. \tag{7.11}$$

The model is said to satisfy an infinity norm bound on the absolute approximation error. A significant advantage of this framework is that the poles of the reduced-order model retain their physical interpretation, some modes for example are expected to exhibit significant contribution on the bridge's aeroelastic behaviour. Furthermore, the procedure is automatic while retaining the poles which contribute mostly to the associated transfer function.

### 7.3.2 Computation of Dominant Poles

The poles of the transfer function in Eq.(7.6), $\lambda \in \mathbb{C}$ satisfy the condition $\lim_{s\to\lambda}||G(s)||_2 = \infty$. The reciprocal of the transfer function is then considered

$$H : \mathbb{C} \to \mathbb{C} : s \to \frac{1}{G(s)}. \tag{7.12}$$

For a pole $\lambda$ of $G(s)$, $\lim_{s\to\lambda} H(s) = 0$. In other words, the poles are the roots of $H(s)$ and a Newton method is usually employed for finding them. Furthermore, the derivative of $H(s)$ with respect to s is given by

$$H'(s) = \frac{G'(s)}{G^2(s)}. \tag{7.13}$$

And the derivative of $G(s)$ with respect to $s$ is

$$G'(s) = -C_f(sE_f - A_f)^{-1}E_f(sE_f - A_f)^{-1}B_f. \tag{7.14}$$

Making use of equations (7.13) and (7.14) leads to the following Newton scheme

$$s_{k+1} = s_k - \frac{H(s_k)}{H'(s_k)} = s_k + \frac{1}{G(s_k)}\frac{G^2(s_k)}{G'(s_k)} = s_k - \frac{C_f(s_kE_f - A_f)^{-1}B_f}{C_f(s_kE_f - A_f)^{-1}E_f(s_kE_f - A_f)^{-1}B_f}. \tag{7.15}$$

Using the notations $v_k = (s_k E_f - A_f)^{-1} B_f$ and $w_k = (s_k E_f - A_f)^{-*} C^*$ Eq. (7.15) can be rewritten as

$$s_{k+1} = \frac{C(s_k E_f - A_f)^{-1} A_f (s_k E_f - A_f)^{-1} B_f}{C_f (s_k E_f - A_f)^{-1} E_f (s_k E_f - A_f)^{-1} B_f} = \frac{w_k^* A_f v_k}{w_k^* E_f v_k}. \tag{7.16}$$

An algorithmic implementation of the DPA by use of the LU-factorization can be found in [160]. If an exact LU-factorization is not available, one has to use inexact Newton schemes, such as Jacobi-Davidson style methods.

For Singe-Input-Single-Output (SISO) systems the transfer function gain can be defined by a single complex number for any frequency. For MIMO systems on the other hand, the transfer function matrix is of dimensions $p \times m$ and hence does not have a unique gain for a given frequency. The SISO concept of single transfer function gain needs to be replaced by a range of gains, having upper and lower bounds [126]. These bounds are expressed in terms of singular values of $G(s)$. Setting $s = i\omega$, where $\omega$ is the frequency range $0 \leq \omega \leq \infty$ and denoting the smallest and largest singular values of $G(i\omega)$ by $\sigma_{min}(\omega)$ and $\sigma_{max}(\omega)$, it follows for square $G(s)$ matrices that

$$\sigma_{min}(\omega) \leq \frac{\|G(i\omega)u(i\omega)\|_2}{\|u(i\omega)\|_2} \leq \sigma_{max}(\omega). \tag{7.17}$$

The singular values of $G(s)$ are also referred to as *principal gains* [80]. Plots of the smallest and largest singular gains against frequency, are referred to as *sigma plots*. Dominant poles of the MIMO system can be observed from the corresponding $\sigma_{max}$-plot of $G(s)$, where peaks occur at frequencies close to the imaginary parts of the dominant poles of $G(s)$. The performance of the effective transfer function can thus be assessed by comparing the sigma plots of the original and reduced system. Moreover, The dominant poles of a MIMO transfer function are those $s \in \mathbb{C}$ for which $\sigma_{max}(G(s)) \to \infty$ and a similar to the DPA case Newton scheme can be proved to converge. The interested reader is referred to [126] for further details.

### 7.3.3 Application of Model Reduction on the Bridge Aeroelastic Model

The MIMO variant of the DPA is used here to approximate the aeroelastic model of the partially complete Humber Bridge shown in Fig. 7.2. In the model reduction study the


Figure 7.2 Partially complete Humber Bridge used in model reduction study.

central span comprises 7 (out of 39) of the 36 m deck elements installed, the Hessle side comprises the cables only and the Barton side has 3, 50 m deck elements installed. The high-order open-loop system has approximately 860 state variables, which describe the bridge dynamics as well as bridge and flap aerodynamics. This configuration corresponds to an intermediate stage in the actual erection process. The central 5 elements on the central span are assumed fitted with leading- and trailing-edge flaps; flaps have not been included on the free end elements in order to avoid modelling 3D aerodynamic tip effects. Although finite aspect-ratio deck sections affect the aerodynamics in the erection stage, the influence of these effects decrease with increasing reduced frequency. Reduced order models are computed for each wind speed in the range of interest. Fig. 7.3 shows the eigenvalue spectrum of the original system at a wind speed of 55 m/s wind speed as well as the corresponding dominant poles after the MIMO dominant pole procedure (MDP) was applied. Fig. 7.4 further reduces the state space size through implementation of the balanced truncation procedure [80], to further reduce the number of states to 25. The unstable poles are preserved unaltered.

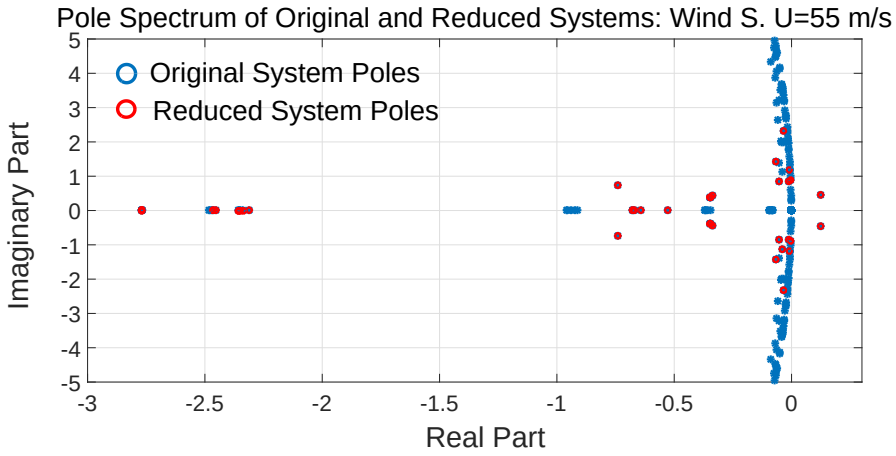


Figure 7.3 Pole locations of the original and reduced systems after implementation of the MIMO dominant pole algorithm. The original system has 864 states and the reduced-order model 74 states.

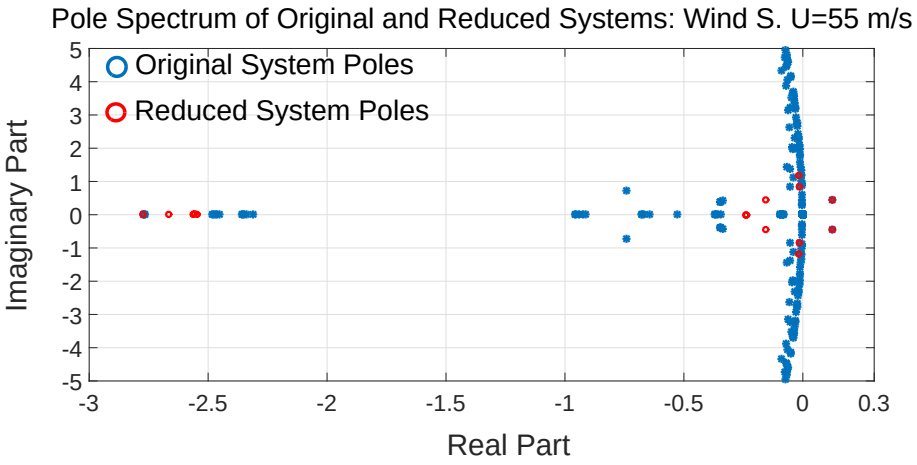


Figure 7.4 Pole locations of the original and reduced systems after implementation of dominant pole algorithm and balanced truncation. The original system has 864 states and the reduced-order model 25 states.

The frequency-gain properties of MIMO systems are best expressed in terms of the frequency-dependent transfer function matrix singular values [80]. Fig. 7.5 shows the effect of the model approximation process on the model's input-output properties. The transfer function studied here is ten-by-ten, with the ten inputs the torques applied to the five leading- and trailing-edge flaps. The ten outputs are the corresponding ten flap angle rates.

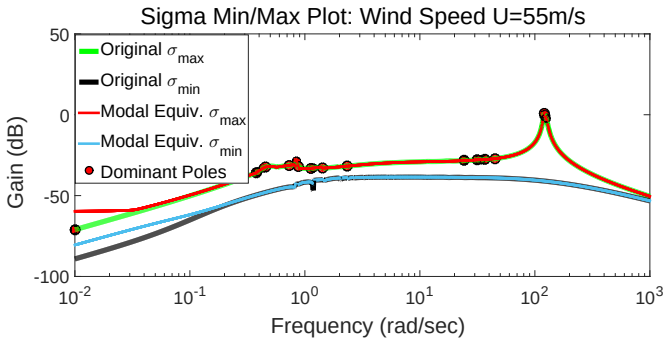


(a) MDP

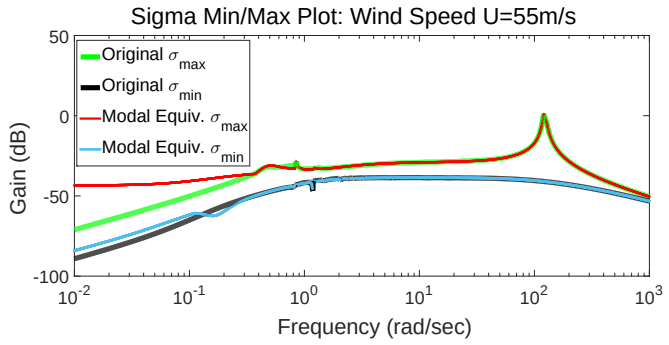


(b) MDP and Balanced Truncation

Figure 7.5 Largest and smallest singular values of the $10 \times 10$ transfer function that maps the ten flap torques into the corresponding ten flap angles. Figure (a) shows the characteristics of a 74-state reduced-order model computed using the MDP, [126]. Figure (b) shows the effect of a further balanced-truncation model reduction step to 25 states.

It can be concluded that the reduced-order equivalent model has frequency responses that closely matched those of the full-order model.

## 7.4 Overall Framework and End Flow Effects

### 7.4.1 Overall Framework

All the modelling and control system optimisation techniques are now in place; an overview summary and flow diagram is provided with regard to the modelling and control system synthesis processes in Fig. 7.6. The first step is to develop a structural model that reproduces the bridge's important modal characteristics, both as a complete structure, and at various stages of the erection process; see Chapter 3. The kinematics of the flaps, which are connected to the deck by a spring and damper, are included as FE elements. The introduction

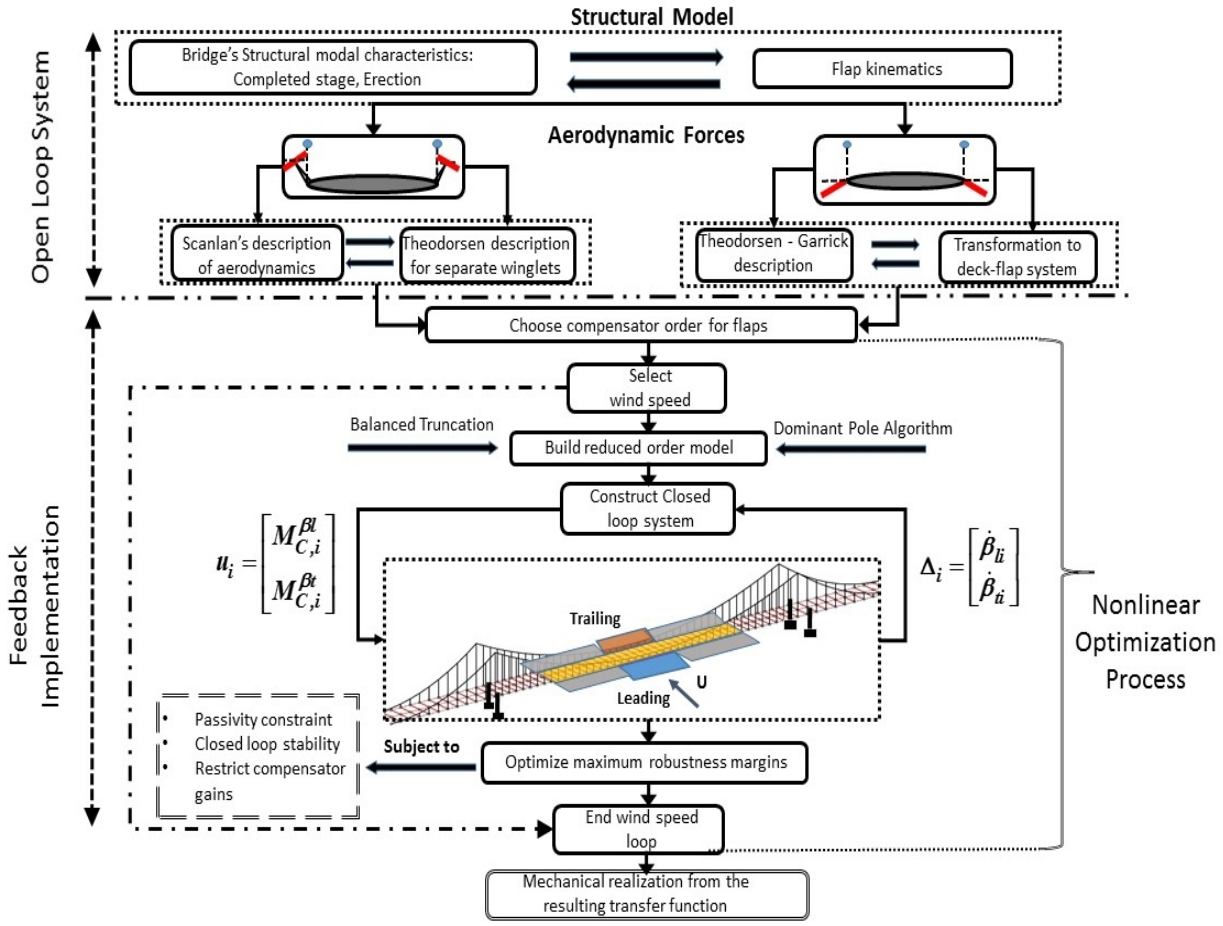


Figure 7.6 Controller-development flow diagram

of aerodynamic forces into the deck-flap system can be achieved in two different ways. If the deck and winglets can be considered aerodynamically separate, flutter derivatives, obtained from wind tunnel experiments or CFD simulations, can be used to describe self-excited forces on the deck; it is appropriate to model the winglets as thin aerofoils. Alternatively, if the deck and flaps interact aerodynamically, potential flow theory as developed by Theodorsen and Garrick [186, 187] can be used, following transformation described in section 5.2.1, to describe the aeroelastic process dynamics. A reduced-order model of the MIMO system is then constructed using a two-step model reduction process. The first model-reduction step is directed to retaining the dominant modes of the system and removing the others; this process does not destroy the physical insight associated with the retained modes. The second model-reduction step uses standard balanced truncation [80] as

is explained in Section 7.3. The reduced-order state-space description has the same number of inputs and outputs as the original system, but a significantly lower state dimension.

In order to introduce feedback control, the order of the compensator transfer function, at the flap connections, needs to be selected; first-order compensators are used here. These controllers are realised as a network of passive components that include springs, dampers and inerters [177]. The design optimisation of the parameters of the selected mechanical network components is achieved using a nonlinear programming code. Optimization constraints are introduced that ensure closed-loop stability, the passivity of the controller and introduce a limit to the compensator gain. Low controller gains are important, because high gains can cause large flap movements, which will in turn introduce flow separation that reduces the efficacy of the flaps.

### 7.4.2 End Flow Effects during Erection

A concern in the determination of aeroelastic stability boundaries during the deck erection process relates to the modelling of the flow effect around the free end of the suspended deck. In this work the aerodynamic loading distribution assumes a two-dimensional aerofoil assumption, which is very accurate for high-aspect ratio bodies but neglects aerodynamic features when it comes to lower aspect ratio finite spans. Such effects, which are effectively similar to finite wing aerodynamic modelling, have been omitted in this work due to lack of wind tunnel comprehensive experimental validations for bridge decks under erection. Furthermore, one of the few experimental examinations by Tanaka and Gimsing for the streamlined deck of the Hoga Kusten Bridge [184] estimated that considering flow three-dimensionality would result in a 5-10% higher flutter boundary. Their analysis was based on measuring the aerodynamic derivatives separately for a short span model with open edges and found that the obtained aerodynamic data were comparable to the two-dimensional results, but their magnitude, particularly of the pitching moment components, was significantly reduced due to edge effects. Tanaka et al. also reported in [185] that for the case of the shortest deck, typically 2 to 3 times longer than the deck width, the strip

theory assumption, without considering edge effects, would underestimate critical flutter speed by approximately 6%.

The afore mentioned results are conceptually consistent with the three-dimensional wing problem which predicts a smaller lift component and a smaller effective angle of attack depending on wing geometry. Finite span wings result in added wingtip vortices. The pressure difference between the top and the bottom wing, which generate these vortices, also produce an overall spanwise flow. Air over the top of the wing flows somewhat inward, while air on the bottom flows outward. The result is that small vortices form along the trailing edge where the inward and outward flows meet. Since the relative deflection of the two flows is smallest at the wing roots, the vortices there are less intense than the tip. The weaker inboard trailing edge vortices quickly merge downstream with the stronger wingtip vortex. The most wide spread approach for expressing the three-dimensionality of the flow in finite spans is through *Prandtl's Lifting Line Theory*. The theory assumes a number of spanwise *horseshoe* shaped vortices, which consist of a bound vortex carried in the wing and two trailing counter-rotating vortices [97].

Lifting line theory results in the following corrected expressions for the lift slope of a wing having an aspect ratio $AR$

$$\frac{dC_L}{d\alpha} = \frac{2\pi}{1+\frac{2}{AR}(1+\tau)}, \tag{7.18}$$

where $AR = \frac{l^2}{S}$ is the wing's aspect ratio, $S$ is the wing's area over the full span and $\tau$ is a correction factor depending on the wing's shape and aspect ratio. It is reminded that the lift slope of an ideal aerofoil is $2\pi$ [10], consequently Eq.(7.18) would indeed result in reduced lift. Furthermore, Eq.(7.18) is valid for relatively larger aspect ratios $AR > 4$. When the ratio is smaller the wing representation using a single lifting line across the span of the wing is not anymore valid. An approximate relation for the lift slope of low-aspect ratio

straight wings was obtained by Helmbold in 1942

$$\frac{dC_L}{d\alpha} = \frac{2\pi}{\sqrt{1+\left(\frac{2}{AR}\right)^2}+\frac{2}{AR}}. \tag{7.19}$$

Furthermore, the finite wing effect will also have as a consequence an increased drag component, *induced drag*, which needs to be considered in the model accordingly [10]. For the case of the Humber Bridge when 10% is erected the aspect ratio is $AR = \frac{l}{2b} = \frac{141}{28.8} = 4.95$, consequently the afore mentioned correction parameters could be accounted for in the aerodynamic model. However, care should also be placed in understanding how flow unsteadiness near flutter instability would affect the lift magnitude. Palacios et al. [150] examined how different models compare in capturing unsteady aerodynamic loads in relation to the wing's aspect ratio for different degrees of wing flexibility. For the stiffer sections, which would be applicable to a bridge case scenario, with $AR = 2$, the corrected strip theory agrees very well with *vortex lattice method* estimations at very low reduced frequencies (quasi-steady case). However, as the frequency increases, so does the discrepancy. For $AR = 10$, a similar bahaviour can be observed at very low reduced frequencies but at higher ones uncorrected strip theory is closer to the more computational robust estimations. When $AR = 10$ and reduced frequency is $k = 0.2$, which is close to the flutter boundary, neglecting aerodynamic end effects will actually provide more realistic results. In summary, a more reliable aerodynamic model could be pursued for the early erection stages but emphasis should be placed to the afore mentioned issues and further experimental investigation would be required.

## 7.5 Simulation results and control effectiveness

The procedure described in the previous section is now used to examine the incomplete deck scenario. The 18 % complete deck case (see Fig. 7.2) is used for illustration, since it represents a point of high vulnerability in the construction process. As is evident in Fig. 4.13, coloured column, the critical flutter and divergence wind speeds are estimated as

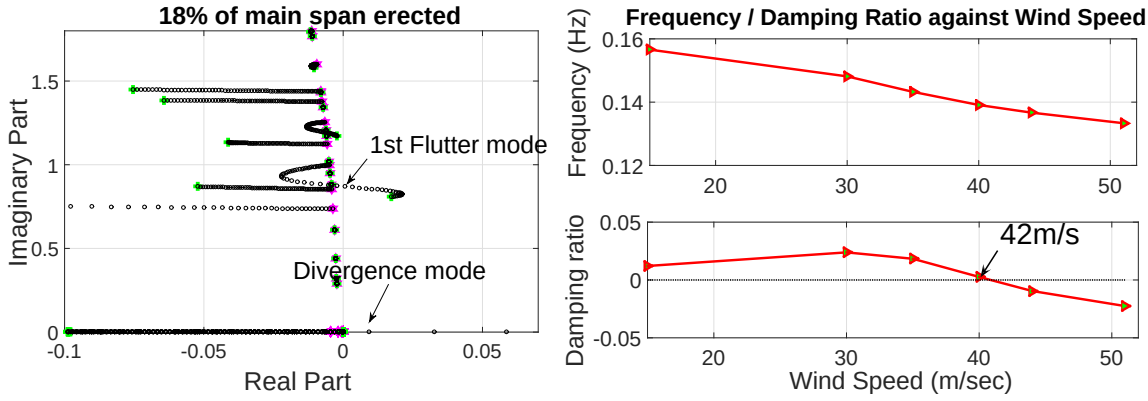


(a) (b)

Figure 7.7 (a) Root locus of the Humber bridge when 18 % of the main span is erected. The first and only flutter mode becomes unstable at $42\,m/s$. The torsional divergence mode reaches instability at $52\,m/s$. (b) Natural frequency (Hz) and damping ratio of the flutter mode as a function of wind speed.

$42\,m/s$ and $53\,m/s$ using thin aerofoil theory; the flaps are assumed rigidly attached to the deck. These critical speeds are significantly lower than the complete-structure values of 65 m/s and 72 m/s respectively; see Fig. 6.10 (a). Fig. 7.7 (a) shows the system root locus for the 18 % complete deck; the unstable flutter and torsional divergence modes are clearly visible.

Fig. 7.7 (b) presents the frequency and damping ratio of the flutter mode as a function of wind speed; the damping ratio goes negative at 42 m/s indicating flutter instability at this wind speed. At zero wind speed, where the aerodynamic influences are small, the mode's natural frequency and damping ratio is that of the first structural torsional mode. Fig. 7.8 presents the heave and torsional structural freedoms for the flutter mode as a function of wind speed. Since the phase information cannot be accurately conveyed in a diagram of this type, only the magnitudes of the real parts of the appropriate eigenvector components have been plotted.

At low wind speeds the heave motion is dominated by the second vertical symmetric mode, with the first vertical mode taking over at higher wind speeds. It is also evident from these figures that at all wind speeds the structural parts of the flutter mode are dominated by the fundamental torsional mode. The flat part of the torsion mode in the centre of the main span corresponds to completed section of the deck; see Fig. 7.2. The critical flutter

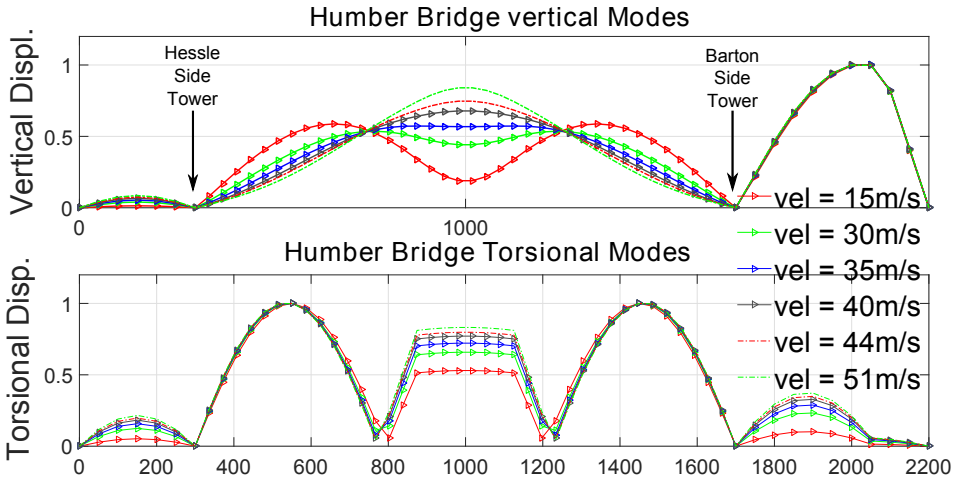


Figure 7.8 The heave and torsional components of the first flutter mode as a function of wind speed.

speed for the equivalent heave-pitch system was computed at $32\,m/s$, which is very close to the flutter speed limit reported in the literature as reproduced in Fig. 4.13. The difference highlighted by the red panel suggests that the higher order modes have a beneficial effect on the critical flutter speed.

The system used to increase the critical flutter speed at this stage of the construction comprises of movable leading- and trailing-edge flaps with a width of 2.75 m on either side of the central 180 m (five 36 m elements); of the 252 m (seven 36 m elements) assembled main span. Since there are five flap-equipped FEs, the feedback system has 10 inputs and 10 outputs. The $10 \times 10$ controller matrix is diagonal, since the flap compensators are decoupled from each other; the same compensators are used on each of the 5 leading- and trailing-edge flaps. Following the analysis presented in Sec.6.3.5, the flap hinge connections are located at the outside flap edges $l_d = 1, t_d = 1$. In contrast to the 4 DOF study presented in Section 6.3.4, the mechanical compensators produced a negligible improvement in the system robustness and so were omitted in this case. The system's robustness to variations in its mechanical properties did, however, improve as compared to its 4-DOF counterpart. Fig.7.9 shows that the closed-loop system has a critical flutter speed of $62\,m/s$ and a critical divergence speed of $82\,m/s$. In order to assess the system stability robustness, the structural stiffness matrix was perturbed from its nominal value with calculations showing that a

$\pm 6\,\%$ variation in stiffness can be tolerated for wind speeds up to 62 m/s. In the case of a $6\,\%$ decrease in stiffness, one is on the soft flutter stability boundary. In this case flutter locus starts from the first structural (vertical) heave mode as opposed to the first torsion (pitch) mode as seen in Fig. 6.10 (a).

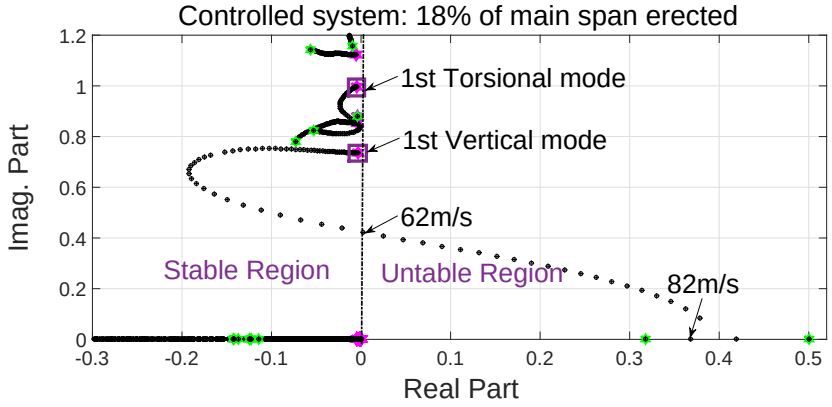


(a) Original

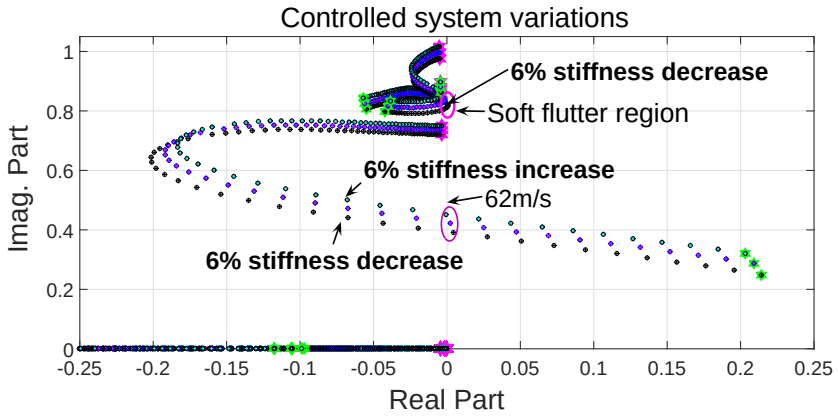


(b) Variations

Figure 7.9 (a) Root loci for the controlled 18% erected main span. The wind speed is swept from 0 to 83 m/s. The critical flutter speed is computed at 62 m/s and the torsional divergence speed at 82 m/s. The flap retention network is comprised of single springs and dampers in parallel with values: $K_\beta = 0.56 \times 10^5 KNm/m$, $K_\gamma = 1.47 \times 10^5 KNm/m$, $\zeta_\beta = 0.47\%$, $\zeta_\gamma = 0.77\%$ (b) Root loci of the nominal closed-loop system with variation of $\pm 6\%$ in the structural stiffness matrix. Wind speed is swept from 0 to 70m/s.

Fig. 7.10 demonstrates the efficacy of the flap support components $K_\beta$ and $K_\gamma$, $C_\beta$ and $C_\gamma$, in equations (6.11)-(6.12). The deck response corresponds to an initial twisting of the main deck by $2^o = 0.035$rad at its midpoint; the wind speed is $U = 51$ m/s, which is above the open-loop frozen-flap critical flutter speed of 42 m/s; the influence of the flap support components is clear.

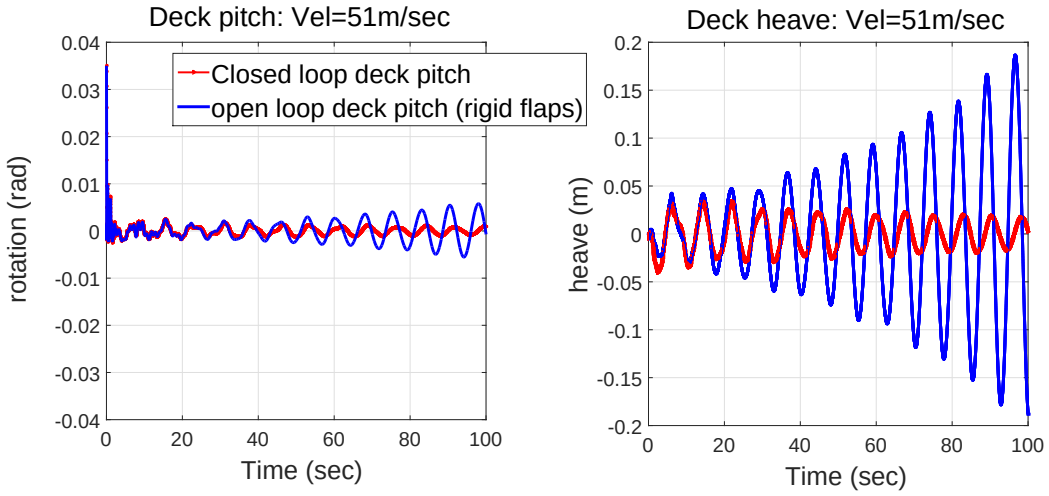


Figure 7.10 Time response of heave and pitch for the uncontrolled and controlled 18 % erected deck at wind speed $U = 51\,m/s$.

In an attempt to keep the further feedback design analysis as simple as possible, the network designed for the 18 % case is used at other mid-construction phases. Fig. 7.11 demonstrates the efficacy of the flap support components on the aeroelastic limits during several deck assembly stages. The percentage of flap length, in terms of the main-span length, used at every stage is also indicated in the graph, maximum amount of flap length is 33% of the main span implemented symmetrically around the midpoint.

In Section 6.3.4 it was observed that the proper selection of the spring stiffnesses $K_\beta$ and $K_\gamma$, the damping constants $C_\beta$ and $C_\gamma$ in equations (6.11) and (6.12) as well as the flap pivot locations in Fig. 6.9 would significantly increase the critical flutter speed. However, without an external control network, the system attained poor robust stability margins. It is apparent from Fig.7.11 that this lack of robustness is again evident. While the flap retention components are effective in increasing both the critical flutter and divergence speed at early stages of construction, their efficacy reduces as the bridge construction progresses beyond the 50 %-complete stage. As is evident from Fig. 7.11, towards the end of completion, the movable flaps are having a relatively small influence on increasing the critical flutter and divergence speeds. This is not entirely surprising, because the stiffness and damping parameter values were not re-tuned for subsequent construction phases. Furthermore, strong multimodal behaviours are presented in the intermediate stages, with higher flutter modes

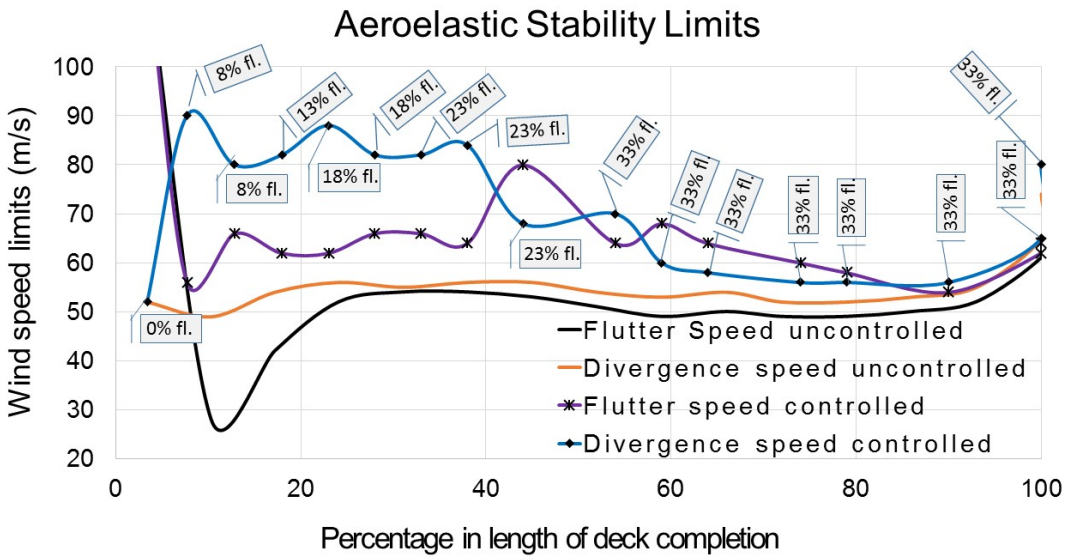


Figure 7.11 Aeroelastic stability limits against percentage deck completion for the rigid flap and movable flap cases. The flap support components are those determined in the 18 % completion study. The length of the leading- and trailing-edge flaps in each erection stage is indicated as a percentage of the main span length (fl=flap length), and the flap width is $2.75\,m$.

entering the response at wind speeds close to the first critical flutter speed. At completion, the computed flutter speed is only $U = 64$ m/s, which is slightly lower than the uncontrolled (rigid flap) flutter speed of $U = 65$ m/s; the rigid- and movable-flap divergence speeds are $U = 72m/s$ and $U = 80m/s$ respectively. If the optimization process is repeated for the complete bridge stage considering a passive compensator of the form given in Eq.(6.3.4), with the flaps covering the middle 33% of the main span, the resulting aeroelastic limits are significantly improved. It should also be stressed that as seen from the following figure there is a step increase in the full-bridge critical flutter speed when temporary end connections are replaced with permanent ones. Table.7.1 summarizes the attained aeroelastic limits and the control passive components for the completed bridge case.

| Flutter Speed | Tor. Divergence Speed | Max. Stiffness Variation | Stiffness $K_\beta$ $(kNm/m)$ | Stiffness $K_\gamma$ $(kNm/m)$ | Damp. Ratio $\zeta_\beta$ |
|---|---|---|---|---|---|
| 102m/s | 84m/s | 7% | $5.29 \times 10^5$ | $1.25 \times 10^5$ | 0.25% |
| Damp. Ratio $\zeta_\gamma$ | Transfer Func. LF | Transfer Func. TF | LF Network (c: $Nmsec/radm$) ($b$ : $kgm^2/m$) | TF Network (c: $Nmsec/radm$) ($b$ : $kgm^2/m$) | $l_d = t_d$ |
| 0.56% | $\frac{0.59\times10^6 s+356.9}{26.09s+2507}$ | $\frac{3.66\times10^7 s+815.5}{114.7s+4452}$ | $c1 = 22614$<br>$c2 = 0.14$<br>$b = 235.3$ | $c1 = 319090$<br>$c2 = 0.18$<br>$b = 8221$ | 1 |

Table 7.1 Aeroelastic stability limits, robustness margin and mechanical compensator characteristics for the full controlled bridge FE model. The flaps span the central 33 % of the main span.

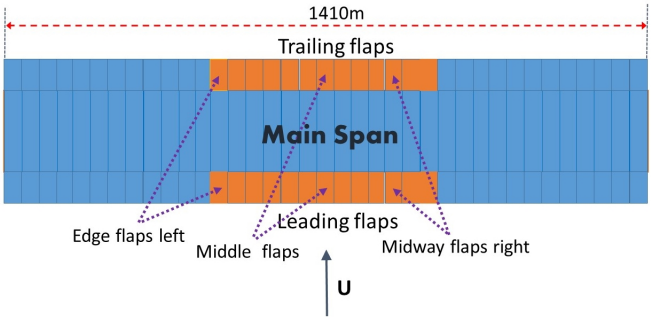


Figure 7.12 Plan view of main span with leading and trailing flaps.

Fig.7.13 illustrates the transient movement of the flaps following a deck pitch disturbance; three leading- and trailing-edge flaps in the FE model are illustrated, according to Fig.7.12. The initial disturbance consists of 0.035 rad twisting of the main span at its midpoint, for a wind speed just below the critical divergence speed ($U = 84$ m/s in this case). The resulting flap rotations are observed to be small compared to the deck's pitching motion justifying the assumption of *small rotations*, implicit in the use of thin airfoil theory.

In the final control investigation, the flap controllers are re-tuned at four intermediate erection stages and the aeroelastic stability limits are recomputed. The flap length as a percentage of the main span is kept the same is in the preceding investigation, Fig.7.11. Fig.7.14 presents the bridge's attained aeroelastic performance for the re-tuned mechanical networks.

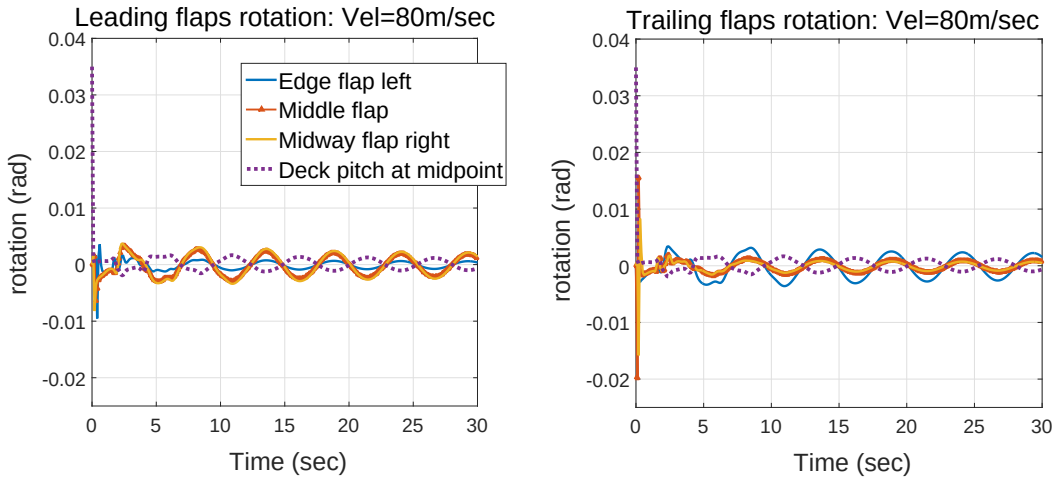


Figure 7.13 Flap angles transient response for the case of the completed bridge with flaps in the main 33% of the span.

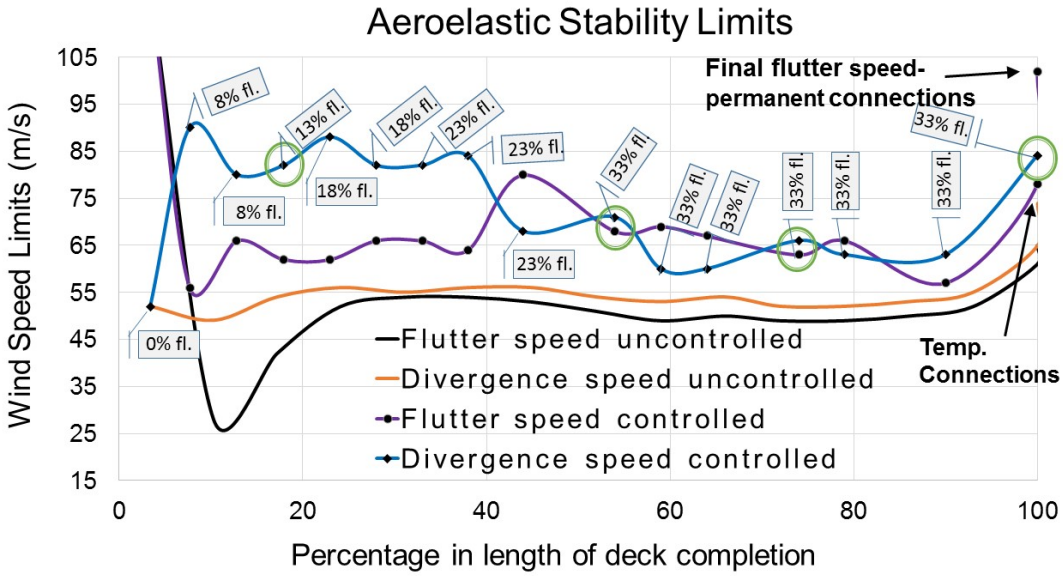


Figure 7.14 Aeroelastic stability limits against deck percentage completion for the uncontrolled, flaps rigidly attached to the deck, and the controlled deck. The implemented controllers were re-tuned at four intermediate stages, marked with green circles. The flap width is 2.75$m$.

All the leading- and trailing-edge flaps used follow the same control law respectively. Although performance improvements are achieved in the intermediate stages between 50% and 100% complete, these improvements were not as significant as the introduction of compensation networks in the first instance. A more complicated control network

distribution, with different controllers at each flap element, could potentially improve the system performance as this would help suppress higher flutter modes, prevalent in the intermediate stages. In summary, the final conclusion drawn is that the proposed mechanical network implementations presented in Fig.7.11 and Fig.7.14 are relatively easy to implement and lead to a significant increase in the critical flutter and divergence speed at the early stages of erection and at the completed stage, after permanent connections are applied.

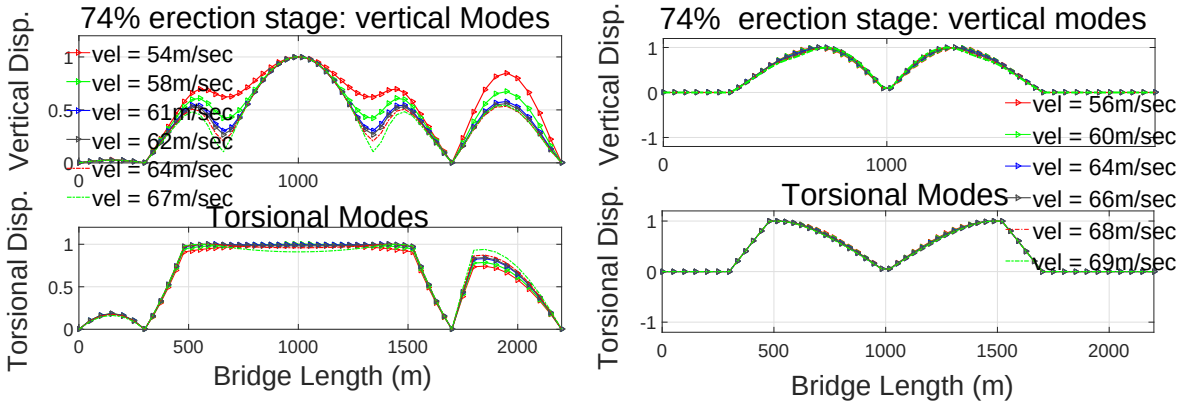


(a) First flutter mode

(b) Second flutter mode

Figure 7.15 (a)Normalized real part of the vertical and torsional component of the complex flutter mode at distinct wind speeds, for the controlled deck-flap system when 74% of the main span is erected. (b) similarly for the second flutter mode.

Fig.7.16 presents the Root Loci for the uncontrolled and controlled bridge-flap system, when 74% of the main deck is erected. It is observed that two flutter modes reach instability for the uncontrolled system and three flutter modes for the controlled system, before wind speed reaches $U = 70m/s$. The instability of these modes takes place in a narrow wind speed band, a fact that poses difficulty in the control design when the control law for the leading and trailing flap compensators respectively is kept the same. In other words without differential movement of the flaps it is difficult to suppress multiple instability modes which pertain to coupling of different structural modes. Fig.7.15 presents the real part of the complex valued vertical and torsional component of the first two flutter modes, for the controlled case, at wind speed in proximity to the aeroelastic instability boundary. For the first flutter mode, one can observe the coupling of higher vertical modes with the first

torsional mode. On the other hand, the second flutter mode results from the coupling of the first vertical with the first torsional antisymmetric mode.

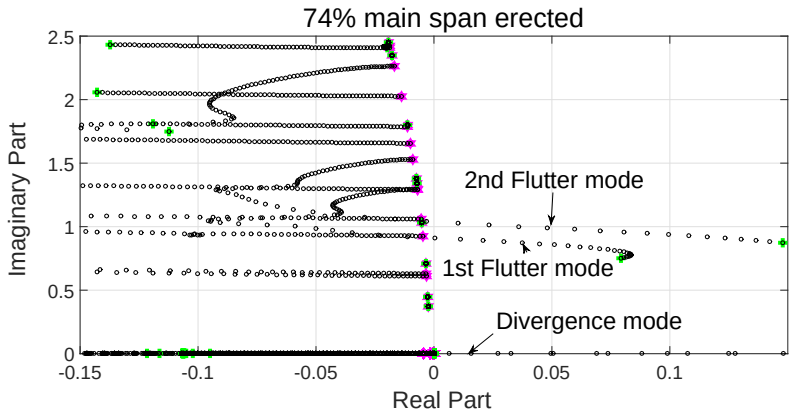


(a) Uncontrolled

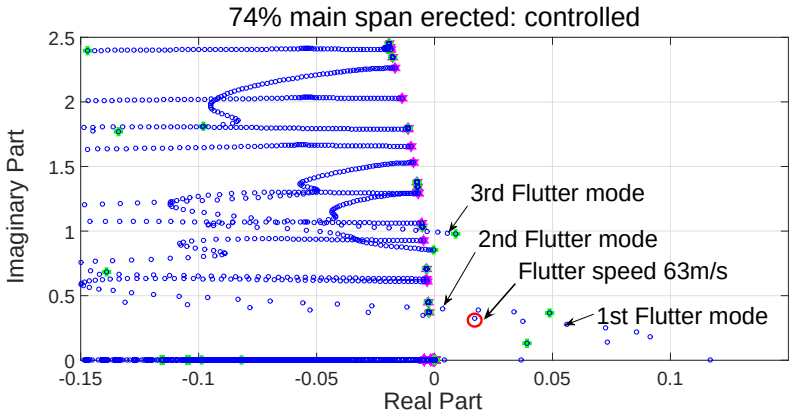


(b) Controlled

Figure 7.16 (a)Root Loci of uncontrolled bridge-deck system when 74% of the main span is erected. Wind speed is swept from 0 to 70 m/s. The critical flutter is computed at $49m/s$ and the torsional divergence speed at $52m/s$. (b) Root Loci of the controlled system, movable flap compensators cover 33% of the main span. The critical flutter is computed at $63m/s$ and the torsional divergence speed at $66m/s$.

The aeroelastic modal analysis presents a particularity because of the non-proportional damping due to aerodynamic contributions, aerodynamic damping matrix. The concept of mode shapes, having a clearly defined physical meaning for the proportional damping case, is more difficult to analyze and visualize when the modes become complex. In the latter case points on a structure no longer move in a clear pattern of either in or out of phase, but their phase angle is varied between 0 and 180 degrees. This means that points on a vibrating structure do not pass through the equilibrium position at the same time, although

they still have the same oscillatory frequency. The nodal points of the structure are not fixed either, but move with a certain period dictated by the complexity of the mode.

A graphical visualization of the a complex mode can be aided by using *Argand* diagrams, or *Phasor* diagrams, in which each nodal point of the bridge deck is represented by a normalized arrow showing the phase and magnitude of the associated complex mode coordinate. Because complex modes appear in conjugate pairs, their vectors at a given node counter-rotate with the same circular frequency ω. Phasor diagrams are helpful in demonstrating the relative phases as well as relative amplitudes of an eigenvector. A larger angle phase difference signifies stronger complex behaviour of a mode. Fig.7.17 presents the phasor diagrams for the torsional and vertical components of the second flutter mode, shown in Fig.7.16(a), at different wind speeds near the flutter boundary. It can be observed that the vertical component presents a phase scatter but the points move torsionally almost in phase or anti-phase. However, there is always a significant phase difference between the vertical and torsional component, a necessary condition for the flutter phenomenon.

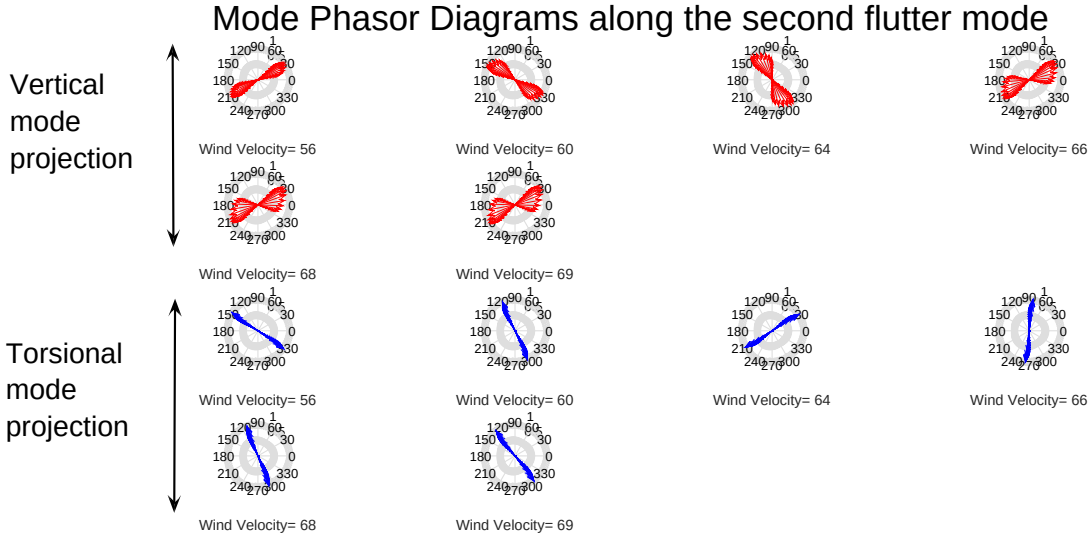


Figure 7.17 Phasor diagrams, each arrow represents the magnitude and phase of each node in the FE mesh. The complex modes chosen correspond to points along the second flutter mode of the 74% erected case.

## 7.6 Discussion and Concluding Remarks

This chapter extends the sectional deck-flap system passive configuration on the finite element aeroelastic model. In this framework the flap retention components and flap pivot locations are determined via a nonlinear optimization code which seeks to maximize stability margins of the closed loop system. The proposed mechanical network has the advantages of: simultaneously increasing flutter and torsional divergence limits, being easily implementable as well as dispensing the need to be anchored in an inertial reference frame. Furthermore, the flap-deck connection avoids the use of external linkages and because of the nature of the feedback minimum interference with the deck's sway motion is anticipated. Further addition of an auxiliary first order mechanical compensator at the flap pivot points proved, in most cases, to significantly improve the system's stability margins. The model reduction framework here implemented to facilitate the optimization computations, has the advantage of preserving the systems original modes and corresponding poles, which contribute the most to the system's MIMO large scale transfer function.

Implementation of the proposed feedback mechanism to the bridge aeroelastic model proves its effectiveness during early stages of construction as well as during the completed stage. In all cases, the flap span length was restricted to 33% of the main span. It was shown that re-tuning the flap mechanical network at different erection stages provides reasonable improvement, which is however hindered by the model's pronounced multi-modal interactions at the erection intermediate stages. Of course, the exhibited behaviour is unique for each bridge structure and different levels of controller complexity can lead to different levels of performance. The aim of this work however is to propose a servo-aeroelastic framework covering all design facets for building a successful compensator network.

# Chapter 8

# Conclusions and Future Research

## 8.1 Research Conclusions

The work presented in this thesis addressed the problem of suppressing aerodynamic instabilities on long-span suspension bridges using trailing- and leading-edge controllable flaps in combination. The most important instability mode is flutter, which presents itself as an oscillatory aeroelastic interaction between the air stream and the structural pitch and heave modes. The secondary non-oscillatory aeroelastic instability is torsional divergence that is reminiscent of paper pitching up in front of a fan. As was presented in the literature review, the idea of using active or passive flaps to improve a bridge's aerodynamic performance is not new, however there has been no practical application of the proposed methodology up to date. The reasons for this are twofold: Firstly, design experience gained from record breaking projects such as the Akashi Bridge, along with preliminary analysis of the Messina Bridge [28] and the the Gibraltar strait project [106], attest to the fact that aerodynamic tailoring of the deck either by using the twin-box girder approach or the slotted deck solution has demonstrated promising results in the quest to improve aerodynamic performance.

The second reason is that previously proposed solutions including flaps have either concentrated on implementing power driven active control techniques, e.g. optimal control and pole placement algorithms, or on the implementation of passive networks which are

however designed based on a simplistic control approach. Analytic investigation of the latter systems also neglected phase compensation and attained robustness properties of the feedback mechanism. Proper account of stability margins due to physical uncertainties has also not been properly investigated in previous aeroelastic studies using active control. In the bridge construction field, passive networks are preferable as they eliminate the need for a powered computer control system; a commodity that is likely to fail during stormy weather conditions when flutter instabilities are most likely to occur. Furthermore, there is always the need of a simple mechanical network which preserves the aerodynamic properties of the original deck section and can be relatively easily maintained and adjusted.

The work presented in this thesis has focused on the second reason, and has tackled the issue of robustness quantification both using an active control scheme on a bridge finite element model and passive network feedback systems. The proposed passive control alternatives remedy many of the shortcomings of previous models. It was finally demonstrated that a passive control approach using leading and trailing edge flaps proves to be an efficient countermeasure against aeroelastic instability; both during the deck erection process and in the final completion state.

The initial part of this study dealt with the mathematical formulation for capturing the essential aeroelastic characteristics of suspension bridges using a reduced size structural model. A finite element approach for describing the dynamic behaviour for vertical, torsional and lateral vibrations of suspension bridges based on a linearized theory was implemented. The procedure resulted in simplified structural elements which consider both the contribution of the girder and the main cables. The attained modal characteristics were compared to experimentally identified modes and other analytical studies from the literature, confirming the correctness of the structural model.

The aerodynamic part of this work makes use of classical results from potential flow theory and recasts them in a form suitable for control analysis and design in the Laplace domain. The procedure is extended to a finite element framework and the prediction of aeroelastic limits was compared to previous experimental and analytic studies, again

finding good agreement. The transformation of the wing-aileron-tab to the leading flap-deck-trailing flap configuration using a feedback control approach and a high-fidelity minimum phase approximation of the circulatory terms is used to model the aerodynamic effect of the flaps.

The aeroelastic finite element procedure was also modified to consider experimentally obtained flutter derivatives. The analysis revealed that for bridges having streamlined deck girders, such as the Great Belt Bridge, the system's aerodynamic behaviour is similar to that predicted by thin aerofoil theory, thus supporting the validity of the latter for all the following control analyses.

Considerable attention was given to modelling the deck erection process of a suspension bridge. By mimicking the deck assembly process of the Humber Bridge, it was shown that the evolution of dynamic characteristics can be attained using slightly modified structural elements. The aeroelastic limits during erection are in agreement with prior analyses based on sectional models, but also suggest that higher-order modes have a beneficial effect on the critical flutter wind speed.

The first stage of the control synthesis investigation employed an $H_\infty$ design procedure for an active control framework that also accounts for stability margins of the bridge-flap system. This novel approach successfully quantifies structural and aerodynamic uncertainty and gives further insight into the applicability of a control strategy using controllable winglets. It was shown that, although the stabilization of the system can be relatively easily achieved, robustness of the closed loop system declines rapidly beyond the uncontrolled structure's torsional divergence speed boundary. This forms an important result; and sets a qualitative limit for the performance of all controllers using leading- and trailing-edge winglets. It also provides an estimate with respect to the length of control surfaces needed in order to improve the structure's aeroelastic limits while preserving good robustness margins. For the case of the Great Belt bridge, flap surfaces covering 33% of the main span about its midpoint were deemed sufficient to raise the critical flutter speed up to the torsional divergence limit. This high order control investigation also served as a precursor

for the low order passive system network synthesis, which aimed at dispensing with the need for external power source and sensors.

The passive network control investigation initially considered a sectional flexible four DOF bridge model interacting with a constant velocity airstream. The novelty of the presented approach consists in devising a passively controlled deck-flap feedback system which can be realized without resorting to external, difficult to implement linkages. The first proposed mechanical configuration makes use of trailing and leading flaps adjacent to the deck, the motion of which is triggered by a combination of springs, dampers and inerters at the pivot locations. An important advantage of the proposed methodology is that the network layout is determined by an optimization process and not preselected. In-depth analytic investigation demonstrated that by optimizing for the flap retention components and the flap pivot location, flutter and torsional divergence boundaries can be significantly improved while achieving good robustness margins.

The second passive strategy focuses on combining the benefits of tuned mass damper systems with those resulting from optimum flap kinematics. The proposed design methodology overcomes inherent shortcomings associated with TMDs such as large vertical mass oscillations and frequency tuning sensitivity. In addition, the realization of a transmission system which links the tuned masses to the flaps results in increased flap effectiveness by furnishing additional structural damping. Although this design does introduce some complexity the use of external structural elements is avoided. Such elements would undermine the solution's technical applicability as well as the deck's aerodynamic integrity.

The two passive network approaches developed in this work are not only appealing because of their practical simplicity, but can furthermore exhibit improved performance when compared to active control analysis. The reason for this is predominantly based on the optimized arrangement of deck-flap kinematics; this results in elevated torsional divergence boundaries which in turn allows the system to be stabilized using smaller flap angle magnitudes and modest controller flap torques.

The final investigation examines the implementation of the simpler of the two passive flap mechanisms on the full bridge aeroelastic model. This enables us to consider the full multi-modal interactions as well as the effect of flap kinematics on the bridge structure. Because of the nature of the feedback minimum interference with the deck's sway motion is anticipated. The introduction of auxiliary first order mechanical compensators at the flap pivot points proved, in most cases, to significantly improve the system's stability margins. In addition, it was established that the mechanical network realization includes an inerter component suggesting that better performance is attained with increased apparent mass. Implementation of the proposed feedback mechanism to the bridge aeroelastic model proves its effectiveness during the early stages of construction as well as during the completed stage. In all cases, the flap span length was restricted to 33% of the main span.

To summarize, the major contributions of this work are as follows:

- Development of a computationally efficient and reliable aeroelastic framework in the Laplace domain, which exposes the full multi-modal interaction of suspension bridges.
- Investigation of the evolution of aeroelastic limits during the deck's erection process using the established multi-modal framework.
- Thin aerofoil theory comparison with an aerodynamic multi-modal procedure using experimentally obtained flutter derivatives. The drawn conclusion is that the flat plate assumption is a good approximation when streamlined box girders are used.
- Implementation of the $H_\infty$ control framework for active flap compensator design and for the feedback system's tolerance quantification against unstructured uncertainties.
- It is shown that above the torsional divergence limit a precipitous loss in stability limits occurs.
- Two passive mechanical networks are introduced, in which flap retention components and flap pivot locations are tuned via a nonlinear optimization code that seeks to

maximize stability margins of the closed-loop system. It is concluded that favourable aeroelastic performance is attained when the connection location is close to the outer edge of the flaps.

- The newly introduced flap mass damper network is most successful in improving flutter and torsional divergence limits while simultaneously achieving good closed system robustness properties. The introduced linkage between the tuned masses and the flap compensators helps overcome inherent shortcomings of the TMDs.

- An innovative model reduction technique based on the notion of dominant poles is introduced to the aeroelastic framework. Since the preserved dominant poles are a subset of the original system eigenvalues, the poles of the reduced-order model retain their physical significance.

- The mechanical realization of a generic flap compensator transfer function is achieved by using pure passive components; springs, dampers and inerters.

- It is established that inerters act favorably on the system's structured robustness.

- It is shown that adopting a simple passive mechanical network, without modifying the deck's streamlined shape, can result in significantly improved aeroelastic performance during the erection process as well as in the completed stage.

## 8.2 Future Research Recommendations

Since the presented work focused on flutter and torsional divergence instabilities, it is suggested that future research should be geared towards investigating passive network performance against buffeting suppression. In terms of network design it should be possible to stabilize the system against aeroelastic instabilities, while simultaneously suppressing buffeting, using a similar passive mechanical feedback methodology; the control approach should be based on a mixed $\frac{H_2}{H_\infty}$ formulation. The full bridge buffeting analysis should consider a multi-mode response by computing cross spectra of the deck response to turbulent

wind. The resulting interaction between the FE model and flap-deck kinematics should be thoroughly investigated.

Multimodal flutter has been thoroughly discussed in this thesis. Since the flap-deck aerodynamic interference was based on the thin airfoil theory assumption, the aeroelastic influence of sway modes was considered inert. Due to the nature of the passive network, consisting of simple hinged connections, no significant interaction between the flaps and deck's sway motion is expected. However this assumption should be further investigated analytically and experimentally. An alternative flap implementation strategy, despite the drawbacks pointed out in earlier chapters, is to introduce flap surfaces at a distance from the deck. In the latter configuration, the deck being aerodynamically independent, can be analytically treated by using the flutter derivatives approach; comparison should be made to the deck-flap system presented in this work.

Due to the analytic nature of this work, wind tunnel experiments should be conducted to assess the feasibility and performance of the proposed passive network configurations. Already completed experimental investigation [78] has focused on a control implementation using motors which can in principle, be replaced by passive mechanical networks that would require little or no servicing. However, a pure passive experimental demonstration would help illustrate the feasibility of the method.

Future investigations could also include examination of nonlinearity in system performance. Non linear aerodynamic effects associated with larger angles of attack can be analytically implemented in the finite element model using modified quasi-steady theory. Alternatively, time domain analysis involving structural nonlinear components would provide insight with regard to the controller's ability to overcome disturbances of this sort.

# Bibliography


[1] Abdel-Ghaffar, A. (1978). Free lateral vibrations of suspension bridges. *Journal of Structural Division ASCE*, 104(ST3):503–525.

[2] Abdel-Ghaffar, A. (1979). Free torsional vibrations of suspension bridges. *Journal of Structural Division ASCE*, 105(ST4):767–788.

[3] Abdel-Ghaffar, A. (1980). Free vertical vibrations of suspension bridges. *Journal of Structural Division ASCE*, 105(ST10):2053–2076.

[4] Abdel-Ghaffar, A. M. (1976). *Dynamic Analysis of Suspension Bridge Structures*. PhD thesis, California Institute of Technology.

[5] Abdel-Ghaffar, A. M. and Scanlan, R. H. (1985a). Ambient vibration studies of golden gate bridge I: Suspended structure. *Journal of Engineering Mechanics*, 111:463–482.

[6] Abdel-Ghaffar, A. M. and Scanlan, R. H. (1985b). Ambient vibration studies of the golden gate bridge II: Pier-tower structure. *Journal of Engineering Mechanics, ASCE*, 111.

[7] Agar, T. J. A. (1989). Aerodynamic analysis of suspension bridges by modal technique. *Journal of Engineering structures*, 11:75–82.

[8] Ammann, O. H., von Karman, T., and woodruff, G. B. (1941). *The failure of the Tacoma Narrows Bridge*. Federal Works Agency, Washington D.C.

[9] Anderson, B. D. O. and Vongpanitlerd, S. (1973). *Network Analysis and Synthesis*. Prentice-Hall,Engelwood Cliffs, NJ.

[10] Anderson, J. D. (2012). *Introduction to Flight*. McGraw Hill.

[11] Argentini, T., Pagani, A., Rocchi, D., and Zasso, A. (2014). Monte Carlo analysis of total damping and flutter speed of a long span bridge: Effects of structural and aerodynamic damping. *Journal of Wind Engineering and Industrial Aerodynamics*, 128.

[12] Astiz, M. A. (1998a). Flutter stability of very long span bridges. *Journal of Bridge Engineering*, 3(3):132–139.

[13] Astiz, M. A. (1998b). Flutter stability of very long suspension bridges. *Journal of Bridge Engineering*, 3:132–139.

[14] Astrom, K. J. and Murray, R. M. (2008). *Feedback Systems*. Princeton University Press.

[15] Bakis, K. N., Massaro, M., Williams, M. S., and Graham, J. M. R. (2015a). Passive control of bridge wind-induced instabilities by tuned mass dampers and movable flaps. *Journal of Engineering Mechanics*, submitted:xx.

[16] Bakis, K. N., Massaro, M., Williams, M. S., and Limebeer, D. J. N. (2015b). Aeroelastic control of long span suspension bridges during erection. In *IABSE conference, Elegance in Structures*, Nara, Japan.

[17] Bakis, K. N., Massaro, M., Williams, M. S., and Limebeer, D. J. N. (accepted, in press). Aeroelastic control of long-span suspension bridges with controllable flaps. *Journal of Structural Control and Health Monitoring*.

[18] Bartoli, G. and Righi, M. (2006). Flutter mechanism for rectangular prisms in smooth and turbulent flow. *Journal of Wind Engineering and Industrial Aerodynamics*, 94:275–291.

[19] Basu, B., Bursi, O. S., Casciati, F., Casciati, S., Grosso, A. E. D., Domaneschi, M., Faravelli, L., Szulc, J. H., Irschik, H., Krommer, M., Lepidi, M., Martelli, A., Ozturk, B., Pozo, F., Pujol, G., Rakicevic, Z., and Rodellar, J. (2014). A european association for the control of structures joint perspective. recent studies in civil structural control across europe. *Journal of Structural Control and Health Monitoring*, 21:1414–1436.

[20] Bielawa, R. L. (2006). *Rotary wing structural dynamics and aeroelasticity*. American Institute of Aeronautics and Astronautics.

[21] Billah, K. Y. and Scanlan, R. H. (1991). Resonance, Tacoma Narrows bridge failure, and undergraduate physics textbooks. *American Journal of Physics*, 59(2):118–124.

[22] Birnbaum, W. (1924). *Das ebene problem des schlagenden flugels.* Zeitschrift fur angewandte Mathematik und Mechanik (in German).

[23] Bisplinghoff, R. L., Ashley, H., and Halfman, R. L. (1996). *Aeroelasticity*. Dover Publications, New York.

[24] Bleich, F., M. C. R. R. and Vincent, G. (1950). The mathematical theory of vibration in suspension bridges. *U.S. Bureau of Public Roads, Government Printing Office, Washington 25, D.C.*

[25] Borglund, D. and Kuttenkeuler, J. (2002). Active wing flutter suppression using a trailing edge flap. *Journal of Fluids and Structures*, 16:271–294.

[26] Borri, C., Costa, C., and Zahlten, W. (2002). Non-stationary forces for the numerical simulation of aeroelastic instability of bridge decks. *Computers and Structures*, 80:1071–1079.

[27] Brancaleoni, F. (1992). The construction phase and its aerodynamic issues. In *Aerodynamics of Large Bridges, A. Larsen*, pages 147–158, Rotterdam, Netherlands.

[28] Brancaleoni, F., Diana, G., Faccioli, E., Fiammenghi, G., Firth, I. P. T., Gimsing, N. J., Jamiolkowski, M., Sluszka, P., Solari, G., Valensie, G., and Vullo, E. (2010). *The Messina Strait Bridge, A challenge and a dream.* CRC Press, Taylor and Francis Group.

[29] Brown, W. C. (1996). Development of the deck for the 3300m span Messina Crossing. In *15th IABSE Congr. Report, IABSE, Zurich*, pages 1019–1030, Zurich.

[30] Brownjohn, J. M. R., Dumanoglu, A. A., Severn, R. T., and Taylor, C. A. (1987). Ambient vibration measurements of the Humber Suspension Bridge and comparison with calculated characteristics. *Proceedings Institution of Civil Engineers Part 2*, 83:561–600.

[31] Brownjohn, J. M. W., Bocciolone, M., Curami, C., Falco, M., and Zasso, A. (1994). Humber bridge full-scale measurement campaigns 1990-1991. *Journal of Wind Engineering and Industrial Aerodynamics*, 52:185–218.

[32] Brownjohn, J. M. W., Dumanoglu, A. A., Severn, R. T., and Blakeborough, A. (1989). Ambient vibration survey of the Bosporus Suspension Bridge. *Earthquake Engineering and Structural Dynamics*, 18:263–283.

[33] Brownjohn, J. M. W., Magalhaes, F., Caetano, E., and Cunha, A. (2010). Ambient vibration re-testing and operational modal analysis of the Humber Bridge. *Engineering Structures*, 32:2003–2018.

[34] Bucher, C. G. and Lin, Y. K. (1988). Stochastic stability of bridges considering coupled modes. *Journal of Engineering Mechanics, ASCE*, 114:384–400.

[35] Buonopane, S. G. and Billington, D. P. (1993). Theory and history of suspension bridge design from 1823 to 1940. *Journal of Structural Engineering*, 119(3):954–977.

[36] Burnett, E. L., Atkinson, C., Beranek, J., Holm-Hansen, B., and Nicolai, L. (2010). Ndof simulation model for flight control development with flight test correlation. In *Proc. AIAA Modelling Simulation Technology Conference*, pages 7780–7794.

[37] Caracoglia, L. and Jones, N. P. (2003). Time domain vs frequency domain characterization of aeroelastic forces for bridge deck sections. *Journal of Wind Engineering and Industrial aerodynamics*, 91:371–402.

[38] Casado, C. M., Diaz, I. M., Sebastian, J., Poncela, A. V., and Lorenzana, A. (2013). Implemenation of passive and active vibration control on an in-service foorbridge. *Journal of Structural Control and Health Monitoring*, 20:70–87.

[39] Chen, M. Z. Q., Schneibe, C. P. F., Wang, F. C., and Smith, M. C. (2009). The missing mechanical circuit. *IEE Circuits and Systems Magazine*, 1531-636X:10–26.

[40] Chen, X. and Kareem, A. (2000). Efficacy of tuned mass dampers for bridge flutter control. *Journal of Structural Engineering ASCE*, 129:1291–1300.

[41] Chen, X. and Kareem, A. (2001). Aeroelastic analysis of bridges under multicorrelated winds: Integrated state-space approach. *Journal of Engineering Mechanics*, 89:1335–1350.

[42] Chen, X. and Kareem, A. (2002). Advances in modelling of aerodynamic forces on bridge decks. *Journal of Engineering Mechanics (ASCE)*, 128:1193–1205.

[43] Chen, X., Matsumoto, M., and Kareem, A. (2000). Aerodynamic coupling effects of flutter and buffeting of bridges. *Journal of Engineering Mechanics*, 126:17–26.

[44] Chen, Z. Q., Yu, X. D., Yang, G., and Spencer, B. F. (2005). Wind-induced self-excited loads on bridges. *Journal of Structural Engineering ASCE*, 131(12):1783–1793.

[45] Cheng, J., Cai, C. S., Xiao, R. C., and Chen, S. R. (2005). Flutter reliability analysis of suspension bridges. *Journal of Wind Engineering and Industrial Aerodynamics*, 93.

[46] Cobo, D. (1998). *An analysis of wind stability. Improvements to the response of suspension bridges*. Tesis doctoral de la Universitat de Catalunya.

[47] Cornwell, P., Farrar, C. R., Doebling, S. W., and Sohn, H. (1999). Environmental variability of modal properties. *Experimental Techniques*, 23:45–48.

[48] Davenport, A. G. (1961a). The application of statistical concepts to the wind loading of structures. *Proceedings Institution Civil Engineers*, 19:449 – 472.

[49] Davenport, A. G. (1961b). The spectrum of horizontal gustiness near the ground in high winds. *Quarterly Journal of the Royal Meteorological Society*, 87:194–211.

[50] Davenport, A. G. (1962). Buffeting of a suspension bridge by stormy winds. *Journal of Structural division ASCE*, pages 233–264.

[51] del Arco, D. C. and Aparicio, A. C. (1999). Improving suspension bridge wind stability with aerodynamic appendages. *Journal of Structural Engineering*, 125(12):1367–1375.

[52] Den Hartog, J. P. (1985). *Mechanical Vibration*. Dover, New York.

[53] Diana, G., Cheli, F., Zasso, A., Collina, A., and Brownjohn, J. (1992). Suspension bridge parameter identification in full scale test. *Journal of Wind Engineering and Industrial Aerodynamics*, pages 165–176.

[54] Diana, G., Federico, C., Alberto, Z., Colina, A., and Bruni, S. (1998). Aerodynamic design of very long-span suspension bridges. In *Long-Span and High-Rise Structures, IABSE Symposium*, pages 115–130, Kobe.

[55] Diana, G., Resta, F., and Rocchi, D. (2008). A new numerical approach to reproduce bridge aerodynamic non-linearities in time domain. *Journal of Wind Engineering and Industrial Aerodynamics*, 96:1871–1884.

[56] Dowell, E. H. et al. (2004). *A modern course in aeroelasticity*. Kluwer Academic Publishers, New York.

[57] Doyle, J. C., Glover, K., Khargonekar, P. P., and Francis, B. A. (1989). state-space solutions to standard $H_2$ and $H_\infty$ control problems. *IEEE Transactions on Automatic Control*, 34:831–847.

[58] Dumanoglu, A. A., Brownjohn, J. M. R., and Severn, R. T. (1992). Seismic analysis of the Fatih Sultan Mehmet (Second Bosporus) Suspension Bridge. *Earthquake Engineering and Structural Dynamics*, 21:881–906.

[59] Dyrbye, C. and Hansen, S. O. (1997). *Wind loads on structures*. Wiley.

[60] Edwards, J. W. (1977). *Unsteady Aerodynamic Modelling and Active Aeroelastic Control*. PhD Thesis, Centre for Systems Research, Stanford University.

[61] Ehsan, F. and Scanlan, R. H. (1990). Vortex-induced vibration of flexible bridges. *Journal of Engineering Mechanics, ASCE*, 116:1392–1411.

[62] Evangelou, S., Limebeer, D. J. N., Sharp, R. S., and Smith, M. C. (2007). Mechanical steering compensators for high-performance motorcycles. *Transactions of the ASME, Journal of Applied Mechanics*, 74:332–346.

[63] Falco, M., Curami, A., and Zasso, A. (1992). Nonlinear effects in sectional model aeroelastic parameters identification. *Journal of Wind Engineering and Industrial Aerodynamics*, pages 1321–1332.

[64] Farquharson, F. B. (1949-54). *Aerodynamic Stability of Suspension Bridges*. Parts 1-5 Structural Research Laboratory, University of Washington.

[65] Fujino, Y. (2002). Vibration, control and monitoring of long-span bridges - recent research, developments and practise in japan. *Journal of Constructional Steel Research*, 58:71–97.

[66] Fujino, Y. and Abe, M. (1993). Design formulas for tuned mass dampers based on a perturbation technique. *Earthquake Engineering and Structural Dynamics*, 22:833–855.

[67] Fuller, R. (2000). Twin views of the Tacoma Narrows Bridge collapse. *American Association of Physics Teachers*.

[68] Fung, Y. C. (1969). *An introduction to the Theory of Aeroelasticity*. Dover, New York.

[69] Garrick, I. E. (1938). On some reciprocal relations in the theory of nonstationary flows. *NACA Report, TR-629*.

[70] Ge, Y. J. and Tanaka, H. (2000a). Aerodynamic flutter analysis of cable-supported bridges by multi-mode and full-mode approaches. *Journal of Wind Engineering and Industrial Aerodynamics*, 86:123–153.

[71] Ge, Y. J. and Tanaka, H. (2000b). Aerodynamic stability of long-span suspension bridges under erection. *Journal of Structural Engineering*, pages 1404–1412.

[72] Ge, Y. J. and Xiang, H. F. (2008). Bluff body aerodynamic application in challenging bridge span length. In *BBAA VI International Colloquium on: Bluff Bodes Aerodynamics & Applications*, Milano, Italy.

[73] Ge, Y. J. and Xiang, H. F. (2009). Aerodynamic stabilization for box-girder suspension bridges with super-long span. In *EACWE 5*, Florence, Italy.

[74] Ge, Y. J., Xiang, H. F., and Tanaka, H. (2000). Application of a reliability analysis model to bridge flutter under extreme winds. *Journal of Wind Engineering and Industrial Aerodynamics*, 86.

[75] Gimsing, N. J. (1997). *Cable Supported Bridges*. John Wiley & Sons.

[76] Glover, K. and McFarlane, D. (1989). Robust stabilization of normalized comprime factor plant descriptions with $H_\infty$-bounded unceratinty. *IEEE TRANSACTIONS ON AUTOMATIC CONTROL*, 34:821–830.

[77] Goodman, J. (2001). Accurate subcritical damping solution of flutter equation using piece-wise aerodynamic function. *Journal of Aircraft*, 18(3):755–763.

[78] Gouder, K., Zhao, X., Limebeer, D. J. N., and Graham, J. M. R. (2015). Experimental aerodynamic control of a long-span suspension bridge section using leading- and trailing-edge control surfaces. *IEEE Transactions on Control System Technology*, PP, 99:1–13.

[79] Graham, J. M. R., Limebeer, D. J. N., and Zhao, X. (2011). Aeroelastic control of long-span suspension bridges. *ASME Journal of Applied Mechanics*.

[80] Green, M. and Limebeer, D. J. N. (1995). *Linear Robust Control*. Prentice Hall, Englewood Cliffs, New Jersey.

[81] Han, S. M., Benaroya, H., and Wei, T. (1999). Dynamics of transversely vibrating beams using four engineering theories. *Journal of Sound and Vibration*, 225(5):935–988.

[82] Hansen, H. I. and Thoft-Christensen, P. (2001). Active flap control of long suspension bridges. *Journal of Structural Control*, 8(1):33–82.

[83] Hodges, D. H. and Pierce, G. A. (2002). *Introduction to structural dynamics and aeroelasticity*. Cambridge Aerospace Series.

[84] Ikago, K., Saito, K., and Innoue, N. (2012). Seismic control of single-degree-of-freedom structure using tuned viscous damper. *Earthquake engineering and structural dynamics*, 41:453–474.

[85] Irvine, H. M. (1974). *Studies in the Statics and Dynamics of Simple Cable Systems*. California Institute of Technology, Technical Report.

[86] Irvine, H. M. (1981). *Cable Structures*. The MIT Press, Cambridge, Massachusetts.

[87] Irwin, H. P. A. H. and Wardlaw, R. L. (1977). *Experiments on a full aeroelastic model of Lions' gate Bridge in smooth and turbulent flow*. National Research Council of Canada, NAE-LA-205.

[88] Iwanami, K. and Seto, K. (1984). Optimum design of dual tuned mass dampers and their effectiveness. In *Proc JSME(C) 50 (449)*, pages 44–52.

[89] Jakkula, A. A. (1936). The theory of the suspension bridge. *Publications, International Association of Bridge and Structural Engineering*.

[90] Jakobsen, J. B. and Hansen, E. H. (1995). Determination of the aerodynamic derivatives by a system identification method. *Journal of Wind Engineering*, 57:295–305.

[91] Jones, R. T. (1938). Operational treatment of the nonuniform-lift theory. *NACA Report, TR-667*.

[92] Jurado, J. A., Hermandez, S., Nieto, F., and Mosquera, A. (2011). *Bridge Aeroelasticity: Sensitivity Analysis and Optimum Design*. WITpress.

[93] Kailath, T. (1980). *Linear Systems*. Prentice-Hall.

[94] Karman, T. and Sears, W. R. (1938). Airfoil theory for non-uniform motion. *Journal Aeronautical Sciences*, 5(10):379–390.

[95] Karuna, R. (2002). *Structural Modelling of Suspension Bridges with Particular Reference to the Humber Bridge*. PhD Thesis, Department of Mechanical Engineering, Brunel University.

[96] Katsuchi, H., Jones, N. P., and Scanlan, R. H. (1999). Multimode coupled flutter and buffeting analysis of the Akashi-Kaikyo Bridge. *Journal of Structural Engineering*, 125:60–70.

[97] Katz, J. and Plotkin, A. (2001). *Low-Speed Aerodynamics*. Cambridge University Press.

[98] Kloeppel, K. V. and Thiele, F. (1967). *Modellversuche im windkanal zur Bemessung von Bruecken gegen die Gefahr winderregter Schwingungen*. Der Stahlbau 12.

[99] Kobayashi, H. and Nagaoka, H. (1992). Active control of flutter of a suspension bridge. *Journal of Wind Engineering and Industrial Aerodynamics*, 41:143–151.

[100] Kovacs, I., Svensson, H. S., and Jordet, E. (1992). Analytical aerodynamic investigation of the cable stayed Helgeland Bridge. *Journal of Engineering (ASCE)*, 118:147–168.

[101] Kussner, J. (1935). *Zussamenfassender Bericht uder den instationaren Auftrieb von Flugeln*. Luftfahrt-forschung, 13(12), pp. 410-424.

[102] Kwon, S. and Park, K. S. (2004). Suppresion of bridge flutter using tuned mass dampers based on robust performance design. *Journal of Wind Engineering and Industrial Aerodynamics*, 92:919–934.

[103] Larose, G. L. (2003). The spatial distribution of unsteady loading due to gusts on bridge decks. *Journal of Wind Engineering and Industrial Aerodynamics*, 91:1431–1443.

[104] Larsen, A. (1993). Aerodynamic aspects of the final design of the 1624 m suspension bridge accross the Greal Belt. *Journal of Wind Engineering and Industrial Aerodynamics*, 48:261–285.

[105] Larsen, A. (1997). Prediction of aeroelastic stability of suspension bridges during erection. *Journal of Wind Engineering and Industrial Aerodynamics*, 72:265–274.

[106] Larsen, A. and Astiz, M. A. (1998). Aeroelastic considerations for the Gibraltar Bridge feasibility study. In *Larsen A, Esdahl S, eds Bridge Aerodynamics*, Rotterdam: Balkema.

[107] Larsen, A., Esdahl, S., Andersen, J., and Verjum, T. (2000). Storebaelt Suspension Bridge: vortex shedding excitation and mitigation by guide vanes. *Journal of Wind Engineering and Industrial Aerodynamics*, 88:283–296.

[108] Larsen, A. and Larose, G. L. (2015). Dynamic wind effects on suspension and cable-stayed bridges. *Journal of Sound and Vibration*, 334:2–28.

[109] Larsen, A., Vejrum, T., and Esdahl, S. (1998). Vortex models for aeroelastic analysis assessment of multi-element bridge decks. In *Bridge aerodynamics, Larsen&Esdahl*, Balkema,Rotterdam.

[110] Lazar, I. F., Neild, S. A., and Wagg, D. J. (2014). Using and inerter-based device for structural vibration suppression. *Earthquake engineering and structural dynamics*, 43:1129–1147.

[111] Lazzari, M. (2005). Time domain modelling of aeroelastic bridge decks: a comparative study and an application. *International Journal for Numerical Methods in Engineering*, 62:1064–1104.

[112] Leishman, J. G. (2006). *Principles of Helicopter Aerodynamics*. Cambridge University Press.

[113] Li, K., Ge, Y. J., Guo, Z. W., and Zhao, L. (2015). Theoretical framework of feedback aerodynamic control of flutter oscillation for long-span suspension bridges by the twin-winglet system. *Journal of Wind Engineering and Industrial Aerodynamics*, 145:166–177.

[114] Liepmann, H. W. (1952). On the application of statistical concepts to the buffeting problem. *Journal of the Aeronautical Sciences*, 19:793–800.

[115] Limebeer, D. J. N., Graham, J. M. R., and Zhao, X. (2011). Buffet suppression in long-span suspension bridges. *Annual Reviews in Control*, 35:235–246.

[116] Lin, Y. K. (1979). Motion of suspension bridges in turbulent winds. *Journal of Engineering Mechanics Division, ASCE*, 105:921–932.

[117] Lin, Y. K. and Yang, J. N. (1983). Multimode bridge response to wind excitations. *Journal of Engineering Mechanics Division, ASCE*, 109:586–603.

[118] Lin, Y. Y., Cheng, C., and Lee, C. (2003). A tuned-mass damper for suppressing the coupled flexural and torsional buffeting response of long-span bridges. *Journal of Engineering Structures*, 22:1195–1204.

[119] Liu, G., Meng, F., and Wang, X. (2006). Mechanism of flutter control of suspension bridge by winglets. In *Proc., The fourth International Symposium on Computational Wind Engineering (CWE2006)*, Yokohama,Japan.

[120] Lopes, G. B. R. and Silva, R. S. (2010). Time domain modelling and bridge deck flutter and applications. *Mecanica Computational*, 14:529–553.

[121] Maher, F. (1948). Wind tunnel tests of suspension bridge section models. *Bulletin No. 69, Engineering experimental Station, Virginia Polytechnique Institute*, 41:1–50.

[122] Makoto, K. (2004). Technology of the Akashi Kaikyo Bridge. *Journal of Structural Control and Health Monitoring*, 11:75–90.

[123] Mannini, C. and Bartoli, G. (2015). Aerodynamic uncertainty propagation in bridge flutter analysis. *Journal of Structural Safety*, 52.

[124] Marian, L. and Giaralis, A. (2014). Optimal design of a novel tuned mass-damper-inerter (tmdi) passive vibration control configuration for stochastically support-excited structural systems. *Journal of Probabilistic Engineering Mechanics*, 38:146–164.

[125] Martins, N., Lima, T. G., and Pinto, J. C. R. (1996). Computing dominant poles of power system multivariable transfer functions. *IEEE Transaction of Power Systems*, 1:162–170.

[126] Martins, N. and Quintao, P. E. M. (2003). Computing dominant poles of power system multivariable transfer functions. *IEEE Transaction of Power Systems*, 18:152–159.

[127] Massaro, M., Bakis, K. N., Limebeer, D. J. N., and Graham, M. J. R. (2015). Flutter and buffeting of long span suspension bridges in fully erected and partially erected conditions. In *International Forum on Aeroelasticity and Structural Dynamics*, Saint Petersburg, Russia.

[128] Massaro, M. and Graham, J. M. R. (2015). The effect of three-dimensionality on the aerodynamic admittance of thin sections in free stream turbulence. *Journal of Fluids and Structures*, 57:81–90.

[129] Matsumoto, M. (1996). Aerodynamic damping of prisms. *Journal of Wind Engineering and Industrial Aerodynamics*, 59:159–175.

[130] Matsumoto, M., Mizuno, K., Okubo, K., Ito, Y., and Matsumiya, M. (2007). Flutter instability and recent development in stabilization of structures. *Journal of Wind Engineering and Industrial Aerodynamics*, 95:888–907.

[131] Matsumoto, M., Yagi, T., Hatsuda, H., Shima, T., and Tanaka, M. (2010). Dry galloping characteristics and its mechanism of inclined/yawed cables. *Journal of Wind Engineering and Industrial Aerodynamics*, 98.

[132] McFarlance, D. C. and Glover, K. (1990). *Robust Controller Design Using Normalized Coprime factor Plant Descriptions*. Lecture Notes in Control and information Sciences, 138, Springer-Verlag Berlin, Heidelberg.

[133] McRobie, A., Morgenthal, G., Abrams, D., and Prendergast, J. (2013). Parallels between wind and crowd loading of bridges. *Philosophical Transactions of the Royal Society*, 371:1–17.

[134] Meirovitch, L. (1989). *Dynamics and Control of Structures*. John Wiley & Sons.

[135] Meirovitch, L. (2001). *Fundamentals of Vibrations*. McGraw-Hill.

[136] Miyata, T. and Yamaguchi, T. (1993). Theory and history of suspension bridge design from 1823 to 1940. *Journal of Wind Engineering and Industrial Aerodynamics*, 48:287–325.

[137] Miyata, T., Yokohama, K., Yasuda, M., and Hikami, Y. (1992). Bluff body aerodynamic application in challenging bridge span length. In *Larsen A.(ed) Aerodynamics of large bridges*, pages 217–236, Balkema, Totterdam.

[138] Morgenthal, G. (2000). *Fluid-Structure Interaction in Bluff-Body Aerodynamics and Long-Span Bridge Design:Phenomena and Methods*. Technical Report No. CUED/D-Struct/TR.187.

[139] Myerscough, M. and Hayward, C. (2013). Suspension bridges: past and present. *The Structural Engineer*, 91, Issue 7:12–21.

[140] Namini, A. (1991). Analytical modelling of flutter derivatives as finite elements. *Journal of Computers and Structures*, 41(5):1055–1064.

[141] Namini, A. H., Albrecht, P., and Bosch, H. (1992). Finite element based flutter analysis of cable suspended bridges. *Journal of Structural Engineering ASCE*, 118(6):1509–1526.

[142] NMI (1977). *NMI Reports on the aerodynamic stability of the Humber Bridge in erection conditions*. NMI, 89/0353 and 89/0361.

[143] Omenzetter, P. (1999). *Aerodynamic Control of Wind Induced Instabilities of Long Span Bridges by Auxiliary Flaps*. PhD thesis, the University of Tokyo, Department of Civil Engineering.

[144] Omenzetter, P., Wilde, K., and Fujino, Y. (2000a). Suppression of wind-induced instabilities of a long span bridge by a passive deck-flaps control system part I: Formulation. *Journal of Wind Engineering*, 87:61–79.

[145] Omenzetter, P., Wilde, K., and Fujino, Y. (2000b). Suppression of wind-induced instabilities of a long span bridge by a passive deck-flaps control system part II: Numerical simulations. *Journal of Wind Engineering*, 87:81–91.

[146] Omenzetter, P., Wilde, K., and Fujino, Y. (2002). Study of passive deck-flaps flutter control system on full bridge model 1: Theory. *Journal of Engineering Mechanics*, March:264–279.

[147] Ostenfeld, K. H. and Larsen, A. (1992). Bridge engineering and aerodynamics. In *Aerodynamics of Large Bridges, Proceedings of the First International Symposium on Aerodynamics of Large Bridges*, Copenhagen,Denmark.

[148] Otsuki, Y., Washizu, K., Tomizawa, H., and Ohya, A. (1974). A note on the aeroelastic instability of a prismatic bar with square section. *Journal of Sound and Vibration*, 34(2):233–248.

[149] Packard, A. and Doyle, J. (1993). The complex structured singular value. *Automatica*, 29:71–109.

[150] Palacios, R., Murua, J., and Cook, R. (2010). Structural and aerodynamic models in nonlinear flight dynamics of very flexible aircraft. *AIAA Journal*, 11:2648–2659.

[151] Peters, D. A. (2008). Two-dimensional incompressible unsteady airfoil theory — an overview. *Journal of Fluids and Structures*, 24(3):295–312.

[152] Petroski, H. (1996). *Engineers of Dreams*. New York: Vintage Books.

[153] Phongkumsing, S., Wilde, K., and Fujino, Y. (2000). Analytical study on flutter suppression by eccentric mass method on a FEM model of a long-span suspension bridge. *Journal of Wind Engineering and Industrial Aerodynamics*, 89:515–534.

[154] Pourzeynali, S. and Datta, T. K. (2002). Reliability analysis of suspension bridges against flutter. *Journal of Sound and Vibration*, 254:143–162.

[155] Pourzeynali, S. and Datta, T. K. (2005). Semiactive fuzzy logic control of suspension bridge flutter. *Journal of Structural Engineering, ASCE*, 131:900–912.

[156] Przemieniecki, J. S. (1968). *Theory of Matrix Structural Analysis*. Dover Publications, Inc. New York.

[157] Rahbari, R., Niu, J., Brownjohn, J. M. W., and Koo, K. Y. (2015). Structural identification of Humber Bridge for performance prognosis. *Smart Structures and Systems*, 15(3):665–682.

[158] R.Hughes, T. J. (2000). *The Finite Element Method*. Dover Publications.

[159] Roger, K. L. (1997). *Airplane math modelling methods for active control design*. AGAPO-CP-228, New York.

[160] Rommes, J. (2007). *Methods for eigenvalue problems with applications in model order rduction*. PhD Thesis, Utrecht, The Netherlands.

[161] Sarkar, P. P., Jones, N. P., and Scanlan, R. H. (1994). Identification of aeroelastic parameters of flexible bridges. *Journal of Engineering Mechanics*, 120:1718–1742.

[162] Scanlan, R. (1990). Bridge aeroelasticity: Present state and future challenges. *Journal of Wind Engineering and Industrial Aerodynamics*, 36:63–74.

[163] Scanlan, R. H. (1978). The action of flexible bridges under wind, I: Flutter theory. *Journal of Sound and Vibration*, 60(2):187–199.

[164] Scanlan, R. H. (1993). Problematics in formulation of wind-force model for bridge deck. *Journal of Engineering Mechanics*, 119:1353–1375.

[165] Scanlan, R. H. (2012). Observations on low-speed aeroelasticity. *Journal of Engineering Mechanics*, 128:1254–1258.

[166] Scanlan, R. H., Beliveau, J. G., and Budlong, K. S. (1974). Indicial aerodynamic functions for bridge decks. *Journal of Engineering Mechanics, ASCE*, 100:657–672.

[167] Scanlan, R. H. and Gade, R. H. (1977). Motion of suspended spans under gusty wind. *Journal of Structural Division, ASCE*, 103 No.9:1867–1883.

[168] Scanlan, R. H. and Jones, N. P. (1990). Aeroelastic analysis of cable stayed bridges. *Journal of Structural Division, ASCE*, 116 No.2:279–297.

[169] Scanlan, R. H. and Tomko, J. J. (1971). Airfoil and bridge deck flutter derivatives. *Journal of Engineering Mechanics*, 97(6):1717–1737.

[170] Scruton, C. (1952). Experimental investigation of aerodynamic stability of suspension bridges with special reference to the proposed Severn Bridge. In *Proceedings of the Institute of Civil Engineers*, volume 1 issue 2, pages 189–222.

[171] Sears, W. R. (1940). Operational methods in the theory of airfoils in non-uniform motion. *Journal of the Franklin Institute*, 230:95–111.

[172] Sears, W. R. (1941). Some aspects of non-stationary airfoil theory and its practical application. *AIAA Journal Special Supplement: Centennial of powered flight*, 8(3):104–108.

[173] Selberg, A. (1961). *Oscillation and Aerodynamic Stability of Suspension Bridges*. Acta Polytechnica Scandinavica, No.308, Stockholm.

[174] Sherwood, H. T. and Wiliams, M. A. (1988). Nonlinear programming extensions to rational function approximation methods for unsteady aerodynamic forces. *NACA Report, TR-2776*.

[175] Simiu, E. and Scanlan, R. H. (1996). *Wind Effects on Structures: Fundamentals and Applications to Design*. Wiley-Interscience.

[176] Skogestad, S. and Postlethwaite, I. (2006). *Multivariable Feedback Control: Analysis and Design*. 2nd Ed. Wiley.

[177] Smith, M. C. (2002). Synthesis of mechanical networks: The inerter. *IEEE Trans. Automatic Control*, 47(10):1648–1662.

[178] Starossek, U. (1993). Prediction of bridge flutter through use of finite elements. *Structural Engineering review*, 5(4):301–307.

[179] Starossek, U. (1998). Complex notation in flutter analysis. *Journal of Structural Engineering*, pages 975–977.

[180] Starossek, U. and Aslan, H. (2008). Passive control of bridge deck flutter using tuned mass dampers and control surfaces. In *7th European Conference on Strcutural Dynamics*, Southampton,United Kingdom.

[181] Starossek, U., Aslan, H., and Thiesemann, L. (2009). Experimental and numerical identification of flutter derivatives for nine bridge deck sections. *Wind and Structures*, 12 No.6:519–540.

[182] Steinam, D. B. (1922). *A Practical Treatise on Suspension Bridges*. John Wiley & Sons, Inc., New York.

[183] Tanaka, H. and Ge, Y. (1999). Aerodynamic consideration of cable supported bridges during erection. In *International Conference on Suspension, Cable Supporte, and Cable Stayed Bridges*, pages 91–100, Hyderbad, India.

[184] Tanaka, H. and Gimsing, N. J. (1999). Aerodynamic stability of non-symmetrically erected suspension bridge girders. *Journal of Wind Engineering and Industrial Aerodynamics*, 80:85–104.

[185] Tanaka, H., Larose, G. L., and Kimura, K. (1992). Aerodynamics of long-span bridges during erection. In *Aerodynamics of Large Bridges (ed. Larsen)*, pages 119–127, Balkema.

[186] Theodorsen, T. (1934). General theory of aerodynamic instability and the mechanisms of flutter. *NACA Report, TR-496*.

[187] Theodorsen, T. and Garrick, I. E. (1942). Nonstationary flow about a wing-aileron-tab combination including aerodynamic balance. *NACA Report, TR-736*.

[188] Tuanjie, L. and Yujuan, M. (2011). Robust vibration control of flexible tensegrity structure via $\mu$ synthesis. *Journal of Structural Control and Health Monitoring*, 20:173–186.

[189] Ueda, T., Tanaka, T., and Matsushita, Y. (1998). Aerodynamic stabilization of super long-span suspension bridges. In *Proc. IABSE symposium- Long-Span and High-Rise Structures*, pages 721–728, Kobe, Japan.

[190] Ukegushi, N., Sakata, H., and Nishitani, H. (1966). An investigation of aeroelastic instability of suspension bridges. In *Proc. of International Symposium on Suspension Bridges*, pages 273–284, Lisbon.

[191] Vandiver, J. K. and Seto, K. (2000). Predicting lock-in on drilling risers in sheared flows. In *Flow-Induced Vibration 2000 Conference, Lucerne, Switzerland*.

[192] Vidyasagar, M. and Kimura, H. (1986). Robust controllers for uncertain linear multivariable systems. *Automatica*, pages 85–94.

[193] Vincent, G. S. (1952). Mathematical prediction of suspension bridge behaviour in wind from dynamic section model tests. *International Association for Bridge and Structural Engineering*, 12:303–321.

[194] Wagner, H. (1925). Uber die entstehung des dynamisches auftriebes von tragflugeln. *Zeitschrift fur Angewandte Mathematik und Mechanik*, 591:17–35.

[195] Walshe, D. E. (1963). The use of models to predict the oscillatory behaviour of suspension bridges. In *Proc. International Conference on Wind Effects on Buildings and Structures*, National Physical Laboratory, Teddington, England.

[196] Wang, F. C., Chen, C. W., Liao, M. K., and Hong, M. F. (2007). Performance analysis of building suspension control with inerters. In *Proceedings of the 46th IEEE conference on Decision and Control*, pages 3786–3791, New Orleans, LA, USA.

[197] Wardlaw, R. L. (1994). Flutter and torsional instability. In *Wind-excited vibrations of structures: CISM Courses and Lectures No. 335*, pages 217–236, SPRINGER-VERLAG WIEN.

[198] Weight, A. J. (2009). Critical analysis of the Great Belt East Bridge, Denmark. In *Proc. of Bridge Engineering 2 Conference*, pages 273–284, University of Bath, Bath, U.K.

[199] Weisshaar, T. A. (1995). *Aeroelasticity, an introduction to fundamental problems*. Purdue University.

[200] West, H. and Robinson, A. R. (1967). *A Re-Examination of the Theory of Suspension Bridges*. PhD Dissertation, University of Illinois Urbana.

[201] Wilde, K., Fujino, Y., and Kawakami, T. (1999). Analytical and experimental study on passive aerodynamic control of flutter of a bridge deck. *Journal of Wind Engineering and Industrial Aerodynamics*, 80:105–119.

[202] Wilson, J. C. and Gravelle, W. (1991). Modelling of a cable-stayed bridge for dynamic analysis. *Earthquake Engineering and Structural Dynamics*, 20:707–721.

[203] Xiang, H. F. and Ge, Y. J. (2003). On aerodynamic limit to suspension bridges. In *11th International Conference on Wind Engineering*, Texas USA.

[204] Xu, Y. L. (2013). *Wind Effects on Cable-Supported Bridges*. Wiley.

[205] Xu, Y. L., Sun, D. K., Ko, J. M., and Lin, J. H. (2000). Fully coupled buffeting analysis of the Tsing Ma suspension bridge. *Journal of Wind Engineering and Industrial Aerodynamics*, 85:97–117.

[206] Zasso, A. and Curami, A. (1993). Extensive investigation of bridge deck aeroelastic coefficient: Average angle, Reynolds number and other parameters effects. In *Proc., 3rd Asian Pacific Symposium on Wind Engineering*, pages 143–148, Hong Kong.

[207] Zhao, X., Limebeer, D. J. N., and Graham, J. M. R. (2011). Flutter control of long-span suspension bridges. In *50th IEEE Conference on Decision and Control and European Control Conference (CDC-ECC)*, Orlando,FL,USA.

[208] Zhao, X., Limebeer, D. J. N., and Graham, M. J. R. (2014). Modelling and control of a suspended-span bridge section. In *19th World Congress, The International Federation of Automatic Control*, Cape Town,South Africa.

[209] Zhou, K. and Doyle, J. C. (1998). *Essentials of Robust Control*. Prentice-Hall, Inc.

# Appendix A

# Cable Tension and Configuration

In order to evaluate the structural stiffness matrices reported in Appendix B, both the horizontal cable force $H$ and the cable configuration, namely the average hanger length $l_h$ at each element, need to be computed at every erection stage. The approach reported in [85] is here briefly summarized.

It is assumed that the cable is of uniform cross section, obeys Hooke's law, and has negligible flexural rigidity. In addition it is assumed that the cable's weight is uniformly distributed along the span rather than along the cable: this results in a parabolic rather than a catenary profile. The latter approximating assumption is accurate provided that the sag to span ratio is kept small ($1/8$ or less), which is common for most long span bridges. The first step consists in evaluating the single cable horizontal dead force $H_i$ assuming cable inextensibility

$$H_i = \frac{(m_c g/2)\, l^2}{8 f_i}, \tag{A.1}$$

where, $m_c$ is the mass of both cables per unit length, $g$ is the gravity acceleration, $l$ is the span length and $f_i$ is the sag of the inextensible cable. Note that the $H_i$ is constant along the cable, while the cable tension $T$ varies, $T = H/\cos(\alpha)$, with $\alpha$ being the inclination of the cable profile. Note that $T$ is minimum and equal to $H_i$ at the mid span and maximum at the supports.

Secondly, the effect of cable elasticity (stretching) is included to account for the reduction in cable tension and the increase in sag

$$H_s = H_i\,(1-H_*)\,, \qquad f_s = f_i\,(1+f_*)\,, \tag{A.2}$$

where $H^*$ and $f^*$ depend on the factor $\lambda$

$$\lambda^2 = \left[\frac{(m_c g/2)\,l}{H_i}\right]^2 \frac{l}{\left(\frac{H_i L_e}{E_c A_c}.\right)} \tag{A.3}$$

$E_c$ denotes the Young modulus of the cable, $A_c$ is the cable section area and $L_e$ is defined as

$$L_e = l\left(1+8\left(\frac{f_i}{l}\right)^2\right). \tag{A.4}$$

If $\lambda^2$ is large ($>100$), as is the case for most long span suspension bridges ($\lambda^2 > 900$ in the case of Great Belt bridge), $H^*$ and $f^*$ can be expressed through the following simple formulas

$$H_* \approx \frac{1}{3+\frac{\lambda^2}{12}}, \qquad f_* \approx \frac{1}{2+\frac{\lambda^2}{12}}. \tag{A.5}$$

Thirdly, the loading related to the deck weight (transmitted through the hangers) is considered, and the related increase in cable tension and sag are computed as follows

$$H_l = H_s\,(1+h_*)\,, \qquad f_l = f_s + \frac{(m_e g/2)\,l^2}{H_s} v_*\left(x=\frac{l}{2}\right), \tag{A.6}$$

where, $h^*$ is the (positive root) solution of the following polynomial

$$\begin{aligned} &h_*^3 + \left(2+\tfrac{\lambda^2}{24}\right)h_*^2 + \left(1+\tfrac{\lambda^2}{12}\right)h_* - \tfrac{\lambda^2}{2}\left[\tfrac{1}{2}\left(\left(\tfrac{x_3}{l}\right)^2 - \left(\tfrac{x_2}{l}\right)^2\right) - \tfrac{1}{3}\left(\left(\tfrac{x_3}{l}\right)^3 - \left(\tfrac{x_2}{l}\right)^3\right)\right] p_* \\ &-\tfrac{\lambda^2}{2}\left[\tfrac{1}{3}\left(\left(\tfrac{x_3}{l}\right)^3 + 2\left(\tfrac{x_2}{l}\right)^3\right) - \tfrac{x_3}{l}\left(\tfrac{x_2}{l}\right)^2 - \tfrac{1}{4}\left(\left(\tfrac{x_3}{l}\right)^2 - \left(\tfrac{x_2}{l}\right)^2\right)^2\right] p_*^2 = 0, \end{aligned} \tag{A.7}$$

where

$$p_* = \frac{m_e g/2}{m_c g/2} = \frac{m_e}{m_c}. \tag{A.8}$$

$m_e$ being the deck mass per unit length, $m_c$ the mass of both cables per unit length, $x_2$ and $x_3$ the ends points of application for the distributed load ($x_2 = 0$ and $x_3 = l$ when the full bridge is erected, while $x_2 > 0$ and $x_3 < l$ during the erection stages). The additional cable deflection related to the deck loading is computed using the following formulas for each of the cases: left unloaded section ($0 < x < x_2$), central loaded section ($x_2 < x < x_3$) and right unloaded section ($x_3 < x < l$).

$$v_*\left(0 < \tfrac{x}{l} < \tfrac{x_2}{l}\right) = \tfrac{1}{1+h_*}\left[\left(\left(\tfrac{x_3}{l}\right) - \left(\tfrac{x_2}{l}\right) - \tfrac{1}{2}\left(\left(\tfrac{x_3}{l}\right)^2 - \left(\tfrac{x_2}{l}\right)^2\right)\right)\left(\tfrac{x}{l}\right) - \tfrac{h_*}{p_*}\left(\tfrac{1}{2}\left(\tfrac{x}{l}\right) - \tfrac{1}{2}\left(\tfrac{x}{l}\right)^2\right)\right] \quad \text{(A.9)}$$

$$v_*\left(\tfrac{x_2}{l} < \tfrac{x}{l} < \tfrac{x_3}{l}\right) = \tfrac{1}{1+h_*}\left[\left(-\tfrac{1}{2}\left(\tfrac{x_2}{l}\right)^2 + \left(\tfrac{x_3}{l}\right)\left(\tfrac{x}{l}\right) - \tfrac{1}{2}\left(\tfrac{x}{l}\right)^2 - \tfrac{1}{2}\left(\left(\tfrac{x_3}{l}\right)^2 - \left(\tfrac{x_2}{l}\right)^2\right)\left(\tfrac{x}{l}\right)\right) - \tfrac{h_*}{p_*}\left(\tfrac{1}{2}\left(\tfrac{x}{l}\right) - \tfrac{1}{2}\left(\tfrac{x}{l}\right)^2\right)\right] \quad \text{(A.10)}$$

$$v_*\left(\tfrac{x_3}{l} < \tfrac{x}{l} < 1\right) = \tfrac{1}{1+h_*}\left[\tfrac{1}{2}\left(\left(\tfrac{x_3}{l}\right)^2 - \left(\tfrac{x_2}{l}\right)^2\right)\left(1 - \tfrac{x}{l}\right) - \tfrac{h_*}{p_*}\left(\tfrac{1}{2}\left(\tfrac{x}{l}\right) - \tfrac{1}{2}\left(\tfrac{x}{l}\right)^2\right)\right] \quad \text{(A.11)}$$

Only Eq.(A.11) is necessary when the full bridge is erected, and the additional sag is computed by evaluating Eq.(A.11) for $x/l = 1/2$. It is easily concluded that the horizontal tension $H$ from both cables and the sag $f$ is given by

$$H = 2H_l, \qquad f = f_l. \quad \text{(A.12)}$$

The average hanger length $l_h$ at each element is easily computed from geometric considerations, since the whole cable profile has been determined. Note that when the bridge is partially erected the cable profile is no more parabolic, while it is parabolic before deck erection and at the completion stage.

In practice, the inextensible sag $f_i$ in Eq.(A.1) is guessed and the final sag $f$ in Eq.(A.12) is checked against the sag of the real bridge until convergence is reached. Alternatively, if the length of the inextensible cable $L_i$ is known, the inextensible sag $f_i$ can be computed from the following relationship

$$L_i = \int_0^l \sqrt{1 + \left[\frac{4f_i}{l}\left(1 - 2\frac{x}{l}\right)\right]^2}\, dx. \quad \text{(A.13)}$$

# Appendix B

# Structural Finite Element matrices

In addition to the elemental stiffness matrices for the vertical and torsional vibration case, the cable strain energy caused by the additional vibrational cable tension results in a symmetric well distributed array over the entire stiffness structure, which cannot be brought in an elemental form [3, 2], a general form of these well distributed matrices is shown schematically in Figure B.1. The equations describing the additional stiffness terms are given by the following expressions for the vertical vibration case

$$\mathbf{K}_{CEV} = \frac{E_c A_c}{L_e} \sum_{e=1}^{n_e} \left( \frac{w^*}{H} \mathbf{f}_{v,e} \right) \left( \frac{w^*}{H} \mathbf{f}_{v,e}^T \right), \tag{B.1}$$

where $n_e$ is the number of elements, and

$$\mathbf{f}_{v,e}^T = \left[ \begin{array}{cccc} \frac{L}{2}, & \frac{-L^2}{12}, & \frac{L}{2}, & \frac{L^2}{12},, \end{array} \right] \tag{B.2}$$

the virtual length given by the expression

$$L_e = l \left( 1 + 8 \left( \frac{f}{l} \right)^2 \right). \tag{B.3}$$

$l$ denotes the bridge span length, $w^*$ the total weight per unit length and $f$ the cable sag. Similarly for the torsional vibration case

$$\mathbf{K}_{CET} = \frac{2E_cA_c}{L_e} b_c^2 \sum_{e=1}^{n_e} \left(\frac{w^*}{H}\mathbf{f}_{t,e}\right)\left(\frac{w^*}{H}\mathbf{f}_{t,e}^T\right), \tag{B.4}$$

where

$$\mathbf{f}_{t,e} = \left[\begin{array}{cc} \frac{L}{2}, & \frac{L}{2} \end{array}\right]. \tag{B.5}$$

For the following matrices degrees of freedom 1..6 and 9..14 are related to the bridge

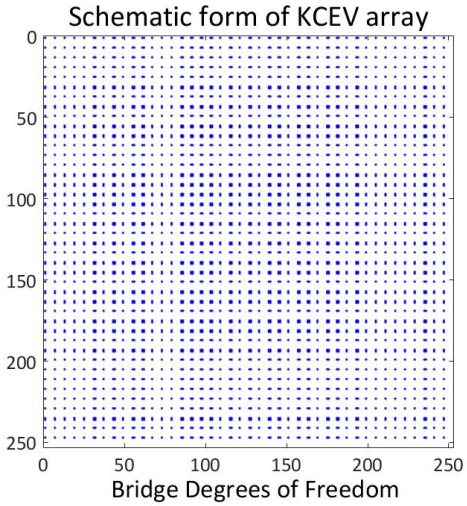


Figure B.1 Schematic form of partially complete distributed *KCEV* array.

structure according to Fig.3.4. The degrees of freedom $7,8$ and $15,16$ are associated with the leading and trailing edge flap rotations at nodes $i$ and $i+1$ of each element respectively.

| | |
|---|---|
| $K_s^e(1,1) = \frac{12EI_y}{L^3} + \frac{36H}{30L}$ | $K_s^e(4,12) = K_s^e(12,4) = \frac{(2-\Phi)EI_z}{L} - 3L^2\frac{WseL}{420l_h}$ |
| $K_s^e(1,2) = K_s^e(2,1) = -\frac{6EI_y}{L^2} - \frac{3H}{30}$ | $K_s^e(4,13) = K_s^e(13,4) = 14L\frac{WseL}{420l_h}$ |
| $K_s^e(1,9) = K_s^e(9,1) = -\frac{12EI_y}{L^3} - \frac{36H}{30L}$ | $K_s^e(5,5) = 140\left(1+\frac{l_h}{ye}\right)\frac{WseL}{420l_h} + +2\frac{WseL}{6ye} + \frac{2H}{L} + 2\frac{(Wse+Wce)}{6ye}$ |
| $K_s^e(1,10) = K_s^e(10,1) = -\frac{6EI_y}{L^2} - \frac{3H}{30}$ | $K_s^e(5,11) = K_s^e(11,5) = -63\frac{WseL}{420l_h}$ |
| $K_s^e(2,2) = \frac{(4+\Phi)EI_y}{L} + \frac{4HL}{30}$ | $K_s^e(5,12) = K_s^e(12,5) = -14L\frac{WseL}{420l_h}$ |
| $K_s^e(2,9) = K_s^e(9,2) = \frac{6EI_y}{L^2} + \frac{3H}{30}$ | $K_s^e(5,13) = K_s^e(13,5) = 70\left(1+\frac{l_h}{ye}\right)\frac{WseL}{420l_h} - -\frac{2H}{L} + \frac{Wse+Wce}{6ye} + \frac{WseL}{6ye}$ |
| $K_s^e(2,10) = K_s^e(10,2) = \frac{(2-\Phi)EI_y}{L} - \frac{HL}{30}$ | $K_s^e(6,6) = K_s^e(14,14) = \frac{GI_a}{L} + \frac{36Hb_c^2}{15L}$ |
| $K_s^e(9,9) = \frac{12EI_y}{L^3} + \frac{36H}{30L}$ | $K_s^e(6,14) = K_s^e(14,6) = -\frac{GI_a}{L} - \frac{36Hb_c^2}{15L}$ |
| $K_s^e(9,10) = K_s^e(10,9) = \frac{6EI_y}{L^2} + \frac{3H}{30}$ | $K_s^e(7,7) = \frac{K_\beta L}{2}$ |
| $K_s^e(10,10) = \frac{(4+\Phi)EI_y}{L} + \frac{4HL}{30}$ | $K_s^e(8,8) = \frac{K_\gamma L}{2}$ |
| $K_s^e(3,3) = \frac{12EI_z}{L^3} + 156\frac{WseL}{420l_h}$ | $K_s^e(11,11) = \frac{12EI_z}{L^3} + 156\frac{WseL}{420l_h}$ |
| $K_s^e(3,4) = K_s^e(4,3) = -\frac{6EI_z}{L^2} - 22L\frac{WseL}{420l_h}$ | $K_s^e(11,12) = K_s^e(12,11) = \frac{6EI_z}{L^2} + 22L\frac{WseL}{420l_h}$ |
| $K_s^e(3,5) = K_s^e(5,3) = -147\frac{WseL}{420l_h}$ | $K_s^e(11,13) = K_s^e(13,11) = -147\frac{WseL}{420l_h}$ |
| $K_s^e(3,11) = K_s^e(11,3) = -\frac{12EI_z}{L^3} + 54\frac{WseL}{420l_h}$ | $K_s^e(12,12) = \frac{(4+\Phi)EI_z}{L} + 4L^2\frac{WseL}{420l_h}$ |
| $K_s^e(3,12) = K_s^e(12,3) = -\frac{6EI_z}{L^2} + 13L\frac{WseL}{420l_h}$ | $K_s^e(12,13) = K_s^e(13,12) = -21L\frac{WseL}{420l_h}$ |
| $K_s^e(3,13) = K_s^e(13,3) = -63\frac{WseL}{420l_h}$ | $K_s^e(13,13) = 140\left(1+\frac{l_h}{ye}\right)\frac{WseL}{420l_h} + +2\frac{WseL}{6ye} + \frac{2H}{L} + 2\frac{(Wse+Wce)}{6ye}$ |
| $K_s^e(4,4) = \frac{(4+\Phi)EI_z}{L} + 4L^2\frac{WseL}{420l_h}$ | $K_s^e(15,15) = \frac{K_\beta L}{2}$ |
| $K_s^e(4,5) = K_s^e(5,4) = 21L\frac{WseL}{420l_h}$ | $K_s^e(16,16) = \frac{K_\gamma L}{2}$ |
| $K_s^e(4,11) = K_s^e(11,4) = \frac{6EI_z}{L^2} - 13L\frac{WseL}{420l_h}$ | |

Table B.1 Elemental Structural Matrices.

| | |
|---|---|
| $M_s^e(1,1) = M_s^e(3,3) = 156\frac{m_e L}{420}$ | $M_s^e(5,5) = 2\frac{m_c L}{6}$ |
| $M_s^e(1,2) = M_s^e(2,1) = -22L\frac{m_e L}{420}$ | $M_s^e(5,13) = M_s^e(13,5) = \frac{m_c L}{6}$ |
| $M_s^e(1,9) = M_s^e(9,1) = 54\frac{m_e L}{420}$ | $M_s^e(6,6) = I_m\frac{L}{3}$ |
| $M_s^e(1,10) = M_s^e(10,1) = 13L\frac{m_e L}{420}$ | $M_s^e(9,9) = M_s^e(11,11) = 156\frac{m_e L}{420}$ |
| $M_s^e(2,2) = M_s^e(4,4) = 4L^2\frac{m_e L}{420}$ | $M_s^e(9,10) = M_s^e(10,9) = 22L\frac{m_e L}{420}$ |
| $M_s^e(2,9) = M_s^e(9,2) = -13L\frac{m_e L}{420}$ | $M_s^e(10,10) = M_s^e(12,12) = 4L^2\frac{m_e L}{420}$ |
| $M_s^e(2,10) = M_s^e(10,2) = -3L^2\frac{m_e L}{420}$ | $M_s^e(11,12) = M_s^e(12,11) = M_s^e(9,10)$ |
| $M_s^e(3,4) = M_s^e(4,3) = M_s^e(1,2)$ | $M_s^e(13,13) = 2\frac{m_c L}{6}$ |
| $M_s^e(3,11) = M_s^e(11,3) = M_s^e(1,9)$ | $M_s^e(14,6) = M_s^e(6,14) = I_m\frac{L}{6}$ |
| $M_s^e(3,12) = M_s^e(12,3) = M_s^e(1,10)$ | $M_s^e(14,14) = I_m\frac{L}{3}$ |
| $M_s^e(4,11) = M_s^e(11,4) = M_s^e(2,9)$ | $M_s^e(1,7) = M_s^e(7,1) = M_s^e(9,15) = = M_s^e(15,9) = \frac{L}{2}S_\beta$ |
| $M_s^e(4,12) = M_s^e(12,4) = M_s^e(2,10)$ | $M_s^e(1,8) = M_s^e(8,1) = M_s^e(10,16) = = M_s^e(16,10) = \frac{L}{2}S_\gamma$ |
| $M_s^e(6,7) = M_s^e(7,6) = \frac{L}{2}[-(I_\beta - bc_l S_\beta)]$ | $M_s^e(14,16) = M_s^e(16,14) = \frac{L}{2}[(I_\gamma + bc_t S_\gamma)]$ |
| $M_s^e(14,15) = M_s^e(15,14) = M_s^e(6,7)$ | $M_s^e(14,16) = M_s^e(16,14) = M_s^e(6,8)$ |

Table B.2 Elemental Mass Matrices.

| | |
|---|---|
| $E$ : Young's Modulus of Elasticity | $G$ : Shear Modulus of Elasticity |
| $I_y$ : Second moment of inertia about horizontal axis | $I_z$ : Second moment of inertia about vertical axis |
| $I_a$ : Torsional moment of inertia | $m_e$ : Mass of the bridge per unit length |
| $L$ : Element Length | $b_c$ : Half chord distance between the cable plane |
| $h_e + y_e$ : Tower height measured from deck | $m_c$ : Mass of the cables per unit length |
| $H$ : Horizontal Cable Force | $I_m$ : Mass moment of inertia |
| $\Phi = \frac{12EI_y}{G\mu L^2}$ : Shear Coefficient | $\mu = (5/6)A$ : Effective shear area |
| $W_{se}$ : Weight of the suspended structure per unit length | $G\mu$ : Shear rigidity |
| $W_{ce}$ : Weight of the cable per unit length | $E_c$ : Young's modulus for the cables |
| $l_h$ : Average hanger length or each element | $A_c$ : Area of the cable |
| $K_\beta$ : spring connection for leading flap | $K_\gamma$ : spring connection for trailing flap |
| $S_\beta$ : First moment of inertia leading flap | $S_\gamma$ : First moment of inertia trailing flap |
| $I_\beta$ : Second moment of inertia leading flap | $I_\gamma$ : Second moment of inertia trailing flap |
| $c_l b$ : Location of the leading flap hinge | $c_t b$ : Location of the trailing flap hinge |

Table B.3 Notation

# Appendix C

# Functions T and Y

The functions $T_i(\cdot)$s, $Y_i(\cdot,\cdot)$s are derived from [187]. $T_i(\cdot)$s are functions of one variable, namely $c_l$ or $c_t$ whereas $Y_i(\cdot,\cdot)$s are functions of both variables. Here for notation simplicity we express in terms of variables $c$ and $d$.

$$T_1 = c \times cos^{-1}(c) - \frac{1}{3}(2+c^2)\sqrt{1-c^2} \tag{C.1}$$

$$T_2 = c(1-c^2) - (1+c^2)\sqrt{1-c^2}cos^{-1}(c) + c \times (cos^{-1}(c))^2 \tag{C.2}$$

$$T_3 = -\frac{1}{8}(1-c^2)(5c^2+4) + \frac{1}{4}c(7+2c^2)\sqrt{1-c^2}cos^{-1}(c) - \left(\frac{1}{8}+c^2\right)(cos^{-1}c)^2 \tag{C.3}$$

$$T_4 = c\sqrt{1-c^2} - cos^{-1}(c) \tag{C.4}$$

$$T_5 = -(1-c^2) + 2c\sqrt{1-c^2}cos^{-1}(c) - (cos^{-1}(c))^2 \tag{C.5}$$

$$T_6 = T_2(c) \tag{C.6}$$

$$T_7 = \frac{1}{8}c(7+2c^2)\sqrt{1-c^2} - \left(\frac{1}{8}+c^2\right)cos^{-1}(c) \tag{C.7}$$

$$T_8 = -\frac{1}{3}(1+2c^2)\sqrt{1-c^2} + c \times cos^{-1}(c) \tag{C.8}$$

$$T_9 = \frac{1}{6}(1-c^2)\sqrt{1-c^2} \tag{C.9}$$

$$T_{10} = \sqrt{1-c^2} + cos^{-1}(c) \tag{C.10}$$

$$T_{11} = (2-c)\sqrt{1-c^2} + (1-2c)cos^{-1}(c) \tag{C.11}$$

$$T_{12} = (2+c)\sqrt{1-c^2} - (1+2c)cos^{-1}(c) \tag{C.12}$$

$$T_{13} = -\frac{1}{2}(cT_1(c) + T_7(c)) \tag{C.13}$$

$$T_{15} = (1+c)\sqrt{1-c^2} \tag{C.14}$$

$$T_{16} = T_1(c) - T_8(c) - cT_4(c) + \frac{1}{2}T_{11}(c) \tag{C.15}$$

$$T_{17} = -2T_9(c) - T_1(c) - \frac{1}{2}T_4(c) \tag{C.16}$$

$$T_{18} = T_5(c) - T_4(c)T_{10}(c) \tag{C.17}$$

$$T_{19} = -\frac{1}{2}T_4(c)T_{11}(c) \tag{C.18}$$

$$T_{20} = -\sqrt{1-c^2} + cos^{-1}(c) \tag{C.19}$$

$$T_{21} = \sqrt{\frac{1+c}{1-c}} \tag{C.20}$$

$$T_{22} = 2\sqrt{1-c^2} - \sqrt{\frac{1+c}{1-c}} \tag{C.21}$$

$$T_{23} = (-1-2c)\sqrt{1-c^2} \tag{C.22}$$

$$T_{24} = T_8(c) + cT_4(c) \tag{C.23}$$

$$T_{25} = T_4(c) - (1-c)\sqrt{1-c^2} \tag{C.24}$$

$$T_{26} = 2\sqrt{1-c^2}T_{20}(c) + T_4(c)\sqrt{\frac{1+c}{1-c}} \tag{C.25}$$

$$T_{27} = T_4(c)T_{10}(c) - \sqrt{1-c^2}T_{11}(c) \tag{C.26}$$

$$T_{28} = 2[1+c+log(N(c,d))] \tag{C.27}$$

$$T_{29} = 2\sqrt{1-c^2}T_{10}(c) \tag{C.28}$$

$$Y_1 = -\sqrt{1-c^2}\sqrt{1-d^2} - cos^{-1}(c)cos^{-1}(d) + d\sqrt{1-d^2}cos^{-1}(c) + c\sqrt{1-c^2}cos^{-1}(d) - (d-c)^2 log(N(c,d)) \quad \text{(C.29)}$$

$$Y_2 = 2\sqrt{1-d^2}cos^{-1}(c) - 2(d-c)log(N(c,d)) \quad \text{(C.30)}$$

$$Y_3 = \frac{1}{3}(c+2d)\sqrt{1-c^2}\sqrt{1-d^2} + dcos^{-1}(c)cos^{-1}(d) - \frac{1}{3}(2+d^2)\sqrt{1-d^2}cos^{-1}(c) - \frac{1}{3}(1+3cd-c^2)\sqrt{1-c^2}cos^{-1}(d) + \frac{1}{3}(d-c)^3 log(N(c,d)) \quad \text{(C.31)}$$

$$Y_4 = \frac{1}{3}(d+2c)\sqrt{1-c^2}\sqrt{1-d^2} + c \times cos^{-1}(c)cos^{-1}(d) - \frac{1}{3}(2+c^2)\sqrt{1-c^2}cos^{-1}(d) - \frac{1}{3}(1+3cd-d^2)\sqrt{1-d^2}cos^{-1}(c) - \frac{1}{3}(d-c)^3 log(N(c,d)) \quad \text{(C.32)}$$

$$Y_5 = -\sqrt{1-c^2}\sqrt{1-d^2} + (2c-d)\sqrt{1-d^2}cos^{-1}(c) + (d-c)^2 log(N(c,d)) \quad \text{(C.33)}$$

$$Y_6 = -\frac{1}{2}\sqrt{1-c^2}\sqrt{1-d^2}\left[1+\frac{1}{6}c^2+\frac{1}{6}d^2+\frac{11}{12}cd\right] - \left(\frac{1}{8}+cd\right)cos^{-1}(c)cos^{-1}(d) + \frac{1}{3}\left[\frac{1}{4}d\left(\frac{5}{2}-d^2\right)+c\left(2+d^2\right)\right]\sqrt{1-d^2}cos^{-1}(c) + \frac{1}{3}\left[\frac{1}{4}c\left(\frac{5}{2}-c^2\right)d\left(2+c^2\right)\right]\sqrt{1-c^2}cos^{-1}(d) + \frac{1}{12}(d-c)^4 log(N(c,d)) \quad \text{(C.34)}$$

$$Y_7 = 2\sqrt{1-c^2}cos^{-1}(d) + 2(d-c)log(N(c,d)) \quad \text{(C.35)}$$

$$Y_8 = -\sqrt{1-c^2}\sqrt{1-d^2} + (2d-c)\sqrt{1-c^2}cos^{-1}(d) + (d-c)^2 log(N(c,d)) \quad \text{(C.36)}$$

$$Y_9 = Y_1(c,d) - T_4(c)T_{10}(d) \quad \text{(C.37)}$$

$$Y_{10} = Y_3(c,d) - Y_4(c,d) - \frac{1}{2}T_4(c)T_{11}(d) \quad \text{(C.38)}$$

$$Y_{11} = Y_7(c,d) - 2\sqrt{1-c^2}T_{10}(d) \quad \text{(C.39)}$$

$$Y_{12} = Y_1(c,d) - Y_8(c,d) - \sqrt{1-c^2}T_{11}(d) \tag{C.40}$$

$$Y_{13} = Y_2(c,d) + T_4(c)T_{21}(d) \tag{C.41}$$

$$Y_{14} = Y_1(c,d) - Y_8(c,d) - \sqrt{1-c^2}T_{11}(d) \tag{C.42}$$

$$Y_{15} = 2\sqrt{1-c^2}T_{21}(d) + 2log(N(c,d)) \tag{C.43}$$

$$Y_{16} = Y_2(c,d) - Y_7(c,d) + 2\sqrt{1-c^2}T_{10}(d) \tag{C.44}$$

$$Y_{17} = Y_1(c,d) - T_4(d)T_{10}(c) \tag{C.45}$$

$$Y_{18} = Y_4(c,d) - Y_3(c,d) - \frac{1}{2}T_4(d)T_{11}(c) \tag{C.46}$$

$$Y_{19} = Y_2(c,d) - 2\sqrt{1-d^2}T_{10}(c) \tag{C.47}$$

$$Y_{20} = Y_1(c,d) - Y_5(c,d) - \sqrt{1-d^2}T_{11}(c) \tag{C.48}$$

$$Y_{21} = Y_7(c,d) + T_4(d)T_{21}(c) \tag{C.49}$$

$$Y_{22} = -Y_1(c,d) + Y_8(c,d) + T_{10}(c)T_4(d) \tag{C.50}$$

$$Y_{23} = 2\sqrt{1-d^2}T_{21}(c) + 2log(N(c,d)) \tag{C.51}$$

$$Y_{24} = Y_7(c,d) - Y_2(c,d) + 2\sqrt{1-d^2}T_{10}(c) \tag{C.52}$$

where

$$N(c,d) = \left| \frac{1 - cd - \sqrt{1-c^2}\sqrt{1-d^2}}{d-c} \right|. \tag{C.53}$$